# INFORMATION TO USERS

This manuscript has been reproduced from the microfilm master. UMI films the text directly from the original or copy submitted. Thus, some thesis and dissertation copies are in typewriter face, while others may be from any type of computer printer.

**The quality of this reproduction is dependent upon the quality of the copy submitted.** Broken or indistinct print, colored or poor quality illustrations and photographs, print bleedthrough, substandard margins, and improper alignment can adversely affect reproduction.

In the unlikely event that the author did not send UMI a complete manuscript and there are missing pages, these will be noted. Also, if unauthorized copyright material had to be removed, a note will indicate the deletion.

Oversize materials (e.g., maps, drawings, charts) are reproduced by sectioning the original, beginning at the upper left-hand corner and continuing from left to right in equal sections with small overlaps.

Photographs included in the original manuscript have been reproduced xerographically in this copy. Higher quality 6" x 9" black and white photographic prints are available for any photographs or illustrations appearing in this copy for an additional charge. Contact UMI directly to order.

ProQuest Information and Learning
300 North Zeeb Road, Ann Arbor, MI 48106-1346 USA
800-521-0600

# Random Delamination of Graphite/Epoxy Laminated Composites: Stress Analysis, Failure Criteria, Experimental Characterization and Stochastic Modeling

Chao Zhang

A Thesis
in
The Department
of
Mechanical Engineering

Submitted in Partial Fulfillment of the Requirements
for the Degree of Doctor of Philosophy
Concordia University
Montreal, Quebec, Canada

June 2001

# ABSTRACT

**Random Delamination of Graphite/Epoxy Laminated Composites: Stress Analysis, Failure Criteria, Experimental Characterization and Stochastic Modeling**

Chao Zhang, Ph.D.
Concordia University, 2001

The delamination failure of laminated composites exhibits two distinct characteristics; (1) the corresponding failure strengths display considerable scatter, and (2) the morphologies of the fracture surfaces and the interlaminar strengths are dependent on the magnitude of the fiber orientation difference (abbreviated as FOD below) angle between the two adjacent plies of the interface. These characteristics need to be thoroughly investigated in order to have accurate information on the failure strengths governed by the delamination failure.

A *Stochastic Delamination Model* is hereby developed to comprehensively investigate the probabilistic characteristics of delamination failure, wherein the dependence of interlaminar strengths on the magnitude of FOD angle between two adjacent unidirectional plies in laminated composites, is viewed as a stochastic process. *The Stochastic Delamination Model* consists of four major aspects of research; stress analysis, failure criteria, experimental characterization and stochastic modeling.

A variational solution technique is developed to determine the three-dimensional edge effect stresses around pin-loaded holes in symmetric laminated composites. The stress state around the holes is divided into two parts, one the in-plane stress state determined using the Classical Laminated Plate Theory (CLPT) and the other the boundary layer stress state arising from the edge effects which only exists in the vicinity of the holes. The equilibrium equations of boundary layer stress state with zeroth-order approximation are derived from a set of power expansions. Analytical solutions for the boundary layer stress state are then obtained by imposing zeroth-order stress functions on the variational principle of complementary energy. The developed variational solution technique is versatile, which can be used to calculate the edge

effect stresses at straight free edges, curved free edges and pin-loaded hole edges with or without friction in laminated composites.

An experimental investigation is conducted to study the effects of fiber orientations on the interlaminar shear (ILS) strengths of CYTEC® G40-800/5276-1 graphite/epoxy laminated composites. The ILS strengths at the θ-interfaces (θ = 0°, 10°, 20°, 30°, 40°, 50°, 60°, 70°, 80° and 90°), around which the two neighboring plies have a FOD angle θ, are experimentally characterized using the modified double notch shear specimens with an elaborately designed lay-up. Because of the potentially considerable scatter in the matrix-dominated ILS strengths, each data set at a specified interface is obtained through a larger sample with 35 specimens. The variation tendencies and probabilistic characteristics of the ILS strengths with respect to θ are then studied on the basis of statistical analysis techniques.

A stochastic simulation model is proposed in a phenomenological sense, in which the probabilistic dependence of ILS strengths on the FOD angles θ is simulated as a non-Gaussian nonstationary stochastic process within the bounded interval [0, π/2]. The random trigonometric polynomials with unknown correlated random parameters are employed to approximately represent this type of stochastic process. The correlated random parameters are then determined based on the probabilistic characteristics of the experimental sample data sets at 10 particular values of θ at which the experiments are performed. With the generated stochastic process, the individual probability density functions and the other probabilistic characteristics of the ILS strengths can be obtained at any particular values of θ at which experiments are not performed.

Two innovative delamination criteria in terms of quadratic and cubic polynomials in each case, are developed based on the Malmeister strength theory and Hashin assumption. The intent of the developed criteria is to include the effects of θ-dependent and directionally-dependent interlaminar strengths into the failure evaluation of laminated composites, as demonstrated by the experiments in the present thesis. This intent is achieved by introducing the capability of strength tensor transformation to the delamination criteria. The random delamination failure induced by the straight edge effect stresses in two types of laminated composites under uniaxial tension is examined by applying the two developed criteria.

# ACKNOWLEDGEMENTS

I would first like to express my sincere gratitude to my thesis supervisor Dr. Suong V. Hoa for his invaluable guidance, continuous support and encouragement throughout the course of this research. His acute abilities to catch the weakest points in my papers are impressive.

I would also like to thank my thesis co-supervisor Dr. R. Ganesan for his valuable guidance in this research and careful examination on my publications.

I am deeply indebted to my wife, Cathy, for her love, understanding, patience and sacrifice during the five years I went through my thesis.

My special gratitude is given to Profs. Larry B. Lessard and James A. Nemes in the Department of Mechanical Engineering at McGill University. It was they who helped me come to Canada and provided me useful guidance when I started my graduate studies in McGill University.

I would like to thank Dr. Ming Xie and Mr. Paul Ouellette for their technical supports in the experiments, Ms. Lan Li for her introduction to ANSYS® Software, and Dr. Siyu Zhang for his assistance in the establishment of statistical analysis methods.

My special appreciation goes to Mr. Vincent D'arienzo at Bell Helicopter – Textron (Mirable, Quebec) for his help which made it possible for me to obtain the composite materials and calibrate the technical data for the curing cycle.

Special thanks are given to Natural Science and Engineering Research Council of Canada (NSERC), Canadian Space Agency Committee, Fonds pour la Formation de Chercheurs et l'Aide a la Recherche (FCAR), and Concordia University, for their awards and scholarships during the course of this research.

Finally, I would like to thank Velan Inc. (St-Laurent, Quebec) and Pratt & Whitney Canada Inc. (Longueuil, Quebec) for providing me the employment opportunities during the course of my thesis.

# TABLE OF CONTENTS

# LIST OF FIGURES

# LIST OF TABLES

# LIST OF NOMENCLATURE

**Chapter 3:**

| | |
|---|---|
| $A^{(i)}$, $B^{(i)}$, $C^{(i)}$ | parameters related to the stress functions |
| $F^{(i)}(\xi,\eta)$, $G^{(i)}(\xi,\eta)$ | stress functions for the i-th ply |
| $f_i$, $g_i$, $h_i$ | parameters used in the complementary energy principle |
| $f_{(i)}(\xi,\eta,\theta)$ | boundary layer stress coefficients |
| $g_{(i)}(\xi,\eta,\theta)$ | boundary layer strain coefficients |
| H | laminate thickness |
| h | ply thickness |
| n | number of plies in a laminate |
| P | load applied to the pin |
| $p^{(i)}(\eta)$, $q^{(i)}(\eta)$ | functions for boundary layer stress distribution in the ply thickness direction in the i-th ply |
| R | radius of pin-loaded holes |
| $S_{ij}^{(i)}$ | material compliances in the cylindrical coordinate system |
| $u_{r0}^{c}$ | radial displacement at the contact surfaces |
| $\alpha$, $\beta$, $\gamma$ | real and positive parameters |
| $\lambda$ | root of characteristic equations |
| $\varepsilon^{(i)}$ | total strains in the i-th ply |
| $\varepsilon^{c}$ | laminate strains obtained from the Classical Laminated Plate Theory (CLPT) |
| $\varepsilon^{e(i)}$ | boundary layer strains in the i-th ply |
| $\varepsilon_0^{c}$ | laminate strains along hole edges obtained from the CLPT |
| $\sigma^{(i)}$ | total stresses in the i-th ply |
| $\sigma^{c(i)}$ | in-plane stresses obtained from the CLPT in the i-th ply |
| $\sigma^{e(i)}$ | boundary layer stresses in the i-th ply |
| $\sigma_0^{c(i)}$ | in-plane stresses along hole edges obtained from the CLPT in the i-th ply |
| $\sigma_{r0}^{c}$ | average in-plane radial stress across the laminate thickness along hole edges that is obtained from the CLPT |
| $\xi$, $\eta$ | dimensionless variables in the radial and thickness directions respectively |
| $\Phi(\xi)$, $\Psi(\xi)$ | common functions for boundary layer stress distribution in the radial direction for all the plies |

| | |
|---|---|
| $\Phi^{(i)}(\xi)$, $\Psi^{(i)}(\xi)$ | functions for boundary layer stress distribution in the radial direction in the i-th ply |
| $\Pi$ | complementary energy |
| $\Gamma$ | functional |

**Chapter 4:**

| | |
|---|---|
| $X_t$ | longitudinal tensile strength of unidirectional layers |
| $Y_t$ | transverse tensile strength of unidirectional layers |
| $S_{12}$ | in-plane shear strength of unidirectional layers |
| $\theta$ | fiber orientation difference angle of two adjacent plies which constitute the *so-called* $\theta$-interface |
| $Z_t$ | interlaminar tensile strength at the $\theta$-interfaces |
| $Z_c$ | interlaminar compressive strength at the $\theta$-interfaces |
| $S_{13}$ | longitudinal interlaminar shear strength at the $\theta$-interfaces |
| $S_{23}$ | transverse interlaminar shear strength at the $\theta$-interfaces |
| $P_{ut}$ | ultimate load of specimens |
| $\tau^0_{xz}$ | nominal uniform shear stress at the central planes of modified double notch shear specimens between two notches |
| $\delta$ | correction parameter of modified double notch shear specimens |
| s | notch space of modified double notch shear specimens |

**Chapter 5:**

| | |
|---|---|
| $X_t$ | longitudinal tensile strength of unidirectional layers |
| $Y_t$ | transverse tensile strength of unidirectional layers |
| $S_{12}$ | in-plane shear strength of unidirectional layers |
| $\theta$ | fiber orientation difference angle of two adjacent plies |
| $Z_t$ | interlaminar tensile strength at the $\theta$-interfaces |
| $Z_c$ | interlaminar compressive strength at the $\theta$-interfaces |
| $S_{13}$ | longitudinal interlaminar shear strength at the $\theta$-interfaces |
| $S_{23}$ | transverse interlaminar shear strength at the $\theta$-interfaces |
| f(x) | probability density function of random variable X |
| F(x) | probability distribution function of random variable X |
| $M_i$ | i-th-order moment of random variables |

| | |
|---|---|
| $t_\alpha$ | confidence limit with a given confidence $(1-\alpha)\%$ in Rank-Sum Test |
| $W_X$ | sum of the rank of random variable X in Rank-Sum Test |

## Chapter 6:

| | |
|---|---|
| $X(t)$ | target non-Gaussian nonstationary stochastic process with respect to t |
| $X'(t)$ | simulated non-Gaussian nonstationary stochastic process |
| $A_i, B_i$ | correlated random parameters |
| $u(t)$ | mean of $X(t)$ |
| $k(t, s)$ | second-order joint moment of $X(t)$ |
| $k(t, s, \tau)$ | third-order joint moment of $X(t)$ |
| $k(t, s, \tau, \sigma)$ | fourth-order joint moment of $X(t)$ |
| $u'(t)$ | mean of $X'(t)$ |
| $k'(t, s)$ | second-order joint moment of $X'(t)$ |
| $k'(t, s, \tau)$ | third-order joint moment of $X'(t)$ |
| $k'(t, s, \tau, \sigma)$ | fourth-order joint moment of $X'(t)$ |
| $a_i, a_{ij}, a_{ijk}, a_{ijkl}$ | Fourier coefficients |
| $\theta$ | fiber orientation difference angle of two adjacent plies |
| $S(\theta)$ | target stochastic process denoting the interlaminar shear (ILS) strengths with respect to $\theta$ |
| $S'(\theta)$ | simulated stochastic process denoting the ILS strengths with respect to $\theta$ |
| $\delta_{ij}$ | Delta function |
| $c(t, s)$ | second-order joint central moment of $S(\theta)$ |
| $c(t, s, \tau)$ | third-order joint central moment of $S(\theta)$ |
| $c(t, s, \tau, \sigma)$ | fourth-order joint central moment of $S(\theta)$ |
| $c'(t, s)$ | second-order joint central moment of $S'(\theta)$ |
| $c'(t, s, \tau)$ | third-order joint central moment of $S'(\theta)$ |
| $c'(t, s, \tau, \sigma)$ | fourth-order joint central moment of $S'(\theta)$ |
| $u(\theta)$ | stationary time series denoting the lower or higher bound of $S'(\theta)$ |
| $R(\tau)$ | autocorreleation function |
| $s(\omega)$ | sample spectrum |
| $w(i)$ | Bartlett lag window |
| $\rho(t, s)$ | correlation coefficient function |

**Chapter 7:**

| | |
|---|---|
| $X_t$ | longitudinal tensile strength of unidirectional layers |
| $Y_t$ | transverse tensile strength of unidirectional layers |
| $\theta$ | fiber orientation difference angle of two adjacent plies |
| $Z_t$ | interlaminar tensile strength at the $\theta$-interfaces |
| $Z_c$ | interlaminar compressive strength at the $\theta$-interfaces |
| $S_{13}$ | longitudinal interlaminar shear strength along the direction $\phi = \phi_o$ at the $\theta$-interfaces |
| $S_{23}$ | transverse interlaminar shear strength along the direction $\phi = \phi_o$ at the $\theta$-interfaces |
| $\sigma_z$ | interlaminar normal stress |
| $\tau_{1z}$ | longitudinal interlaminar shear stress |
| $\tau_{2z}$ | transverse interlaminar shear stress |
| 1, 2, z | coordinate system along arbitrary directions at the $\theta$-interfaces |
| 1′, 2′, z | coordinate system along the principal material directions at the $\theta$-interfaces |
| $\phi$ | angle denoting the directions of arbitrary coordinate systems at the $\theta$-interfaces |
| $\phi_o$ | angle denoting the direction of the coordinate system at the $\theta$-interfaces where interlaminar strength components are experimentally characterized |
| $F_i$ | second-rank strength tensor |
| $F_{ij}$ | fourth-rank strength tensor |
| $F_{ijk}$ | sixth-rank strength tensor |
| $\lambda$ | load parameter |
| D | discriminate of the third-order failure equation |
| $a_0$ | characteristic length over which the singular interlaminar stresses are averaged for the evaluation of delamination initiation |
| $\sigma_u$ | failure strength of laminated composites governed by delamination initiation |
| $F(\sigma)$ | probability distribution function |

# CHAPTER 1

## INTRODUCTION

A fiber-reinforced composite material is defined as a material system that contains a fiber reinforcement material with significant stiffness and strength supported by a matrix material. In aircraft primary structures, laminated continuous fiber-reinforced composite materials have been one of the most extensive structural applications, because they are easier to design, produce and standardize than other types of composite materials although some specific types are under growing development, such as braiding, three-dimensional weaving, etc. The laminated composite materials are formed of unidirectional layers of fiber or woven-cloth reinforced materials that are bound together with the fibers of each layer oriented in different directions. Thus the strength and stiffness of laminated fiber-reinforced composites can be tailored to the specific design requirement of the structures being built. Therefore, the layer (also named as lamina below) is the basic construction element in laminated composites and thus the lamina material properties are the basic design parameters in the optimization of aircraft composite structures using macromechanics of composite materials.

Laminated fiber-reinforced composite materials are characterized by considerable variability in their mechanical properties. This uncertainty is attributed to the variable nature of constituent properties of fiber and matrix, and the randomness introduced in the manufacturing process (e.g., variations in fiber volume fraction, fiber orientations, and void volume fraction, etc.). Traditionally, in the practice of designing aircraft structures using advanced fiber-reinforced composite materials, one usually adopts the methodology of MIL-HDBK-5A A base allowable (i.e., 99% probability of survival with a confidence of 95%) for primary structures and MIL-HDBK-5A B base allowable

(i.e., 90% probability of survival with a confidence of 95%) for secondary structures to account for the variability in material strengths (Hadcock, 1972). Furthermore, safety factors are specified to account for the randomness in service loadings, environment conditions and structural geometry, etc. Therefore, all the design parameters are simplified to be deterministic quantities in the traditional design scheme. This approach usually results in overly conservative design and can not ensure safety of aircraft composite structural systems in all cases. Obviously, the deterministic design methodology is one of the major reasons that the application of advanced composite materials in aircraft structures could not provide further weight reduction. Hence, reliability-based design of aircraft composite structures is of great importance due to the rigorous requirements of structure safety and the considerable uncertainty in the mechanical behaviour of composite materials. As a matter of fact, the concept of variability in the properties of structural materials and the inherent randomness in service loadings and environmental conditions, etc., is increasingly being accepted and the approach of analyzing structural systems using reliability techniques thus becomes more and more imperative to improve the weight efficiency of advanced composite materials.

The first motivations for uncovering the variability in the behaviour of structural materials may be dated back to the study of the strength of brittle homogeneous materials by Weibull (1939 ) and the attempt to predict the fatigue life of a structure by Miner (1945). The study of uncertain behaviour of composite materials began in the 1960's. Rosen in 1964 extended the fiber bundle theory, which was developed by Danials in 1945 to predict the statistical properties of the combined strength of bundles of threads in textile yarns from the given statistics of the strengths of individual threads, to a method for predicting the strength statistics of a single-ply layer of composite materials. In 1970's, probabilistic analysis method was applied to the design, manufacturing, quality control and testing of the graphite-epoxy truss tubes of the NASA's applications technology satellite (Maxwell *et al.*, 1975), and structural integrity assessment of filament-wound glass-epoxy cylinders and rocket motor cases under actions of dynamic fracture due to internal pressure loadings (Ienoe and Neal, 1975). In recent years, the NASA-Lewis Research Center has accomplished and financially supported many programs on the aspect of probabilistic analysis of composite structures.

Following Rosen's study, many investigations have been conducted on the aspects of probabilistic failure strength of composite materials (Scop and Argon, 1967, Zweben, 1968, Larder

and Beadle, 1976, Fukuda and Kawabata, 1976, Harlow and Phoenix, 1978, Zhu and Zong, 1993). A detailed review examining this field is given in Chapter 2. On a microscopic scale, some approaches have been developed to predict the probabilistic behaviour of unidirectional composites. In these models, the establishment of relationships between the statistical properties of the constituents and those of unidirectional composites are completed. Some studies on this aspect can be found in the review paper of Harlow and Phoenix (1981). However, as mentioned above, the aircraft designers are more interested in macromechanical properties of the lamina in an average sense to design optimum lay-up sequences for the laminated structures. In fact, the probabilistic distribution functions of the material properties, such as strength components, Young's moduli and Poisson's ratios for the lamina, can be obtained by the experimental data.

On the other hand, some efforts have been devoted to the evaluation of the probabilistic failure strength of laminated composite materials on a macroscopic scale. Most of existing research work on probabilistic quantification of the ultimate strength of laminated composites has been achieved based on the bundle models. That is, the laminates are viewed as a parallel system consisting of a number of layer groups with individual fiber orientations. Each layer group is assumed to be statistically homogeneous in material properties. The failure probability of each layer group under complex stress state is conveniently determined by a number of existing approaches in conjunction with the Classical Laminated Plate Theory. Then, the failure probability of the laminates can be approximately evaluated from the bundle model. However, because the bundle model only provides the bounds of reliability limit for laminated composites, these approaches are inadequate to address the problem of quantifying the damage evolution and even ultimate strength of laminated composites.

Due to the insufficiency of the probabilistic structural analysis, researchers' attentions are addressed to an emerging field, namely stochastic structural analysis, which is expected to model random behaviour in both the damage evolution and ultimate strength of laminated composites. *A stochastic process can be defined as a family of random variables that are functions of a physical parameter such as time or space.* The nonhomogeneous properties, such as strength, modulus and density, of fiber-reinforced composite materials exhibit considerable spatial random variations, and thus can be reasonably simulated by a stochastic process in space (or a random field). On the other hand, the damage evolution until the final failure of laminated composites is a successive

accumulative process; the future damage state strongly depends on the current damage state. Therefore, the damage growth in laminated composites could be typically modeled as a time-dependent stochastic process. Hence, the stochastic structural analysis approach can be expected to include all the sources of variability into the modeling scheme and yield a reliable prediction of the structural response and the failure of laminated composites.

## 1.1 LITERATURE REVIEW ON STOCHASTIC STRUCTURAL ANALYSIS

With a literature review beginning on the aspect of stochastic structural analysis for laminated composites, it should be manifested that the present thesis covers several topics. Hence, the literature reviews for the respective topics are going to be executed in the relevant chapters for the purpose of being concise. In particular, previous research work in the field of probabilistic structural analysis on composite materials is summarized in Chapter 2.

Although some remarkable efforts have been devoted to the study of random behaviour of composite materials (reviewed in Chapter 2), few of them fall into the category of stochastic process modeling. Hence, limited work on stochastic structural analysis of laminated composites is available up to date. The stochastic modeling of damage evolution and ultimate strength of laminated composites is an extremely complicated task due to multiple damage modes on several structural levels and damage-induced stress redistribution, but more information regarding damage growth history can be provided in a probabilistic sense. The development of stochastic modeling approaches in the structural analysis of laminated composites is still at an initial stage at present.

Wang *et al.* (1984) proposed a stochastic model for the growth of matrix cracks in cross-ply laminated composites with initial random flaws under static load and fatigue load, wherein the applied static load and fatigue cycle number are viewed as a stochastic process in each case. The randomness of the effective flaw size and the space between two adjacent flaws are characterized by normal probability functions. Under static load, the first failure of the 90° layer is determined by the existence of the worst flaw with the largest size, which thus forms the onset of the transverse cracking process. With the applied load increased, transverse cracks are continually formed from the flaws with lesser sizes until the final failure of the cross-ply laminates, thereby a stochastic procedure is established to simulate the entire load-sequence process of the multiple crack

formation. In this model, the formation of individual transverse cracks is governed by the material's critical energy release rate. Under fatigue load, the effective sizes of all the flaws increase continuously with time, following a conventional power law. The transverse cracks are formed when the size of the corresponding flaws is developed to a characteristic size, thus a stochastic process is yielded to simulate a time-sequence crack formation process under fatigue loading. In this stochastic model, a Monte Carlo simulation routine is employed for numerically evaluating the stochastic process of crack formation.

Deodatis *et al.* (1989) developed a finite element scheme with the aid of the Monte Carlo simulation technique to determine the randomness in the ultimate failure strength for the angle-ply laminates, wherein the material strength components are idealized as a multi-dimensional stochastic field. Accordingly, each layer is divided into an equal number of elements and the strength components of each element are digitally generated following the Monte Carlo simulation procedure. At different levels of external loading, the number of failure elements is evaluated based on various failure criteria, and the loading level at which the defined number of failure elements concurrently occur for the first time is considered as the ultimate failure strength of the laminates. Therefore, this finite element scheme can be conveniently used to study the statistical size effect of composite materials using the same size element discretization of the laminates with different areas, but the prediction of ultimate failure strength is more conservative without the consideration of stress redistribution after the failure of some elements.

Hilton and Yi (1993) conducted an investigation on the time-dependent stochastic viscoelastic delamination onset of angle-ply laminated composites by evaluating the failure probability. The involved stochastic processes consist of random anisotropic viscoelastic material properties influenced by stochastic temperature fields, moisture contents and boundary conditions as well as random loads. Hence, the evaluation of stochastic delamination onset is performed on two levels in their research work: (1) the calculation of stochastic field of interlaminar stresses due to random loads and materials properties; (2) the assessment of failure probability using appropriate failure criteria including time-dependent random material strength components.

Yushanov and Joshi (1995) formed a stochastic model to determine the probability distribution of longitudinal tensile strength for unidirectional continuous and short fiber reinforced

composites. Given the loading rate, the model evaluates the failure probability of the unidirectional composites at any moment of time based on a discrete step-by-step damage evolution process from the nucleation site to the final failure, which is modeled by a multidimensional Markovian pure birth process. Three damage modes, including fiber breakage, matrix cracking and fiber/matrix interface debonding, are considered in the process of damage evolution. The transition rates of damage evolution at all steps, which are required as known parameters in the Markovian pure birth process, are obtained by considering the sequential occurrence probabilities of all possible damage modes based on micromechanical stress analysis. The final failure of the unidirectional composites is defined by a macrocrack formation which is represented by the existence of infinite number of adjacent broken fibers. Hence, this stochastic model presents a whole history of possible damage evolution and the failure probability at any moment of time with the applied load increasing.

The stochastic finite element techniques have also been emerging as a powerful tool to deal with the response of complex structures with spatial parametric uncertainties. Usually, the first-order second-moment approximate technique is employed for the stochastic finite element analysis and thus the structural responses are obtained in the forms of mean values and related covariances. One of noticeable features in the analysis procedure is to discretize the stochastic fields by expanding the space-dependent random variables through shape functions. Hence, this analysis procedure has the ability to model the correlation involved in spatial fields, which are represented in the forms of orthotropic autocorrelation functions. Due to the limitation of the first-order second-moment technique, this approach is found to be accurate only for stochastic fields with small coefficients of variation. Engelstad and Reddy (1993) developed a stochastic nonlinear finite element analysis procedure for the random postbuckling behaviour of laminated composites with space-dependent stochastic material properties and geometric dimensions. Chang and Yang (1992) also investigated the random postbuckling behaviours of laminated composites with space-dependent geometric imperfections using the stochastic finite element technique.

## 1.2 OBJECTIVE OF THE THESIS

The main objective of the present thesis is to establish a *Stochastic Delamination Model* to comprehensively investigate the probabilistic characteristics of delamination failure. One of the most salient features in the *Stochastic Delamination Model* is that the dependence of interlaminar

strength components on the magnitude of fiber orientation difference (abbreviated as FOD below) between two adjacent unidirectional layers in laminated composites, are viewed as a stochastic process (named as θ-dependent stochastic process below). Hence, the present thesis consists of four major aspects of research:

(1) developing a new analytical approach to calculate deterministic edge effect stresses arising at the complex boundaries of laminated composites;

(2) experimentally characterizing the stochastic behaviour of θ-dependent interlaminar strength components at a number of discrete FOD angles;

(3) phenomenologically modeling the θ-dependent stochastic process of interlaminar shear strength components so as to obtain the stochastic behaviour of these strength components at all values of FOD angles based on the discrete experimental data sets;

(4) developing innovative quadratic and cubic stress-based delamination criteria with the abilities of strength tensor transformation and then performing probabilistic evaluation on delamination failure in various types of laminated composites.

## 1.3 MOTIVATION AND CONTENTS

Laminated fiber-reinforced composites typically fail in a unique or a combined form of the following fundamental failure modes: matrix cracking, fiber/matrix debonding, fiber breakage and delamination. The complete understanding of the mechanisms behind these fundamental failure modes is essential for the failure evaluation of laminated composites. Most of research work has further distinguished the failure of laminated composites in two distinct modes. That is, the in-plane failure mode of matrix cracking, fiber/matrix debonding and fiber breakage is considered to be caused by the in-plane stress state, while the delamination mode occurs as a result of the interlaminar stress state. Hence, the two distinct failure modes are respectively modeled using the corresponding failure criteria in a deterministic sense. In the case of the first failure mode, some interactive failure criteria, such as the Tsai-Hill (Tsai, 1968) and Tsai-Wu (1971) criteria, have been developed to take into account the in-plane stresses working collectively towards the failure of laminated composites. In the case of the second failure mode, delamination criteria, such as the quadratic delamination criterion (Brewer and Lagace, 1988), have been developed to consider the interactive nature of individual interlaminar stress components on the delamination failure of laminated composites.

As one of the fundamental failure modes of laminated composites, the deterministic behaviour of delamination failure induced by interlaminar stresses has been under an extensive investigation for the past thirty years. Interlaminar stresses in multidirectional laminated composites can arise from material discontinuities, geometry discontinuities, and eccentricities in the load path. The most commonly known example is the edge effect in flat laminated composites subjected to in-plane loading due to material property mismatch between individual layers (Pipes and Pagano, 1970, Puppo and Evensen, 1970). Interlaminar stresses are also generated in tapered laminated composites (Hoa *et al.*, 1988, Fish and Lee, 1989, Vizzini, 1995) and in flat laminated composites with transverse matrix cracks (Fish and O'Brien, 1992, O'Brien and Hooper, 1993, Zhang and Zhu, 1996). Another example for the generation of interlaminar stresses is the curved laminated composites subjected to flexural loading in the plane of curvature (Kedward *et al.*, 1989, Paul, *et al.*, 1992). Because the interlaminar tensile and shear strengths are typically a few percentage of the longitudinal tensile strength, interlaminar stresses might induce a through-the-thickness mode of failure, which is terminologically called as delamination. This failure mode has been observed not only in laboratory specimens but also in aircraft composite structures as well. For example, it is believed that the interlaminar stresses prompted the failure of the L-1011 composite vertical fin (Jackson, 1983). Although delamination of laminated composites is not necessarily considered to be an ultimate structural failure, it is an initiation of damage, which might undergo stable or unstable propagation and then cause entire structural disintegration. Delamination also may cause a severe reduction of buckling strengths of laminated structures (Kutlu and Chang, 1992, Whitcomb, 1992). Moreover, delamination initiation in the control surfaces of aircrafts may have a deleterious effect on their aerodynamic behaviours without totally destroying their flight capabilities (Herakovich, 1981).

Delamination failure of fiber-reinforced laminated composites can be predicted by two distinct methodologies; one is based on fracture mechanics (O'Brien, 1982, 1984), and the other is based on mechanics of materials (Sun and Chou, 1988, Brewer and Lagace, 1988). The fracture mechanics approach employs the delamination criteria that are in terms of strain energy release rates. Therefore, the strain energy release rates need to be calculated using the classical elasticity theory and then are compared with their critical values in the associated criteria. The mechanics of materials approach makes use of stress-based delamination criteria and thus a local 3D stress analysis is necessary. The Mode I, Mode II and Mode III critical strain energy release rates in the

fracture mechanics approach and the interlaminar shear and normal strength components in the mechanics of materials approach can be considered as material properties, which characterize the resistance of composite materials against delamination. In the past, the great majority of work has been focused on the aspects to experimentally measure these material properties by performing simple loading tests on the unidirectional specimens (i.e., at the 0/0 interface), and then substitute them into the associated criteria to evaluate the delamination failure. However, in practical laminated composite structures, delamination usually occurs at the interfaces between two adjacent plies with different fiber orientations. Therefore, the critical strain energy release rates or the strengths (shear and normal) at the interfaces between different fiber oriented plies rather than those in the unidirectional composites are of considerable importance to more accurately evaluate the delamination failure. Recently the effects of fiber orientations in laminated composites on the Mode I and II critical strain energy release rates (i.e., $G_{IC}$ and $G_{IIC}$) have been extensively investigated using the END and ENF test techniques (see detailed literature review in Chapter 2). It is also found that in most cases the critical strain energy release rates depend on the fiber orientations of two adjacent plies surrounding the interfaces. However, the investigations are not continued towards further stage where innovative failure criteria should be developed in order to properly use these critical release rates to evaluate delamination failure generated by the combined stress state. On the other hand, the resistance of laminated composites against delamination can also be quantified by the magnitudes of interlaminar shear and normal strengths at the interfaces between different fiber orientated plies, as mentioned earlier. In contrast to the effects of fiber orientations on critical strain energy release rates, the corresponding effects on the interlaminar shear (abbreviated as ILS below) strength components, to the author' knowledge, have not so far been investigated.

A large amount of experimental research work has shown that the failure strength of laminated composites governed by delamination failure mode also exhibits considerable scatter from specimen to specimen mainly because of the existence of random defects at the interfaces. After a thorough literature survey, however, it is found that only Hilton and Yi (1993) studied the scatter of delamination failure in angle-ply laminates as a result of the time-dependent random viscoelastic creep interlaminar stress state and interlaminar strength components. Wherein, the associated model and the involved random material property parameters related to the viscoelastic creep process are not straightforward. In the author's opinion, the insufficiency of probabilistic

delamination failure analysis may be attributed to the lack of efficient experimental techniques and the lesser understanding of the variability of interlaminar strength components, because the calculation of delamination failure probability of laminated composites can be approached in a general way of substituting random interlaminar strength components into the deterministic delamination criteria. In fact, even in the problem of deterministic delamination failure analysis, fewer comprehensive failure theories have been developed compared with the in-plane failure analysis and the most often utilized quadratic delamination criterion usually results in the disagreement between theory and experiment (Brewer and Lagace, 1988). Hence, the problem of probabilistic evaluation of delamination failure is still a virgin field with more comprehensive research required.

In the present thesis, a *Stochastic Delamination Model* is developed to comprehensively investigate the probabilistic characteristics of delamination failure. The *Stochastic Delamination Model* consists of four major aspects of research which are distributed in individual chapters; stress analysis (Chapter 3), experimental characterization (Chapters 4 and 5), stochastic modeling (Chapter 6 ) and failure criteria (Chapter 7).

Edge effects of laminated composites constitute a fully three-dimensional problem, and thus it is quite difficult to find the accurate distribution of the involved stresses. The finite element approach has been one of the most commonly used numerical techniques to calculate this three-dimensional stress field. However the predicted results of the highly concentrated edge effect interlaminar stresses severely vary from coarse meshes to fine meshes and thus are acceptable to the stress-based delamination failure criteria only after a mesh-dependent convergence is achieved. This procedure is usually restricted by the computer storage and computing cost. In this regard, edge effect stresses defined by analytical closed form solutions with enough accuracy are preferable to evaluate the delamination onset. In Chapter 3, analytical solutions with high accuracy are developed to calculate the edge effect stress field in symmetric laminated composites with the aid of the variational principle of complementary energy. The developed approach is convenient since the analytical solutions have the simple form of exponential functions, and versatile since they can be used to account for the edge effects resulting from straight free edges, curved free edges and pin-loaded hole edges with or without friction in laminated composites.

As mentioned above, the limited knowledge on random behaviour of interlaminar strength components results in the insufficiency of probabilistic delamination failure analysis. Compared with the experimental characterization of the in-plane strength components, the corresponding work on the interlaminar strength components is much more cumbersome. In order to establish the *Stochastic Delamination Model* in the present thesis, the probability distribution functions of interlaminar strength components must be known as primitive input data. Because these strength components have to be obtained by performing tests on the laminated specimens, two problems must be solved: (1) how to introduce loading onto the specimens for the interlaminar tensile strength component and (2) how to eliminate edge effects in the specimens for ILS strength components. In Chapters 4 and 5, detailed evaluation and stress analysis on various specimen configurations are performed, and then an experimental scheme is elaborately designed to yield the probabilistic parameters for the interlaminar strength components at 10 discrete values of FOD angles. The angle values are set to be $\theta = 0°$, $10°$, $20°$, $30°$, $40°$, $50°$, $60°$, $70°$, $80°$, and $90°$, and the sample size is set to be 35 at each given angle. Furthermore, the probability distributions of in-plane strength components are also experimentally determined using the customary test methods.

The experimental program only provides the interlaminar strengths at a number of discrete FOD angles. Therefore, analytical investigations are necessary to study the effects of fiber orientations on the ILS strengths in the whole domain of FOD angles, i.e., $\theta \in [0°, 90°]$, based on the experimental data sets. Due to the lack of knowledge of appropriate physical law and the considerable variability potentially behind these strength components, phenomenological models in a probabilistic sense offer a powerful technique to describe the relationships between the ILS strengths and FOD angles. In Chapter 6, a stochastic simulation model is proposed, in which the probabilistic dependence of ILS strengths on the FOD angles $\theta$ is simulated as a non-Gaussian nonstationary stochastic process within the bounded interval $[0°, 90°]$. The random trigonometric polynomials with unknown correlated random parameters are employed to approximately represent this type of stochastic process. The correlated random parameters are then determined based on the probabilistic characteristics of the experimental sample data sets at 10 particular values of $\theta$ at which the experiments are performed. With the generated stochastic process, the individual probability density functions and the other probabilistic characteristics of the ILS strengths can be obtained at any particular values of $\theta$ at which experiments are not performed.

The existing stress-based delamination criteria were empirically established on the basis of the assumptions that the interlaminar strength components are directionally independent material properties. Therefore, these criteria are not applicable to the directionally dependent strength components, as demonstrated by the experiments in the present thesis. In Chapter 7, new quadratic and cubic delamination criteria are developed based on Malmeister Strength Theory (Malmeister, 1967) and Hashin Assumption (Hashin, 1980) in order to take into account the effects of $\theta$-dependent interlaminar strength components into the delamination failure. These new criteria have the abilities of strength tensor transformation, thereby predicting the delamination failure if the interlaminar strength components in one arbitrary coordinate system are experimentally obtained. Then, the random delamination failure induced by straight free edge effect stresses in laminated composites under uniaxial tension is investigated as an exemplified case to illustrate the validity of the developed *Stochastic Delamination Model*. In the quadratic and cubic delamination criteria, the $\theta$-dependent interlaminar strength components are substituted as random variables with determined probability distributions. The interlaminar stress state, however, is regarded to be deterministic for the reason of brevity, since the variability of the edge effect stress state arising from the variability of fiber orientation, layer thickness, and material elastic properties is believed to be much less than that of strength components if the external load applied to the laminates is deterministic. The probability that delamination failure takes place at each interface is calculated using the Monte Carlo simulation technique.

# CHAPTER 2

# LITERATURE SURVEY

This chapter is dedicated to a literature survey on two individual fields: probabilistic structural analysis and delamination failure of laminated composites. In the case of probabilistic structural analysis, the currently existing research work on the stress-based reliability evaluation of unidirectional and laminated composites under complex stress states is surveyed. Furthermore, the probabilistic finite element techniques, as an efficient numerical solution approach for the random structural responses of complex systems, are also examined. In the case of delamination failure, the delamination mechanism, including onset and propagation, in laminated composites is reviewed, and the stress-based delamination onset criteria are discussed in details. Some existing empirical delamination onset criteria and their advantages and limitations are also evaluated. Because the delamination failure is a problem related to the three-dimensional stress state, two-dimensional stress-based failure criteria are not considered herein.

## 2.1 PROBABLISTIC STRUCTURAL ANALYSIS

Basically, probabilistic structural analysis deals with the determination of structural response variability and the assessment of structural reliability. The objective of the first category is to investigate the effects of structural parameter uncertainties on the stiffness-based structural response, such as the displacement field, stress distribution, vibration, buckling, etc. The random structural parameters can include the modulus of elasticity, mass density, geometry dimension, imperfections, and so on. The analytical formulation can simply be described as obtaining the output random response Y of a system from the input random vector X. The objective for the

second category is to quantify the failure probability (or reliability) of structural systems based upon various failure criteria. For example, in a general stress-based model of the probability evaluation, the internal stress introduced by operating conditions and the material strengths are viewed as random variables, then the probability that the stress state exceeds the strengths, or in other words, that the safety margin is less than zero, is calculated. Thus, this is a computational procedure related to the integration of joint probability density functions within failure or safety domains. Herein, the literature review on these two categories is performed, focusing the first category on the probabilistic finite element analysis and the second category on the stress-based reliability evaluation for laminated composites.

### 2.1.1 Assessment of Structural Reliability

In structural reliability analysis, the failure criterion can be expressed as a limit state function, g(X), which separates the random vector space into failure ($g(X) \geq 1$) and safe ($g(X) < 1$) regions. The limit state function includes a n-dimensional random vector X representing stress components and strength components with uncertainties. Therefore, the failure probability is obtained through an integration formulation, as follows:

$$P_f = P[g(x_1, x_2, \ldots, x_n) \geq 1] = \int_{\Omega} f(x_1, x_2, \ldots, x_n) dx_1 dx_2 \ldots dx_n \tag{2.1}$$

where f(X) is a joint probability density function of X, and $\Omega$ denotes the failure domain. It is only a mathematical problem to solve the above integration equation and in fact there exists a number of optimization approaches to obtain the numerical value for simple structural systems. Especially, some approaches for the evaluation of failure probability of unidirectional laminated composites have been developed, such as the analytical method, the fast probability integration method, the first-order reliability method, etc. Because most of currently existing failure criteria are developed on a scale of unidirectional lamina, one has to calculate the failure probability from Equation (2.1) for each lamina in a laminated composite (assuming that the stress state in each lamina has been determined), and then assess the failure probability of the entire laminate by a ply-by-ply procedure based on some special models, including the Monte Carlo simulation method, failure tree method, and bundle method. On the other hand, the failure probability for laminated composites can be directly evaluated from Equation (2.1) if the failure criteria can predict the ultimate strength of

laminated composite without demonstrating the lamina failure progression, as in the case of the Yamada-Sun criterion (Yamada and Sun, 1978) which has attained a wider application.

#### 2.1.1.1 Closed Form Expansion Method

This approach (Wetherhold, 1981) offers a systematic way to calculate the statistical information for a limit state function including several random variables. The failure index R, which is a function of principal stresses and strength components, is a random variable and $R \geq 1$ denotes the failure of materials, thus the failure probability is

$$P_f(R(X)>1)=\int_1^{\infty} f_R(R)dR \tag{2.2}$$

The main purpose of this approach is to obtain a closed form approximate expression for the probability density function $f_R(R)$, thus making the direct integration operation in Equation (2.2) possible. After approximately expanding the function R into a Taylor series around the mean values of X with terms up to second order, the mean value $\mu(R)$, the second central moment $\mu_2(R)$ and third central moment $\mu_3(R)$ can be conveniently calculated from the random characteristics of strength components (wherein the stress state is assumed to be deterministic). Then the probability density function of R could be approximated using a Gramer-Charlier expansion (Gramer, 1946), as follows:

$$f_R(R)=\Phi(z)-\frac{1}{3!}\frac{\mu_3(R)}{(\mu_2(R))^{(3/2)}}\Phi^{(3)}(z) \tag{2.3}$$

where

$$\Phi(z)=\frac{1}{\sqrt{2\pi}}\int_{-\infty}^{z} e^{-y^2/2}dy \tag{2.4}$$

$$\Phi^{(3)}(z)=\frac{1}{\sqrt{2\pi}}(z^2-1)e^{-z^2/2} \tag{2.5}$$

and

$$z=\frac{R-\mu(R)}{\sqrt{\mu_2(R)}} \tag{2.6}$$

Therefore, the probability density function of the random failure index is approximately simplified

as a closed form equation with one variable z. The number of terms used in the Gramer-Charlier expansion in Equation (2.3) is not critical to obtain a good approximation for the mean value and variance of R. A normal distribution can be obtained through retaining only the first term of the expansion. The most important addition to the overall accuracy of the expansion is to include higher order terms in the Taylor series when one calculates the central moments of the failure index. Wetherhold (1981) evaluated the reliability of off-axis tensile unidirectional laminates using this approximation model and the results showed a good agreement with the experimental data. The advantage of this technique is that the simulation results can be obtained only based on the mean value, variance and various order central moments of the strength components, while the shortcoming is that this approach could not account for the random stress state.

#### 2.1.1.2 First-Order Reliability Method

The advanced first-order reliability method was developed by Hasofer and Lind (1974) and then extended by Rackwitz and Fiessler (1978). The main principle of this approach is to yield the shortest distance, namely safety index $\beta$, from the origin to the failure surface (i.e., the limit state surface) defined by the limit state function in a normalized independent random vector space. Hence, the basic random vector X must be statistically independent and normally distributed, otherwise it has to be transformed into independent and standard normal vector U using statistical techniques, thereby the limit state function is expressed in terms of the transformed random vector, i.e., g(U). By assuming that there is only one minimum distance point U* on the limit state surface, the limit state function g(U) can be expanded into the first-order Taylor series around U* and the safety index $\beta$ is found by letting

$$U^* = \beta\alpha \tag{2.7}$$

where $\alpha$ is a unit vector in the standard normal vector space and its i-th component can be interpreted as the important measurement for the corresponding random variable $x_i$. Therefore, one can understand that the safety index $\beta$ is a function of the first and second moments (mean value and variance) of the linear approximation of the limit state function. Various optimization schemes can be obtained to determine the value of $\beta$, such as the Lagrangian multiplier method (Ang and Tang, 1984), iterative method (Hasofer and Lind, 1974, Rackwitz and Fiessler, 1978), and linear

mathematical programming method (Shinozuka, 1983), etc. The probability of failure $P_f$ is then evaluated from the standard normal cumulative distribution table as

$$P_f = \Phi(-\beta) \tag{2.8}$$

This approach has been extensively used in the assessment of reliability for composite structural systems and a few example applications reported in published literature are given as follows. Engelstad and Reddy (1993) performed a reliability analysis on laminated composites with first ply failure during the process of postbuckling after the probabilistic stresses were computed by a probabilistic nonlinear finite element analysis. Miki *et al.* (1990 and 1993), Nakayasu *et al.* (1989), Cederbaum and Elishakoff (1990) and Shao *et al.* (1993) optimized the multidirectional or unidirectional laminate parameters based on a prescribed reliabilty requirement subject to the probabilistic conditions of applied loads and material properties.

#### 2.1.1.3 Fast Probability Integration Method

Instead of the closed form expansion method and the first-order reliability method, an alternative approach, namely the fast probability integration (FPI) method (Mase *et al.*, 1991), has been developed to more quickly obtain the integral value of Equation (2.1). FPI can help generate the required integral value with reasonable accuracy and more information than the Monte Carlo simulation method. For example, FPI can offer the output variable sensitivity information based on the probabilistic inputs. A brief overview of FPI is given below.

Consider a random vector X in a limit state function g(X) in Equation (2.1). The non-normally distributed random variables $x_1$, $x_2$, ..., $x_n$ are transformed into a set of independent, standard normal variables $u_1$, $u_2$, ..., $u_n$, then the FPI method approximates the function g using a Taylor series expansion

$$g(U) = a_0 + \sum a_i(u_i - u_i^*) + \sum b_i(u_i - u_i^*)^2 + \ldots \tag{2.9}$$

where $u^*_i$ is the most probable value of the random variables $u_i$, which are critical to the accuracy of approximation in Equation (2.9). The determination of the coefficients $a_0$, $a_i$, and $b_i$ is difficult and

can be achieved numerically. Based upon the requirement of accuracy, one can truncate a number of terms in Equation (2.9) to approximate the normalized limit state function g(U), and then take a series of data sets the number of which is equal to the total number of the coefficients in the truncated Taylor series, thus constituting a set of linear homogeneous equations. A typical data set of FPI is composed of one perturbed independent variable and the other (n–1) variables are kept at their mean values. For the linear case (only keeping the first order terms), each variable is perturbed with one standard deviation from its mean value. In the quadratic case (keeping both the first and second order terms), the independent variables are perturbed twice with one standard deviation, each on both sides of the mean value. After the coefficients are determined, the integral value can be easily evaluated from the normal standard distributed vector U. Hence, FPI is only a computational method to obtain the approximate value of probability integral. Mase *et al.* (1991) employed this method to assess the probability distributions of the effective modulus and effective thermal expansion coefficient of a quasi-isotropic laminate based on the probabilistic behaviours of constituent materials (fiber and matrix). Shiao *et al.* (1993) used this technique to determine the cumulative distribution functions of buckling load and vibration frequency of composite structures with the numerically determined functional relationship and the known probability density functions of the primitive random variables.

#### 2.1.1.4 Monte Carlo Simulation Method

The Monte Carlo Simulation (MCS) technique is a method of statistical trials and has wide application in many fields. A general description of this method is given in the following. If y is a known deterministic function of the independent or correlated random variables $x_1$, $x_2$, ..., $x_n$

$$y = M(x_1, x_2, \ldots, x_2) = M(X) \tag{2.10}$$

where the probability distributions of $x_1$,$x_2$, ..., $x_n$ are known, then y is also a random variable. The probability distribution of y can be obtained by analytical methods, however, it is usually very difficult. If the functional relationship between X and y is a strongly non-linear relationship, then exact solutions to the probability density function of y can not be obtained easily if not impossible. The MCS is the only recourse at this juncture. The MCS is a computer-numerical method which can yield an approximate probability distribution of y on a histogram (i.e., frequency plot). The

procedure to generate the histogram is briefly summarized as follows:

(1) A sample set of X is simulated as a set of correlated or uncorrelated random variables using the probability distribution functions of $x_1$, $x_2$, ..., $x_n$ and their joint probability density functions. The detailed description for this simulation process can be referred to Ang and Tang's book (1984).
(2) A corresponding value (sample function) of y is obtained by substituting the sample set of $x_i$'s into the function $y = M(X)$.
(3) This step is repeated many times by separately generating a number of sample functions of X to obtain the corresponding sample function of y.
(4) A histogram of the y's is then set up within a given interval.

The MCS technique has been extensively used to evaluate the structural reliability and randomness in the strength of composite materials subjected to the complex stress state from limit state functions. Yamada and Sun (1978), and Sun and Yamada (1978) proposed a failure criterion for the ultimate strength of laminated composites because the prediction of the ultimate strength based on ply failure is extremely complex due to the randomness of multiple failure modes. Then the probability distribution of the ultimate strength was estimated from the probability distribution functions of strength components along the fiber direction and "*in-situ* shear strength". Larder and Beadle (1976) described the probabilistic tensile behaviour of unidirectional composites using the MCS. In this probabilistic analysis, the fibers are discretized into many small elements and each element is assumed to be statistically homogeneous. The basic strength properties for each element are randomly generated from their probability distributions. Then, the damage evolution and ultimate strength of the system are modeled using finite element method or shear-lag model. Deodatis *et al.* (1989) introduced a probabilistic model for the spatial variability of the strength components of composite materials. The laminated composites are discetized into a number of small elements to account for the statistical size effect. Each time after the basic strength properties for every element are randomly given, the number of failure elements in the laminates can be found subjected to loadings that are large enough. The final failure of the laminates is defined by the specific number of failed elements. Besides the limit state functions in structural reliability assessment, the Monte Carlo simulation technique is also applied to the analysis of structural response with primitive random parameters in conjunction with the probabilistic finite element analysis. In this technique, the finite elements must be fine enough to simulate a local uniform

distribution of primitive random variables. Shinozuka (1972) analyzed probabilistic structural dynamics problems using the MCS method combined with finite element technique.

The advantage of the MCS technique is that it has the capabilities not only to predict the strength and the damage evolution of composite structures, but also to simulate the statistical size effect in conjunction with the standard finite element method as well. Hence, it is a versatile technique for the probabilistic analysis of structural responses (e.g., strength analysis, stiffness analysis, buckling analysis, vibration analysis, etc.). However, in order to get reasonable accuracy, a large amount of calculation is required, therefore, the MCS is a computationally prohibitive technique. Also, when the stochastic characteristics including power spectral density and autocorrelation functions of material parameters are to be taken into account, it is not possible to perform MCS easily since, the simulation, which is central to MCS method, of stochastic processes has not been fully developed. In the existing work, only random variables have been considered but not a stochastic process approach. Simulation of random variables has been well developed and documented and thus MCS has been possible to conduct. Moreover, when the degree of non-linearity in the relationship between the X and y increases, MCS fails to give a reliable prediction of probability density function of y. The same is the case when the relationship is not completely deterministic as in many cases of composites.

#### 2.1.1.5 Failure Tree Method

Based on the incremental loading method proposed by Moses (1982), Yang (1988-1989) and Yang and Ma (1989) developed a failure tree method to estimate the reliability of laminated composites. In this model, each laminate consists of four kinds of layer-groups, the orientations of which are 0°, 90°, 45°, and -45° respectively, therefore, a laminate is a parallel system that is composed of four components with random basic strength properties. Under a certain general loading, each layer-group may fail in random sequence because of the randomness of basic strength properties (the Young's moduli and Poisson's ratio are assumed to be deterministic in this model). According to each layer-group failure sequence, the mean value and variation of ultimate strength of a laminate can be calculated from the mean values and variations of basic strength properties using the Classical Laminated Plate Theory in conjunction with the ply failure criterion. In order to reduce the number of possible failure sequences, a concept of critical members is introduced, that is, only the layer group with maximum failure index ($R_{max}$) calculated from the ply failure criterion

and the layer groups with failure index ($R_i$) within a specific range may fail (e.g., $R_i/R_{max} \geq 0.8$). All the corresponding failure sequences are listed in a failure tree, and the mean value and variation of ultimate strength for each failure sequence is calculated. Then, the failure probability of each failure sequence is obtained if the mean value and the coefficient of variation of external load are given. The failure probability (or reliability) of the parallel system is determined by the failure probability of all sequences using Ditlevsen's narrow bounds theory of reliability (Ditlevsen, 1979), wherein the correlation coefficient between any two failure sequences is considered.

Obviously, the application of a failure tree to the reliability evaluation of laminate composites has the drawback: the branch number of a failure tree quickly becomes very large if the structural system has more components. Furthermore, the assumption of critical numbers to reduce the possible failure modes is highly restrictive.

#### 2.1.1.6 Bundle Method

The bound limit of laminated composites can be predicted by the bundle model, wherein each layer with respective fiber orientation is considered to be the component of a laminate, and the layer is assumed to be statistically homogeneous in its elastic and strength properties. Hence, the failure probability of the laminate can be evaluated from the bundle model if the reliability or failure probability of each layer has been calculated. Basically, the random distribution of the complex stress state in each layer can be determined from the Classical Laminated Plate Theory. Therefore the failure probability of each layer under the complex stress state can be determined by the Monte Carlo simulation method (Sun and Yamada, 1978), Taylor series expansion method Wetherhold (1981), first-order reliability method (Engelstad and Reddy, 1993). It is assumed that a laminate is composed of n layer-groups and $R_i$ is the reliability of the i-th layer group, thus, there are n failure units for the system.

**(1) Weakest link model**

This model assumes that the final failure of the laminate occurs when any one of the units fail, and the individual failure units behave independently. Hence, the *in-situ* responses such as constraint effects and stress redistribution due to damaged layers are neglected. This model gives a lower bound limit for the reliability of the laminate which is the product of the individual unit reliabilities

$$R_{laminate} = \prod_{i=1}^{n} R_i \tag{2.11}$$

This model has been used by Cassenti (1984) and Murotsu *et al.* (1994) to estimate the reliability of multidirectional laminated composites.

**(2) Strongest link model**

This model assumes that the influence of the laminate on the individual failed units will dominate, so that the final failure of a laminate will not occur until every individual unit has failed. Therefore, a lower bound limit of the failure probability of the laminate can be given by this model, which is equal to the product of the failure probabilities of individual units. Hence, the upper bound limit of the reliability of the laminate is thus written as

$$R_{laminate} = 1 - \prod_{i=1}^{n} (1 - R_i) \tag{2.12}$$

The application of this model in the reliability assessment of multidirectional laminated composites can be found in the work of Starlinger *et al.* (1993) and Thomas and Wetherhold [1991(a)].

**(3) Load sharing model**

The weakest link model and the strongest link model only provide the bound limits for the reliability of a given laminate, because some laminates may continue to carry increased loading after a first ply failure and reach a largest load-carrying capacity before the last ply failure. The load sharing model is capable to more closely model the mechanism of the damage evolution. There are a number of methods to consider the load redistribution after some plies fail. Thomas and Wetherhold [1991(b)] proposed three approaches to account for the load redistribution in unfailed plies under in-plane loading: global redistribution, local redistribution, and tapered redistribution. The failure probability of the laminated composite is then obtained by the MCS method. The author of the present thesis thinks that the Classical Laminated Plate Theory and some accurate damage accumulation analysis technique should be incorporated into the load sharing model since the MCS determines the randomness of the ultimate strength through enumerating a large number of

deterministic events.

**(4) Sublaminate bundle model**

In the sublaminate bundle model, the sublaminates, the statistical behaviours of which are assumed to be known as primitive parameters, are considered as the components in a laminated composite. Thus, in this model, the laminated composite must be a periodic structure (i.e., composed of a number of same sublaminates) and the random strength distribution and reliability of the laminate can be determined by the sequential multi-step failure of single sublaminates. On the basis of this model, Gurvich and Pipes [1995(a)] evaluated the statistical size effect by examining the failure probabilities of laminated composites with different number of sublaminates. Moreover, Gurvich and Pipes [1995(b)] carried out probabilistic analysis of multi-step failure process of laminated composites in bending beam based on this model and the MCS technique, wherein the laminated composites are also structure-periodic and the stress distribution in each sublaminate is assumed to be uniform through its thickness. Obviously, the sublaminate bundle model is not applied to the laminated composites with a general stacking sequence.

### 2.1.2 Probabilistic Finite Element Method

Probabilistic and stochastic finite element methods are usually used to study the response of complex structural systems with parametric uncertainties. In general, the uncertainty can be mathematically modeled either as random variables, random fields in space or random fields in time. For example, the modulus can be simulated as random variables or random field of spatial coordinates. Correspondingly, probabilistic and stochastic finite element methods may be distinguished from whether random variables or random fields are accounted for in the finite element analysis. Similar to its deterministic counterpart, the probabilistic and stochastic finite element methods must discretize a region into a number of small elements. For the probabilistic finite element method, the mesh division is similar to the deterministic counterpart and finer mesh could give more reliable results. For the stochastic finite element method, however, random functions of spatial coordinates must also be discretized. As in the typical stochastic finite element analysis, each random function b(x) is expanded using shape function $\Psi_i(x)$

$$b(x) = \sum \Psi_i(x) b(x_i) \tag{2.13}$$

where $b(x_i)$ are the values of $b(x)$ at element nodes. Hence, the finite element mesh size depends on the correlation of the random field of spatial coordinates, and the mesh should be fine enough for computation accuracy but large with respect to the correlation length. Perhaps, this is a primary difference between probabilistic and stochastic finite element methods. Discussions regarding the discretization of random field of spatial coordinates can refer to the work of Vanmarcke (1983), Vanmarcke and Grigoriu (1983). It is comparatively convenient to obtain the mean values and covariances of structural response by probabilistic and stochastic finite element methods, and these data are essential for structural elements in order to assess the failure probability of structural systems. Without loss of generality and for illustration purpose, the following review is concentrated on the probabilistic finite element analysis of a general static system with a n-dimensional primitive random vector $a = [a_1, a_2, ..., a_n]^T$. The equilibrium equation for the random system is

$$[K]\{U\} = \{P\} \tag{2.14}$$

where {K} is the stiffness matrix, {P} is the external loads and {U} is the displacement matrix. The stiffness matrix [K] and the external force vector {F} are known and the displacement vector {U} is to be determined.

The perturbation method is a most popular approach in probabilistic finite element analysis. The principle of this method applied to a random system is to replace the random system Equation (2.14) by a summation of theoretically infinite number of identical deterministic system equations and each of these deterministic equations can be solved based on all the lower order equations. However, the infinite series must be truncated in practice, usually down to one or two terms, thus causing an approximate nature of the perturbation method.

The random variables $a_i$ of the structure systems are described as the sum of their mean value and the random variables $\alpha_i$:

$$a_i = E[a_i] + \alpha_i \tag{2.15}$$

The mean value of $\alpha_i$ is equal to zero, thus it has the same standard deviation as $a_i$. After expanding the matrix [K] into a mean-centered Taylor series with respect to the random vector $\alpha$ and truncating it up to second-order, the stiffness matrix is approximated as:

$$K = K^0 + \sum K_i^I \alpha_i + \frac{1}{2}\sum\sum K_{ij}^{II} \alpha_i \alpha_j \tag{2.16}$$

where $K^0$ is the zero-order stiffness matrix evaluated at $\alpha = 0$ which is identical to the deterministic stiffness matrix. The higher order stiffness matrices $K_i^I$ and $K_{ij}^{II}$ are the partial derivatives of K at the mean values of random variable vector $\alpha$ defined as follows:

$$K_i^I = \frac{\partial K}{\partial \alpha_i}\Big|_{\alpha=0} \tag{2.17}$$

$$K_{ij}^{II} = \frac{\partial^2 K}{\partial \alpha_i \partial \alpha_j}\Big|_{\alpha=0} \tag{2.18}$$

The external force vector F also involves random variables and can be expanded in the form similar to that for K. Because the nodal displacements are influenced by the structural uncertainties, the displacement vector U also possesses the approximate expression

$$U = U^0 + \sum U_i^I \alpha_i + \frac{1}{2}\sum\sum U_{ij}^{II} \alpha_i \alpha_j \tag{2.19}$$

thus the coefficient vector $U^0$, $U_i^I$, and $U_{ij}^{II}$ are determined by the following set of recursive equations:

$$U_0 = (K^0)^{-1} F^0 \tag{2.20}$$

$$U_i^I = (K^0)^{-1}(F_i^I - K_i^I U^0) \tag{2.21}$$

$$U_{ij}^{II} = (K^0)^{-1}(F_{ij}^{II} - K_i^I U_j^I - K_j^I U_i^I - K_{ij}^{II} U^0) \tag{2.22}$$

The strains and stresses of each element are also expanded in the similar series forms and the corresponding coefficients can be determined. Thus, the mean values and covariances for the

displacements, strains and stresses of the structural system are approximately solved for based on a second-order expansion in terms of the mean value and covariance of the random vector a. The above reviewed technique is usually named as the first-order-second-moment method.

It is the advantage that the first-order second-moment technique can follow all the steps of a conventional deterministic analysis scheme, and thus can capitalize on existing techniques and algorithms. This method has been proved to be quite effective and accurate for analyzing structural systems with the parametric uncertainties of small variability. The extensive applications of this technique can be found in a large amount of literature, and some of it are cited here: nonlinear response of composite structures in Engelstad and Reddy (1993), uncertain eigenvalue analysis of composite laminated plates in Nakagiri *et al.* (1987), structural response of initially compressed uncertain laminated plates in Liaw and Yang (1991), reliability assessment of uncertain flexible laminated skewed plates under random compression in Chang and Yang (1992), buckling and first-ply reliability evaluation of composite laminates in Lin and Kam (1996). Some important papers on the general introduction and development of this technique are also listed here: Benaroya and Rehak (1988), Liu *et al.* [1986(a), 1886(b) and 1987], Hisada and Nakagiri (1985), and Vanmarcke *et al.* (1986).

### 2.1.3 Summary

The stress-based failure probability of the composite lamina under complex stress state can be determined by Monte Carlo simulation method, Taylor series expansion method, first-order reliability method if the composite lamina is assumed to be statistically homogeneous. On the scale of laminated composites, limited success has been achieved to calculate the reliability with the failure tree model and the bundle model. The probabilistic finite element technique can be used to quantify the random structural responses (such as buckling, vibration frequency, displacement field, stress field, etc.) of laminated composites, but can not be used to model the random damage evolution and the probability distributions of the ultimate strength of structural systems. Only the Monte Carlo simulation technique is able to simulate the random damage evolution in laminated composites under some restrictive conditions. Hence, the evaluation of the failure probability of laminated composites from stress-based failure criteria is still an open research field.

## 2.2 DELAMINATION FAILURE

The beginning of the study of delamination in laminated composites may be dated back in 1960's with analytical and experimental investigations of such a failure mode at the free edges. In 1967, Hayashi proposed the first analytical model to compute the interlaminar shear stresses that then has come to be known as the popular terminology "free edge effect". In 1970, Foye and Baker made the first report on experimental observations in free-edge-effect induced delamination. After these pioneering researches, many efforts have been devoted to this problem, mainly focused on the calculation of edge effect stress field and the development of failure criteria, and some design techniques against this type of failure mode have been developed. More detailed information about the progression and achievements in this field refers to two books edited by Pagano (1989) and Newaz (1991) respectively.

Basically, there exist two distinct approaches to predict the delamination onset in laminated composites, one related to mechanics of materials, the other to fracture mechanics. The mechanics of materials technique is based on the local three-dimensional stress analysis in conjunction with stress-based failure criteria (Kim and Soni, 1984, Sun and Zhou, 1988). Recently, the development of some efficient analytical and numerical solution techniques for the calculation of interlaminar stresses at free edges has made the stress analysis more convenient. However, because of a weak interlaminar stress singularity at free edges, an average stress approach, similar to the Whitney-Nuismer criterion (Whitney and Nuismer, 1974) for the strength of notched composites must be adopted by averaging interlaminar stress components over a characteristic length from the free edges. Usually, the characteristic length is viewed as a material constant, even though it seems to be dependent on the laminate's configurations (Chang *et al.*, 1984). Moreover this approach suffers from the difficulties in measuring the interlaminar strength components (discussed in Chapter 4). The fracture mechanics technique is based on the assumption that delamination is modeled as an edge crack and thus either stress intensity factor or strain energy release rate can be determined by the classical elasticity approach to be compared with their critical values (Rybicki *et al.*, 1977, O'Brien, 1982 and 1984). These critical values are assumed to be material constants and thus can be experimentally characterized. Due to the difficulties in computing interlaminar stress intensity factor, the strain energy release rate approach is more popular. The advantage of the strain energy release rate approach is that there have been convenient test methods to reliably measure the critical

values for all the three interlaminar fracture modes, and no critical length is required to characterize interlaminar stress concentrations. This approach can also be extended to predict delamination growth because strain energy release rate remains nearly constant during delamination propagation (Wang *et al.* 1985, Law, 1984). However, it is tedious to calculate strain energy release rate due to delamination by the finite element technique. At present, it is difficult to make a comparison between these two methodologies due to their individual advantages and disadvantages.

Compared with delamination onset, delamination propagation is a more complex problem. The growth speed rate is governed not only by the failure modes of delamination onset, but by the interaction between delamination and matrix transverse cracks as well (Crossman and Wang, 1982). For instance, laminated composites can further carry loads beyond the free edge delamination onset which is caused by the interlaminar normal stress component (Zhou and Sun, 1990), while a disintegration failure of laminated composites takes place immediately after delamination onset which is caused by the interlaminar shear stresses (Soni and Kim, 1986). Also, experimental results indicate that matrix transverse cracks subsequently occur after delamination onset and are followed by the simultaneous growth of transverse cracks and delamination areas (Lagace and Brewer, 1987). In order to mathematically model this kinematic problem, a common assumption has been adopted that the delamination grows in a one-dimensional self-similar manner (Wang *et al.*, 1985). This assumption makes it possible to calculate strain energy release rate as a function of delamination crack length by the finite element approaches. Furthermore, it is found that the critical values of strain energy release rates for delamination growth with the one-dimensional self-similar manner remains approximately independent of the delamination crack length, therefore the values of $G_{IC}$, $G_{IIC}$ and $G_{IIIC}$ could be experimentally characterized under simple loading conditions. Delamination growth depends on the mixed-mode strain energy release rates $G_I$, $G_{II}$ and $G_{III}$ governed by the stress state at the crack tip. Under static loading conditions, the generation of new surface area at initiation could be evaluated by some failure criteria in terms of three distinct fracture modes of strain energy release rates and their corresponding critical values (O'Brien, 1982, Wang *et al.*, 1985, Law, 1984, Jurf and Pipes, 1982, Johnson and Mangalgiri, 1987, Lee, 1988). Under fatigue loadings, the relationship between the delamination crack length and the number of cycles could be evaluated by some power failure criteria represented in terms of maximum strain energy release rate, load ratio and some material constants (O'Brien, 1982, Wang *et al.*, 1985, Ramkumar and Whitcomb, 1985, Poursartip, 1987, Martin *et al.*, 1996, Russell and Street, 1989)

### 2.2.1 General Strength Theories for Anisotropic Homogeneous Materials

One of the most important tasks of material characterization and structure design is to set up failure criteria to predict the material failure strength due to complex stress states based upon their basic material properties. In the historic development of strength theories, failure criteria concerned with isotropic homogeneous materials are well established, in which the Von Mises distortional energy theory proposed in 1913 has been most widely employed. Anisotropic materials have more complicated failure mechanisms than isotropic materials because of the anisotropic characteristics of different moduli and different strengths in different directions, hence all six three-dimensional stress components and more interaction terms should appear in anisotropic failure criteria. There have been numerous strength theories developed and proposed for anisotropic materials, most of which are focused on the in-plane stress state. In the review papers (Sendeckyj, 1972, Tsai, 1984, Nahas, 1986, Fan, 1987), discussions of various strength theories for composite materials have been presented.

#### 2.2.1.1 Von Mises Anisotropic Yield Criterion

Von Mises in 1928 extended his isotropic yield criterion to anisotropic homogenous materials and proposed an anisotropic yield criterion, to be homogeneous quadratic in stress components:

$$k_{ij}\,\sigma_i\,\sigma_j = 1 \tag{2.35}$$

where the contracted notation is used for i, j = 1, 2, ..., 6 and $k_{ij}$ is the strength tensor of the 4nd rank. Hence, there are 21 independent constants in the general form of the Von Moses anisotropic yield criterion due to the fact that strength tensor is symmetric. It is seen that the Bauschinger effect was not considered in Von Mises anisotropic criterion because no linear terms are included. Hill (1948) then modified this criterion by adding linear terms $k_i\sigma_i$ to account for the Bauschinger effect.

#### 2.2.1.2 Gol'denblat-Kopnov Criterion

Gol'denblat and Kopnov in 1966 proposed a more generalized failure criterion for both yield and brittle fracture of anisotropic materials

$$(k_i\sigma_i)^{\alpha}+(k_{ij}\sigma_i\sigma_j)^{\beta}+(k_{ijk}\sigma_i\sigma_j\sigma_k)^{\gamma}+\ldots=1 \tag{2.36}$$

where $k_i$, $k_{ij}$ and $k_{ijk}$, ..., are the strength tensors of the 2nd, 4nd and 6nd, ..., rank, and $\alpha$, $\beta$ and $\gamma$,..., are material parameters experimentally determined.

### 2.2.1.3 Malmeister Criterion

Also, Malmeister (1967) proposed an anisotropic tensor polynomial failure criterion:

$$k_i\sigma_i+k_{ij}\sigma_i\sigma_j+k_{ijk}\sigma_i\sigma_j\sigma_k+\ldots=1 \tag{2.37}$$

At a first glance, Equation (2.37) is a special form of Equation (2.36) when $\alpha = \beta = \gamma = \ldots = 1$. However, there are certain differences between Malmeister criterion and Gol'denblat-Kopnov criterion, since $\alpha$, $\beta$, $\gamma$ are material constants and not necessarily equal to one.

The above three failure criteria are the fundamental strength theories for anisotropic homogeneous materials. Up to the present, most of the strength theories for fiber-reinforced composite materials could be regarded as the development of these general anisotropic failure criteria under some particular assumptions. Fiber-reinforced composite materials are a special kind of anisotropic materials because they can have the characteristics of orthotropy. We can hope that the Gol'denblat-Kopnov criterion and the Malmeister criterion have better predictions because more related terms are included. In practical applications, the Malmeister criterion is more preferable because of the difficulty in experimentally measuring the material parameters $\alpha$, $\beta$, $\gamma$... in the Gol'denblat-Kopnov criterion. The Von Mises yield criterion can be regarded to be the special form of the Malmeister criterion only with fourth rank strength tensors. In Tsai and Wu's paper (Tsai and Wu, 1971), the terms with higher orders than 2, such as $k_{ijk}\sigma_i\sigma_j\sigma_k$, were neglected in the Malmeister criterion because the large number of terms make mathematical operations impractical. Moreover, failure surfaces of quadratic criteria in the stress space are ellipsoid, while failure surfaces of the criteria with cubic terms become open-ended, that is, "infinite strengths" are predicted. Tennyson and his colleagues (Tennyson *et al.*, 1978, Tennyson *et al.*, 1980, Jiang and Tennyson, 1989) argued that quadratic criterion are too conservative and a cubic formulation is thus required. They conducted the experimental and analytical evaluation of the cubic tensor polynomial failure

criterion by laminated composites in the plane stress state, and developed an analytical method to ensure the closure of cubic tensor polynomial failure criterion. It could be expected that higher order tensor polynomial formulations can provide more comparable results with experiments. However from the view of engineering standpoint, it is expensive, even sometimes impractical since more interaction parameters are required. Currently, the quadratic failure criteria are most widely accepted.

### 2.2.2 Literature Review of Delamination Onset Criteria

Most of failure criteria are focused on a unidirectional lamina scale because of extreme nonhomogeneity and difficulty in mathematical operations of multidirectional laminates. A macroscopically homogeneous filamentary lamina always possesses three mutually orthogonal planes of symmetry. The intersections of these planes are then known as the axes of anisotropic symmetry (sometimes as principal material axes). If a Cartesian coordinate system (1, 2, 3) is considered with 1 axis fixed in the direction of the fiber, 2 axis perpendicular to the fiber direction in the lamina plane, and 3 axis normal to the lamina plane, then 1, 2 and 3 axes are the ones of anisotropic symmetry. The mathematical operations of failure criteria for filamentary composites should be performed in this Cartesian coordinate system of anisotropic symmetry because the tensor transformation of strength properties is much more complex than that of stiffness properties (Jones, 1975). Because, fiber-reinforced composite materials exhibit a great difference between tensile and compressive compressive strengths, but exhibit identical strengths for positive and negative shear, there are nine strength components for a homogeneous orthotropic lamina along the axes of anisotropic symmetry which are denoted as follows:

$X_t$ – tensile strength component in 1 direction (longitudinal)

$X_c$ – compressive strength component in 1 direction (longitudinal)

$Y_t$ – tensile strength component in 2 direction (transverse)

$Y_c$ – compressive strength component in 2 direction (transverse)

$Z_t$ – tensile strength component in 3 direction (out-of-plane)

$Z_c$ – compressive strength component in 3 direction (out-of-plane)

S, Q, R – shear strength components in the 1-2, 2-3, and 1-3 planes of the lamina

These strength components are uniaxial and pure shear test data measured from standard test methods of unidirectional specimens. Generally, unidirectional fiber composites in uniaxial loadings exhibit linear or non-linear behaviours in the longitudinal and transverse directions, which depends on the type of material system, but always exhibit nonlinear behaviours in shear (Petit and Waddoups, 1969, Hahn and Tsai, 1973). Hence, the strength theories for fibrous composites slightly differ from the concept of the yield criteria in the theory of plasticity. In stress space, the yield surfaces (yield criteria) represent a limit of linear elastic behaviours under the complex stress states, while the failure surfaces (failure criteria) represent the existence of material failure even though yielding has taken place at lower stress levels, i.e., the failure surface is not restricted to be the limit of multidirectional linear elastic behaviour. Thus, the strength components in the directions of anisotropic symmetry are accepted to be the ultimate values that specimens can carry. Correspondingly, a general combined stress state in a three-dimensional continuum body has six stress components: the normal stresses $\sigma_1$, $\sigma_2$ and $\sigma_3$, and the shear stresses $\tau_{12}$, $\tau_{23}$ and $\tau_{13}$. These stress components are oriented in the directions of anisotropic symmetry, otherwise they must be transformed.

Delamination is a problem related to out-of-plane stress components, hence, theoretically all the three-dimensional failure criteria can predict delamination failure. At a given interface, one failure criterion must be applied to both the adjacent layers because of the discontinuity of in-plane stress components at the interface, and delamination happens if the stress state in any of the two layers reach the failure strength. Herein, the Tsai-Hill (Hill, 1950, Azzi and Tsai, 1965, Tsai and Azzi, 1966), Hoffman (1967) and Tsai-Wu (1971) three-dimensional failure criteria are reviewed. Although the Norris (Norris, 1962) and Yeh-Stratton (Yeh and Kim, 1994) failure criteria also can account for the three-dimensional failure mode, they are not discussed in this chapter because these two criteria are composed of three individual equations and thus do not consider all the interaction effects of different delamination failure modes where the interlaminar stress components play a major role.

#### 2.2.2.1 Tsai-Hill Three-Dimensional Criterion

Hill (1950) generalized the Von Mises isotropic yield criterion to orthotropic plastic bodies. The Hill orthotropic yield criterion has the form

$$F(\sigma_2-\sigma_1)^2+G(\sigma_3-\sigma_1)^2+H(\sigma_3-\sigma_2)^2+2L\sigma_4^2+2M\sigma_5^2+2N\sigma_6^2=1 \qquad (2.38)$$

where F, G, H, L, M and N are material parameters. Azzi and Tsai (1965) postulated that the failure of unidirectional fibrous lamina has the same mathematical form as the Hill yield criterion. The coefficients in Equation (2.38) can be easily determined in terms of the strength components and the mathematical operations can be found in Azzi and Tsai (1965). Finally, the Hill failure criterion for unidirectional laminas is given by

$$(\frac{\sigma_1}{X})^2+(\frac{\sigma_2}{Y})^2+(\frac{\sigma_3}{Z})^2-(\frac{1}{X^2}+\frac{1}{Y^2}-\frac{1}{Z^2})\sigma_1\sigma_2-(\frac{1}{Y^2}+\frac{1}{Z^2}-\frac{1}{X^2})\sigma_1\sigma_3-(\frac{1}{Y^2}+\frac{1}{Z^2}-\frac{1}{X^2})\sigma_2\sigma_3$$
$$(\frac{\tau_{12}}{S})^2+(\frac{\tau_{23}}{Q})^2+(\frac{\tau_{13}}{R})^2=1 \qquad (2.39)$$

where X, Y and Z denote the strength components in 1, 2 and 3 directions, respectively. In the Hill criterion, the interactions between normal stress components are considered, thus the failure surface in stress space is smooth. However, this criterion assumes that composite materials exhibit same strengths in tension and compression (i.e., $X_t = X_c = X$, $Y_t = Y_c = Y$ and $Z_t = Z_c = Z$), or, in other words, the Bauschinger effect is not included. Indeed, most of composite materials have strong difference between tensile and compressive strengths because they exhibit brittle failure. Hence, the Hill yield criterion is an empirical strength theory. By the way, Marin (1957) is the first one who suggested a strength theory for nonisotropic materials with different strengths in tension and compression in 1957.

The Tsai-Hill criterion is a modified Hill criterion where Tsai and Azzi (1966) assumed that the Hill criterion remains applicable for composite materials with different strength components in tension and compression. In this criterion, the strength components are substituted into Equation (2.39) based upon the corresponding stress components, that is, tensile strength components for positive stresses and compressive strength components for negative stresses. Hence, the Tsai-Hill criterion can account realistically for the difference in tensile and compressive strengths that characterize brittle fracture behaviours. This criterion has been frequently employed in the design of composite structures due to its simplicity, even though it is an empirical formula. Sun and Kelly (1988) attained good correlation between test and analysis for delamination by applying the three-

dimensional Tsai-Hill criterion with assuming transverse isotropy in strength components.

### 2.2.2.2 Hoffman Three-Dimensional Criterion

Hoffman (1967) noted that the Bauschinger effect (i.e., linear terms) is absent in the Hill yield criterion in Equation (2.38), therefore he modified the Hill criterion by adding three linear terms, as follows:

$$F(\sigma_2-\sigma_1)^2+G(\sigma_3-\sigma_1)^2+H(\sigma_3-\sigma_2)^2+A\sigma_1+B\sigma_2+C\sigma_3+ 2L\sigma_4^2+2M\sigma_5^2+2N\sigma_6^2=1 \tag{2.40}$$

Similar to those in the Tsai-Hill criterion, all the nine coefficients in Equation (2.40) can be determined by strength components under simple loading conditions, and thus the Hoffman three-dimensional criterion is given by

$$\frac{1}{2}\left(\frac{1}{Y_tY_c}+\frac{1}{Z_tZ_c}-\frac{1}{X_tX_c}\right)(\sigma_2^2-\sigma_3^2)+\frac{1}{2}\left(\frac{1}{Z_tZ_c}+\frac{1}{X_tX_c}-\frac{1}{Y_tY_c}\right)(\sigma_3^2-\sigma_1^2)+\frac{1}{2}\left(\frac{1}{X_tX_c}+\frac{1}{Y_tY_c}-\frac{1}{Z_tZ_c}\right)(\sigma_1^2-\sigma_2^2)+\left(\frac{1}{X_t}-\frac{1}{X_c}\right)\sigma_1+\left(\frac{1}{Y_t}-\frac{1}{Y_c}\right)\sigma_2+\left(\frac{1}{Z_t}-\frac{1}{Z_c}\right)\sigma_3+ \left(\frac{\tau_{12}}{S}\right)^2+\left(\frac{\tau_{23}}{Q}\right)^2+\left(\frac{\tau_{13}}{R}\right)^2=1 \tag{2.41}$$

Hence, the Hoffman criterion can distinguish the difference between positive and negative stress induced failure modes. Narayanaswami and Adelman (1977) evaluated that this criterion can give excellent agreement with the experimental results obtained from unidirectional test specimens under off-axis loading.

### 2.2.2.3 Tsai-Wu Three-Dimensional Criterion

Tsai and Wu in 1971 developed an operationally simple strength criterion for unidirectional composites. This criterion was a definite improvement over previously existing criteria because it was completely derived from the Malmeister anisotropic tensor polynomial failure criterion in Equation (2.37) by picking up two strength tensors. Besides the considerations of the Bauschinger effect and interaction terms between individual stress components, this criterion satisfies the

invariant requirements of coordinate transformation, and treats interaction terms as independent components, therefore the strength tensors can be transformed with respect to different coordinate systems. Because the change in the sign of shear stress components does not change the failure strength (i.e., shear strengths are all uncoupled), the interaction terms related to shear stress components vanish in the quadratic tensile polynomial failure criterion. The principal coefficients $k_i$ and $k_{ii}$ in Equation (2.37) can be determined from the strength components. Finally, the Tsai-Wu criterion is written as

$$\frac{\sigma_1^2}{X_t X_c} + \frac{\sigma_2^2}{Y_t Y_c} + \frac{\sigma_3^2}{Z_t Z_c} + 2k_{12}\sigma_1\sigma_2 + 2k_{23}\sigma_2\sigma_3 + 2k_{13}\sigma_1\sigma_3 + \frac{X_c - X_t}{X_t X_c}\sigma_1 + \frac{Y_c - Y_t}{Y_t Y_c}\sigma_2 + \frac{Z_c - Z_t}{Z_t Z_c}\sigma_3 + (\frac{\tau_{12}}{S})^2 + (\frac{\tau_{23}}{Q})^2 + (\frac{\tau_{13}}{R})^2 = 1 \qquad (2.42)$$

where the remaining interaction coefficients $k_{12}$, $k_{23}$, and $k_{13}$ have to be determined by combined stress experiments. However, no evidence shows that the values determined by different combined stress states will be same or even close. Some literature (Wu, 1972, Pipes and Cole, 1973, Evans and Zhang, 1987) discussed various methods to determine the value of $k_{12}$ and found that it is difficult to evaluate this stress interaction term. The best method to get these three interaction terms is to fit a series of experimental data. The Tsai-Wu three-dimensional criterion has been used to predict the delamination initiation by Herakovich *et al.* (1981) and Kim and Soni (1986).

#### 2.2.2.4 Quadratic Delamination Criterion

Hashin (1980) assumed that failure along a surface results from its out-of-plane stress components rather than in-plane stress components, thus only the out-of-plane stresses appear in the failure criteria if the failure surface can be determined in advance. The Hashin assumption has been extensively accepted into the investigation of delamination phenomena, since this type of failure always takes place at the interfaces between layers of different fiber orientations. A quadratic delamination criterion based on the Hashin assumption has been frequently used to model delamination failure, which is in a completely quadratic term of three interlaminar stress components. Let $\sigma_z$, $\tau_{yz}$ and $\tau_{xz}$ denote the interlaminar normal and shear stresses, and $S_z$, $S_{yz}$ and $S_{xz}$ denote the corresponding interlaminar strength components corresponding to these stress components in a Cartesian coordinate system whose z axis is parallel to the thickness direction of a

lamina, then when interlaminar normal stress is tensile, i.e., $\sigma_z > 0$, the delamination criterion is

$$(\frac{\sigma_z}{S_z})^2 + (\frac{\tau_{yz}}{S_{yz}})^2 + (\frac{\tau_{xz}}{S_{xz}})^2 = 1 \qquad (2.43.a)$$

and when interlaminar normal stress is compressive, i.e., $\sigma_z < 0$, the delamination criterion is

$$(\frac{\tau_{yz}}{S_{yz}})^2 + (\frac{\tau_{xz}}{S_{xz}})^2 = 1 \qquad (2.43.b)$$

In the case of compressive interlaminar normal stress, the term associated with this component is neglected because it is believed that the interlaminar compressive strength is much greater than the tensile strength. For the purpose of simplification, the interlaminar tensile strength $S_z$ is approximated to be equal to the transverse tensile strength component of unidirectional lamina $Y_t$, while both interlaminar shear strengths $S_{yz}$ and $S_{xz}$ are approximated to be equal to the in-plane shear strength component of unidirectional lamina S. This is the most popular stress-based failure criterion to model free edge delamination in conjunction with a average stress criterion (discussed in the later section).

### 2.2.3 Dependence of Interlaminar Strengths on Fiber Orientations

It has been well recognized that the transverse tensile strength of a lamina in a laminate strongly depends on the thickness of the lamina and the fiber orientations of its surrounding laminae (Flaggs and Kural, 1982, Peter, 1984, Herokovich, 1982). Three main effects on the transverse tensile strength have been observed in experiments and modeling: (1) this strength is greater than that measured from standard unidirectional specimen tests, (2) when the thickness of a unidirectional lamina (with more identical-fiber-orientation plies) increases, its in situ strength will decrease, and (3) adjacent laminae with different fiber orientations will strengthen the central lamina. Similar tendency has also been observed in the in-plane shear strength of a lamina in laminated composites (Chang and Chen, 1987, Chang *et al.*, 1987, Pindera *et al.*, 1987), although the variation degree in the shear strength is different from that in the transverse tensile strength. Both the effects on the lamina transverse and shear strengths are associated with the initiation and growth of matrix transverse cracks. Therefore, stress-based failure criteria should be incorporated

with the effects of these strength components to accurately predict failure of laminated composites. The failure analysis of laminated composites has been carried out using failure criteria including these effects by Chang and Lessard (1991).

Similar investigations have been extensively conducted on Mode I and II critical strain energy release rates on the interfaces surrounded by differently-oriented plies using the end notch deflection (END) and the end notch flexure (ENF) test technique. The experimental results seem to demonstrate two contrast conclusions, concerning whether the critical release rates at the interfaces depend on the fiber orientations of their surrounding plies. Tohgo *et al.* (1996) experimentally measured by the END test technique the Mode I critical strain energy release rate, and found that the mean value seems to be independent of the fiber orientation difference. However, Nicholls and Gallagher (1983), and Robinson and Song (1992) established a contrary conclusion based on their experimental results.

For Mode II critical strain energy release rate, apparent dependence was reported by Xiao and Li for the Aramid/Epoxy material system (1989), Chou *et al.* for the T800H/No. 3631 material system (1995), Compston *et al.* for the marine-used Glass/Vinyl Ester material system (1997), and Tao and Sun for the AS4/3501-6 material system (1998). Little dependence, however, was reported by Russell and Street for AS1/3501-6 material system (1982), Davidson *et al.* for the Ciba Geigy C6000/R6376 material system (1994), and Hudson *et al.* for the Ciba Geigy C12K/R6376 material system (1995).

Xiao and Li (1989) performed a test on the $[0_5//\theta/\theta/0_5]$ specimens with the cracks at the $0/\theta$ interfaces ($\theta = 0°$, 15°, 30°, 60°, 75° and 90°) and found that the $G_{IIC}$ reaches the maximum at $\theta = 30°$ and the minimum at $\theta = 90°$ (the ratio is 1.61). The $G_{IIC}$ corresponds to the initiation of crack propagation, which is represented by a sudden loading drop in the load versus deflection curves. The crack propagation behaviours were not reported in their paper. Chou *et al.* (1995) used the $[\theta/-\theta/0_8/-\theta/\theta//-\theta/\theta/0_8/\theta/-\theta]$ specimens with cracks at the central planes ($\theta = 0°$, 30°, and 60°). Because the load versus load-line deflection curves obtained from the ENF test exhibit a nonlinear response, three types of critical release rates are calculated based on the curves; $G_{IIC(NL)}$ corresponding to the initiation of nonlinear response, $G_{IIC(5\%)}$ corresponding to the 5% reduction of secant modulus, and $G_{IIC(max)}$ corresponding to the maximum load. The value for $G_{IIC(NL)}$ was

found to be highest at the 0/0 interface and lowest at the 30/-30 interface; the maximum to minimum ratio is 1.32, but the values for $G_{IIC(5\%)}$ and $G_{IIC(max)}$ to be higher at the 60/-60 interface and lower at the 0/0 interfaces; the maximum to minimum ratio is 1.21. It was observed that although the delamination cracks are initiated at the -θ/θ central planes, the cracks always jump through one θ or -θ plies and then propagate along the interfaces between the θ (or -θ) and 0° plies. Compston *et al.* (1997) investigated the $G_{IIC}$ at the 0/0, 30/30 and 30/-30 interfaces that are located at the central planes of the specimens. The specimen lay-ups were not reported in their paper. The $G_{IIC}$ corresponding to the initiation of crack growth was found to be dependent on the fiber orientations and the ratio of the maximum at the 0/0 interface to the minimum at the 30/-30 interface is 1.32. However, the $G_{IIC}$ measured from the precracked specimens seems to be less dependent on the fiber orientations, wherein the precracks are made by propagating the initial cracks to some degree through the first loading and then the $G_{IIC}$ corresponding to the initiation of precrack growth is obtained by applying the second loading. The crack jumping from interface to interface was also observed. After a series of tentative experiments, Tao and Sun (1998) found that the pure delamination cracks could propagate only at the 0/θ interfaces and thus designed the $[(0_{10}/90/0_{10})//\theta/(0_{10}/90/0_{10})]$ specimens to characterize the critical release rates (θ = 0°, 30°, 45°, 60° and 90°). In each specimen, only one θ ply surrounded by the 0° plies is located in the middle, therefore the delamination cracks always grow along the 0/θ interfaces even though the cracks jump across the θ ply. Their experimental results demonstrate that the $G_{IIC}$ decreases as the off-axis angle θ increases, and the maximum to minimum ratio is 1.41.

Russell and Street (1982) studied the critical strain energy release rates at the 0/0, 0/45 and 0/90 interfaces for the AS1/3501-6 Graphite/Epoxy composites (detailed lay-up information for the specimens was not reported). Two types of critical release rates are evaluated; $G_{IIC}$ corresponding to the initiation of crack propagation from the roots of the teflon-made cracks, and $G'_{IIC}$ corresponding to the crack extension at which the initial cracks are arrested. Their experimental results presented that fiber orientations seem to have little effect on the values of either $G_{IIC}$ or $G'_{IIC}$. Davidson *et al.* (1994) investigated the critical release rates $G_{IIC}$ at five types of interfaces; 0/0, +15/+15, +30/+30, +15/-15 and +30/-30. The detailed lay-up information can be referred to their paper. All the specimens are not precracked, and the critical release rates $G_{IIC}$ correspond to the onset of macro-crack advance at the roots of the teflon-made cracks, which is

denoted by a sharp peak in the load versus displacement curves. Their experimental results show that for the material system studied, the values of $G_{IIC}$ seem to be independent of the fiber orientations. Furthering the experimental work (Davidson *et al.* 1994), Hudson *et al.* (1995) measured the $G_{IIC}$ using both the precracked and non-precraked ENF specimens with $[\pm 30/0_{12}/\mp 30]_s$ (central crack) and $[\pm 30/0_{12}/\mp 30//\mp 30/0_{12}/\pm 30]$ lay-ups respectively. It also was reported that there are "clearly" no significant effects of fiber orientations on the $G_{IIC}$ by comparing the experimental values at the 30/-30 and 30/30 interfaces for both precracked and non-precracked specimens.

### 2.2.4 Singular Interlaminar Stresses

The strength prediction of fiber-reinforced composite materials with stress concentration is very conservative, if the aforementioned failure criteria are directly applied to the point with most highly concentrated stresses based on the strength components obtained from standard specimens. The failure strength of a brittle body is believed to strongly depend on its volume because more inherent flaws of various dimensions are distributed throughout a body with a larger volume (Weibull, 1951, Wisnom, 1991). For instance, the stress required to break a single fiber within a unidirectional composite is much higher than that is required to break the composite. The size effect (i.e., scale effect) is a complicated phenomenon and can be limitedly explained by the Weibull weakest link theory. Hence, the failure strength of the composites with stress concentration is strongly associated with the size of the region over which the stresses are higher than the strength experimentally obtained from standard specimens, rather than with the actual magnitude of the stress concentration at a single point. This evidence can be easily illustrated from the fact that the tensile strength of laminated composites containing circular holes depends on the hole sizes. It is well known that the stress intensity factors of a composite are identical at the edge of holes with various diameters. However, the stress concentration is much more localized for smaller holes, thus a smaller volume of material is subjected to higher stress in a laminated composite containing small holes, which results in a higher failure strength than that of laminated composites with larger holes.

It is believed that the approach of progressive damage models can effectively account for the failure of composite materials subjected to localized (or nonuniform) stresses (Chang and Lessard, 1991, Chang and Chang, 1987, Chang *et al.* 1991). The other one, namely the size effect approach discussed below, is still of engineering value due to the simplicity, which may be dated

back in 1964 with Weil and Daniel's investigation on fracture probabilities of nonunifromly stressed brittle materials using the Weibull theory (Weil and Daniel, 1964). Waddoups *et al.* (1971) proposed that the size effect of holes could be modeled using the concept of linear elastic fracture mechanics by assuming the existence of an intense energy region at each side of the holes where new cracks are expected to be generated. The effective size of the intense energy is represented by a characteristic length, which is regarded as a material constant. Whitney and Nuismer (1974) developed a so-called "average stress criterion" to deal with the failure strength of laminated composites containing stress concentration. Wherein it was assumed that the stress-based failure criteria are still applicable in such cases, instead of stress values at a single point, all the stress components in these criteria are replaced by their average values, which are taken over some distance, $a_0$, away from the discontinuity edges:

$$\overline{\sigma}_{ij} = \frac{1}{a_0}\int_0^{a_0} \sigma_{ij}\, dy \tag{2.44}$$

The distance is usually named as the characteristic length, and assumed to be a material constant independent of laminate geometry and stress distribution.

**Table 2.1.** The values of characteristic length used for the prediction of delamination onset.

| Characteristic Length | | |
|---|---|---|
| References | Materials | Values* |
| Kim and Soni (1984) | T300/5208 | 1.00 |
| Soni and Kim (1986) | T300/1034 | 1.00 |
| Sun and Zhou (1988) | AS4/3501-6 | 2.00 |
| Brewer & Lagace (1988) | AS4/3501-6 | 1.05 |
| Joo and Sun (1992) | AS4/3501 | 1.50 |

* times of ply thickness

The average stress criterion has been widely used to predict the delamination onset in conjunction with the quadratic delamination criterion in Equation (2.43). Because the prediction of interlaminar stress distribution near the free edges is of significant difference from various existing

analytical methods, the characteristic length is usually determined by best fitting the experimental results. Hence, even for a single laminated composite, the characteristic length is changeable in the average criterion when different analytical methods are used to calculate the interlaminar stresses. The values of the characteristic length adopted by various papers are tabulated in Table 2.1.

### 2.2.5 Summary

Despite considerable work on Mode I and II critical strain energy release rates, no research work has so far been reported on the dependence of interlaminar strength components at the interfaces on the fiber orientations of their surrounding plies. Furthermore, in order to uncover the more detailed mechanism behind the delamination failure and yield more accurate prediction, the effects of fiber orientations on interlaminar strength components should be incorporated into the delamination criteria. Therefore, two aspects of research are expected; (1) to perform experimental investigations on the effects of fiber orientations on interlaminar strength components, and (2) to develop innovative delamination criteria to include these effects.

# CHAPTER 3

# CURVED EDGE EFFECT STRESSES: A VARIATIONAL SOLUTION

In this chapter, a variational approach is developed to determine the three-dimensional edge effect stresses around traction-free holes and pin-loaded holes in symmetric laminated composites. Based on the superposition principle of linear elasticity theory, the stress state around the holes is divided into two parts, one the in-plane stress state determined using the Classical Laminated Plate Theory (CLPT) and another the boundary layer stress state arising from the edge effects which only exists in the vicinity of the holes. The equilibrium equations of boundary layer stress state with zeroth-order approximation are derived from a set of power expansions. An analytical closed form solution for the boundary layer stress state is then obtained by imposing zeroth-order stress functions on the variational principle of complementary energy.

## 3.1 INTRODUCTION

Ever since composite materials were adopted into structural applications, the edge effects in laminated composites have been of significant interest. At the edges of laminated composites, interlaminar stresses arise from the mismatch of elastic properties between layers and potentially induce delamination failure there. Hence, the stress distribution near the edges is three-dimensional even though the laminates are only subjected to in-plane loadings. The Classical Laminated Plate Theory (CLPT) can not be used to calculate all of the stress components, and a three-dimensional stress and failure analysis is thus expected to provide more information about the edge effect problem. Typically, edge effects occur at the free boundaries of cutouts, and the

contact boundaries of pin/bolt-loaded holes in laminated composites. In the past, much research has been performed on the problem of interlaminar stresses at straight free edges of laminated composites under in-plane uniaxial loading (Pipes and Pagano, 1970, Pipes, 1972, Pagano, 1974, Wang and Choi, 1982, Wang and Crossman, 1977, Kassapoglou and Lagace, 1986 and 1987, Kassapoglou, 1990). However, only a limited number of authors have investigated the interlaminar stresses in laminate composites with cutouts under in-plane loading. Even less research work has been performed on the edge effects in the pin-loaded laminated composites. Further research is therefore required, especially on the aspects of three-dimensional stress analysis around traction-free holes and pin-loaded holes in laminated composites.

Curved edge effects in laminated composites with traction-free circular holes have been studied in a few research works through numerical and analytical solution techniques. The finite element approach has been one of the most commonly used numerical techniques in the past investigations. Rybicki and Schmueser (1978) investigated the effect of stacking sequence and lay-up angle on the free edge stresses around circular holes, while Lucking *et al.* (1984) investigated the effect of the hole radius to laminate thickness ratio on the interlaminar stresses in a $[0/90]_s$ composite. Both studies made use of the conventional three-dimensional displacement formulated isoparametric elements and were based on the potential energy principle. Ericson *et al.* (1984) used singular elements with assumed strain field to treat the interlaminar stress concentration along hole free edges. Some special finite element techniques have also been developed to perform the stress analysis for the curved free edge problem. Nishioka and Atluri (1982) proposed an assumed-stress hybrid finite element method based on the modified complementary energy principle, wherein the approach is to embed analytical asymptotic solutions into the "special-hole elements" for the analysis of three-dimensional stress state near a circular hole. More recently, Hoa and Feng (1996) developed a global/local approach using partial hybrid elements, in which the domain of laminated composites with curved free edges is divided into a local region, a transition region and a global region in order to reduce the number of active degrees of freedom without loss of accuracy. The finite element methods however have suffered from the difficulties of handling the curved free edge effects in thick laminated composites due to the limitation of computing costs. Furthermore, caution must be taken when conventional displacement formulated isoparametric elements are used to model free edge

problems, since it is believed that unreliable results of calculated stresses at free edges may arise from the inability to exactly satisfy the traction free conditions at edges and traction continuity conditions at layer interfaces (Spilker and Chou, 1980, Whitcomb *et al.*, 1982).

On the other hand, analytical closed form solutions are preferable to define the potentially high interlaminar stress gradient field near circular hole free edges of laminated composites. Unfortunately, the curved edge effects constitute a fully three-dimensional problem, and it is thus very difficult to find stress or displacement functions that satisfy the three-dimensional equilibrium and compatibility equations in a cylindrical coordinate system, if not impossible. Therefore, the boundary layer theory, originally proposed by Reiss (1963) for isotropic plates with circular holes and then extended to laminated composites by Tang (1977 and 1979) is frequently employed as a powerful tool in the analysis of curved free edge effect (Bar-Yoseph and Avrashi, 1985, Ko and Lin, 1992). In the boundary layer theory, a small variable is introduced so as to eliminate some terms in equilibrium and compatibility equations, thereby making it possible to find stress functions (or displacement functions) for these simplified equations. Tang (1977 and 1979) developed the "zeroth-order" solutions for curved free edge effects in thin laminated composites with only parts of boundary conditions being guaranteed in an average sense. Ko and Lin (1992) obtained the "zeroth-order" solutions for the curved free edge effects of laminated composites, wherein the two stress functions are assumed to be in the forms of exponentials to exactly satisfy all the traction-free and traction continuity conditions. However, the involved works are still a little tedious in the determination of constants in the exponential functions using the principle of complementary energy.

Compared with the edge effects of traction-free holes, relatively few research work has been conducted on the edge effect problems of pin-loaded holes in laminated composites because of the extreme complexity of boundary conditions at the pin/composite contact interface. Currently, no analytical closed form solutions are available to predict the three-dimensional stresses in laminated composite pinned/bolted joints. A number of researchers (Matthews *et al.*, 1982, Sperling, 1985, Marshall *et al.*, 1989, Shokrieh and Lessard 1996, Lessard *et al.*, 1993) have devoted their efforts to the problem of interlaminar stresses around pin/bolt-loaded holes in laminated composites using fully three-dimensional finite element analyses. However, the fully

three-dimensional finite element analysis requires a large amount of computer storage and run-time, thereby making it rather difficult to obtain accurate results. As a matter of fact, most of their works are restricted to the cases of $[0/90]_s$ and $[90/0]_s$ cross-ply laminates. Matthews *et al.* (1982) developed a 20-node isoparametric brick element consisting of a number of layers to compute the three-dimensional edge effects around pin-loaded holes in multidirectional laminates. Sperling (1985), and Marshall *et al.* (1989) made use of high order displacement formulated elements with coarse meshing for the problem of edge effects. Recently, Shokrieh and Lessard (1996) and Lessard *et al.* (1993) formed a computational model that includes more 20-node isoparametric brick elements through the thickness of each layer so as to attempt a higher accuracy in the quantification of the edge effects in cross-ply laminates. By performing a mesh dependence study, they showed that element meshing is of great importance for the results of edge effects in finite element analysis. As a result, Sperling (1985) and Marshall *et al.* (1989) reported that the interlaminar shear stresses are smaller than the interlaminar normal stress around pin-loaded holes in cross-ply laminates, but Shokrieh and Lessard (1996) and Lessard *et al.* (1993) established a conclusion to the contrary. Therefore, reliable results for the curved edge effect problem can be obtained from finite element analysis, only when the element meshing is fine enough.

The major objective of the present chapter is to develop a variational technique to obtain an elastic solution for edge effects around traction-free holes and pin-loaded holes in symmetric laminated composites. Following the boundary layer theory (Tang, 1977), curved edge effect stresses can be approximately represented by a zeroth-order boundary stress state, for which two stress functions are then determined by imposing the procedure of the calculus of variations on to the complementary energy of the elastic system. From the developed technique, the fully three-dimensional stress state around the two types of holes can be predicted, based on the knowledge of average in-plane stress state around the holes which is rather easily determined using the CLPT. As a special case of curved free edge effects, the three-dimensional stress state at straight free edges (i.e., with infinite radius) of symmetric laminated composites can also be conveniently calculated using the present technique. The onward formulation development is focused on the problem of edge effects around pin-loaded holes in laminated composites, since the formulation

for edge effects of traction-free holes is same as that of pin-loaded holes inside the domain with no-contact surfaces.

## 3.2 PROBLEM DESCRIPTION

The problem of interest consists of a symmetric laminate with a circular hole, to which a load P is applied by a pin, as shown in Figure 3.1. The pin-loaded hole edge is divided into two regions, one is the contact surface where the pin and the hole edge are in contact and the other is the no-contact surface where a clearance exists. The region of contact surface (i.e., contact angle) is determined by several factors, such as tolerance, material properties, and loading magnitude, etc. The hole has a radius of R, but the pin radius depends on the tolerance between the pin and the hole, and is thus not necessarily equal to R. The laminate is composed of n orthotropic and homogeneous plies with individual fiber orientations and the thickness for each ply is denoted by h (see Figure 3.2), and thus the laminate thickness H is equal to nh. The origin of a cylindrical coordinate system is fixed at the center of the hole on the bottom surface of the laminate. Therefore, in the defined coordinate system, the interface between the i-th and (i+1)-th plies is located at $z_i = ih$, and further it is defined that $z_0 = 0$.

The contact interactions between pins and holes are simulated by applying a prescribed radial displacement boundary condition on the contact surfaces and traction free conditions on the no-contact surfaces. Similar to most research works on composite pinned joints (Matthews *et al.*, 1982, Sperling, 1985, Marshall *et al.*, 1989, Shokrieh and Lessard 1996, Lessard *et al.*, 1993), the friction effects between pins and hole surfaces are neglected, thus making the contact surfaces free of shear-traction. In order to further simplify the model formulation in the present study, it is assumed that (a) the pin is infinitely rigid and (b) the laminate is infinitely large. The influence of these two common assumptions on the model simulation of composite pinned joints is unimportant. This is due to the fact that the dimensions for edge distance and side distance of composite pinned joints are usually designed to be much larger than the radius of pin-loaded holes in order that the joints fail in a bearing mode because this failure is not catastrophic (Matthews, 1988). Also, the effect of pin elasticity on the stress distribution around pin-loaded

holes is so small that the pin elasticity is usually neglected because the stiffness of metal pins is considerably larger than that of polymer-matrix composites (Hyer and Klang, 1985).

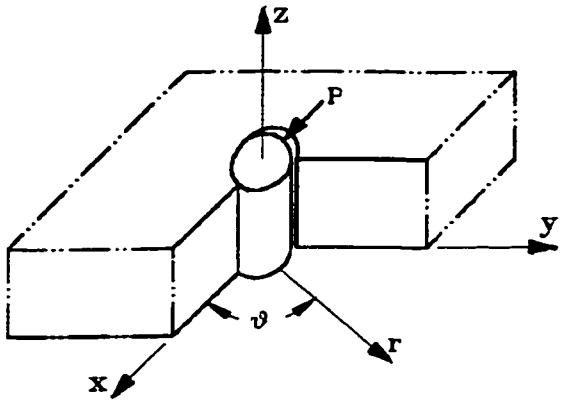


**Figure 3.1.** Schematic representation of laminated composite pinned joints.

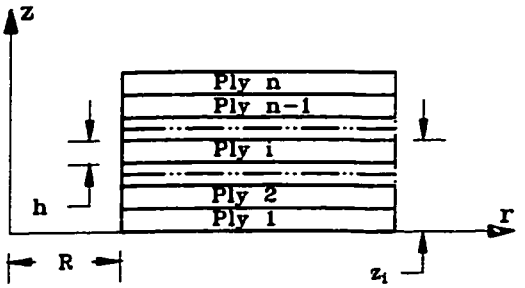


**Figure 3.2.** Laminate geometry and construction. .

Previous research works have shown that edge effects in laminated composites exist in the vicinity of edges (namely, the boundary layer region) and quickly disappear away from edges (Tang, 1977 and 1979, Ko and Lin, 1992). Hence, it is not adequate to describe the mechanical behavior of laminate edges by the in-plane anisotropic elasticity theory (Lekhnitskii, 1968) in conjunction with the CLPT. In fact, the in-plane anisotropic elasticity theory only gives average values of in-plane stresses over laminate thickness, but out-of-plane stresses are ignored in the boundary layer regions. Even the in-plane stresses in each layer are not distributed according to the CLPT. Thus, based on the superposition principle of linear elasticity theory (Timoshenko and Goodier, 1970), the stress and strain fields in the boundary layer regions can be considered as the

summation of two parts (Tang, 1977 and 1979, Ko and Lin, 1992, Kim and Atluri, 1994). One is the in-plane state predicted by the CLPT and another is the additional three-dimensional state, hereafter named as boundary layer state, resulting from edge effects. For the problem of composite pinned joints, the average values of in-plane stresses and displacements over the laminate thickness can be calculated using Hyer and Klang's (1986), Zhang and Ueng's (1984) or de Jong's (1977) analytical solutions. Particularly, it is assumed that the in-plane anisotropic solutions give an accurate boundary condition for the radial displacement along the contact surface, where the radial displacement must be uniform across the laminate thickness. Therefore, the boundary layer stress state causes no additional radial displacement on the contact surface of the laminate, thus constituting a prescribed radial displacement boundary condition in the present model. Now the total stresses and strains in ply i are given by

$$
\begin{aligned}
\sigma_r^{(i)} &= \sigma_r^{c(i)} + \sigma_r^{e(i)} & \varepsilon_r^{(i)} &= \varepsilon_r^{c} + \varepsilon_r^{e(i)} \\
\sigma_\theta^{(i)} &= \sigma_\theta^{c(i)} + \sigma_\theta^{e(i)} & \varepsilon_\theta^{(i)} &= \varepsilon_\theta^{c} + \varepsilon_\theta^{e(i)} \\
\sigma_z^{(i)} &= \sigma_z^{e(i)} & \varepsilon_z^{(i)} &= \varepsilon_z^{c} + \varepsilon_z^{e(i)} \\
\tau_{zr}^{(i)} &= \tau_{zr}^{e(i)} & \varepsilon_{zr}^{(i)} &= \varepsilon_{zr}^{e(i)} \\
\tau_{z\theta}^{(i)} &= \tau_{z\theta}^{e(i)} & \varepsilon_{z\theta}^{(i)} &= \varepsilon_{z\theta}^{e(i)} \\
\tau_{r\theta}^{(i)} &= \tau_{r\theta}^{c(i)} + \tau_{r\theta}^{e(i)} & \varepsilon_{r\theta}^{(i)} &= \varepsilon_{r\theta}^{c} + \varepsilon_{r\theta}^{e(i)}
\end{aligned}
\qquad (3.1)
$$

In the above, the superscripts "c" associated with $\sigma$ and $\varepsilon$ refer to the stresses and strains obtained from the CLPT. Therefore, it is assumed that the corresponding in-plane strains remain constant across the laminate thickness. In a similar manner, the superscripts "e" refer to the boundary layer stresses and strains arising from the edge effects, which satisfy the Hooke's constitutive relationships in the cylindrical coordinate system as:

$$\begin{Bmatrix} \varepsilon_r^{(0)} \\ \varepsilon_\theta^{(0)} \\ \varepsilon_z^{(0)} \\ \varepsilon_{zr}^{(0)} \\ \varepsilon_{z\theta}^{(0)} \\ \varepsilon_{r\theta}^{(0)} \end{Bmatrix}^{(i)} = \begin{bmatrix} S_{11} & S_{12} & S_{13} & 0 & 0 & S_{16} \\ S_{12} & S_{22} & S_{23} & 0 & 0 & S_{26} \\ S_{13} & S_{23} & S_{33} & 0 & 0 & S_{36} \\ 0 & 0 & 0 & S_{44} & S_{45} & 0 \\ 0 & 0 & 0 & S_{45} & S_{55} & 0 \\ S_{16} & S_{26} & S_{36} & 0 & 0 & S_{66} \end{bmatrix}^{(i)} \begin{Bmatrix} \sigma_r^{(0)} \\ \sigma_\theta^{(0)} \\ \sigma_z^{(0)} \\ \sigma_{zr}^{(0)} \\ \sigma_{z\theta}^{(0)} \\ \sigma_{r\theta}^{(0)} \end{Bmatrix}^{(i)} \tag{3.2}$$

In Figure 3.1, there are several boundary conditions that need to be satisfied.

(a) The top and bottom surfaces of the laminate are free of tractions, i.e.,

$$\sigma_z^{(1)} = 0; \qquad \tau_{z\theta}^{(1)} = 0; \qquad \tau_{zr}^{(1)} = 0 \qquad \text{at } z = 0 \tag{3.3.a}$$

$$\sigma_z^{(n)} = 0; \qquad \tau_{z\theta}^{(n)} = 0; \qquad \tau_{zr}^{(n)} = 0 \qquad \text{at } z = H \tag{3.3.b}$$

(b) At any interface between two plies, traction continuity conditions must be guaranteed.

$$\sigma_z^{(i)} = \sigma_z^{(i+1)}; \quad \tau_{zr}^{(i)} = \tau_{zr}^{(i+1)}; \quad \tau_{z\theta}^{(i)} = \tau_{z\theta}^{(i+1)} \quad \text{at } z = z_i \ (i = 1, \ldots, n\text{-}1) \tag{3.3.c}$$

(c) The contact surface is only free of shear tractions, but subjected to the boundary condition of a prescribed radial displacement $u_{r0}^c$ determined by the in-plane anisotropic theory, while the no-contact region is free of tractions.

$$\tau_{r\theta}^{(i)} = 0; \qquad \tau_{zr}^{(i)} = 0; \qquad u_r^{(i)} = u_{r0}^c \quad \text{on contact surface } (r = R) \tag{3.3.d}$$

$$\tau_{r\theta}^{(i)} = 0; \qquad \tau_{zr}^{(i)} = 0; \qquad \sigma_r^{(i)} = 0 \quad \text{on no-contact surface } (r = R) \tag{3.3.e}$$

(d) Because edge effects only exist in the immediate neighboring region of the hole edges, the solution of the CLPT is recovered and the boundary layer stresses are thus equal to zero far from the hole edges, i.e.,

$$\sigma_\theta^{(i)} = \sigma_\theta^{c(i)}; \qquad \sigma_r^{(i)} = \sigma_r^{c(i)}; \qquad \tau_{r\theta}^{(i)} = \tau_{r\theta}^{c(i)} \qquad \text{as } r \to \infty \tag{3.3.f}$$

$$\sigma_z^{(i)} = 0; \qquad \tau_{z\theta}^{(i)} = 0; \qquad \tau_{zr}^{(i)} = 0 \qquad \text{as } r \to \infty \tag{3.3.g}$$

Strictly speaking, the displacement continuity conditions at ply interfaces also should be satisfied. These conditions are relaxed in the present model and are approximately guaranteed by making complementary energy stationary.

## 3.3 THE VARIATIONAL PRINCIPLE OF COMPLEMENTARY ENERGY

The equilibrium stress state that produces a stationary value of complementary energy provides a good approximation for the displacement field of the system. The complementary energy of the present system is the summation of respective ply contribution and written as

$$\Pi = \Pi_c + \frac{1}{2}\int_v \{\sigma^e\}^T [S]\{\sigma^e\} dv + \int_v \{\sigma^e\}^T \{\varepsilon^c\} dv - \int_s \{P^e\}^T \{\underline{u}\} ds \tag{3.4}$$

where $\Pi_c$ is the complementary energy resulting from the CLPT stress state, v is the volume in which the complementary is considered, and $\{P^e\}$ is the boundary layer tractions applied to the boundary s with prescribed displacements $\{\underline{u}\}$. The first term has a determined value and thus does not affect the stationarity of the complementary energy of the system, the second term is the strain energy arising from the boundary layer stress components, the third term is the work representing the coupling effect between the boundary layer stresses and the strains from the CLPT, and the fourth term is the work done by boundary layer stresses on the prescribed displacement boundary. It should be mentioned that, in the analytical models of free edge effects (Ko and Lin, 1992, Kim and Atluri, 1994), the contribution of the third term to the complementary energy is usually ignored to simplify the mathematical work.

### 3.3.1 Boundary Layer Equilibrium Equations

Because edge effects constitute a fully three-dimensional problem, each ply in the laminate is treated as a separate three-dimensional elastic body with all six stress components. The total stresses of the system are required to obey the three-dimensional equilibrium equations in the cylindrical coordinate system. The CLPT stress state, one part of the total stresses, has already satisfied the equilibrium conditions and therefore this part can be removed out of the equilibrium equations. Hence, only the boundary layer stress state, another part of the total

stresses, is kept in these equilibrium equations. This means that the equilibrium conditions can be guaranteed in the present system only if the boundary layer stress state satisfies these equilibrium equations. Therefore, after introducing the following two dimensionaless variables

$$\xi = \frac{r-R}{h} \tag{3.5.a}$$

$$\eta = \frac{z}{h} \tag{3.5.b}$$

the equilibrium equations governing the i-th ply can be written only in terms of corresponding boundary layer stress state, as follows

$$\frac{1}{h}\frac{\partial \tau_{r\theta}^{e(i)}}{\partial \xi} + \frac{1}{\xi h + R}\frac{\partial \sigma_{\theta}^{e(i)}}{\partial \theta} + \frac{1}{h}\frac{\partial \tau_{z\theta}^{e(i)}}{\partial \eta} + \frac{2\tau_{r\theta}^{e(i)}}{\xi h + R} = 0 \tag{3.6.a}$$

$$\frac{1}{h}\frac{\partial \sigma_{r}^{e(i)}}{\partial \xi} + \frac{1}{\xi h + R}\frac{\partial \tau_{r\theta}^{e(i)}}{\partial \theta} + \frac{1}{h}\frac{\partial \tau_{zr}^{e(i)}}{\partial \eta} + \frac{\sigma_{r}^{e(i)} - \sigma_{\theta}^{e(i)}}{\xi h + R} = 0 \tag{3.6.b}$$

$$\frac{1}{h}\frac{\partial \tau_{zr}^{e(i)}}{\partial \xi} + \frac{1}{\xi h + R}\frac{\partial \tau_{z\theta}^{e(i)}}{\partial \theta} + \frac{1}{h}\frac{\partial \sigma_{z}^{e(i)}}{\partial \eta} + \frac{\tau_{zr}^{e(i)}}{\xi h + R} = 0 \tag{3.6.c}$$

Suppose the boundary layer stresses can be expanded into an asymptotic power series of a small parameter (h/R), such that h/R << 1 (Tang, 1977).

$$\sigma^{e(i)} = \sum_{m=0}^{\infty} f_{(i)}^{(m)}(\xi, \eta, \theta)\left(\frac{h}{R}\right)^{m} \tag{3.7}$$

where the superscript "m" in $f_{(i)}^{(m)}(\xi,\eta,\theta)$ denotes the order and that in $(h/R)^m$ denotes the corresponding power. Substituting Equation (3.7) into equilibrium Equations (3.6) and comparing the terms with the equal power of h/R yield a series of equilibrium equations for boundary layer stress coefficients. For m =0, one has

$$\frac{\partial f_{r\theta(i)}^{(0)}}{\partial \xi} + \frac{\partial f_{z\theta(i)}^{(0)}}{\partial \eta} = 0 \tag{3.8.a}$$

$$\frac{\partial f_{r(i)}^{(0)}}{\partial \xi} + \frac{\partial f_{zr(i)}^{(0)}}{\partial \eta} = 0 \tag{3.8.b}$$

$$\frac{\partial f_{zr(i)}^{(0)}}{\partial \xi} + \frac{\partial f_{z(i)}^{(0)}}{\partial \eta} = 0 \tag{3.8.c}$$

For $m \geq 1$, one has

$$\frac{\partial f_{r\theta(i)}^{(m)}}{\partial \xi} + \frac{\partial f_{z\theta(i)}^{(m)}}{\partial \eta} + \xi\left(\frac{\partial f_{r\theta(i)}^{(m-1)}}{\partial \xi} + \frac{\partial f_{z\theta(i)}^{(m-1)}}{\partial \eta}\right) + \frac{\partial f_{\theta(i)}^{(m-1)}}{\partial \theta} + 2f_{r\theta(i)}^{(m-1)} = 0 \tag{3.9.a}$$

$$\frac{\partial f_{r(i)}^{(m)}}{\partial \xi} + \frac{\partial f_{zr(i)}^{(m)}}{\partial \eta} + \xi\left(\frac{\partial f_{r(i)}^{(m-1)}}{\partial \xi} + \frac{\partial f_{zr(i)}^{(m-1)}}{\partial \eta}\right) + \frac{\partial f_{r\theta(i)}^{(m-1)}}{\partial \theta} + f_{r(i)}^{(m-1)} - f_{\theta(i)}^{(m-1)} = 0 \tag{3.9.b}$$

$$\frac{\partial f_{zr(i)}^{(m)}}{\partial \xi} + \frac{\partial f_{z(i)}^{(m)}}{\partial \eta} + \xi\left(\frac{\partial f_{zr(i)}^{(m-1)}}{\partial \xi} + \frac{\partial f_{z(i)}^{(m-1)}}{\partial \eta}\right) + \frac{\partial f_{z\theta(i)}^{(m-1)}}{\partial \theta} + f_{zr(i)}^{(m-1)} = 0 \tag{3.9.c}$$

The boundary layer theory (Tang, 1977, Ko and Lin, 1992) has confirmed that the zeroth-order boundary layer stress coefficients can approximately represent the boundary layer stresses resulting from the edge effects in Equation (3.1). These zeroth-order coefficients subjected to zeroth-order boundary layer equilibrium Equation (3.8) and corresponding boundary conditions can be determined by the variational principle of complementary energy. The stress coefficient $f_{\theta(i)}^{(0)}$ drops out of zeroth-order boundary layer equilibrium Equations (3.8) but can be obtained by setting the boundary layer circumferential strain $\varepsilon_\theta^{c(i)}$ to be zero (Tang, 1977, Ko and Lin, 1992). It is an important conclusion that curved edge effects do not cause additional circumferential strain, such as the case of traction-free circular holes numerically verified by Raju and Crews, Jr. (1982). Therefore, from the second row of the Hooke's constitutive relationships in Equation (3.2), one can obtain

$$f_{\theta(i)}^{(0)} = -\frac{S_{12}^{(i)} f_{r(i)}^{(0)} + S_{23}^{(i)} f_{z(i)}^{(0)} + S_{26}^{(i)} f_{r\theta(i)}^{(0)}}{S_{22}^{(i)}} \tag{3.10}$$

An important feature of the boundary layer theory is that there are no partial derivative terms with respect to θ in the zeroth-order boundary layer equilibrium equations [Equation (3.8)]. Hence, the mathematical operations to determine the six zeroth-order boundary layer coefficients are not performed on the values of θ in the variational procedure of complementary energy. However, all the zeroth-order boundary layer stress coefficients still depend on θ, and thus are functions of ξ, θ and η. From this point onward, therefore, the θ-dependence is not shown explicitly in the equations for reason of clarity. Moreover, the symbols for stress coefficients $f^{(0)}$ are onwards replaced by that for boundary layer stresses $\sigma^e$.

### 3.3.2 Boundary Layer Stress Functions

The equilibrium Equations (3.8) can be identified as two groups. The first group consists of Equations (3.8.b) and (3.8.c). The stresses $\sigma_r^{e(i)}$, $\sigma_z^{e(i)}$ and $\tau_{zr}^{e(i)}$ in Equations (3.8.b) and (3.8.c) are considered to be the stress components in the z-r plane strain state. Therefore, these three stress components can be related by an Airy function $F^{(i)}(\xi,\eta)$ that satisfies plane strain equilibrium equations. The second group consists of Equation (3.8.a). The stresses $\tau_{r\theta}^{e(i)}$ and $\tau_{z\theta}^{e(i)}$ are related by a stress function $G^{(i)}(\xi,\eta)$ that ensures the satisfaction of equilibrium Equation (3.8.a). Suppose that the stress functions on ξ and η can be separated according to

$$F^{(i)}(\xi,\eta) = \Phi^{(i)}(\xi)p^{(i)}(\eta) \tag{3.11}$$

$$G^{(i)}(\xi,\eta) = \Psi^{(i)}(\xi)q^{(i)}(\eta) \tag{3.12}$$

Then, the boundary layer stress components can be written as

$$\sigma_r^{e(i)} = \frac{\partial^2 F^{(i)}}{\partial \eta^2} = \Phi^{(i)}(\xi)\frac{d^2 p^{(i)}(\eta)}{d\eta^2} \tag{3.13.a}$$

$$\sigma_z^{e(i)} = \frac{\partial^2 F^{(i)}}{\partial \xi^2} = \frac{d^2\Phi^{(i)}(\xi)}{d\xi^2}p^{(i)}(\eta) \tag{3.13.b}$$

$$\tau_{zr}^{e(i)} = -\frac{\partial^2 F^{(i)}}{\partial\xi\partial\eta} = -\frac{d\Phi^{(i)}(\xi)}{d\xi}\frac{dp^{(i)}(\eta)}{d\eta} \tag{3.13.c}$$

and

$$\tau_{r\theta}^{e(i)} = \frac{\partial G^{(i)}}{\partial \eta} = \Psi^{(i)}(\xi)\frac{dq^{(i)}(\eta)}{d\eta} \tag{3.14.a}$$

$$\tau_{z\theta}^{e(i)} = -\frac{\partial G^{(i)}}{\partial \xi} = -\frac{d\Psi^{(i)}(\xi)}{d\xi}q^{(i)}(\eta) \tag{3.14.b}$$

The stress component $\sigma_\theta^{e(i)}$ can be obtained from Equation (3.10) (i.e., $\sigma_\theta^{e(i)} = f_{\theta(i)}^{(0)}$ ).

For functions $p^{(i)}(\eta)$ and $q^{(i)}(\eta)$, the assumptions made in (Kassapoglou and Lagace, 1986 and 1987, Kassapoglou, 1996, Ko and Lin, 1992, Zhang and Ueng, 1988) are adopted. That is, $p^{(i)}(\eta)$ and $q^{(i)}(\eta)$ are expressed as a second degree polynomial in $\eta$ and a first degree polynomial in $\eta$ respectively in the following form

$$p^{(i)}(\eta) = \frac{1}{2}\eta^2 + A^{(i)}\eta + B^{(i)} \tag{3.15}$$

$$q^{(i)}(\eta) = \eta + C^{(i)} \tag{3.16}$$

where $A^{(i)}$, $B^{(i)}$ and $C^{(i)}$ are parameters which are determined for each ply. The above assumptions result in two in-plane boundary layer stress components which are uniform through the ply thickness, that is, $\sigma_r^{e(i)} = \Phi^{(i)}(\xi)$ and $\tau_{r\theta}^{e(i)} = \Psi^{(i)}(\xi)$.

In order to satisfy the traction continuity conditions at every ply interface, functions $\Phi^{(i)}$ and $\Psi^{(i)}$ throughout the laminate thickness must be represented by a common function in each case and related parameters. Furthermore, because both the existence of boundary layer stress state and the difference of in-plane stress state from the CLPT in each ply are attributed to the mismatch of relative elastic properties between plies, the two in-plane boundary layer stress components are assumed to be proportional to their counterparts obtained from the CLPT in each ply. Noting that $\sigma_{r0}^{c(i)}$ and $\tau_{r\theta 0}^{c(i)}$ (the subscripts "0" represent the variables along the pin-loaded hole edge) denote the in-plane radial and shear stress components in the i-th ply along the hole edge obtained from the CLPT, and that $\sigma_{r0}^{c}$ denotes the average in-plane radial stress component across the laminate thickness along the hole edge, one can write

$$\sigma_r^{e(i)} = \Phi^{(i)}(\xi) = (\sigma_{r0}^{c(i)} - \sigma_{r0}^{c})\Phi(\xi) \tag{3.17}$$

$$\tau_{r\theta}^{e(i)} = \Psi^{(i)}(\xi) = \tau_{r\theta 0}^{c(i)}\Psi(\xi) \tag{3.18}$$

wherein $\sigma_{r0}^{c}$ is equal to zero on the no-contact surface. These assumptions thus yield a zero resultant for the two in-plane boundary layer stresses over the laminate thickness. For the problem of free edge effects, similar assumptions have been made to constitute the stress functions (Ko and Lin, 1992, Kim and Atluri, 1994, Zhang and Ueng, 1988, Lin *et al.*, 1995). Due to the assumptions in Equations (3.17) and (3.18), the restrictive conditions in Equations (3.3) are changed as follows:

$$\Psi(0) = -1; \quad \Phi'(0) = 0; \quad u_r^{(i)}(0) = u_{r0}^{c} \quad \text{on contact surface} \tag{3.19.a}$$

$$\Psi(0) = -1; \quad \Phi'(0) = 0; \quad \Phi(0) = -1 \quad \text{on no-contact surface} \tag{3.19.b}$$

$$\Phi(\infty) = 0; \quad \Phi'(\infty) = 0; \quad \Phi''(\infty) = 0 \tag{3.19.c}$$

$$\Psi(\infty) = 0; \quad \Psi'(\infty) = 0 \tag{3.19.d}$$

and the condition $\sigma_\theta^{(i)}(\xi \to \infty) = \sigma_\theta^{c(i)}$ is thus automatically satisfied, following the conditions in Equations (3.19.c) and (3.19.d).

From the assumptions regarding the stress functions, the parameters $A^{(i)}$, $B^{(i)}$ and $C^{(i)}$ in functions $p^{(i)}(\eta)$ and $q^{(i)}(\eta)$ are determined by enforcing the traction continuity conditions at interfaces in Equation (3.3.c) and the traction free conditions on the bottom and top surfaces of the laminate in Equations (3.3.a) and (3.3.b), as follows: for the first ply

$$A^{(1)} = 0; \quad B^{(1)} = 0; \quad C^{(1)} = 0 \tag{3.20.a}$$

and for the other plies (i.e., $i \geq 2$)

$$A^{(i)} = \frac{1}{(\sigma_{r0}^{c(i)} - \sigma_{r0}^{c})} \sum_{k=1}^{i-1} (\sigma_{r0}^{c(k)} - \sigma_{r0}^{c}) - (i-1) \tag{3.20.b}$$

$$B^{(i)} = -\frac{1}{(\sigma_{r0}{}^{c(i)} - \sigma_{r0}{}^{c})}\sum_{k=1}^{i-1}[\frac{1}{2}(\sigma_{r0}{}^{c(k)} - \sigma_{r0}{}^{c})(2k-1)] + \frac{(i-1)^2}{2} \tag{3.20.c}$$

$$C^{(i)} = \frac{1}{(\tau_{r\theta 0}{}^{c(i)})}\sum_{k=1}^{i-1}(\tau_{r\theta 0}{}^{c(k)}) - (i-1) \tag{3.20.d}$$

Especially, it can be derived from the above that

$$A^{(n)} = -n; \qquad B^{(n)} = -\frac{n^2}{2}; \qquad C^{(n)} = -n \tag{3.20.e}$$

Hence, although $p^{(i)}(\eta)$ and $q^{(i)}(\eta)$ in terms of higher order degree polynomials are preferable because a better accuracy can be expected for stress distribution across the laminate thickness, they are assumed to be a second degree polynomial and a first degree polynomial respectively in the present model in order that all the parameters related to them can be determined from the traction continuity conditions at ply interfaces and the traction free conditions on the surfaces of the laminate. Previous research works (Kassapoglou and Lagace, 1986 and 1987, Kassapoglou, 1990, Bar-Yoseph and Avrashi, 1985, Ko and Lin, 1992, Kim and Atluri, 1994, Zhang and Ueng, 1988, Lin *et al.*, 1995, Bar-Yoseph, 1983) have verified that the lower degree approximations in the laminate thickness direction can yield reliable values, especially for interlaminar shear stress component $\tau_{z\theta}$ at interfaces in the problem of curved free edge effects.

### 3.3.3 Governing Equations

As state above, the mathematical operations are not performed on the values of $\theta$ in the varitional procedure, therefore the complementary energy can be considered in a domain of $0 \le z \le H$ and $R \le r \le \infty$ for all values of $\theta$. Because of the fact that the summation of the boundary layer stress $\sigma_{r0}{}^{e(i)}$ is equal to zero over the laminate thickness, the fourth term in Equation (3.4) is null in the present system, though the radial displacement, remaining uniform across the laminate thickness, is prescribed on the contact surface. After expanding the matrices, the complementary energy $\Pi_e$ which results from the boundary layer stress state, i.e., $\Pi_e = \Pi - \Pi_c$ in Equation (3.4), is expressed by

$$\Pi_e = \frac{1}{2}\int_0^\infty \int_0^n [(S_{11} - \frac{S_{12}^2}{S_{22}})(\sigma_r^e)^2 + (S_{33} - \frac{S_{23}^2}{S_{22}})(\sigma_z^e)^2 + (S_{66} - \frac{S_{26}^2}{S_{22}})(\tau_{r\theta}^e)^2 +$$

$$S_{44}(\tau_{zr}^e)^2 + S_{55}(\tau_{z\theta}^e)^2 + 2(S_{13} - \frac{S_{12}S_{23}}{S_{22}})(\sigma_r^e)(\sigma_z^e) +$$

$$2(S_{16} - \frac{S_{12}S_{26}}{S_{22}})(\sigma_r^e)(\tau_{r\theta}^e) + 2(S_{36} - \frac{S_{23}S_{26}}{S_{22}})(\sigma_z^e)(\tau_{r\theta}^e) + 2S_{45}(\tau_{zr}^e)(\tau_{z\theta}^e) +$$

$$2(\sigma_r^e)(\varepsilon_r^c) + 2(-\frac{S_{12}}{S_{22}}\sigma_r^e - \frac{S_{23}}{S_{22}}\sigma_z^e - \frac{S_{26}}{S_{22}}\tau_{r\theta}^e)(\varepsilon_\theta^c) + 2(\tau_{r\theta}^e)(\varepsilon_{r\theta}^c)]h^2 d\xi d\eta \qquad (3.21)$$

Substituting the expressions for boundary layer stress components in Equations (3.13) and (3.14) into Equation (3.21) and integrating with respect to $\eta$ in the interval $0 \le \eta \le n$, the complementary energy of the system is obtained in terms of functions $\Phi$ and $\Psi$.

$$\Pi_e = h^2 \int_0^\infty \Gamma(\Phi, \Phi', \Phi'', \Psi, \Psi') d\xi \qquad (3.22)$$

where

$$\Gamma(\Phi, \Phi', \Phi'', \Psi, \Psi') = f_1\Phi^2 + f_2(\Phi'')^2 + f_3\Psi^2 + f_4(\Phi')^2 + f_5(\Psi')^2 + f_6\Phi\Phi'' + f_7\Phi\Psi + f_8\Phi''\Psi + f_9\Phi'\Psi' + f_{10}\varepsilon_\theta^c\Phi + f_{11}\varepsilon_\theta^c\Psi + f_{12}\varepsilon_\theta^c\Phi'' \qquad (3.23)$$

The parameters $f_i$ in the above equation are defined in Appendix 3.1. It should be noted that $f_i$ are independent of $\xi$ and $\eta$, but are functions of $\theta$. The complementary energy $\Pi$ and the function $\Gamma$ are also called the functionals of the system because they are functions of other functions $\Phi$ and $\Psi$. Now the governing equations of the system can be yielded by invoking the stationary condition of $\Pi_e$, i.e. $\delta\Pi_e = 0$, with respect to the two functions $\Phi$ and $\Psi$ (Reddy, 1991). In addition, the boundary conditions corresponding to the prescribed displacements (namely, the natural boundary conditions defined below) can be generated and taken into account using the variational principle of complementary energy. Imposing variations onto Equation (3.22) and applying the traction boundary conditions (namely, the essential boundary conditions defined below) in Equations (3.19), we obtain two *Euler-Lagrange* equations.

$$\frac{\partial\Gamma}{\partial\Phi} - \frac{d}{d\xi}(\frac{\partial\Gamma}{\partial\Phi'}) + \frac{d^2}{d\xi^2}(\frac{\partial\Gamma}{\partial\Phi''}) = 0 \qquad (3.24)$$

$$\frac{\partial \Gamma}{\partial \Psi} - \frac{d}{d\xi}\left(\frac{\partial \Gamma}{\partial \Psi'}\right) = 0 \tag{3.25}$$

The natural boundary condition, corresponding to the prescribed radial displacement on the contact surface is obtained as

$$\left[\frac{\partial \Gamma}{\partial \Phi'} - \frac{d}{d\xi}\left(\frac{\partial \Gamma}{\partial \Phi''}\right)\right]\Bigg|_{\xi=0} = 0 \tag{3.26}$$

Substituting Equation (3.23) into Equations (3.24), (3.25) and (3.26), the following equations in which functions $\Phi$ and $\Psi$ yield stationarity of the complementary energy are derived:

$$2f_1\Phi + 2(f_6 - f_4)\Phi'' + (f_8 - f_9)\Psi'' + f_7\Psi + 2f_2\Phi^{IV} + f_{10}\varepsilon_\theta{}^c + f_{12}(\varepsilon_\theta{}^c)'' = 0 \tag{3.27}$$

$$2f_3\Psi + f_7\Phi + (f_8 - f_9)\Phi'' - 2f_5\Psi'' + f_{11}\varepsilon_\theta{}^c = 0 \tag{3.28}$$

$$2f_2\Phi'''(0) + (f_8 - f_9)\Psi'(0) = -f_{12}(\varepsilon_\theta{}^c)'\Big|_{\xi=0} \tag{3.29}$$

Combining Equations (3.27) and (3.28) leads to

$$\Phi^{VI} + g_1\Phi^{IV} + g_2\Phi'' + g_3\Phi = -g_4\varepsilon_\theta{}^c - g_5(\varepsilon_\theta{}^c)'' - g_6(\varepsilon_\theta{}^c)^{IV} \tag{3.30}$$

$$\Psi = h_1\Phi^{IV} + h_2\Phi'' + h_3\Phi + h_4\varepsilon_\theta{}^c + h_5(\varepsilon_\theta{}^c)'' \tag{3.31}$$

where $g_i$ and $h_i$ are $\theta$-dependent parameters to be expressed in Appendix 3.1. The terms related to the circumferential in-plane strain $\varepsilon_\theta{}^c$ from the CLPT constitute particular solutions for $\Phi$ and $\Psi$. From the sixth-order linear differential Equation (3.30), the general and particular solutions of $\Phi$ are obtained by using the standard procedure of linear differential equations with the functions represented in terms of exponentials. The function $\Psi$ is simultaneously obtained from Equation (3.31). The general solution for Equation (3.30) is obtained, using the following characteristic equation:

$$\lambda^6 + g_1\lambda^4 + g_2\lambda^2 + g_3 = 0 \tag{3.32}$$

The particular solutions are governed by the circumferential average strain from the CLPT, thus attain a value of zero far away from the pin-loaded holes.

For general cases, the boundary layer stresses can be represented by two functions. But in some special cases, some boundary layer stress components are identically equal to zero. For example, if $\tau_{r\theta}^{c(i)}$ from the CLPT vanish in each ply, the stress components $\tau_{r\theta}^{e(i)}$ and $\tau_{z\theta}^{e(i)}$ are always equal to zero due to the assumption in Equation (3.18). These situations may be encountered in cross-ply laminates. Thus, the boundary layer stresses are related to one function $\Phi$ and Equations (3.27) and (3.29) are degenerated into

$$\Phi^{IV} + \frac{f_6 - f_4}{f_2}\Phi'' + \frac{f_1}{f_2}\Phi = -\frac{f_{10}\varepsilon_\theta{}^c + f_{12}(\varepsilon_\theta{}^c)''}{2f_2} \tag{3.33}$$

$$2f_2\Phi'''(0) = -f_{12}(\varepsilon_\theta{}^c)'\Big|_{\xi=0} \tag{3.34}$$

and the related characteristic equation is

$$\lambda^4 + \frac{f_6 - f_4}{f_2}\lambda^2 + \frac{f_1}{f_2} = 0 \tag{3.35}$$

## 3.4 SOLUTIONS TO THE PROBLEM

The solution forms for functions $\Phi$ and $\Psi$ are determined by the roots of the characteristic equations, which vary with different material properties and laminate constructions. Also, the roots are not constants but dependent on the values of $\theta$, therefore, even for a given laminate, the solutions for the two functions have different forms at different $\theta$. The following solution cases will be encountered in the numerical examples of next section.

**(1) Case 1**

The solution of characteristic Equation (3.32) has two real roots and four complex roots:

$$\lambda_{1,2} = \pm\alpha; \qquad \lambda_{3,4,5,6} = \pm(\beta \pm \gamma i) \tag{3.36}$$

where $\alpha$, $\beta$ and $\gamma$ are positive and real. The general solution for $\Phi$ involves terms with $e^{\pm\alpha\xi}$, $e^{\pm\beta\xi}\sin\gamma\xi$ and $e^{\pm\beta\xi}\cos\gamma\xi$. In order to ensure that the edge effects disappear and the results of the CLPT are recovered far from the boundaries (functionally expressed in Equations (3.19.c) and (3.19.d)), the terms with positive exponential must be neglected. Thus the complete solution of $\Phi$ is

$$\Phi(\xi) = C_1 e^{-\alpha\xi} + C_2 e^{-\beta\xi}\sin\gamma\xi + C_3 e^{-\beta\xi}\cos\gamma\xi + \Phi_1(\xi) \tag{3.37}$$

where $C_1$, $C_2$ and $C_3$ are parameters involved in the general solution of $\Phi$, and $\Phi_1$ is the particular solution to be determined by the in-plane stress state from the CLPT. Simultaneously, substituting the expression of $\Phi$ into Equation (3.31), the complete solution of $\Psi$ is obtained as

$$\Psi(\xi) = I_1 C_1 e^{-\alpha\xi} + (I_3 C_2 - I_2 C_3)e^{-\beta\xi}\sin\gamma\xi + (I_2 C_2 + I_3 C_3)e^{-\beta\xi}\cos\gamma\xi + \Psi_1(\xi) \tag{3.38}$$

where

$$I_1 = \alpha^4 h_1 + \alpha^2 h_2 + h_3 \tag{3.39.a}$$

$$I_2 = -2\beta\gamma[2(\beta^2 - \gamma^2)h_1 + h_2] \tag{3.39.b}$$

$$I_3 = (\beta^4 + \gamma^4 - 6\beta^2\gamma^2)h_1 + (\beta^2 - \gamma^2)h_2 + h_3 \tag{3.39.c}$$

The particular solution $\Phi_1$ is determined to be

$$\Psi_1(\xi) = h_1\Phi_1^{IV}(\xi) + h_2\Phi_1''(\xi) + h_3\Phi_1(\xi) + h_4\varepsilon_\theta^c + h_5(\varepsilon_\theta^c)'' \tag{3.40}$$

Then, the three parameters $C_1$, $C_2$ and $C_3$ can be determined by the boundary conditions at $\xi = 0$. There are three essential boundary conditions in Equation (3.19.b) on the no-contact surface, and two essential boundary conditions in Equation (3.19.a) and one natural condition in Equation (3.29) regarding the prescribed radial displacement on the contact surface. Imposing both the no-contact and contact surfaces with shear traction free conditions, one gets the following two equations:

$$-\alpha C_1 + \gamma C_2 - \beta C_3 = -\Phi_1'(0) \tag{3.41.a}$$

$$I_1 C_1 + I_2 C_2 + I_3 C_3 = -1 - \Psi_1(0) \tag{3.41.b}$$

The no-contact surface with the radial traction free condition yields the equation

$$C_1 + C_3 = -1 - \Phi_1(0) \tag{3.41.c}$$

and the contact surface with the natural boundary condition yields the following equation:

$$[I_1\alpha(f_8 - f_9) + 2\alpha^3 f_2]C_1 - [(I_3\gamma - I_2\beta)(f_8 - f_9) + 2f_2(3\beta^2\gamma - \gamma^3)]C_2 -$$
$$[-(I_3\beta + I_2\gamma)(f_8 - f_9) + 2f_2(3\beta\gamma^2 - \beta^3)]C_3 = f_{12}(\varepsilon_\theta{}^c)'\big|_{\xi=0} + 2f_2\Phi_1'''(0) + (f_8 - f_9)\Psi_1'(0) \tag{3.41.d}$$

Equations (3.41.a, b, c) are combined to solve for the parameters for the domain inside the no-contact angle, and Equations (3.41.a, b, d) are combined to solve for the parameters for the domain inside the contact angle.

**(2) Case 2**

The solution of Equation (3.32) has six real roots:

$$\lambda_{1,2} = \pm\alpha; \qquad \lambda_{3,4} = \pm\beta; \qquad \lambda_{5,6} = \pm\gamma \tag{3.42}$$

For the same reasons mentioned above, positive roots are neglected and the complete solution for $\Phi$ is

$$\Phi(\xi) = C_1 e^{-\alpha\xi} + C_2 e^{-\beta\xi} + C_3 e^{-\gamma\xi} + \Phi_1(\xi) \tag{3.43}$$

Through Equation (3.31), the complete solution for $\Psi$ is obtained as

$$\Psi(\xi) = I_1 C_1 e^{-\alpha\xi} + I_2 C_2 e^{-\beta\xi} + I_3 C_3 e^{-\gamma\xi} + \Psi_1(\xi) \tag{3.44}$$

where the particular solution $\Psi_1$ has the same form as that in Equation (3.40) and furthermore,

$$I_1 = \alpha^4 h_1 + \alpha^2 h_2 + h_3 \tag{3.45.a}$$

$$I_2 = \beta^4 h_1 + \beta^2 h_2 + h_3 \tag{3.45.b}$$

$$I_3 = \gamma^4 h_1 + \gamma^2 h_2 + h_3 \tag{3.45.c}$$

Imposing the essential and natural boundary conditions on the pin-loaded hole edge, one obtains the following two equations on both the no-contact surface and the contact surface:

$$-\alpha C_1 - \beta C_2 - \gamma C_3 = -\Phi_1'(0) \tag{3.46.a}$$

$$I_1 C_1 + I_2 C_2 + I_3 C_3 = -1 - \Psi_1(0) \tag{3.46.b}$$

and the following equation on the no-contact surface:

$$C_1 + C_2 + C_3 = -1 - \Phi_1(0) \tag{3.46.c}$$

In addition, on the contact surface

$$\begin{aligned}[I_1\alpha(f_8 - f_9) + 2\alpha^3 f_2]C_1 + [I_2\beta(f_8 - f_9) + 2\beta^3 f_2]C_2 + [I_3\gamma(f_8 - f_9) + 2\gamma^3 f_2]C_3 \\ = f_{12}(\varepsilon_\theta{}^c)'\big|_{\xi=0} + 2f_2\Phi_1'''(0) + (f_8 - f_9)\Psi_1'(0)\end{aligned} \tag{3.46.d}$$

Similarly, Equations (3.46.a, b, c) are then combined to determine the three parameters for the domain inside the no-contact angle, and Equations (3.41.a, b, d ) are combined to determine the two parameters for the domain inside the contact angle.

**(3) Case 3**

When the solution of characteristic Equation (3.35) has four complex roots:

$$\lambda_{1,2,3,4} = \pm(\alpha \pm \beta i) \tag{3.47}$$

then the complete solution for $\Phi$ is

$$\Phi(\xi) = C_1 e^{-\alpha\xi} \sin\beta\xi + C_2 e^{-\alpha\xi} \cos\beta\xi + \Phi_1(\xi) \tag{3.48}$$

The shear traction free condition $\Phi'(0) = 0$ on both the contact and no-contact surfaces yield

$$\beta C_1 - \alpha C_2 = -\Phi_1'(0) \tag{3.49.a}$$

The radial traction free condition $\Phi(0) = -1$ on the no-contact surface yields

$$C_2 = -1 - \Phi_1(0) \tag{3.49.b}$$

The natural boundary condition regarding the prescribed displacement $u_r^{(i)}(0) = u_{r0}^{c}$ on the contact surface yields

$$2f_2(3\alpha^2\beta - \beta^3)C_1 + 2f_2(3\alpha\beta^2 - \alpha^3)C_2 = -f_{12}(\varepsilon_\theta{}^c)'\Big|_{\xi=0} - 2f_2\Phi_1'''(0) \tag{3.49.c}$$

Thus, the set of Equations (3.49.a, b) yields the two parameters for the domain inside the no-contact angle, and the set of Equations (3.49.a, c) yields the two parameters for the domain inside the contact angle.

Therefore, if the CLPT stress and strain states around the pin-loaded holes are known *a priori*, the procedure to determine the complete solutions of $\Phi$ and $\Psi$ pose no mathematical difficulty in the present model. It is clear that the $\theta$-dependence of boundary layer stresses arise from the CLPT stress components through the assumptions in Equations (3.17) and (3.18), and the roots of characteristic equations through parameters $f_i$ which are governed by both compliances $S_{ij}$ and the CLPT stress components.

## 3.5 NUMERICAL EXAMPLES AND DISCUSSIONS

The variational solution outlined in the foregoing is applied to investigate the three-dimensional stress states around traction-free holes and pin-loaded holes in cross-ply laminated composites. It can be observed from the previous sections that the general solutions of functions $\Phi$ and $\Psi$ are determined through the parameters $f_i$ by the in-plane stress components of individual plies that are determined using the CLPT right along hole edges, while their particular solutions are related to the circumferential in-plane strain $\varepsilon_\theta^c$ of the laminate around the pin-loaded holes. Hence, the knowledge of average in-plane stress and strain in the laminates containing holes is essential for the calculation of three-dimensional stress state using the present model. Especially, for the case of straight free edges (i.e., $R \to \infty$), the zero-order boundary layer stress coefficients are exactly the boundary layer stresses because the terms with $m \geq 1$ in Equations (3.7) are identical equal to zero. Therefore, the variational solution is also employed to calculate the edge effect stresses arising from the straight free boundaries in cross-ply laminated composites. Detailed numerical results of edge effect stresses in various types of laminated composites are available in the author's published papers [Zhang *et al.*, 1997, 1998(a), 1999(a), Zhang and Yeh, 1998(a)].

### 3.5.1 Interlaminar Stresses at Straight Free Edges

For the comparison purpose, consider a $[0/90]_s$ cross-ply composite laminate (see Figure 3.3) which is subjected to a uniaxial tension, $\sigma_0$, with such a magnitude that the corresponding longitudinal strain is $\varepsilon_x = 0.01$ calculated by the CLPT. In Figure 3.3, taking $(r - R)$ to be the distance from the free edge, the coordinate transformation is $\xi = y/h$ for a straight boundary. The x axis corresponds to the tangential direction $\theta$ and the y axis to the radial direction r in the above

formulations. The composite plate is made of graphite/epoxy plies with the following material properties (Lessard *et al.*, 1993): $E_{11}$ = 137.9 GPa, $E_{22} = E_{33}$ = 14.5 GPa, $G_{12} = G_{13} = G_{23}$ =5.86 GPa, $\nu_{12} = \nu_{13} = \nu_{23}$ = 0.21, h = 0.125 mm. Different from that in composite laminates with curved boundaries, the stress distribution in the tensile loaded composite plate with straight free edges is independent of x. The in-plane normal stress component $\sigma_{y(i)}^{c}$ which is independent of both x and y can determined by the CLPT and the in-plane shear stress component $\tau_{xy(i)}^{c}$ is equal to zero everywhere. Therefore, the three-dimensional boundary layer stresses in the cross-ply laminates can be described by one stress function $\Phi$. The function $\Phi$ for a $[0/90]_s$ graphite/epoxy laminate has the form of the problem solution of case 3. The particular solution $\Phi_1$ is neglected out of the stress function to reduce the amount of involved mathematical work, from which less deviation is believed to arise for the calculated values of free edge effect stresses (Kim and Atluri, 1994). It is noteworthy that for this special case, the present solution is identical to that developed by Kassapoglou (1990) for the straight edge effects in laminated composites.

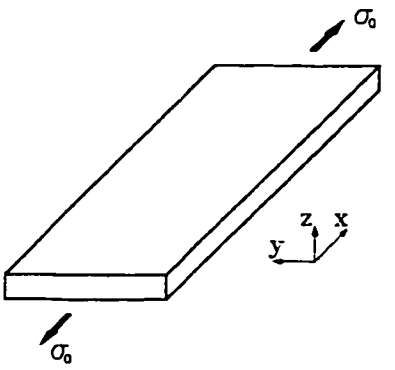


**Figure 3.3.** A tensile loaded cross-ply laminate with straight free edges.

The interlaminar normal stress $\sigma_z$ at the 0/90 interface from the present method and from Lessard *et al.* (1996) is shown in Figure 3.4. The results from the two methods are in very good agreement except very close to the free edge. Lessard *et al.* (1996) have shown the rapid increase of the stress associated with stress singularities at the free edge while the present method obtains a finite stress value of 15.2 MPa. Instead of being determined by stress values at free edges, delamination failure is determined by the average stress values, taken over an averaging distance from the free edge (average stress criterion) (Brewer and Lagace, 1988). Figure 3.4 also displays

interlaminar stresses that only exist within 1mm from free edges which is two times the laminate thickness (H = 0.5 mm), showing that free-edge effects diminish quickly away from free edges. The results indicate that the magnitude and distribution of free-edge stresses is independent of the laminate half-width w, provided that the ratio of w/h > 2. The results from Pipes (1972), Pagano (1974) and Kassapoglou and Lagace (1987) are also included in Figure 3.4 to verify the effectiveness and accuracy of the present method. It is shown that the results obtained by the present method compare very favorably with those obtained by other authors. In fact, the present results are closer to the finite element results than other authors, except of course, at the free edge.

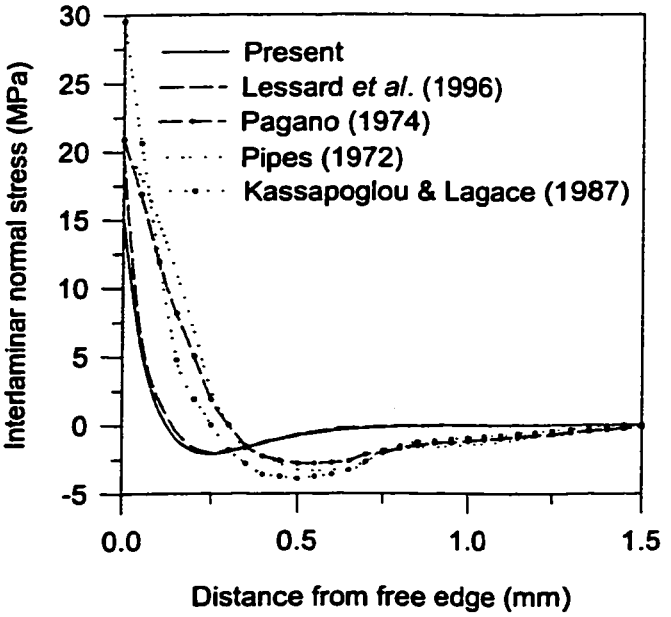


**Figure 3.4.** Distribution of interlaminar normal stress $\sigma_z$ at the 0/90 interface in a $[0/90]_s$ cross-ply laminate.

### 3.5.2 Interlaminar Stresses at Circular Hole Free Edges

The considered example is an infinitely large $[0/90]_s$ cross-ply laminate with a circular hole and uniaxial tension $\sigma_0$ is applied along its principal material direction, as shown in Figure 3.5. The magnitudes of interlaminar stresses around the circular hole calculated using the present approach is compared with the finite element results by Lucking *et al.* (1984), thus the corresponding material properties of the graphite/epoxy system are considered in the present example. That is, $E_{11}$ = 145 GPa, $E_{22} = E_{33}$ = 10.7 GPa, $G_{12} = G_{13}$ = 5 GPa, $G_{23}$ = 3.6 GPa, $\nu_{12}$ =

$\nu_{13} = 0.31$, $\nu_{23} = 0.49$. The average in-plane stresses along the hole edge in an infinitely large anisotropic laminate can be obtained by the Lekhnitkkii's analytical solution (1968), but it is very difficult to obtain the average in-plane stresses and strains away from the circular hole. Hence, the particular solutions $\Phi_1$ and $\Psi_1$, which depend on the circumferential in-plane strain $\varepsilon_\theta^c$, around the circular hole are not included into the stress functions. That is, only the general solutions of $\Phi$ and $\Psi$ are approximately considered to be the related stress functions, thus making the solutions dependent only on the average in-plane stresses along the hole edge.

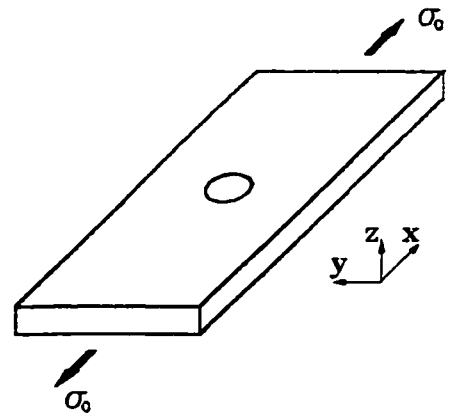


**Figure 3.5.** A tensile loaded laminate with circular hole free edges.

The interlaminar stress component $\tau_{z\theta}$, which is normalized with respect to the far field stress $\sigma_0$, along the hole free edge at the 0/90 interface is shown in Figure 3.6. Because of the fact that the stress intensity factors at circular hole edges with various sizes are of same magnitude in a given laminated composite, the edge effect stress state predicted only by general solutions of $\Phi$ and $\Psi$ are independent of the hole sizes. As a matter of fact, however, it has been observed that the interlaminar stresses caused by circular hole edges are strongly dependent on the radius to thickness ratio (R/H) when R/H < 5, but the radius has less effect on the interlaminar stresses when R/H is out of this range (Zhang and Ueng, 1988, Lucking *et al.*, 1984). Thus, the approximate solutions of the stress functions can efficiently estimate the edge effect stress state caused by larger circular holes in laminated composites. Figure 3.6 displays a good relation between the results from the two different approaches and the present results are much closer to the interlaminar stress value for the circular hole with R/H = 25.

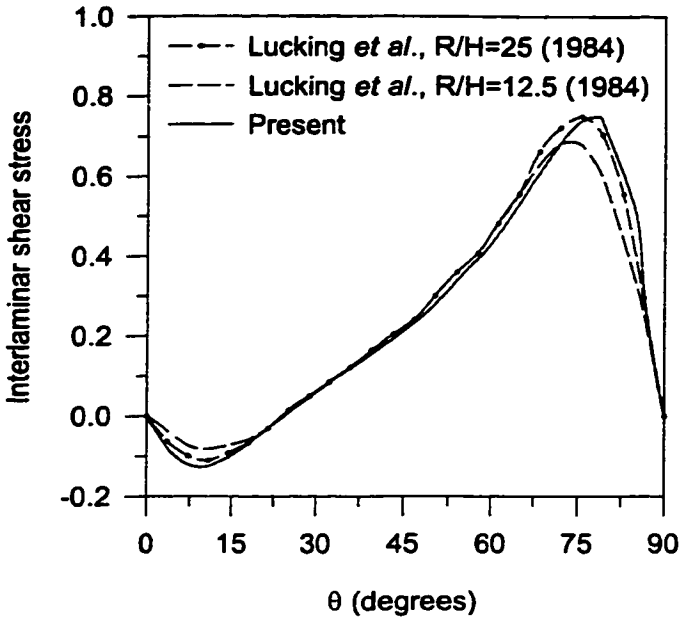


**Figure 3.6.** Angular distribution of interlaminar stress $\tau_{r\theta}$ at the 0/90 interface along the hole edge in a $[0/90]_s$ cross-ply laminate.

### 3.5.3 Interlaminar Stresses at Pin-Loaded Hole Edges

A quantitative comparison between the present results and the finite element results obtained by Lessard *et al.* (1993) and Shokrieh and Lessard (1996) is provided. For the purpose of comparison, the load P is applied to the laminate along one of its principal axes in all numerical examples, that is, the principal axes of the laminate are coincided with the x and y axes as shown in Figure 3.1. Consistent with the boundary conditions in the finite element analysis, the rigid pins are assumed to have the same diameter as the holes, thus forming perfect fitting between them. The basic material properties of the graphite/epoxy system considered in the work of Lessard *et al.* (1993) are adopted here: $E_{11}$ = 150 GPa, $E_{22} = E_{33}$ = 8 GPa, $G_{12} = G_{13}$ = 5 GPa, $G_{23}$ = 3 GPa, $\nu_{12} = \nu_{13} = \nu_{23}$ = 0.3, h = 0.134 mm. The thickness of all the considered laminates is thus: H = 2.144 mm (composed of 16 plies) and the radius of the pin-loaded hole in each laminate is: R = 3.175 mm. In the following results discussed, all the stress components are normalized with the respect to the bearing stress $\sigma_b$ which is equal to P/(2RH).

The Zhang and Ueng's compact analytical solutions (1984) in the forms of Lekhnitskii's complex stress functions for the in-plane anisotropic problem are chosen, since a clear analytical

solution for both average in-plane stresses and displacements along the hole edges can be easily derived from the complex stress functions. The determination of average in-plane stress and strain states near the pin-loaded holes from the complex stress functions, however, is algebraically tedious. In order to overcome this difficulty, a simplified technique [Zhang *et al.*, 1998(b)] is adopted, in which the radial distribution of average in-plane stresses are approximately represented in terms of exponentials associated with the in-plane stress values at the hole edges. From the simplified technique, the circumferential in-plane strain of the laminates around pin-loaded holes can be approximated as

$$\varepsilon_\theta{}^c = \varepsilon_{\theta 0}{}^c e^{-\kappa\xi} \tag{3.50}$$

where $\kappa$ is a non-dimensional constant dependent on laminate geometry and construction, and contact characteristic, thereby making it rather convenient to determine the particular solutions of $\Phi$ and $\Psi$. The exponentials are believed to provide a better approximation because the average in-plane stresses vanish monotonically away from the holes [Zhang *et al.*, 1998(b)].

The values of $\kappa$ in the currently discussed numerical examples are $4.72\times10^{-2}$ for cross-ply laminates. In Zhang and Ueng's compact analytical model (1984), since the region of contact surfaces is set to be: $-90° < \theta < 90°$ (i.e., semi-hole contact), the following numerical results are demonstrated only in the laminates within the region of $0° < \theta < 90°$ with the consideration of geometric symmetry with respect to the x axis. Furthermore, the edge effects in the vicinity of no-contact surfaces are small compared with those in the vicinity of contact surfaces. In the problem of circular hole free edge effects using a similar procedure of complementary energy principle (Ko and Lin, 1992), the particular solutions are abandoned to simplify the formulations, which seems to have significant effects on the numerical results. Accordingly, the influence of the particular solutions of $\Phi$ and $\Psi$ on the edge effects around pin-loaded holes are examined here.

Figures 3.7-3.9 display the circumferential distribution of the normalized interlaminar stresses at the 90/0 interface right at the pin-loaded hole edge in a $[90_4/0_4]_s$ laminate, wherein the results from the present analytical approach with or without consideration of the particular

solutions $\Phi_1$ and $\Psi_1$ (abbreviation P. S. in the figures) in the stress functions are compared with the finite element results obtained from the work of Lessard *et al.* (1993) and Shokrieh and Lessard (1996). After examining the finite element results, it is seen that not only the stress values but the variation trend as well that are obtained from the stress functions with particular solutions included are more preferable. Hence, the inclusion of particular solutions into the stress functions (i.e., complete solutions) is quite important. In the finite element analysis, the interlaminar stress values near pin-loaded hole edges are very sensitive to the element meshing. As a matter of fact, Lessard *et al.* (1993) predicted a much higher interlaminar shear stress concentration through a fine element meshing whereas Shokrieh and Lessard (1996) predicted a lesser stress concentration through a relatively coarse element meshing. The interlaminar shear stress values predicted by the present approach lie between those predicted by the above two finite element solutions. Because of the existence of the potentially high interlaminar stress gradient field near the edges, different methods may predict different peak stress values at the edges (Kassapoglou and Lagace, 1987). For example, it is believed that higher interlaminar stresses concentrations can be predicted if the continuity in displacements at ply interfaces is exactly satisfied (Hsu and Herakovich, 1977). Therefore, the present model based on the variational principle of complementary energy may predict stress values with a lower level of

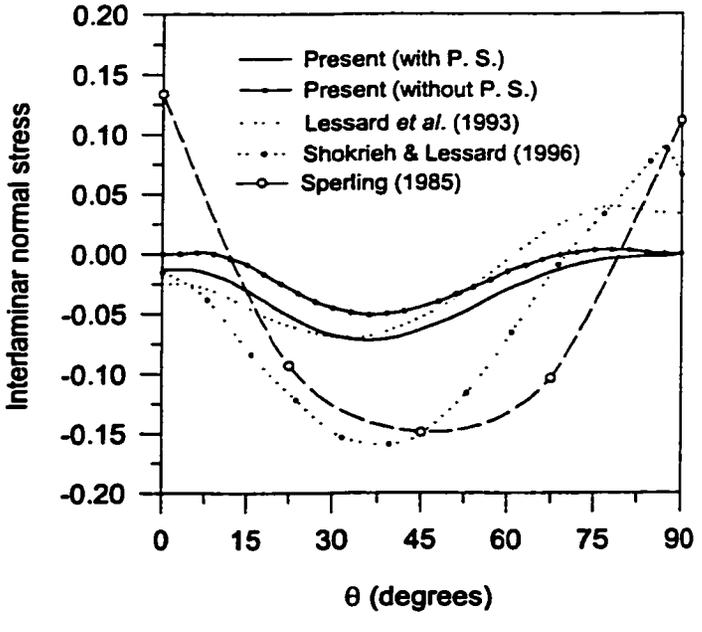


**Figure 3.7.** Angular distribution of interlaminar normal stress $\sigma_z$ at the 0/90 interface along the pin-loaded hole edge in a $[0/90]_s$ cross-ply laminate.

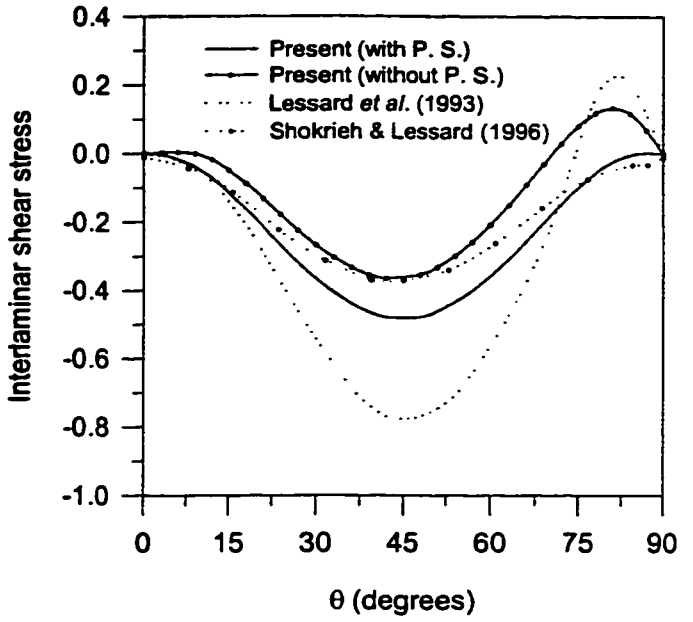


**Figure 3.8.** Angular distribution of interlaminar shear stress $\tau_{xz}$ at the 0/90 interface along the pin-loaded hole edge in a $[0/90]_s$ cross-ply laminate.

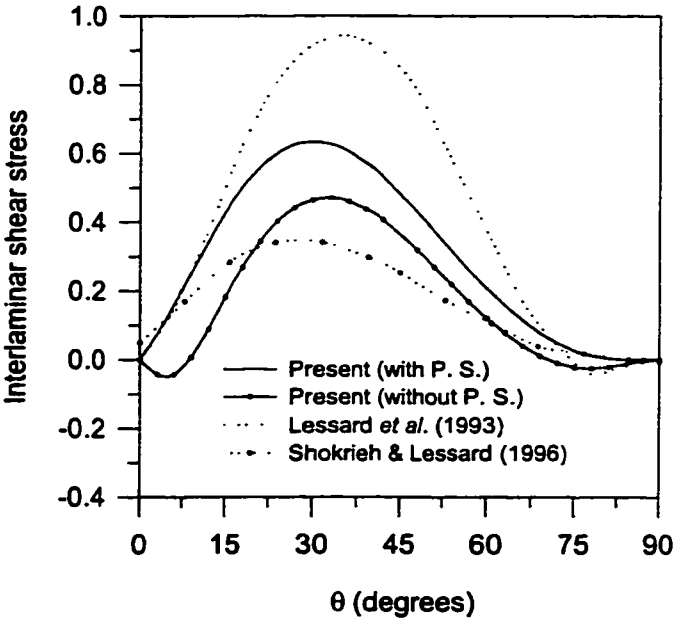


**Figure 3.9.** Angular distribution of interlaminar shear stress $\tau_{yz}$ at the 0/90 interface along the pin-loaded hole edge in a $[0/90]_s$ cross-ply laminate.

concentration along hole edges than that of the actual stress field. The interlaminar shear stresses obtained using the present approach, however, have a good correlation with the finite element

results (Shokrieh and Lessard, 1996, Lessard *et al.*, 1993) except within a small region near $\theta = 90°$. This discrepancy results from the difference in the contact angles used in the finite element analysis (the region of contact surfaces was assumed here to be: $-82.5° < \theta < 82.5°$) (Lessard *et al.*, 1993) and in the Zhang and Ueng's compact analytical solutions (1984). To make further comparison, the finite element results for a $[90_2/0_2]_s$ laminate obtained from Sperling (1985) are also included in Figure 3.9, although the material properties are somewhat different and the hole size and laminate thickness are not reported. The results for the stress $\sigma_z$ from the present solution and the finite element analysis (Lessard *et al.*, 1993) reach a good agreement except within the region near $\theta = 90°$ because of different contact angles in the two models. However, they do not agree with those of Shokrieh and Lessard (1996), and Sperling (1985). For instance, it is especially noticeable that interlaminar tensile normal stress with a higher value near $\theta = 0°$ is predicted by Sperling (1985). This discrepancy is attributed to the element meshing in the finite element analysis since the magnitudes of concentrated interlaminar stresses along the hole edges severely vary from coarse mesh size to fine mesh size. Comparing the finite element results in various papers (Sperling, 1985, Marshall *et al.*, 1989, Shokrieh and Lessard, 1996, Lessard *et al.*, 1993), an interesting evidence may be discovered that for the cross-ply laminates, the finite element models with coarse meshing predict lower magnitudes of interlaminar shear stresses but higher magnitudes of the normal component.

The radial distribution of all the three interlaminar stress components at the 90/0 interface in the $[90_4/0_4]_s$ laminate is provided through a range of $\theta$-values with the aid of the complete solutions of the stress functions in the present analytical model, as shown in Figures 3.10-3.12. It is seen that the stress component $\tau_{z\theta}$ is dominant around the pin-loaded holes and the magnitude of the other two stress components $\tau_{zr}$ and $\sigma_z$ are much smaller. The edge effects characteristically with high stress gradient are localized within about two laminate thickness distance away from the hole edges, and the stresses $\tau_{z\theta}$ and $\sigma_z$ vanish more quickly than the stress $\tau_{zr}$. The sign of all the three interlaminar stresses is changed, but the radial die-away distribution of the component $\tau_{z\theta}$ is close to a monotonic type. An important evidence observed is that the edge effects disappear more rapidly at locations close to the contact center.

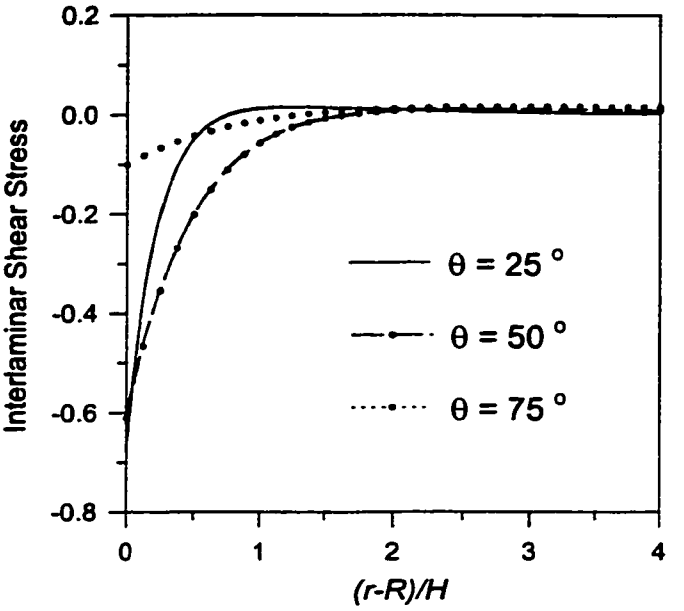


**Figure 3.10.** Radial distribution of interlaminar shear stress $\tau_{z\theta}$ at the 90/0 interface around the pin-loaded hole in a $[90_4/0_4]_s$ laminate.

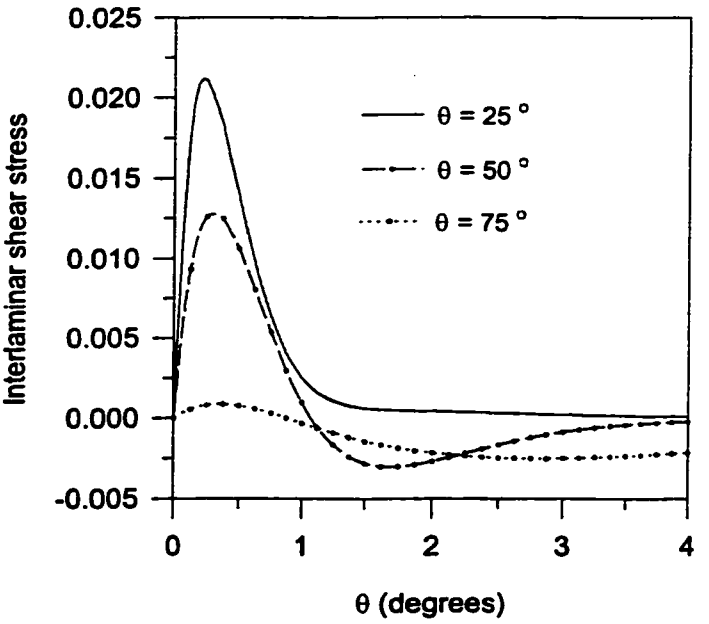


**Figure 3.11.** Radial distribution of interlaminar shear stress $\tau_{zr}$ at the 0/90 interface along the pin-loaded hole edge in a $[0/90]_s$ cross-ply laminate.

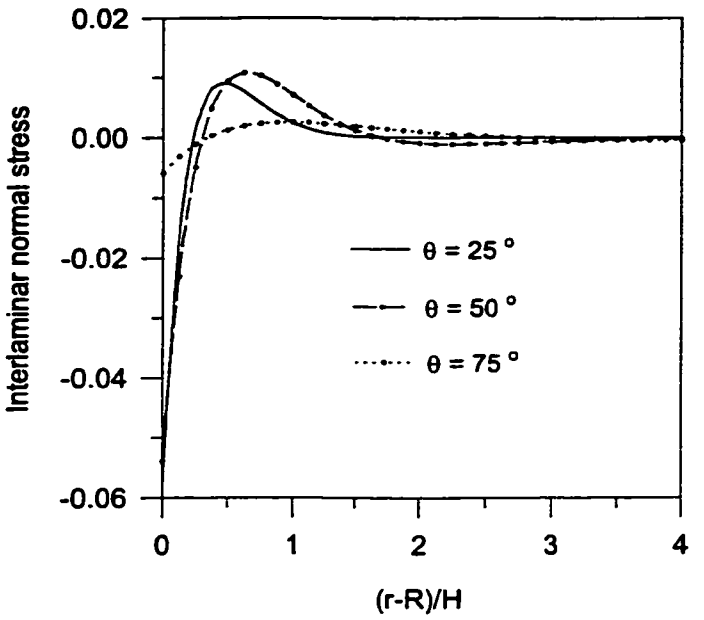


**Figure 3.12.** Radial distribution of interlaminar normal stress $\sigma_z$ at the 0/90 interface along the pin-loaded hole edge in a $[0/90]_s$ cross-ply laminate.

## 3.6 CONCLUSIONS

A variational technique has been developed to yield closed-form solutions for the edge effect stresses around pin-loaded holes in laminated composites. From the present solutions, the three-dimensional stress state resulting from the edge effects can be conveniently determined based on the knowledge of average in-plane stresses and strains around the pin-loaded holes which can be obtained with the in-plane anisotropic theory and the Classical Laminated Plate Theory. In addition, the present solutions for the domain inside the no-contact angle can be used to calculate the three-dimensional stress states resulting from traction-free circular hole edges and straight free edges. The present approach is simple and efficient for the calculation of three-dimensional edge effect stresses in thick laminates since the solutions are given in closed forms.

The present solutions have already been extended to pin-loaded laminated composites with friction considered, which consists of a more complicated contact problem. The formulation development and the associated results are published [Zhang *et al.*, 2000(a)].

## APPENDIX 3.1

The following expressions define the parameters $f_i$, $g_i$ and $h_i$ involved in the formulations of the text.

The expressions for $f_i$ are given below.

$$f_1 = \frac{1}{2}\sum_{i=1}^{n}(S_{11}{}^{(i)} - \frac{S_{12}{}^{(i)2}}{S_{22}{}^{(i)}})(\sigma_{r0}{}^{c(i)} - \sigma_{r0}{}^{c})^2 \tag{A.1}$$

$$f_2 = \frac{1}{2}\sum_{i=1}^{n}(S_{33}{}^{(i)} - \frac{S_{23}{}^{(i)2}}{S_{22}{}^{(i)}})\{\frac{1}{20}[i^5 - (i-1)^5] + \frac{1}{3}A^{(i)2}[i^3 - (i-1)^3] + B^{(i)2} +$$

$$\frac{1}{4}A^{(i)}[i^4 - (i-1)^4] + \frac{1}{3}B^{(i)}[i^3 - (i-1)^3] + A^{(i)}B^{(i)}[i^2 - (i-1)^2]\}(\sigma_{r0}{}^{c(i)} - \sigma_{r0})^2 \tag{A.2}$$

$$f_3 = \frac{1}{2}\sum_{i=1}^{n}(S_{66}{}^{(i)} - \frac{S_{26}{}^{(i)2}}{S_{22}{}^{(i)}})(\tau_{r\theta 0}{}^{c(i)})^2 \tag{A.3}$$

$$f_4 = \frac{1}{2}\sum_{i=1}^{n}S_{44}{}^{(i)}\{\frac{1}{3}[i^3 - (i-1)^3] + A^{(i)}[i^2 - (i-1)^2] + A^{(i)2}\}(\sigma_{r0}{}^{c(i)} - \sigma_{r0}{}^{c})^2 \tag{A.4}$$

$$f_5 = \frac{1}{2}\sum_{i=1}^{n}S_{55}{}^{(i)}\{\frac{1}{3}[i^3 - (i-1)^3] + C^{(i)}[i^2 - (i-1)^2] + C^{(i)2}\}(\tau_{r\theta 0}{}^{c(i)})^2 \tag{A.5}$$

$$f_6 = \sum_{i=1}^{n}(S_{13}{}^{(i)} - \frac{S_{12}{}^{(i)}S_{23}{}^{(i)}}{S_{22}{}^{(i)}})\{\frac{1}{6}[i^3 - (i-1)^3] + \frac{1}{2}A^{(i)}[i^2 - (i-1)^2] + B^{(i)}\}(\sigma_{r0}{}^{c(i)} - \sigma_{ro}{}^{c})^2 \tag{A.6}$$

$$f_7 = \sum_{i=1}^{n}(S_{16}{}^{(i)} - \frac{S_{12}{}^{(i)}S_{26}{}^{(i)}}{S_{22}{}^{(i)}})(\sigma_{r0}{}^{c(i)} - \sigma_{r0}{}^{c})(\tau_{r\theta 0}{}^{c(i)}) \tag{A.7}$$

$$f_8 = \sum_{i=1}^{n}(S_{36}{}^{(i)} - \frac{S_{23}{}^{(i)}S_{26}{}^{(i)}}{S_{22}{}^{(i)}})\{\frac{1}{6}[i^3 - (i-1)^3] + \frac{1}{2}A^{(i)}[i^2 - (i-1)^2] + B^{(i)}\}$$

$$(\sigma_{r0}{}^{c(i)} - \sigma_{r0}{}^{c})(\tau_{r\theta 0}{}^{c(i)}) \tag{A.8}$$

$$f_9 = \sum_{i=1}^{n}S_{45}{}^{(i)}\{\frac{1}{3}[i^3 - (i-1)^3] + \frac{1}{2}(A^{(i)} + C^{(i)})[i^2 - (i-1)^2] + A^{(i)}C^{(i)}\}$$

$$(\sigma_{r0}{}^{c(i)} - \sigma_{r0}{}^{c})(\tau_{r\theta 0}{}^{c(i)}) \tag{A.9}$$

$$f_{10} = -\sum_{i=1}^{n}\frac{S_{12}{}^{(i)}}{S_{22}{}^{(i)}}(\sigma_{r0}{}^{c(i)} - \sigma_{r0}{}^{c}) \tag{A.10}$$

$$f_{11} = -\sum_{i=1}^{n} \frac{S_{26}^{(i)}}{S_{22}^{(i)}} \tau_{r\theta}^{c(i)} \tag{A.11}$$

$$f_{12} = -\sum_{i=1}^{n} \frac{S_{23}^{(i)}}{S_{22}^{(i)}} \{\frac{1}{6}[i^3 - (i-1)^3] + \frac{1}{2} A^{(i)}[i^2 - (i-1)^2] + B^{(i)}\}(\sigma_{ro}^{c(i)} - \sigma_{r0}^{c})^2 \tag{A.12}$$

It should be noted that since $S_{ij}$ and the CLPT stress components depend on $\theta$, then the parameters $f_i$ are also $\theta$-dependent.

The parameters for $g_i$ are given below.

$$g_1 = \frac{(f_8 - f_9)^2 + 4f_5(f_6 - f_4) - 4f_2 f_3}{\Delta} \tag{A.13}$$

$$g_2 = \frac{4f_1 f_5 + 2f_7(f_8 - f_9) - 4f_3(f_6 - f_4)}{\Delta} \tag{A.14}$$

$$g_3 = \frac{f_7^2 - 4f_1 f_3}{\Delta} \tag{A.15}$$

$$g_4 = \frac{f_7 f_{11} - 2f_3 f_{10}}{\Delta} \tag{A.16}$$

$$g_5 = \frac{2f_5 f_{10} + f_{11}(f_8 - f_9) - 2f_3 f_{12}}{\Delta} \tag{A.17}$$

$$g_6 = \frac{2f_5 f_{12}}{\Delta} \tag{A.18}$$

where

$$\Delta = 4f_2 f_5 \tag{A.19}$$

The parameters for $h_i$ are given below.

$$h_1 = \frac{4f_2 f_5}{\Delta^*} \tag{A.20}$$

$$h_2 = \frac{(f_8 - f_9)^2 + 4f_5(f_6 - f_4)}{\Delta^*} \tag{A.21}$$

$$h_3 = \frac{4f_1 f_5 + f_7(f_8 - f_9)}{\Delta^*} \tag{A.22}$$

$$h_4 = \frac{2f_5 f_{10} + f_{11}(f_8 - f_9)}{\Delta^*} \tag{A.23}$$

$$h_5 = \frac{2f_5 f_{12}}{\Delta^*} \tag{A.24}$$

where

$$\Delta^* = -2[f_5 f_7 + f_3(f_8 - f_9)] \tag{A.25}$$

# CHAPTER 4

# EXPERIMENTAL CHARACTERIZATION OF MATERIAL PROPERTIES: TEST METHODOLOGY AND SPECIMEN DESIGN

This chapter is devoted to the determination of test methods and specimen configurations for the stochastic characterization of interlaminar strength components. Hence, detailed evaluation is devoted to various test methods, and stress analysis is performed to optimize the specimen configurations using the ANSYS® finite element software. Because the unsymmetric laminated specimens are necessary to characterize the interlaminar strength components dependent on the fiber orientation difference between adjacent layers, special cautions must be taken in order to avoid the deleterious influences on the experimental results caused by the unsymmetric configurations.

## 4.1 INTRODUCTION

Experimental characterization of composite materials is one of the key areas of concern in research activities and engineering applications. The widely expanding use of composite materials in primary structures has promoted the continuous development of new test methods. Already existing test methods are verified and reexamined, and then some of test methods for composite materials have been standardized by the American Society for Testing and Materials (Anonymous, 1987). The specific feature of anisotropy and inhomogeneity cause considerable complexity in the testing of composite materials. Experimental data significantly depend on not only test methods and specimen geometry but also specimen size (i.e., scale effect). Hence, it is important that the test method and specimen geometry are elaborately designed in order to obtain reliable values of material properties.

In the proposed *Stochastic Delamination Model*, the stochastic process of interlaminar strengths as a function of the fiber orientation difference (FOD) angles is introduced into the delamination criteria as primitive input data. Hence, the experimental work must be performed to yield the probabilistic behaviour (probability distribution, autocorrelation, and so on) of interlaminar strength components at a number of discrete FOD angles, from which the stochastic process can be determined in the whole domain of FOD angles. There seem to be substantial experimental evidence to support that composite material strength components have two-parameter Weibull distributions (Neal *et al.*, 1987). From a literature survey, it is found that Weibull distribution data have been reported by Sun and Yamada (1978) for in-plane strengths of glass/epoxy system, by Kaminski (1973) for longitudinal and transverse tensile strengths of Narmco 5505 boron/epoxy system, by Shyprykevich (1989) for tensile and compressive strengths and unidirectional interlaminar shear strength of E-767/T-300 fabric and tape system, by O'Brien and Salpekar (1993) for transverse tensile strength of AS4/3501-6 system. In the proposed *Stochastic Delamination Model*, however, a general expression for the probability distributions of strength components are yielded from the experimental data using the maximum entropy method (Siddall, 1983), instead of the standard distribution assumption. Hence, the test program should have a large sample size which can approximately represent the corresponding population.

## 4.2 OBJECTIVE OF EXPERIMENTAL INVESTIGATION

The purpose of the test program is to yield the interlaminar strength components at 10 FOD angles (i.e., $\theta = 0°$, 10°, 20°, 30°, 40°, 50°, 60°, 70°, 80°, 90°) and in-plane strength components in the room temperature and dry environment. The CYTEC® G40-800/5276-1 carbon/epoxy pre-impregnated tapes with a nominal thickness of 0.185 mm are employed in the present experimental program due to their extensive aerospace application. Because of the considerable scatter in the interlaminar strengths (O'Brien and Salpekar, 1993, Jackson and Martin, 1993), every data set at each specified value of $\theta$ is obtained by testing 35 effective specimens, so that the $\theta$-dependence of interlaminar strengths is expected not to be masked by the scatter.

It is well known that two ILS strength components that are normal to each other are essential in conjunction with interlaminar tensile and compressive strength components, if the

stress-based delamination criteria are employed to characterize the delamination failure (Sun and Chou, 1988, Brewer and Lagace, 1988). In order to evaluate the effects of fiber orientations, the interlaminar strength components must be measured at the interfaces between two differently-orientated plies. From the point of view of strength theory, the directions which define the two ILS strength components could be arbitrarily selected. However, from the point of view of testing, the directions shall be elaborately selected to generate the experimental values which can best represent the ILS strength components in these directions. With axis 1 fixed along one of the fiber directions of the surrounding plies, the ILS strength components are defined as $S_{13}$ and $S_{23}$ in the present experimental program. The inherent reasons will be given in the coming sections. The in-plane strength components are experimentally measured only for the purpose of comparison.

Therefore, the objective of the present experimental program is to determine the following basic material properties of the CYTEC® G40-800/5276-1 material system:

### 4.2.1 In-Plane Strength Components (Figure 4.1)

$X_t$: longitudinal tensile strength component

$Y_t$: transverse tensile strength component

$S_{12}$: in-plane shear strength component

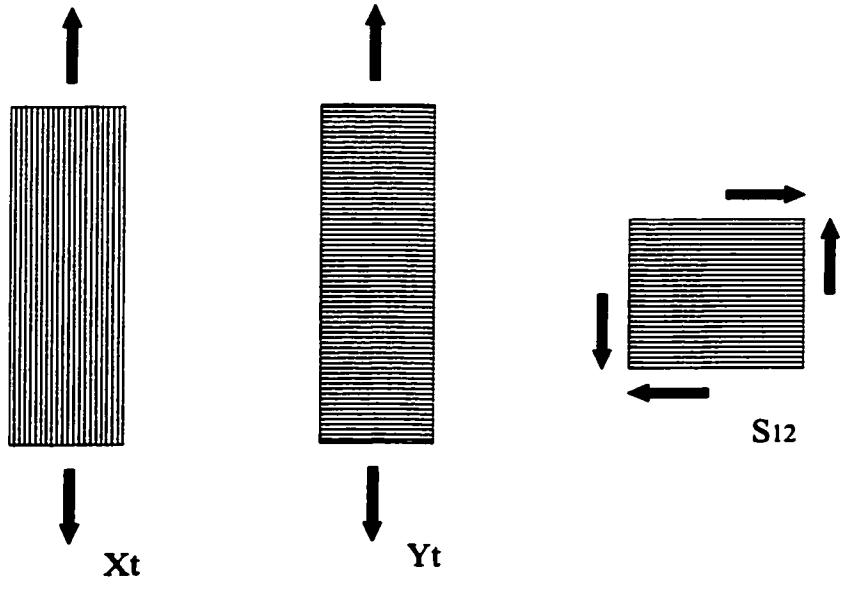


**Figure 4.1.** Schematic description of in-plane strength components.

### 4.2.2 Interlaminar Strength Components (Figure 4.2)

$Z_t$: interlaminar tensile strength component

$Z_c$: interlaminar compressive strength component

$S_{13}$: longitudinal interlaminar shear strength component

$S_{23}$: transverse interlaminar shear strength component

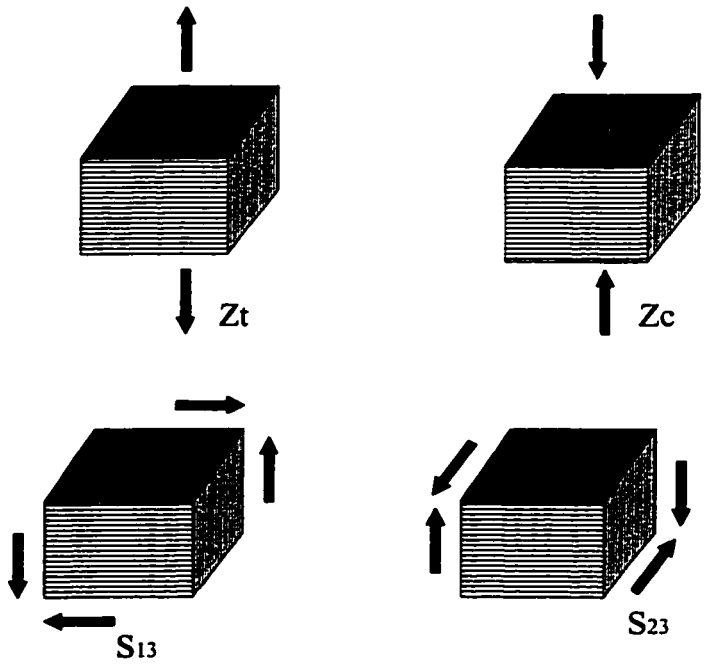


**Figure 4.2.** Schematic description of out-of-plane strength components.

## 4.3 EVALUATION OF TEST METHODS

Many test methods for the experimental characterization of composite material properties (especially for in-plane material properties) are available at present, some of which have been standardized by several technical societies. Even for a single property data, many test methods have been developed. Hence, there is a great deal of confusion as to which test method should be used, and a correct choice of test methods is critical to obtain reliable results of basic material properties. A number of surveys of a variety of test methods can be found in the literature (Whitney *et al.*, 1982, Tarnopol'skii and Kincis, 1982, Munjal, 1989, Chiao *et al.*, 1977). Herein, a brief comment on well-established test methods for the characterization of in-plane material properties is given, and the detailed review and evaluation is focused on the interlaminar strength test methods.

### 4.3.1 Tensile Tests

Tensile tests are performed to determine Young's modulus, tensile strength and Possion's ratio of composite materials. The commonly accepted method is uniaxial tensile test given in ASTM Standard Test Method for Tensile Properties of Fiber-Resin Composites (D 3039) in which the specimen has straight-sides and constant cross-section with adhesively bonded tabs for load introduction. Another preferable method is flexural test (Whitney *et al.*, 1982), which is usually used for the quality control and material specification and is not recommended for generating design data. The tensile strength data from the flexural test method is usually higher than the data from the uniaxial tensile test, and these two types of data are usually employed to scale size effects of polymer matrix composites (O'Brien and Salpekar, 1993, Bullock, 1974). Hence, the uniaxial tensile test in ASTM D 3039 is employed in this test program.

### 4.3.2 Shear Tests

Shear tests are performed to yield shear modulus and shear strength of composite materials. The principal difficulty in the development of shear test methods is to produce the pure shear stress state in specimens and thus to assure sufficient precision for the experimental results. Even though there are so many in-plane shear test methods that have been developed (Munjal, 1989, Chiao *et al.*, 1977), the commonly accepted test methods are ±45° coupon tensile test described in ASTM Standard Practice for In-Plane Shear Stress-Strain Response of Unidirectional Polymer Matrix Composites (D 3518), 10° off-axis tensile test (Pagano and Halpin, 1968), rail shear test described in ASTM Standard Guide for testing In-plane Shear Properties of Composite Laminates (D 4255) and tube torsion test (Pagano and Whitney, 1970, Pagano, 1971).

The ASTM D 3518 ±45° coupon and 10° off-axis tensile test (Pagano and Halpin, 1968) methods can conveniently yield shear strength and modulus of composite materials. However, a combined stress state exists in the layers, in which the values of normal stresses $\sigma_1$ and $\sigma_2$ are larger compared to the shear stress $\tau_{12}$. The presence of normal stress components has a negative effect on the accuracy of measured shear strength and modulus due to tensile-shear coupling (Munjal, 1989). Theoretically, the tube torsion test can provide a pure shear stress state in the specimen and thus would be expected to give reliable shear properties (Pagano and Whitney, 1970, Pagano, 1971). However, it is not a simple test method because it is difficult to fabricate well-qualified tubular

specimen and design a gripping system. Furthermore, it was reported that a strain gradient exists in the tubular specimen (Whitney, 1971). To date, although no specific standards have been appointed for this type of test, the ASTM D 4255 rail shear test method is widely used for the determination of the shear properties. It should be noted that the free edges at the top and bottom of the specimen induce a normal stress concentration. In the present test program, the rail shear test method is used.

### 4.3.3 Interlaminar Tensile Test

Unfortunately, it is very difficult to experimentally characterize the interlaminar tensile strength components due to the lack of fabricating techniques for thick laminate composites with high quality (especially for the prepreg method), thus the laminate thickness is usually much smaller than the length of standard tension specimens. Although a lot of efforts have been devoted to the development of representative specimen configurations, limited success has been achieved. To date, no standard specifications have been established by any industry organizations. Almost all stress-based delamination failure criteria employ the in-plane transverse tensile and shear strength components to estimate the out-of-plane strengths of laminate composites (Brewer and Lagace, 1988, Kim and Soni, 1984). From a survey of literature, it is found that three test methods have been developed for quality control, and sometimes approximate characterization of interlaminar tensile strength.

#### 4.3.3.1 Flatwise Tensile Test

The principle of the flatwise tension test method is to directly apply a load to a specimen in the through-the-thickness direction. Harris and Orringer (1978) first reported a so-called "flatwise tension test", in which two metallic end blocks are attached by glue to two surfaces of a flat specimen to transfer the applied load (Figure 4.3a). This test method is applicable only to laminated composites which interlaminar tensile strength is lower than the strength of the adhesive joints between the specimen and the end blocks. It has been reported that the ground-over specimens provided satisfactory results using this test method (Mao and Owen, 1982). Martin and Sage (1986) proposed a specimen design in which sixteen unidirectional blocks of 24 plies each are adhesively bonded together to create a 384 ply bonded thick laminates. A radius is machined into the specimen to give a minimum area in the center. Aluminum shanks are also bonded to the ends to facilitate the griping (Figure 4.3b). However, failure in the specimens is often close to the bond interfaces. A

similar method was developed by Lagace and Weems (1989) which attempted to use a specimen with 100 plies (the laminate thickness is about 12.5 mm). A neck-down configuration (Figure 4.3c) is also machined to guarantee that the failure occurs in the test section. However, manufacturing thick laminates and machining the neck-down may be the shortcomings of this type of specimen. The interlaminar tensile strength is given by

$$Z_t = \frac{P_{ut}}{A} \tag{4.1}$$

where $P_{ut}$ is the ultimate load the specimen can sustain and A is the cross-section area where failure happens.

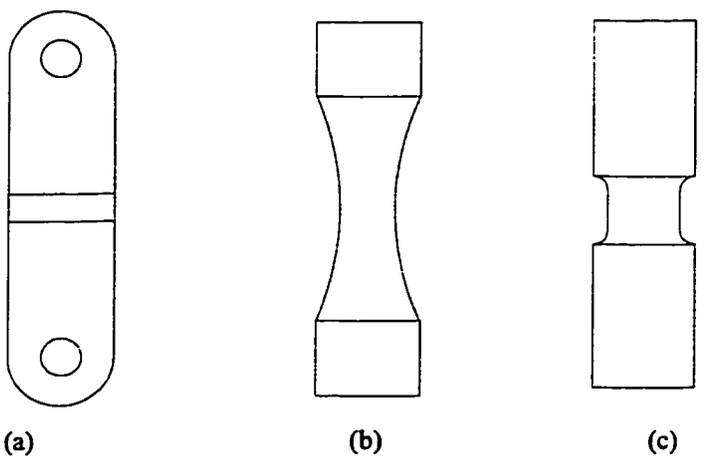


**Figure 4.3.** The configurations for flatwise tension test methods.

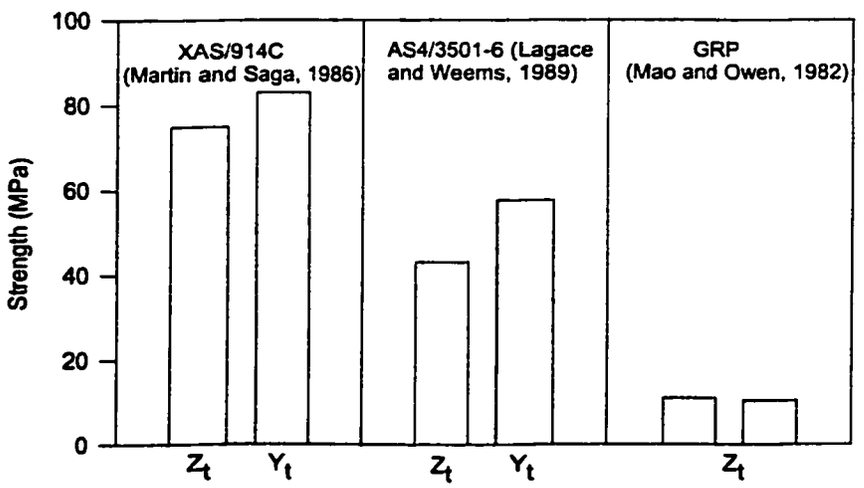


**Figure 4.4.** The comparison between interlaminar tensile strength Zt from flatwise tension tests and transverse tensile strength Yt.

The experimental data of interlaminar tensile strength from several investigations and the comparison with the transverse tensile strength are included in Figure 4.4. Due to the lack of transverse tensile strength data for the material system in the literature (Mao and Owen, 1982), the interlaminar tensile strength from the flatwise tension test is compared with that from the diametrical compression disk test method (discussed in the next section). It is shown that these data from the flatwise tension test method are relatively consistent. Hence, the flatwise tension test may be a reliable method to measure the interlaminar strength components, if the principal problem involved in the bond interface failure could be solved.

#### 4.3.3.2 Diametrical Compression Disk Test

The diametrical compression disk test method (Figure 4.5) was first proposed by Halsey *et al.* (1976) for measuring transverse tensile strength of round pultruded GRP rods, then was extended to measure the interlaminar tensile strength of thick laminated composites (their thicknesses are between 20 mm and 40 mm) by Mao and Owen (1982). When an orthotropic disk is subjected to a compressive load, a comparatively uniform tensile stress perpendicular to the loading direction is induced (see Figure 4.5). If the material is relatively weak in tension, it will fail due to the tensile stress normal to the loading direction. The tensile strength can be calculated from

$$Z_t = \frac{kP_{ut}}{\pi Dt} \tag{4.2}$$

where D is the disk diameter and t is the disk thickness (Mao and Owen, 1982). k = 0.5 for transversely orthotropic materials and k = 1 for transversely isotropic materials.

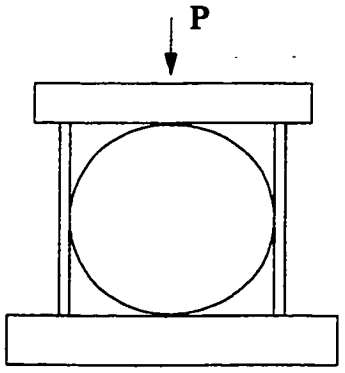


**Figure 4.5.** The configuration for diametrical compression test method.

It is convenient to prepare the disk specimens that are sliced by diamond slitting wheels from the pultruled rods. However, it is a little tedious to prepare the disk specimens from thick laminates (Mao and Owen, 1982). Square bars are cut from thick laminates and turned in the lathe to produce cylinders, which then are sliced. The loading direction must be parallel to the interface to generate the interlaminar tensile stress. Mao and Owen (1982) measured the interlaminar tensile strength of the thick woven roving fabric laminates representative of ship construction materials using this test method. Their experimental results are consistent and comparative well with the data from the other methods. Because the disk specimens must be cut from thick laminates, this test methodology is only applicable to the thick woven roving laminates that can be fabricated by wet lay-up method, but not applicable to the advanced laminated composites that are fabricated in the form of thin plates using the prepreg method.

#### 4.3.3.3 Curved-Beam Test

More recently, efforts at measuring interlaminar tensile strength have been focused on the curved-beam test methods, because of the difficulties in introducing loading onto the flatwise specimens. It is well known from Lekhnitskii's book (1968) that if a homogeneous curved beam is subjected to beam-open bending load, tensile radial and shear stress can be induced throughout the curved beam. Tolf (1983), Chang and Springer (1986), Ko (1988), Ko and Jackson (1989, 1990) respectively conducted the delamination failure investigations on curved laminated composites subjected to bending loads. It is found that a laminated composite specimen in the shape of a semicircular curved beam subjected to the bending moment offers a uniform field of pure radial stress, and even offers a peak pure radial stress at the apex location subjected to end load. Hence, if the load is intense enough, the through-the-thickness mode of failure can take place at the site of peak tensile radial stress (i.e., at the apex location). The interlaminar tensile strength can be calculated from the experimentally measured failure load (a sudden decrease in load-deformation curve) and the known radial stress distribution. Although the curved beam specimen is more difficult to fabricate than the flatwise specimen, it is preferable for the characterization of interlaminar tensile strength component because it is easy to grip this type of specimen in standard test machines. Two types of unidirectional curved specimens, namely C-beam and L-beam, have been developed.

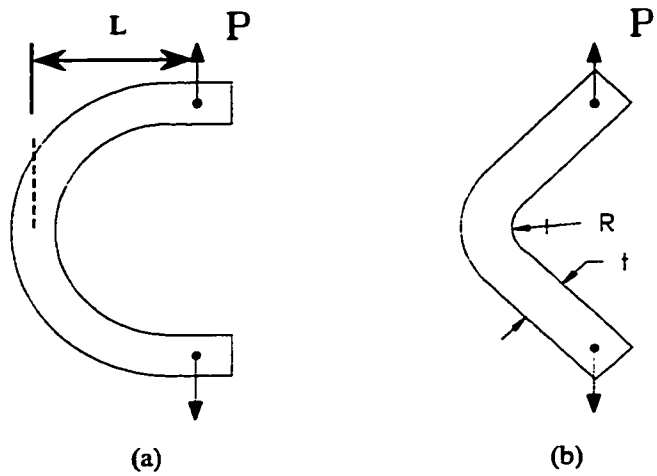


**Figure 4.6.** The configuration for curved beam test method: (a) C-shaped specimen, (b) L-shaped specimen.

The C-beam test fixture simply consists of a test section in a semicircular shape and flat section at which the load P is applied (Figure 4.6a). The calculation from elasticity theory and finite element analysis show that a maximum radial stress occurs at the apex location slightly off the laminate's midplane toward the inner radius. The interlaminar tensile strength may be closely estimated by the following equation (Kedward *et al.*, 1989):

$$Z_t = \frac{3 P_{ut} L}{2bt\sqrt{R_i R_o}} \tag{4.3}$$

where L is the length of moment arm, b is the specimen width, t is the specimen thickness, and $R_i$ and $R_o$ are the inner and outside radii of the semicircular specimen. This design scheme was proposed by Ko (1988), Ko and Jackson (1989, 1990), and Kedward *et al.* (1989). Hiel *et al.* (1991) followed this test method to determine the interlaminar tensile strength of G40-600/5245C carbon/epoxy composites using relatively thick semicircular specimens with a thickness of 9.2 mm. Because curved thick laminates (especially with small curvature) are very difficult to manufacture with consistent quality, these semicircular specimens were of poor quality with high void content and thickness variations. In fact, the test data were too scattered to be considered as design allowables. In order to improve the specimen quality and localize the region of peak radial stress, Hiel *et al.* (1991) manufactured relatively thin T300/934 carbon/epoxy prepreg elliptical specimens with a thickness of 2.8 mm using a female-male mold. For these elliptical specimens, a mean strength was measured which was almost twice the in-plane transverse tensile strength. It seemed

that the extremely high interlaminar tensile strength obtained from these elliptical specimens could not be explained, and therefore was very confused. Perhaps because the test data from the C-beam specimen are not satisfactory, and because this type of specimen can not be adequately representative of most composite structural applications, further investigations have not been continuously conducted on this test method.

The configuration for the L-beam specimen is shown schematically in Figure 4.6(b). The specimens are essentially L-shaped with the interlaminar tensile stress being generated around the angle and the initiation of delamination thus being confined into a small region. A special loading fixture is required so that a load is applied by the standard test machine to open the specimen. Different from the radial stress distribution in a C-beam specimen, the peak radial stress in a L-beam specimen is not at the apex location of the angle, whereas it reaches a maximum at the location slightly off the apex toward the inner radius. The interlaminar tensile strength is estimated from the relationship between applied load and the maximum radial stress calculated by the finite element analysis. A number of papers (Martin, 1992, Jackson and Martin, 1993, Martin and Jackson, 1993, Jackson, 1996, Shivakumar *et al.*, 1994, Avva *et al.*, 1996) have been published on the experimental determination of interlaminar tensile strength following this L-beam test method. It was found from the available test data that the specimen width and loading arm length have little effect on $Z_t$, whereas the inner radius and thickness of the specimen have significant effect on $Z_t$. Jackson and Martin (Martin, 1992, Jackson and Martin, 1993, Martin and Jackson, 1993) have used AS4/3501-6 carbon/epoxy unidirectional curved beam specimens to study the geometry effect of specimens on the interlaminar tensile strength; the experimental results are shown in Figure 4.7. Some similar test data of the AS4/3501-6 and BASF G30-500/Tactix 123 carbon/epoxy unidirectional curved beams (Shivakumar *et al.*, 1994, Avva *et al.*, 1996) are also included in Figure 4.7. The interlaminar tensile strength should be a little lower than the transverse tensile strength because some defects on the interfaces between individual plies may be introduced during the manufacturing process. Comparing the transverse tensile strength from standard flatwise specimens, a conclusion can be reached that the configuration of a high-quality unidirectional L-shaped specimen with a thickness ranging from 2 mm to 4 mm and an inner radius ranging from 5 mm to 7 mm may provide reliable experimental data for interlaminar tensile strength component.

The interlaminar tensile strength from curved-beam test methods appears to be especially sensitive to the presence of porosities, resin pockets, and resin-rich interlayers. These macrospoic defects typically occur due to the difficulty in achieving a uniform pressure in the curved region of the specimen during the curing cycle (Kan *et al.*, 1991). Because these manufacturing defects are most likely the initiation sites of damage, the interlaminar strengths are not accurately calculated from the assumption that material failure take place at the site of peak radial stress. The ideal method is to detect the initiation site of delamination, and then to estimate the strength from the relationship of the applied load and the radial stress value at the initiation site. However, it is extremely difficult to perform this detection. Another severe problem is that high-quality specimens and poor-quality specimens usually can not be distinguished, because macrospoic defects are conveniently detected in flat specimens by the ultrasonic C-scan technique, but are not conveniently detected using the same technique in laminated composite with highly curved regions. Hence, the reported experimental data from curved beam specimens generally fall into a high or a low group of strengths. In the specimens with higher strengths, the inherent flaws are only in a scale of microstructure, as in the case of in-plane test specimens cut from well-qualified laminates, while the inherent flaws in the specimen with lower strength (porosity and epoxy-rich region, etc.) are in a scale of macrostructure that can be observed by a microscopic inspection of polished sections. Therefore, the design allowables for the through-the-thickness mode of failure should be generated by L-shaped beam specimens without macrostructural defects.

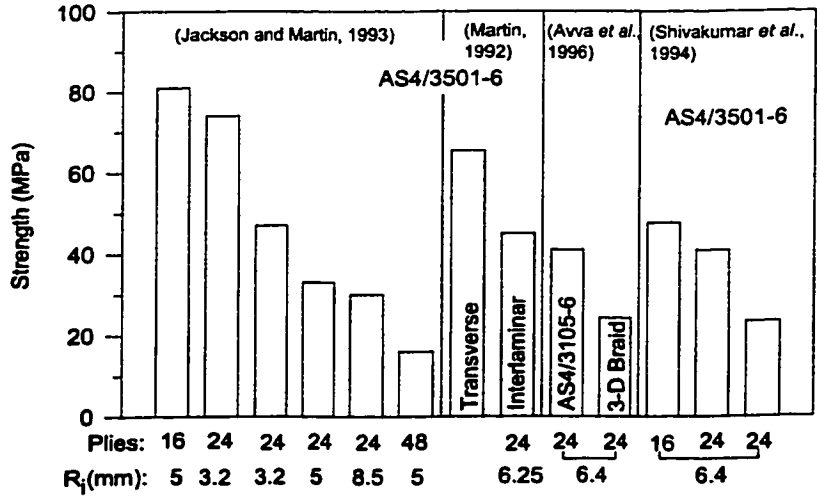


**Figure 4.7.** Comparison of measured interlaminar tensile strength from various authors.

### 4.3.4 Interlaminar Compressive test

Interlaminar (i.e., through-the-thickness) compressive strengths of laminated composites are an essential material property when the failure of composite structures with 3D stress state is evaluated using the quadratic failure theory, i.g., Tsai-Wu or Hoffman criteria (Tsai and Wu, 1971, Hoffman, 1967). The 3D stress state usually exists in thin laminated composites with material discontinuities, geometry discontinuities and load-path eccentricities or in thick laminated composites. Furthermore, through-the-thickness compressive strength could be used to evaluate the autoclave curing quality of thick laminated composites.

The through-the-thickness (abbreviated as TTH hereafter) tensile strength of unidirectional laminated composites has been given a great deal of attention and a number of papers can be found so far, as reviewed previously. However, few papers are available which deal with the TTH compressive strengths; only Goeke (1993) and Benzeggagh *et al.* (1995) performed the associated investigation. In the first paper, Goeke (1993) reported the experimental studies on the compressive strengths of thick glass/polyester and glass/epoxy composites along the thickness and fiber directions in the Army Materials Technology Laboratory (MTL). The end-loaded prism specimens were used, which cut from the thick composite plates. Some important factors that would possibly affect the TTH compressive strengths, e.g., effects of collars, and specimen sizes, were carefully studied in the TTH compressive test. It was concluded by the MTL that the compressive test based on end-loaded prism specimens is valid, because not only does the failure usually take place inside specimen gage section, but also the reproducibility of experimental data is also observed from specimen by specimen. In the second paper, Benzeggagh *et al.* (1995) experimentally measured the TTH compressive strengths of graphite/epoxy T300/914 and glass/epoxy M10 composites in order to evaluate the strength tensors in Tsai-Wu criterion in each case. The end-loaded prism specimens were also used with a 7 mm x 7 mm x 7 mm cubic shape. Because the concerns of their paper are to study the Tsai-Wu strength tensors, detailed testing information and experimental results are not presented.

The compressive test set-up based on the end-loaded prism specimens is schematically demonstrated in Figure 4.8. Technically, the experimental characterization of TTH compressive strengths of composite materials is not a difficult task, because the test technique is

straightforward; i.e., to apply compressive loads to prism composite specimens along the thickness direction. The prism specimens can be conveniently made by cutting through the flat composite plates, while the compressive load can be directly applied to the prism specimens by moving up the plateau of testing machine without any need for load introduction fixture. From the point of view of material failure evaluation, the experimental results used as input data to failure criteria should represent the material properties rather than the structural properties. The interaction between the prism specimens and the collars consists of a contact problem and therefore the coefficient of friction and the modulus of collar material would affect the stress distribution inside specimens. The material failure might be initiated at the contact interface rather than inside the specimen gage section as desired, and thus the actual material properties are not derived from the experiments. Therefore, the effects of friction and collar modulus on the stress distribution inside specimens need to be carefully investigated in order to reduce negative influence on the experimentally measured TTH compressive strengths. Furthermore, the effects of specimen sizes should be studied in order to obtain the material properties from the TTH compressive test.

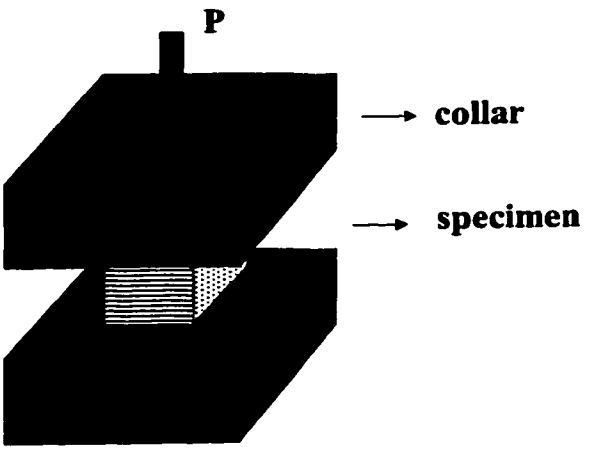


**Figure 4.8.** The test set-up of the TTH compressive test based on end-loaded prism specimens.

### 4.3.5 Interlaminar Shear Test

In most cases, the delamination failure is caused by the combined action of interlaminar shear and tensile stresses, therefore interlaminar shear tests must be performed to evaluate this through-the-thickness failure mode. The experimental characterization of interlaminar shear strength

may be more convenient than that of interlaminar tensile strength. Test methods available for measuring unidirectional interlaminar shear strength include short beam shear test suggested in ASTM Standard Test Method for Apparent Interlaminar Shear Strength of Parallel Fiber Composites by Short-Beam Method (D 2344), and double notch shear test suggested in ASTM Test Method for Interlaminar Shear Strength of Structural Reinforced Plastics at Elevated Temperatures (D 2733) and ASTM Standard Test Method for In-Plane Shear Strength of Reinforced Plastics (D 3846).

#### 4.3.5.1 Short Beam Shear Test

The short beam shear test involves loading a beam under three-point bending. The length to thickness ratio of the beam, L/h, is adjusted so that an interlaminar failure is made to occur at the midplane rather than a tensile failure on the bottom surface of the beam. According to the Classical Beam Theory, the shear stress has a parabolic distribution through the specimen thickness and reaches a peak value at the midplane. The interlaminar shear strength is calculated by

$$S = \frac{3P_{ut}}{4bh} \tag{4.4}$$

where b is the specimen width. The detailed configuration recommended for the short beam shear specimen can be found in ASTM D 2344.

However, even the 0° unidirectional short beam shear specimen usually produces complex fracture modes rather than the expected interlaminar failure at the specimen midplane. Whitney and Browing (1985) tested 16-ply and 50-ply carbon/epoxy specimens respectively and found different failure modes in these two types of specimens. A compressive buckling failure happens on the upper quarter of the 16-ply specimen, while an interlaminar failure in the 50-ply specimen does not occur at the midplane but in the upper quarter. After performing a detailed stress analysis, Whitney (1992) found that high shear stress region exists in the upper quarter (with compressive axial stress) rather than in the specimen center, as illustrated in Figure 4.9. A biaxial compressive stress state also exists in the upper quarter, and the compressive stress in the fiber direction is very large. Due to the actual stress distribution, little interlaminar failure happens in the specimen center.

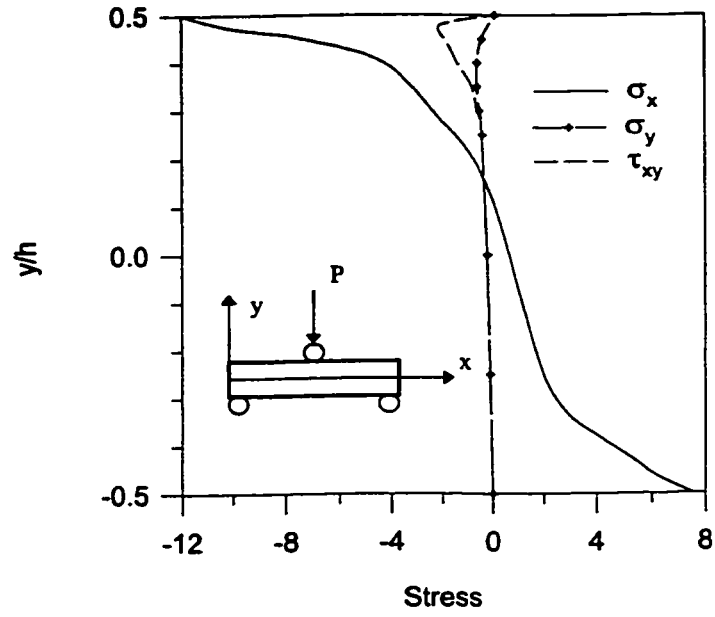


**Figure 4.9.** The normalized stress distribution through the thickness for a short beam, L/h = 4 (Whitney, 1992).

### 4.3.5.2 Double Notch Shear Test

The double notch shear test, referring to ASTM D 2733 and ASTM D 3846, involves a flat plate specimen with two notches cut on opposite surfaces. This type of specimens ensures that the shear failure always takes place on the central plane between two notches. The interlaminar shear strength is obtained by

$$S = \frac{P_{ut}}{bl} \tag{4.5}$$

where b is the specimen width and l is the notch space.

It was reported that the measured interlaminar shear strength is very sensitive to the notch space to thickness ratio (Markham and Dawson, 1975), and the notch depth (Chiao *et al.*, 1977). Markham and Dawson (1975) performed a stress analysis on this type of specimen and found that the stress distribution on the central plane between two notches significantly depends on the ratio of l/t. The distribution of interlaminar shear stress on the central plane is not constant. Stress concentration is also observed in the vicinity of the two notches, and increases with the increasing

ratio of l/t. The concentration of the interlaminar shear stress could decrease the measured interlaminar shear strength that thus depends on the ratio of l/t. Markham and Dawson (1975) investigated the effect of the ratio of l/t on the measured interlaminar shear strength by testing a series of unidirectional carbon/epoxy specimens with various notch spaces, and found that the notch space is a critical parameter for the experimental characterization of interlaminar shear strength. Chiao *et al.* (1977) found that it is difficult to cut the notches to the depth of precisely half the specimen thickness and thus the interlaminar shear strength varies depending on the cut of the notches. For example, a slight undercut gives a high strength than an overcut because of the fiber tearing in the undercut specimen. However, Chaio *et al.* (1977) did not report whether a clamp was used to prevent the bending of the specimen in the tests, which is however recommended in ASTM D 3846. Shokrieh *et al.* (1995) found that if a clamp is used, a slight change of the notch depth has no effect on the measured strength and thus it is not a critical parameter. Hence, the double notch shear test with proper geometry is a preferable method to measure unidirectional interlaminar shear strength.

## 4.4 SPECIMEN DESIGN

### 4.4.1 Longitudinal Tensile Specimen

The geometry of the ASTM D 3039 longitudinal specimen with 8 plies is schematically illustrated in Figure 4.10. Because one of the problems with testing all 0° unidirectional specimens has been the tab-induced failure, the glass/epoxy cross-ply tab with a nominal thickness of 3 mm is used. The edges of specimens are polished after they are cut by diamond slitting wheel because it has been reported that such specimens have 20% increase of measured tensile strength (Manders and Kowalski, 1987). Each prepreg is laid up in the 0° direction as accurately as possible since it has been claimed that a one-degree misalignment of the fibers in the 0° unidirectional specimen could cause up to a 19% decrease in strength (Hart-Smith, 1990). Two strain gages are glued on each specimen to measure the longitudinal and transverse strains within linear range, which are used to measure the longitudinal modulus and major Possion's ratio.

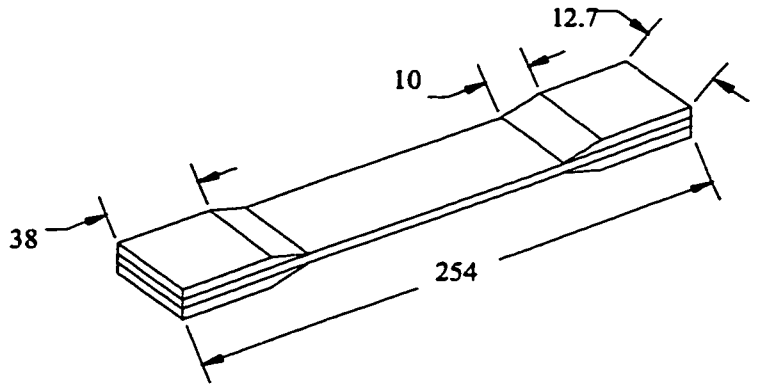


**Figure 4.10.** The geometry of longitudinal tensile specimen.

### 4.4.2 Transverse Tensile Specimen

The geometry of the ASTM D 3039 transverse tensile specimen with 12 plies is illustrated in Figure 4.11. Also, the glass/epoxy cross ply tab with a nominal thickness of 3 mm is used. Two strain gages on each specimen are used to measure the transverse modulus and minor Possion's ratio.

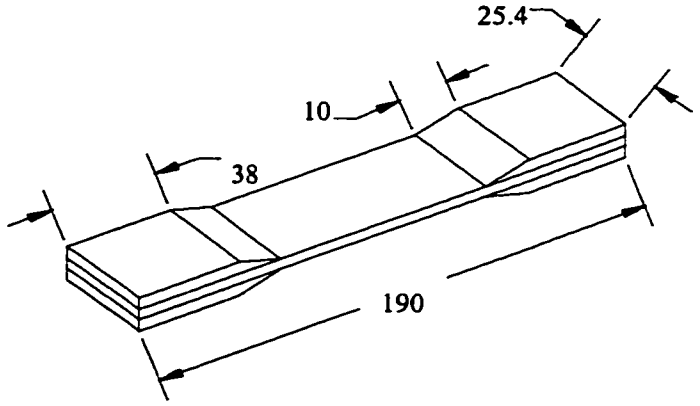


**Figure 4.11.** The geometry of transverse tensile specimen.

### 4.4.3 In-Plane Shear Specimen

The configuration of ASTM D 4255 three rail shear test specimen with 8 plies is outlined in Figure 4.12. Nine 1/2 inch diameter holes are drilled to fasten the specimen to the rail-shear fixture by bolts, which apply an even clamping pressure to the edges to prevent the specimen sliding with respect to the rails. Strain gages are mounted on the geometry center of the specimen to monitor the shear strains. Because the matrix cracks in the unidirectional specimens always develop along the

fiber direction, for the case where the fibers are perpendicular to the rails, the stress concentration due to the holes may induce a lower shear strength (Chang and Chen, 1987). Hence, the specimens are arranged in such a way that the fibers are parallel to the rails.

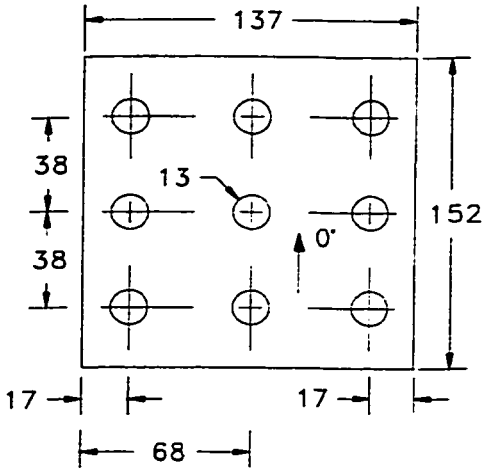


**Figure 4.12.** The geometry of three rail shear specimen.

### 4.4.4 Interlaminar Compressive Specimen

The test set-up employed in the present experimental program can be seen in Figure 4.8. Thick prism specimens composed of 72 plies are used which have a nominal thickness of 13.32 mm. The TTH compressive strengths are studied on $[0]_{72}$ unidirectional and $[0/90]_{36}$ cross-ply laminates respectively in order to uncover the effects of fiber orientations. Moreover, unidirectional specimens with different sizes, as shown in Figure 4.13, are also used to characterize the effects of specimen sizes on the TTH compressive strengths (i.e., scale effects). The nominal specimen sizes (cross-section) and numbers of specimens are tabulated in Table 4.1. Considering the TTH compressive strength of the cross-ply specimens is very high as shown in the following, the TTH compressive test is only performed on the cross-ply prism specimens with small cross-section due to the limitation of loading capacity of testing machine. Furthermore, instead of the aluminum collars for the unidirectional specimens, the carbon steel collars are used for cross-ply specimens because the TTH compressive strengths of the cross-ply laminates are even higher than the yield strength of aluminum. Both the aluminum and carbon steel collars have a thickness of 12.7 mm and their cross-section areas are larger than those of specimens.

**Figure 4.13.** Differently sized prism unidirectional specimens.

**Table 4.1.** Cross-sectional geometry and numbers of unidirectional and cross-ply specimens.

| | Unidirectional | | | | Cross-Ply |
|---|---|---|---|---|---|
| | Group 1 | Group 2 | Group 3 | Croup 4 | |
| Nominal Size (mm × mm) | 8.5 × 8.5 | 10 × 10 | 12.7 × 12.7 | 15 × 15 | 8 × 8 |
| Specimen No. | 5 | 5 | 32 | 5 | 3 |

* All the specimens have a nominal thickness of 13.32 mm.

The effects of friction and collar modulus on the stress distribution inside specimens need to be carefully studied so as to reduce their negative influence on the TTH compressive test, which can be achieved by a finite element analysis (FEA) using the ANSYS® FEA software. Herein the finite element analysis is only performed on the unidirectional specimens together with the aluminum collars, and two cases are considered with the coefficients of friction $f = 0.1$ and $f = 0.3$. The interaction between the specimens and collars is modeled as a surface-to-surface contact problem; the specimens and collars are meshed into 20-node brick elements, and 8-node target elements on the target surface attached to the collars and 8-node contact elements on the contact surface attached to the specimens are extracted. Only one eighth of the system is employed for the finite element analysis due to the structural symmetry. The FEA model is illustrated in Figure 4.14, wherein the origin of the coordinate system is located at the specimen center and the x axis corresponds to the fiber direction of unidirectional specimens. A surface load is applied to the aluminum collar with such a magnitude that generates a nominal TTH compressive stress of 200 MPa inside the specimens. This magnitude of TTH compressive stress is close to the TTH compressive strength, as shown by the experimental results. The inherent purpose is to uncover the loading-dependent interaction between the unidirectional specimens and aluminum collars at the critical moment of specimen failure.

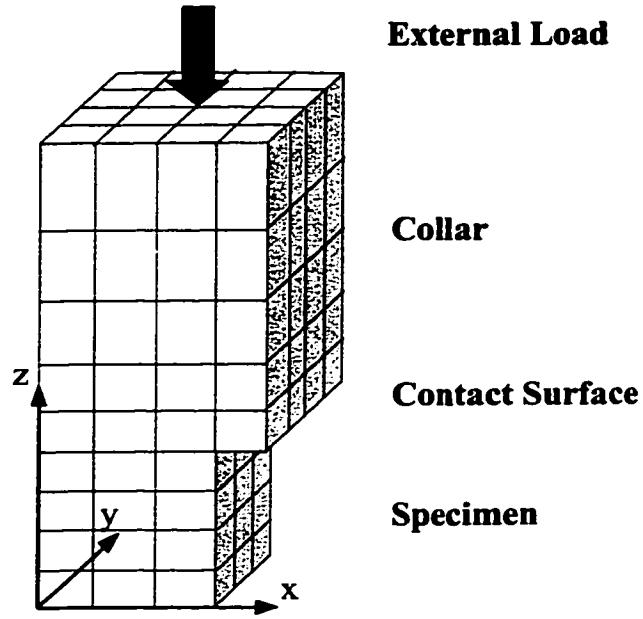


**Figure 4.14.** Finite element model for the collar-specimen contact problem.

The FEA results for the three stress components are displayed in Figures 4.15 and 4.16, which would play an important role in the formation of matrix cracks. It can be seen that the maximum stress state for all the three stress components is generated near the specimen edges; the shear stress $\tau_{yz}$ is along the entire edge parallel to the fiber direction, but the shear stress $\tau_{xz}$ and transverse normal stress $\sigma_y$ are in the middle of the edge perpendicular to the fiber direction. In two cases, the maximum magnitude of the shear stress $\tau_{yz}$ is approximately equal to the product of the coefficient of friction and the nominal TTH compressive stress $\sigma_z$. This indicates that, according to the Coulomb Law, relative slide takes place in the y direction at the local regions of contact surfaces. However, the shear stress $\tau_{xz}$ is of smaller magnitude than the shear stress $\tau_{yz}$, thereby indicating no relative slide happens in the x direction at the contact surfaces. These characteristics are attributed to the large stiffness difference of unidirectional composites in the x and y directions. Under the TTH compressive stress, the free deformation of unidirectional specimens is much larger in the transverse (i.e., y) direction than in the fiber (i.e., x) direction due to the Poisson's effects. The isotropic collars thus impose strong constraints onto the unidirectional specimens through the friction force because of stiffness mismatch between them, especially in the y direction. The maximum friction force the isotropic collars can impose is the

product of the TTH compressive stress and the coefficient of friction at the critical moment when the slide is impending over the contact surfaces. Immediately prior to the specimen failure, the TTH compressive stress which is close to the TTH compressive strength always generate large deformation at the entire edges parallel to the fiber directions so as to make slide occur in the y direction. Therefore, the maximum shear stress $\tau_{yz}$ at the contact surface is proportional to the coefficient of friction, as displayed in Figures 4.15 and 4.16. In the x direction, however, the stiffness mismatch between the isotropic collars and unidirectional specimens is small, and thus there does not exist relative slide in the x direction at the edges perpendicular to the fiber directions. Consequently, the maximum shear stress $\tau_{xz}$ at the contact surface is always smaller than the product of the TTH compressive stress and the coefficient of friction. Moreover, because the free expansion of unidirectional specimens in the y direction is constrained by the aluminum collars, a negative state for the stress $\sigma_y$ is generated near the contact surfaces inside specimens and attains maximum magnitude in the middle (i.e., $y = 0$). Local free deformation in the x direction would result from the stress $\sigma_y$ inside specimens due to the Poisson's effects, which is constrained by the collars. Therefore, the shear stress $\tau_{xz}$ is formed from the combined contributions of the Poisson's effects due to the TTH compressive stress $\sigma_z$ and the transverse normal stress $\sigma_y$. Especially a maximum magnitude of the stress $\tau_{xz}$ exists at the middle of the edges perpendicular to the fiber direction, which results form the Poisson's effects due to the maximum state of the stress $\sigma_y$ in these sites.

Therefore, the coefficient of friction and collar modulus play important role in the determination of stress distribution inside the unidirectional specimens. In order to guarantee that the material failure takes place inside the specimen gage sections and the uniform stress distribution is obtained inside the specimens, the coefficient of friction should be reduced or the collar materials with stiffness matched with the unidirectional specimens in both the longitudinal and transverse should be employed. The first solution could be partially achieved by smearing some grease at the contact surfaces. The second solution, however, is difficult to be achieved since the unidirectional specimens exhibit large stiffness difference in the longitudinal and transverse directions. On the other hand, the modulus of cross-ply specimens is of identical magnitude in the x and y directions, and thus the stiffness mismatch between the cross-ply speci-

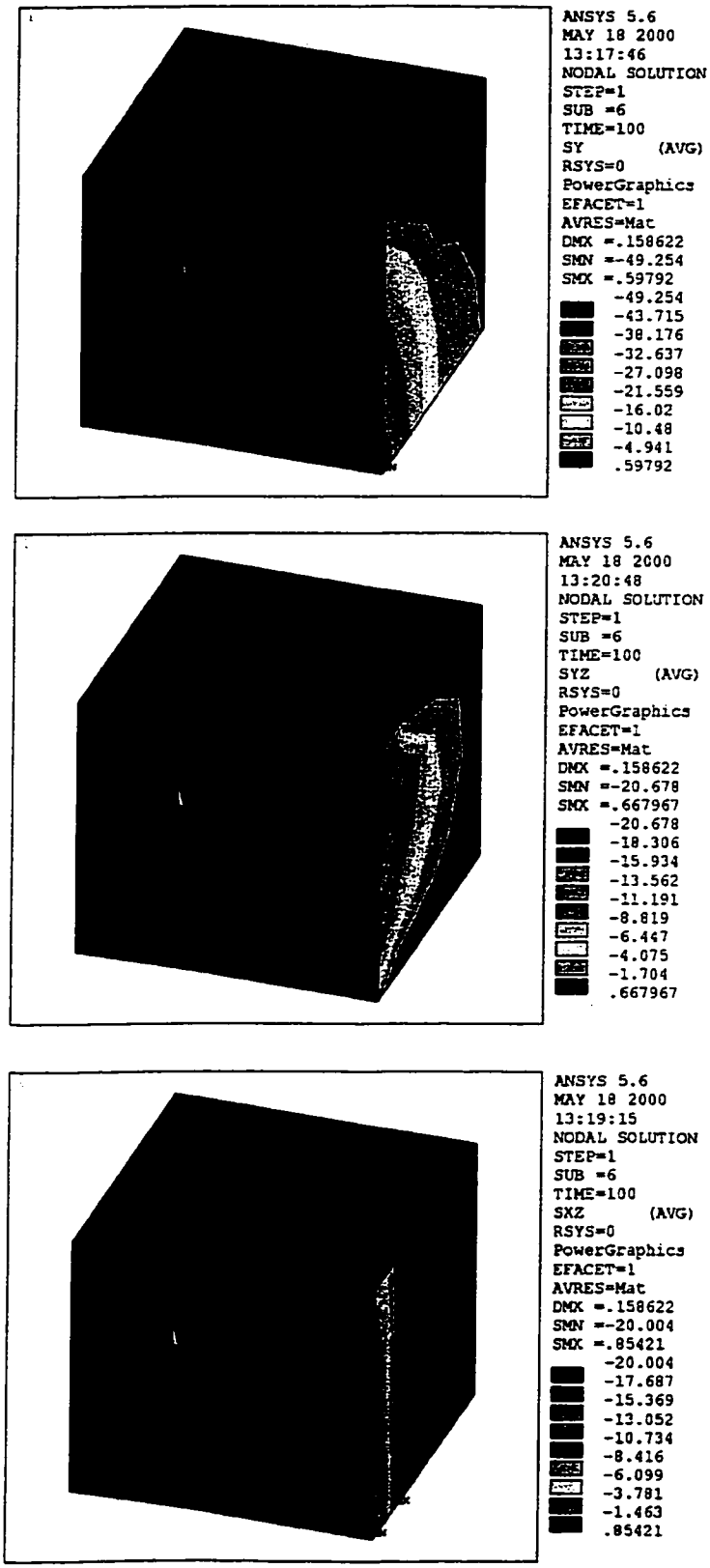


**Figure 4.15.** Distribution of stress components $\sigma_y$, $\tau_{yz}$ and $\tau_{xz}$ inside unidirectional specimens when f = 0.1.

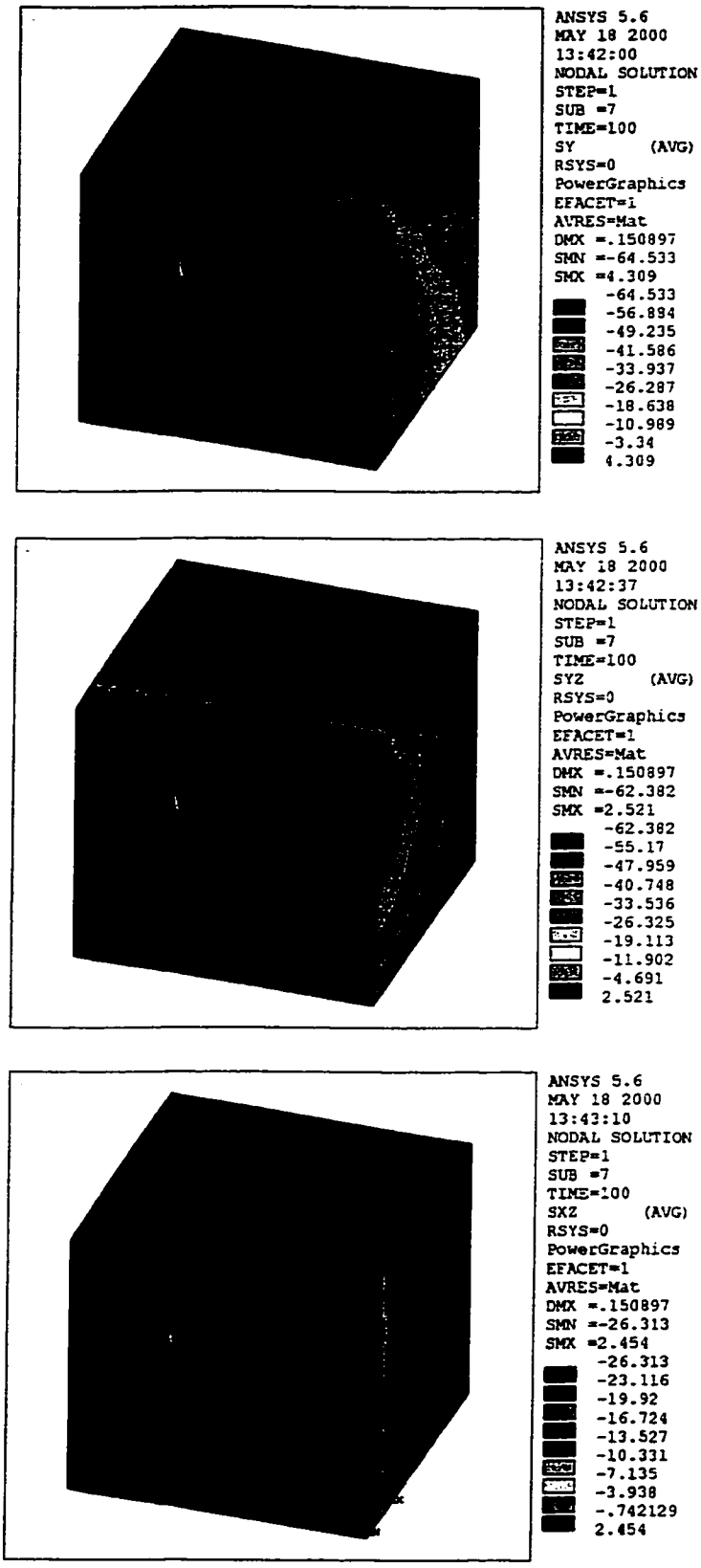


**Figure 4.16.** Distribution of stress components $\sigma_y$, $\tau_{yz}$ and $\tau_{xz}$ inside unidirectional specimens when $f = 0.3$.

mens and steel collars is smaller in both the directions. Even so, the maximum shear stress is still significant at the contact surfaces between cross-ply specimens and steel collars immediately prior to the specimen failure because the TTH compressive strength of cross-ply specimens is much larger than that of unidirectional specimens. Hence, the most efficient approach towards the reliable TTH compressive strengths is to reduce the coefficient of friction at the contact surfaces between the specimens and collars, which will be achieved by smearing some grease there in the present experimental program.

It is noteworthy that the previous stress analysis is performed in an idealistic situation; i.e., the top and bottom surfaces are assumed to be parallel to each other. However, higher shear stress state would be generated, if the non-parallelism between the two surfaces exists. Therefore, it is important to visually examine the parallelism of specimens before testing; only the specimens with parallel surfaces are accepted. One of most efficient approaches in avoiding the non-parallelism is to cut specimens far away from the edges of the thick laminates.

### 4.4.5 Interlaminar Tensile Specimen

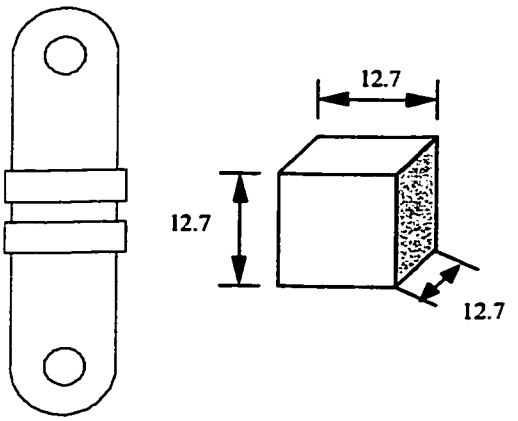


**Figure 4.17.** The configuration for flatwise tension test method with cubic shaped specimen.

The θ-dependent interlaminar strengths have to be measured from multidirectional lay-up specimens. The L-shaped curved beam test with the aforemetioned specimen geometry may be a preferable method to obtain the unidirectional interlaminar tensile strength. However, it is not suitable for the measurement of θ-dependent interlaminar tensile strength because the free edge effects (Martin and Jackson, 1993, Avva *et al.*, 1996, Watanabe and Okada, 1995) and matrix transverse cracks (Martin and Jackson, 1993) in the multidirectional curved beam specimens would

greatly decrease the measured strength. Therefore, the flatwise tension test could be a good candidate to experimentally characterize the θ-dependent interlaminar tensile strength, if the external load could be introduced to the specimens through the bonded interfaces. The specimens with a cubic shape are used in the present experimental program. Two carbon steel bars are adhesively attached to a specimen and further the glass/epoxy strips are bonded to the four sides of the steel bars and specimens to avoid the interface failure on the bonded interfaces. The configuration of this test fixture is shown in Figure 4.17.

Unfortunately, in spite of the aforementioned efforts, the debond failure always took place at the bonded interfaces at a lower loading level. Therefore the flatwise tension test based on the cubic shaped specimens is invalid in the present experimental program. Although it is expectable to enforce the failure inside the specimen gage section through machining the neck-down side surfaces, no further efforts are devoted to the interlaminar tensile test because large number of specimens required by experimentally characterizing probabilistic behaviors of material properties would result in a lot of painstaking machining work. In the *Stochastic Delamiantion Model*, the in-plane transverse tensile strengths are used instead of the interlaminar tensile strengths as an approximate.

### 4.4.6 Interlaminar Shear Specimen

The experimental characterization of θ-dependent ILS strength components is the most important work in the present experimental program, and therefore a lot of effort was devoted to it. As seen in Chapter 7, compared with interlaminar normal strength components, the ILS strength components play a primary role in the evaluation of delamination failure after taking into account the effects of FOD angles of surrounding plies of the interfaces.

It is well known that two ILS strength components that are normal to each other are essential, if the stress-based delamination criteria are employed to characterize the delamination failure (Sun and Chou, 1988, Brewer and Lagace, 1988). In order to experimentally characterize the θ-dependent interlaminar shear strengths, experiments are performed on the laminated composite specimens with θ-interfaces (see Figure 4.18), around which the two plies are oriented with a FOD angle θ. With axis 1 fixed along one of the fiber directions of the surrounding plies, the ILS strength components are defined as $S_{13}$ and $S_{23}$ in the present experiment program.

Corresponding to the two ILS strength components, two types of specimens are designed with the following lay-ups:

Type I Specimen for $S_{13}$: $I(\theta) = [(0/\theta)_3/(\theta/0)_3//(\theta/0)_3/(0/\theta)_3]$

Type II specimen for $S_{23}$: $II(\theta) = [(90/(90\text{-}\theta))_2/0_4/((90\text{-}\theta)/90)_2//((90\text{-}\theta)/90)_2/0_4/(90/(90\text{-}\theta))_2]$

in order that a number of θ-interfaces are formed around the central planes (denoted by "//"). The ILS strengths at 10 θ-interfaces are studied; i.e., θ = 0°, 10°, 20°, 30°, 40°, 50°, 60°, 70°, 80° and 90°. The reasons that the above fiber orientations and stacking sequences are arranged will be given below.

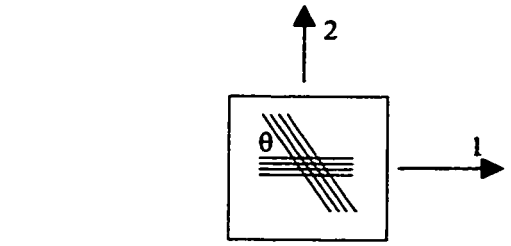


(a) θ-interface

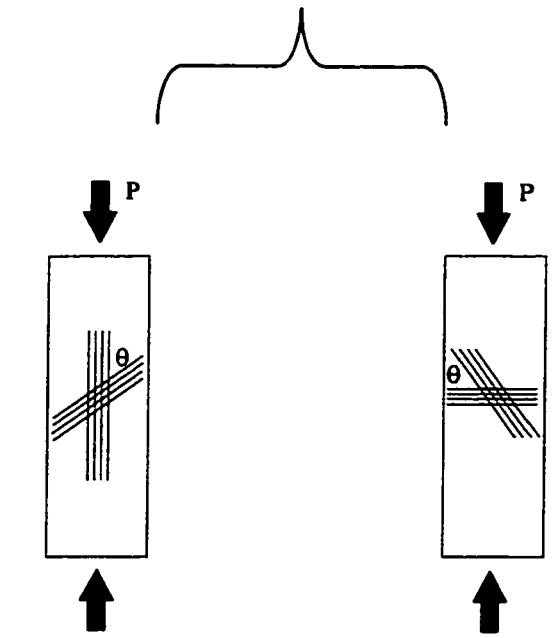


(b) Type I specimen (c) Type II specimen

**Figure 4.18.** Definition of the coordinate system at θ-interfaces and the two types of specimens employed to experimentally measure the two ILS strength components $S_{13}$ and $S_{23}$.

#### 4.4.6.1 Testing Setup

Considering the aforementioned complicated failure modes in the short beam shear specimens, the double notch shear test, involving a flat plate specimen with two notches cut on opposite surfaces, could be a good candidate to experimentally characterize the ILS strengths of unidirectional laminated composites, beacuse the delamination failure could be expected to take place around the central plane of well-designed unidirectional specimens (Shokrieh *et al.* 1995, Munjal, 1989). Hence, the double notch shear testing technique suggested in ASTM Standard D 3846 is modified so that it can be employed to properly characterize the θ-dependent ILS strengths of laminated composite specimens in the present experimental program. The specimens have to contain unsymmetric stacking sequences, because the effects of fiber orientations on the ILS strengths must be experimentally quantified from the specimens with the specified interfaces located at their central planes. Compared with the unidirectional specimens, the unsymmetric laminated composite specimens thus pose a number of special problems, such as residual bending and twisting deformation, edge effects, and coupling effects, etc. These problems will be examined and resolved based on a detailed 3D finite element stress analysis. Besides the aforementioned special problems, some general problems involved in the double shear notch test also need to be dealt with, as follows.

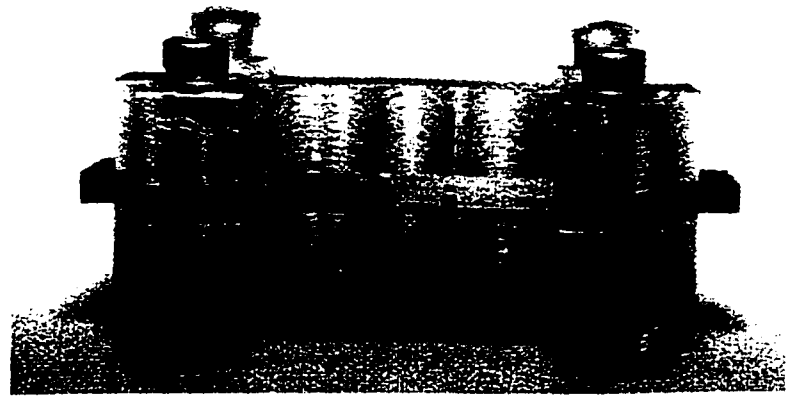

**Figure 4.19.** The double notch shear testing setup.

**(1) Loading**

Because of the two asymmetrically located notches, an undesirable bending moment would appear in the specimens. Moreover, since the matrix tensile strength may be lower than the ILS

strengths, a tensile load would cause transverse matrix cracks prior to the delamination failure. Hence, a compressive load is applied to the double notch shear specimens that is held between a clamp by evenly tightened bolts, as shown in Figure 4.19. The clamp not only prevents the specimens from bending, but also exerts a pressure on the specimens by the bolts in the testing. Because the interlaminar tensile stress from free edge effects plays a significant role in the generation of delamination, the transverse pressure on the specimens can preferably reduce or remove the interlaminar tensile stress, thus partially eliminating the possibility of delamination induced by the free edge effects in the specimens.

**(2) Notch Space**

The distance between two notches (exactly, the ratio of notch space to specimen thickness, s/t) have significant effects on the ILS stress in the specimen gage sections and thus the measured ILS strengths. The stress concentration exists in the vicinity of two notches, and increases with the increasing ratio of s/t (Markham and Dawson, 1975). According to the Saint-Venant principle, the structural discontinuity may cause a local stress concentration near notches, but its effect will disappear far from the notches. If the notch space is large enough, no ILS stress will exist in the middle of the notch space, and a higher stress concentration will be generated near notches. Therefore, the initiation of failure would take place when a lower load is applied to the specimens with large notch spaces, thereby decreasing the measured ILS strengths. However, the stress distribution is not sensitive to a small variation of notch space, thus permitting a manufacturing tolerance. A notch space s = 7 mm is selected. Moreover, thick specimens can yield good experimental results for the ILS strengths due to the more uniform shear stress distribution at the central planes, thus 24 plies are used to stack the specimens with a nominal thickness t = 4.44 mm.

**(3) Notch Width**

In the unclamped double notch shear specimens, the notch width would play an important role on the stress distribution, because a larger bending deformation would be generated in the specimens with bigger notch width, and thus induce higher stress concentration in the vicinity of the notches. In the clamped double notch shear specimens, however, the bending deformation is eliminated by the clamp, thus the notch width has little effect on the measured ILS strengths. Hence, the selection of

the notch width is not a constraint for the clamped specimens. A notch width w = 1.8 mm is selected just based on the thickness of the diamond blade wheel, which is used to cut the notches.

### (4) Notch Depth

The notch depth, which designates the distance from the notch bottom to the specimen surface, seems to be an important parameter. Chiao *et al.* (1977) found that the measured ILS strengths depend on the notch depth; e.g., a slight undercut (i.e., d < t/2) gives a higher strength than an overcut (i.e, d > t/2) due to the fiber tearing in the undercut specimens. However, Shokrieh *et al.* (1995) reported that a slight change of notch depth has little effect on the measured ILS strengths and thus permitting a manufacturing tolerance, if a clamp is used. The effect of notch depth on the stress distribution inside the specimen gage sections is further investigated based on a 3D FEA.

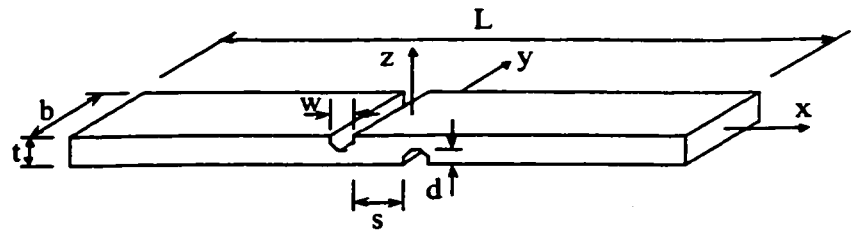


L = 80 mm, b= 12.7 mm
s = 7 mm, t = 4.44 mm
w = 1.8 mm, d = 2.22 mm,
fillet radius = 0.9 mm.

**Figure 4.20.** The geometry and nominal dimension of the double notch shear specimens.

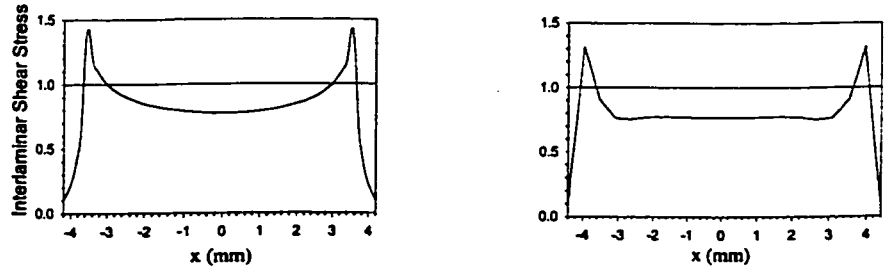


(a) (b)

**Figure 4.21.** Distribution of the ILS stress $\tau_{xz}$ at the central planes in the specimens; (a) non-filleted and (b) filleted.

The geometry and nominal dimensions for the modified double notch shear specimens are given in Figure 4.20. The notch shape is modified; the notch bottoms are chosen to be of round

shape with a fillet radius of 0.9 mm. This modification can not only make it convenient to cut the notches using diamond blade instead of a milling bit, but also reduce the stress concentration in the vicinity of the notches. A 2D stress analysis using 8-node isoparametric elements is conducted on the unidirectional specimens using the ANSYS® finite element software, and the notches with and without fillets are considered in order to observe the influence on the stress distribution at the central planes. The basic material properties of the G40-800/5276-1 system, which were experimentally obtained, are shown in Table 5.2. The stress analysis results are shown in Figure 4.21, where the shear stresses $\tau_{xz}$ at the central planes are demonstrated. It can be seen that the fillets do affect the stress distribution near the notches; the fillets can release the shear stress concentration. In the non-filleted (i.e., rectangular cut) specimens, the shear stress is maximum at the tips of the notches (i.e., at $x = \pm 3.5$ mm) and then quickly drops down to zero. In the filleted specimens, however, the shear stress reaches a maximum value inside the fillet regions at $x = \pm 4$ mm and then quickly disappears. These characteristics of stress distribution indicate that the external load is transferred through the central planes within the two maximum-stressed points, and thus the materials inside the fillet regions are capable of carrying a part of the external load. Therefore the nominal uniform shear stress at the central planes is modified as

$$\tau^{0}_{xz} = \frac{P}{b(s+2\delta)} \tag{4.6}$$

where P is the applied compressive load on the specimen end and $\delta$ is a correction parameter. The correction factors $\delta = 0$ for non-filleted specimens and $\delta = 0.5$ mm for filleted specimens. The ILS strengths are hereby calculated by substituting the measured ultimate load into Equation (4.6). The ILS stresses $\tau_{xz}$ shown in Figure 4.21 are normalized with respect to the nominal uniform ILS stresses $\tau^{0}_{xz}$ in each case.

#### 4.4.6.2 Specimen Lay-Up Design and Finite Element Analysis

An ideal testing technique characterizing basic material properties can provide a known state of relatively uniform stress and strain in the specimen gage section while the stress concentration is minimized in the load introduction section (Whitney *et al.*, 1982). In comparison with their unidirectional counterparts, the double notch shear laminated composite specimens may have a more

non-uniform stress distribution between the notches, because the stiffness mismatch between adjacent plies with different fiber orientations may result in concentrated interlaminar stresses at the free edges. Moreover, if the in-plane shear stresses in the off-axis plies might be high enough to generate transverse matrix cracks, singular interlaminar stresses may occur where the matrix cracks meet the adjacent plies and result in delamination at these sites. Hence, it is critical to properly design the fiber orientation and stacking sequence in the laminated specimens to reduce these negative effects on the experimental results.

A 3D stress analysis using ANSYS® finite element software is performed on the clamped double notch shear specimens subjected to the axial compressive loading. The specimens are modeled using the 8-node 3D layered structural solid elements. For reasons of convenience, the 3D stress analysis is only performed on the non-filleted specimens, because it is quite difficult to mesh the fillet regions using the layered structural solid elements. However, as shown in Figure 4.21, the stress distributions for these two types of specimens (filleted or non-filleted) exhibit same tendency except for some differences in magnitude especially near the notches. Hence, the fiber orientation and stacking sequence have similar effects on the stress distribution in these two types of specimens, especially along the width (y) direction. It is thus reasonable to calculate the stress distribution in the non-filleted specimens to judge the effects of the fiber orientation and stacking sequence on the filleted specimens. Because the stress distribution outside the two notches is not of interest, elements are coarsely distributed there, while elements are finely concentrated near the notches and the free edges because of stress concentration. Following these considerations, the specimens are meshed into 3960 layered structural solid elements. The displacements on top and bottom surfaces are fixed in z direction to simulate the clamp's effect.

**(1) Lay-Up Design for Type I Specimens**

The θ-dependent ILS strengths $S_{13}$ must be measured at the θ-interfaces between two neighboring plies with different fiber orientations. Ideally, it is expected that delamination could be generated along the central planes in the double notch shear specimens. Due to the manufacturing tolerance, a number of θ-interfaces around the central planes are essential, so that the delamination failure always takes place at a θ-interface even though the notches are not cut precisely to half the specimen thickness. Hence, the laminated composite specimens are unsymmetric with respect to

their central planes, which may produce the bending and twist deformations due to the residual stresses during the curing cycle, or due to the applied loading during the testing. The $[(0/\theta)_3/(\theta/0)_3//(\theta/0)_3/(0/\theta)_3]$ [i.e., $I(\theta)$] lay-up is arranged for the specimens, which could thus be viewed to be composed of two sub-laminates with $[(0/\theta)_3]_s$ and $[(\theta/0)_3]_s$ lay-ups that are symmetric with respect to their individual central planes. The numerical results based on the Classical Laminated Plate Theory show that there are no coupling effects of bending and twisting in such type of laminated composites. The 0° and θ plies are alternatively arranged in the specimens in order to reduce the free edge effects. A question naturally arises concerning the loading direction with respect to the fiber orientations; why is the $I(\theta)$ lay-up designed to obtain the θ-interfaces rather than $I'(\theta) = [(\beta/-\beta)_3/(-\beta/\beta)_3//(-\beta/\beta)_3/(\beta/-\beta)_3]$ lay-up ($\beta = \theta/2$)? One of the reasons, as addressed by Tao and Sun (1998), would be that the pure delamination cracks can propagate along the 0/θ interfaces and thus crack jumping from interface to interface can be possibly eliminated. The more important reason, however, is that such type of lay-ups $[I(\theta)]$ can reduce the free edge effects in the laminated composite specimens. Figure 4.22 displays the distribution of the stress $\tau_{xz}$ at the central planes in the I(60) and I'(60) specimens respectively. Hereafter, all the stress states are demonstrated with the normalized coordinate axes; i.e., $\xi = x/s$ and $\eta = y/b$ and normalized with respect to the nominal normal uniform shear stress in Equation (4.6). Large edge effects are observed in the latter specimen, therefore the stress distribution is much more uniform in the former specimen. Moreover, it is also shown that the in-plane shear stress $\tau_{12}$ and transverse stress $\sigma_2$ in the principal material coordinate system are much smaller in the former specimen than that in the latter specimen, which is desired because it can reduce the possibility for the advent of transverse matrix cracks.

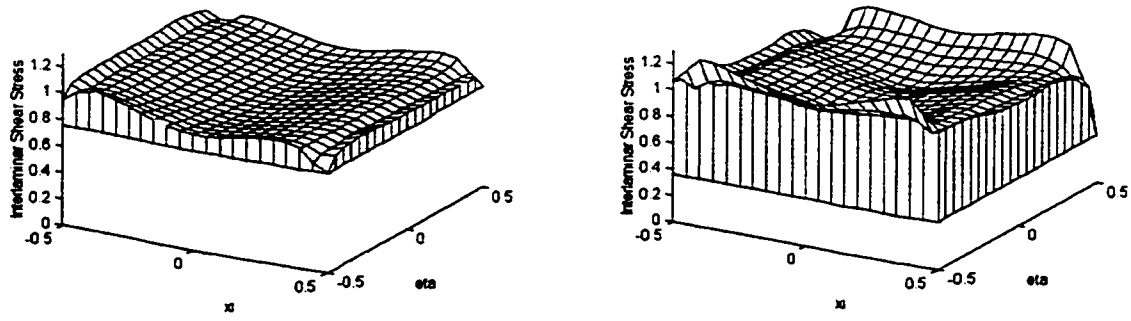


(a) (b)

**Figure 4.22.** Distribution of the ILS stress $\tau_{xz}$ at the central planes in the specimens; (a) I(60) lay-up, and (b) I'(60) lay-up [The demonstrated stress is normalized with respect to the nominal uniform shear stress in Equation (4.6)].

**(2) Lay-Up Design for Type II Specimens**

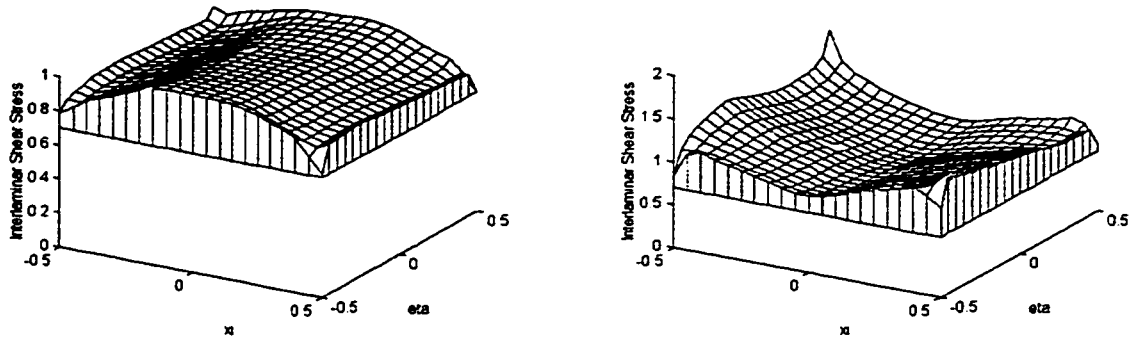


(a) (b)

**Figure 4.23.** Distribution of the ILS stress $\tau_{xz}$ at the central planes in the specimens; (a) II(60) lay-up, and (b) II'(60) lay-up.

Consequently, the first idea emerging in one's mind is to employ II'(θ) = $[(90/90\text{-}\theta)_3/(90\text{-}\theta/90)_3//(90\text{-}\theta/90)_3/(90/90\text{-}\theta)_3]$ specimens to characterize the ILS strengths $S_{23}$. In the present experimental program, the tests on the II'(0) and II'(10) specimens have been performed to determine the ILS strengths $S_{23}$ at the 0°- and 10°-interfaces. Unfortunately, the matrix compressive failure takes place inside the notched parts instead of the desired delamination at the central planes, because the transverse compressive stress inside the notched parts always reaches its ultimate strength prior to the ILS stress. Two solutions can be found to remove the deadlock by enforcing the ILS stress to reach its ultimate strength prior to the transverse compressive stress inside the notched parts; (1) further increasing the specimen thickness, and (2) replacing a number of 90° plies by the 0° plies. The high expense would be the disadvantage of the first solution, which means that more composite materials must be needed and pain-taking tasks have to be taken in cutting and grinding the thick specimens. The disadvantage of the second solution is that the initial delamination would be formed at the 0/90 or 0/(90-θ) interfaces rather than at the 90/(90-θ) interfaces, because the stiffness mismatch of the 0° ply and 90° [or (90° – θ)] ply would result in large edge effects which could generate the delamination failure. However, the inclusion of some 0° plies can provide a more uniform distribution of the stress $\tau_{xz}$ inside the specimen gage sections; Figure 4.23 presents the stress distribution at the central planes in both the II(60) and II'(60) specimens. These positive effects of 0° plies are even more apparent in the II(0) and II(10) specimens. Therefore, the second solution is accepted in the present experimental program, so that

Type II specimens contain a $\Pi(\theta) = [(90/90\text{-}\theta)_2/0_4/(90\text{-}\theta/90)_2//(90\text{-}\theta/90)_2/0_4/(90/90\text{-}\theta)_2]$ lay-up. It is noteworthy that similar to the $I(\theta)$ lay-up designed for Type I specimens, the $\Pi(\theta)$ lay-up also have small free edge effects and thus provide a more relatively uniform stress distribution in the specimen gage sections. In the testing, the experimental data from the specimens initially delaminated at the 0/90 or 0/(90-θ) interfaces are discarded, and therefore more specimens will be prepared and tested. The numerical results from the Classical Laminated Plate Theory also show that no coupling effects of bending and twisting appear in such type of laminated composites.

### (3) Interlaminar Shear Stress Distribution at Central Planes

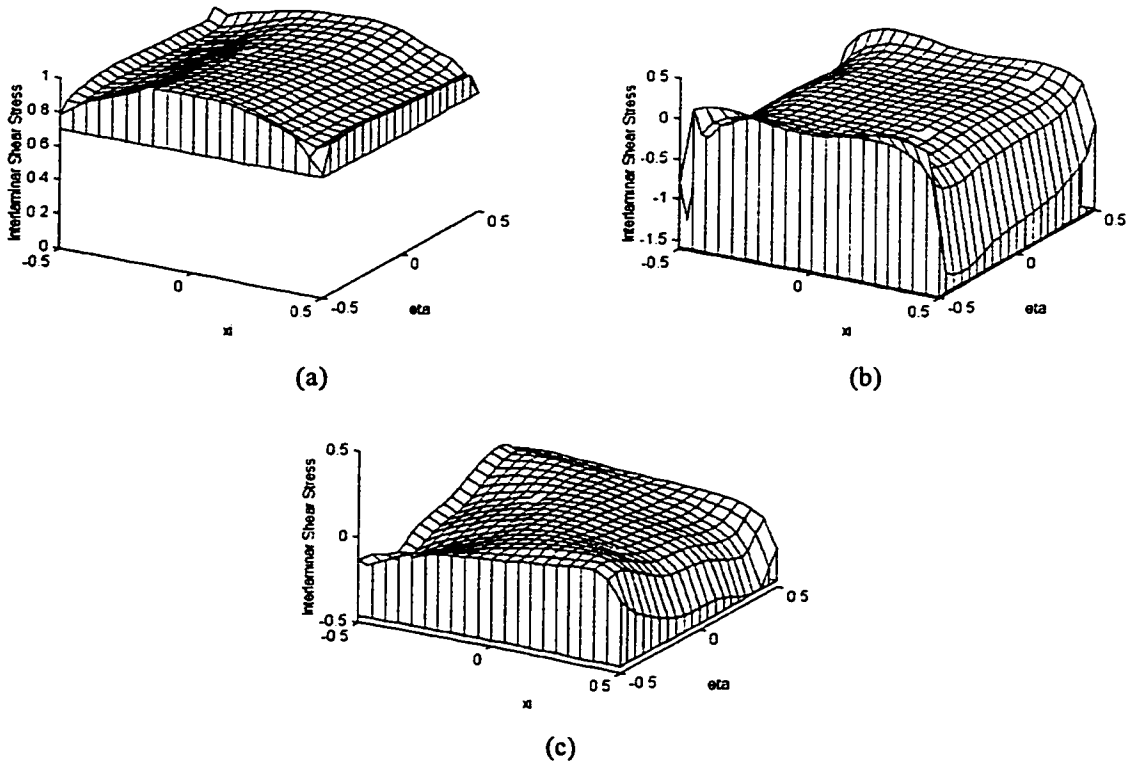


**Figure 4.24.** Stress distribution at the central planes in the I(30) specimens; (a) $\tau_{xz}$, (b) $\sigma_z$, and (c) $\tau_{yz}$.

The 3D finite element results clarify that the ILS stress $\tau_{xz}$ has a uniform distribution at the central planes in the designed specimens. Furthermore, the other two interlaminar stresses $\sigma_z$ and $\tau_{yz}$ at the central planes are close to zero in the middle of the specimens. Near the notches, the stress $\tau_{yz}$ is still of small magnitude, and the stress $\sigma_z$ is of large magnitude but negative (i.e., compressive); therefore, their effects on the failure strengths can be neglected. Due to space limitation, selectively

shown are the stress results only in the specimens with the 30°-interface. The ILS stress distributions at the central planes in the I(30) specimen are presented in Figure 4.24 and those in the II(30) specimen are presented in Figure 4.25. A special case for the ILS strengths is that the strength components $S_{13}$ and $S_{23}$ identically equal to each other at the 90°-interface. Consequently, only one strength component needs to be experimentally measured. Following the foregoing lay-up design, one can have two types of specimens towards the strength components at the 90°-interface; with either the I(90) or II(90) lay-ups. The I(90) lay-up is selected to characterize the ILS strength components at the 90°-interface, since the finite element analysis results show that the stress distribution of $\tau_{xz}$ at the central planes in these two type of specimens do not present any apparent difference. Therefore, the present experimental program consists of 665 effective double notch shear specimens.

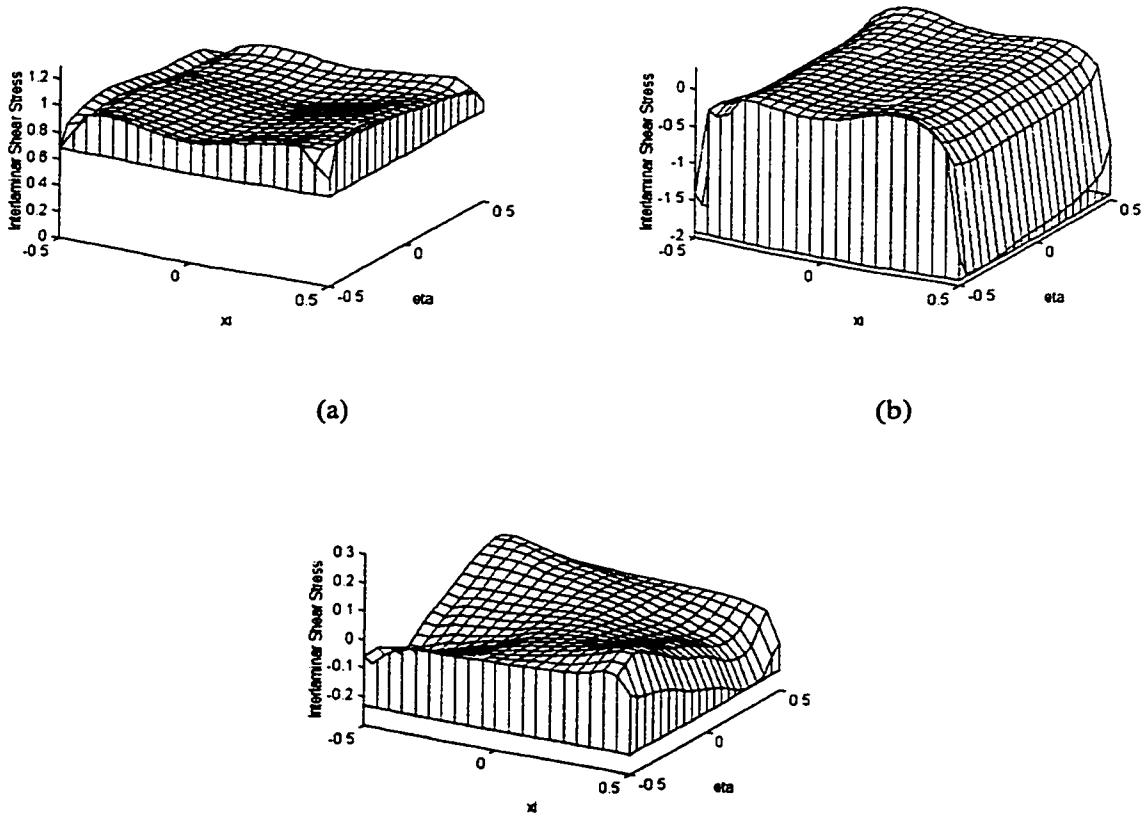


**Figure 4.25.** Stress distribution at the central planes in the II(30) specimens; (a) $\tau_{xz}$, (b) $\sigma_z$, and (c) $\tau_{yz}$.

**(4) Effects of Notch Depth (Overcut and Undercut)**

The above finite element analysis is implemented towards the idealized specimens with the notch depth of precisely half the specimen thickness (d = 2.22 mm). The influence of notch depth on the stress distribution in the specimen gage sections, and thus on the experimentally measured ILS strengths, can also be evaluated by comparing the finite element analysis results from the specimens with different notch depths. Before doing so, special attentions should be addressed that the initial delamination is normally formed at one of the notch bottoms, because there exists the stress concentration, as shown in Figure 4.21b. Therefore, even when the specimens are overcut or undercut, the delamination are still initiated at the notch bottoms rather than at the notch free edges over the bottoms where the stress state is of lower magnitude. Herein, two notch cases are considered; one ply thickness undercut (d = 2.035 mm) and one ply thickness overcut (d = 2.405 mm). Moreover, the overcut or undercut notches are assumed to simultaneously occur in a single specimen, thus the cutting errors are exaggerated for the convenience of the finite element meshing. Under these two assumed notch cases, the initiate delamination would be formed at the two interfaces adjacent to the midplanes of specimens. The influence of notch depth could thus be evaluated by comparing the ILS stress $\tau_{xz}$ at the two interfaces of overcut and undercut specimens with that at the midplane of precisely-cut specimens. The stress distributions are not graphically presented in this chapter, and the three regions, where the stress state is discussed in the following, are schematically displayed in Figure 4.26. Examining the two notch cases, the distribution of the ILS stress $\tau_{xz}$ is found to be slightly changed at the two interfaces adjacent to the midplanes of specimens between the two notches. In the overcut specimens, this stress component at most regions of the two interfaces between the two notches is more uniformly distributed, but is decreased a little bit at the regions over the notch bottoms due to the notch free edges. Overall, the stress $\tau_{xz}$ has the same distribution at the two interfaces of the overcut specimens as that at the midplanes of precisely-cut specimens. Therefore the overcut depth would have little effects on the measured ILS strengths. In the undercut specimens, the stress $\tau_{xz}$ tends to be smaller at larger regions of the two interfaces under the notch bottoms, because the external load is partially suspended in a way of normal stress by the undercut materials. Therefore, compared to the overcut depth, the undercut depth would have a little effect on the stress distribution and thus the measured ILS strengths. The present finite element analysis dealt with the exaggerated undercut depth, but in fact the effects of the undercut

depth can become smaller because it is not difficult to control the notch depth with a cutting tolerance less than one ply thickness. However, the author of this thesis suggests that it is necessary to avoid the undercut in order to yield the reliable experimental results.

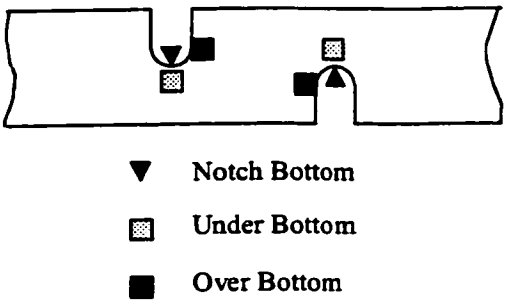


**Figure 4.26.** The three regions where the stress state is of interest due to overcut and undercut.

## 4.5 SUMMARY

After performing a detailed evaluation and stress analysis on a variety of test techniques, the tests accepted in the present experimental program are summarized as follows:

(1) ASTM D3039 tensile test with 8 ply unidirectional specimens for longitudinal tensile strength Xt and 12 ply unidirectional specimens for transverse tensile strength Yt;
(2) ASTM D 4255 three rail shear test with 8 ply unidirectional specimens for in-plane shear $S_{12}$;
(3) Interlaminar compressive test based on the end-loaded prism specimens with $[0]_{74}$ and $[0/90]_{32}$ specimens for interlaminar compressive strength Zc;
(4) Double notch shear test with $[(0/\theta)_3/(\theta/0)_3//(\theta/0)_3/(0/\theta)_3]$ specimens for longitudinal interlaminar shear strength $S_{13}$ and $[(90/(90-\theta))_2/0_4/(90-\theta)/90)_2//((90-\theta)/90)_2/0_4/(90/(90-\theta))_2]$ specimens for transverse interlaminar shear strength $S_{23}$.

# CHAPTER 5

# EXPERIMENTAL CHARACTERIZATION OF MATERIAL PROPERTIES: EXPERIMENTAL RESULTS AND STATISTICAL ANALYSIS

This chapter is contributed to the experimental characterization of material properties for CYTEC® G40-800/5271-1 composite material. Detailed information obtained from the present experimental program is presented, such as fracture surface morphology, probabilistic behavior of each strength component, and so on. For the interlaminar shear (ILS) strengths, the attention is focused on the experimental characterization and statistical analysis of ILS strengths at different θ-interfaces. The inherent relationships between fracture surface morphology and the magnitudes of ILS strengths are explored through the rank-sum test technique. For the interlaminar compressive strengths, the attention is addressed on studying the probabilistic characteristic, the effects of laminate lay-ups and specimen sizes on the magnitudes of strengths. The in-plane material properties, i.e., tensile and shear strength and moduli, are experimentally characterized using the customary test techniques. The probability distributions for all the strength components are then determined through the maximum entropy technique.

## 5.1 SUMMARY OF THE EXPERIMENTAL PROGRAM

The intent of the present experimental program is to experimentally characterize the input data for the proposed *Stochastic Delamination Model*; i.e., the probabilistic behavior of interlaminar strength components. The experimental program is summarized in Table 5.1; detailed information concerning specimen preparation and test procedure will be given in the following separate sections. All the tests are performed in ambient air using a MTS testing machine. It is noteworthy that all the

test-related tasks, such as curing of laminated composites, nondestructive examination, specimen preparation, and testing are completed at the Concordia Centre for Composites.

**Table 5.1.** Summary of experimental program for G400-800/5276-1 composite material.

| Test | Specimen Geometry | Standard | Loading Condition | Strength Comp. | Specimen Number |
|---|---|---|---|---|---|
| Longitudinal Tension | 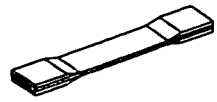 | ASTM D3039 | Tension by hydraulic grips | Xt | Twenty-four effective $[0_8]$ specimens |
| Transverse Tension | 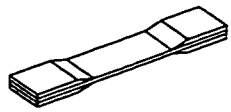 | ASTM D3039 | Tension by hydraulic grips | Yt | Thirty-five $[90_{12}]$ specimens |
| In-Plane Shear | 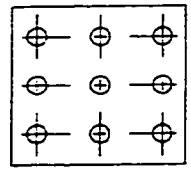 | ASTM D4255 | Compression through rails | $S_{12}$ | Thirty-five $[0_8]$ specimens |
| Interlaminar Shear |  | Modified ASTM D3846 | Compression with clamp | $S_{13}$ | Thirty-five (Type I) $I(\theta) = [(0/\theta)_3/(\theta/0)_3//(\theta/0)_3/(0/\theta)_3]$ for each of ten θ-interfaces |
| | | | | $S_{23}$ | Thirty-five (Type II) $II(\theta) = [(90/(90-\theta))_2/0_4/(90-\theta)/90)_2 // ((90-\theta)/90)_2/0_4/(90/(90-\theta))_2]$ for each of ten θ-interfaces |
| Interlaminar Compression | 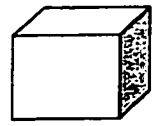 | N/A | Compression through collar | Zc | Forty-two $[0_{72}]$ specimens |
| | | | | | Three $[(0/90)_{36}]$ specimens |

## 5.2 THEORETICAL BACKGROUND OF STATISTIC ANALYSIS

The statistical theory used in this chapter is described as follows, which includes the maximum entropy technique to determine the probability density functions of sample values, the rank-sum test to examine sample independence, and the Kolmogorov-Smirnov test to evaluate good-of-fit of theoretical and sample probability distributions.

### 5.2.1 Maximum Entropy Technique

The maximum entropy technique (Siddall, 1983) was developed to attempt accurate evaluation towards the probability density functions (or probability distributions) of the sample values. Instead of standard distribution assumptions, the maximum entropy technique assumes the probability density function in a general form as

$$f(s) = \exp[\lambda_0 + \sum_{i=1}^{p} \lambda_i s^i] \tag{5.1}$$

where $\lambda_i$'s, are the parameters to be determined from the given sample values. One of the salient features of the maximum entropy technique is that the form of the probability density functions is given *a priori*, and the order $p$ of polynomial in the power is determined by the probabilistic characteristics of the sample variables. Hence, the parameters $\lambda_i$'s can be evaluated by the lower and higher bounds and the moments of the random variable S up to the $p$-th order, which can be estimated from the sample values using the following equation:

$$M_i = E[s^i] = \frac{1}{n} \sum_{j=1}^{n} s_j^i \qquad i = 1, 2, \ldots, p \tag{5.2}$$

In the above, n is the sample size, and i denotes the order of a moment. The estimation accuracy of the probability density functions can be improved by using the higher orders of moments. For most kinds of probability distributions, however, the moments of higher than the 4th or 5th orders do not make much contribution to the estimation accuracy. In the present experimental program, the order p = 4 is found to be adequate to characterize the individual probability density functions of the random strength components. The lower and higher bounds of random strengths are determined by a tentative procedure. The good selection is found that the lower bound equals to 0.92 minimum sample value and the higher bound to 1.08 maximum sample value in each experimental data set.

### 5.2.2 Rank-Sum Test

The rank-sum test technique is usually employed to judge whether two respective samples come from the same population (Larson, 1982). Suppose that $X_i$ (i = 1, ..., n), and $Y_j$ (j

= 1, ..., m) are two sets of sample values that are independently obtained. These two sets of sample values are combined together and ranked in a sequence from the smallest value to the largest value. The sums of the ranks with respect to $X_i$ and $Y_j$ in the combination can thus be calculated, which hereafter are designated as $W_X$ and $W_Y$ respectively. Then, it can be concluded that $X_i$ and $Y_j$ come from the same population with a given confidence (1-$\alpha$)%, provided that $t_{\alpha/2} \leq W_Y \leq t_{1-\alpha/2}$; the confidence limits are defined as

$$t_{\alpha/2} \cong \frac{m(m+n+1)}{2} + z_{\alpha/2}\sqrt{mn(m+n+1)/12} - \frac{1}{2} \tag{5.3}$$

$$t_{1-\alpha/2} \cong \frac{m(m+n+1)}{2} + z_{1-\alpha/2}\sqrt{mn(m+n+1)/12} + \frac{1}{2} \tag{5.4}$$

and $N(z_{\alpha/2}) = \alpha/2$, $N(z_{1-\alpha/2}) = 1-\alpha/2$ (here N denotes the standard normal distribution).

### 5.2.3 Kolmogorov-Smirnov Good-of-Fit Test

After the theoretical probability density function for given sample values is determined by the maximum entropy technique, the good-of-fit between the theoretical probability distributions and the sample distributions is examined by Kolmogorov-Smirnov test technique. That is, the theoretical probability distributions are accepted, if the maximum difference Dn between the theoretical distributions and sample distributions within the range of lower bounds to higher bounds does not exceed the associated acceptance limits. The sample distributions are calculated by k/n, where k is the ordered rank of sample values sequenced from smallest value to largest value in each data set. The theoretical probability distribution at the k-th rank of sample value $s^{(k)}$ is obtained by integrating f(x) from the lower bound (L.B.) to $s^{(k)}$,

$$F[s^{(k)}] = \int_{L.B.}^{s^{(k)}} f(x)dx \tag{5.5}$$

The acceptance limits are equal to $1.36/\sqrt{n}$ at 95% confidence level. Particularly, Kolmogorov-Smirnov good-of-fit test plays an important role in determining the lower and higher bounds of sample values; the accurate bounds should be those that make $F[s^{(1)}]$ as close as possible to 1/n and $F[s^{(n)}]$ to n/n (= 1).

## 5.3 IN-PLANE STRENGTHS

The specimens experimentally characterizing in-plane material properties are made from thin laminated composites; the longitudinal tensile and in-plane shear specimens are composed of 8 plies and the transverse tensile specimens of 12 plies. Therefore, the laminated composites for these specimens are cured in an autoclave following the specified curing cycle and no special procedures are taken. With the glass-fiber/epoxy tabs glued to the laminates for the tensile specimens in advance, these three types of specimens are cut from the laminated composites using a diamond wheel. Strain gages are glued to a number of specimens to monitor the load vs. displacement relationships and measure the Young's modulus and Poisson's ratio. The tests are performed exactly following the procedures specified in ASTM D 3039 for tension and ASTM D 4255 for shear.

The experimental results concerning the mean values and coefficients of variation for these three in-plane strength components, Young's modulus and Poisson's ratio are summarized in Table 5. 2.

**Table 5.2.** Experimental results of the in-plane material properties for the G40-800/5276-1 composite material.

| | $X_t$ (Mpa) | $Y_t$ (MPa) | $S_{12}$ (MPa) | $E_1$ (Gpa) | $E_2$ (GPa) | $G_{12}$ (GPa) | $\nu_{12}$ |
|---|---|---|---|---|---|---|---|
| Mean | 1978.10 | 41.21 | 35.24 | 157.7 | 8.54 | 4.63 | 0.32 |
| C.V. (%) | 8.89 | 11.58 | 15.08 | 0.98 | 3.20 | 1.76 | 5.40 |

### 5.3.1 Longitudinal Tensile Strength

The typical stress-strain curve for the longitudinal tensile specimens is shown in Figure 5.1. A linear relationship between the stress and strain is presented until the final failure. Two fracture modes are observed from the longitudinal tensile specimens, as shown in Figure 5.2. The first fracture mode involves the fiber breakage inside large range of the specimens, thereby providing the effective longitudinal tensile strength sample values. Slight tab debonding near the sloped sides of tabs is observed for these effective specimens. The second fracture mode involves matrix cracks, because the fibers inside the related specimens are slightly misaligned from the loading direction due to the cutting error. The fiber misalignment inside the specimens generates the shear stress along the fiber direction that is large enough to form the matrix cracks before the fiber breakage, and then the external load can not be further increased. Therefore, the

slight fiber misalignment would greatly reduce the tensile strength values from the longitudinal tensile test (Pipes and Cole, 1973). In the present experimental program, 35 tensile specimens are tested; only 24 specimens effectively present the fracture mode of fiber breakage and the other 11 specimens present the fracture mode of matrix crack.

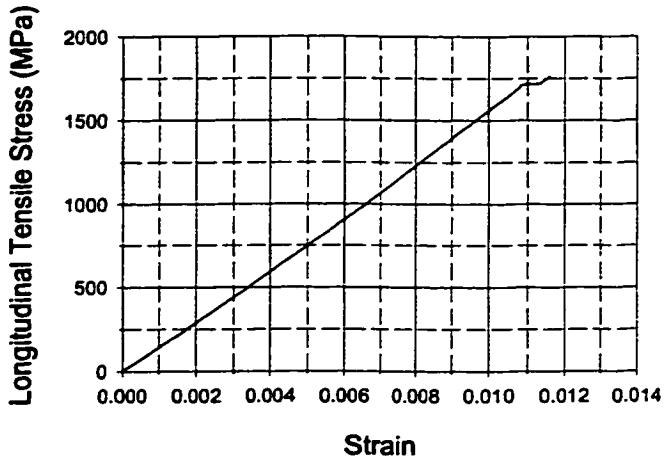


**Figure 5.1.** Typical stress-strain curve for longitudinal tensile specimens.

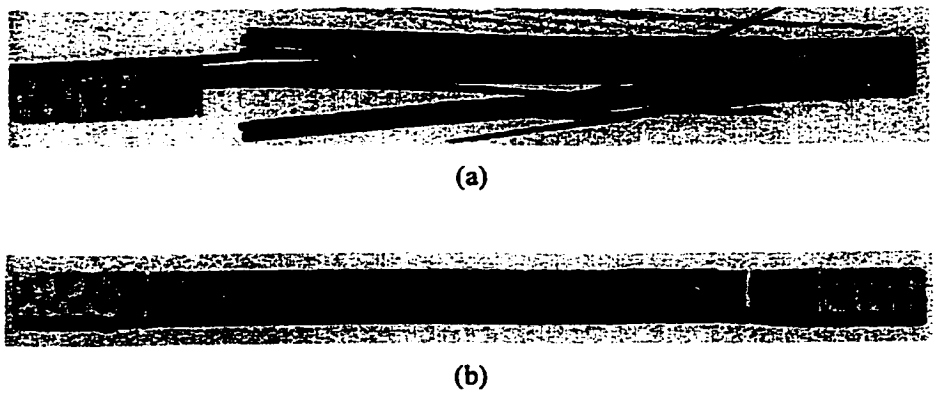


**Figure 5.2.** Fracture modes of the longitudinal tensile test; (a) effective specimen, and (b) ineffective specimens.

From the 24 experimental sample values, the probability density function for the longitudinal tensile strength Xt is obtained using the maximum entropy technique, and plotted in Figure 5.3. It can be seen that the probability distribution of Xt is close to the two-parameter Weibull distribution; i.e., the sample values are concentrated towards the lower bounds. Moreover, the tensile strength Xt has smaller scatter than the other two in-plane strengths Yt and $S_{12}$, because it less dependable on the matrix defects due to manufacturing. The Kolmogorov-

Smirnov statistic, Dn, for the theoretical and sample probability distributions of Xt equals to 0.093, which is much less than the associated acceptance limit of 0.277 with respect to n = 24. This indicates that the probability density function of Xt from the maximum entropy technique is acceptable at a confidence level of 95%.

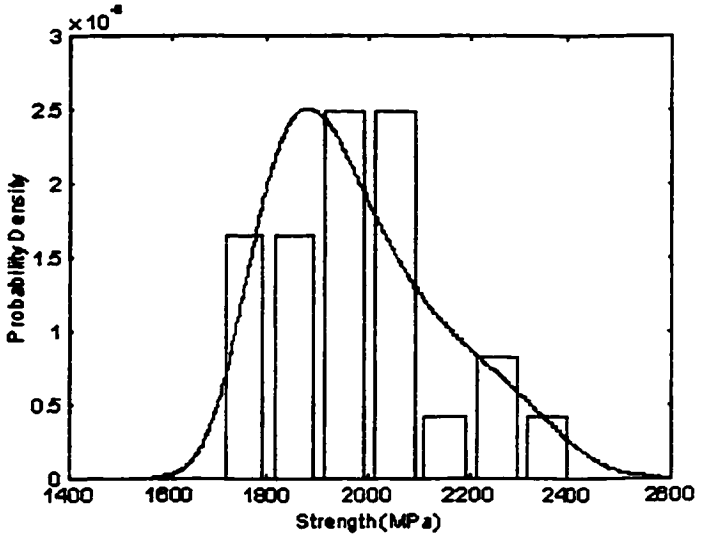


**Figure 5.3.** Probability density function for the longitudinal tensile strength Xt.

### 5.3.2 Transverse Tensile Strength

The typical stress-strain curve for the transverse tensile specimens is displayed in Figure 5.4. Also, a linear relationship between the stress and strain is exhibited in the whole loading process. It is found that a large number of specimens are unexpectedly broken inside the regions of gage sections near the tabs, although special procedure is taken by gluing thick glassfiber/epoxy tabs to the specimens. However, the failure locations do not seem to strongly affect the experimental data (O'Brien and Salpekar, 1993), because the strength values obtained from the specimens with the failure near the tabs are roughly close to those from the specimens with the failure in the central regions of gage sections. Therefore, the sample values from all of the 35 tensile specimens are mixed together to generate the probability density function for the transverse tensile strength Yt. The fracture modes for the transverse tensile specimens are shown in Figure 5.5.

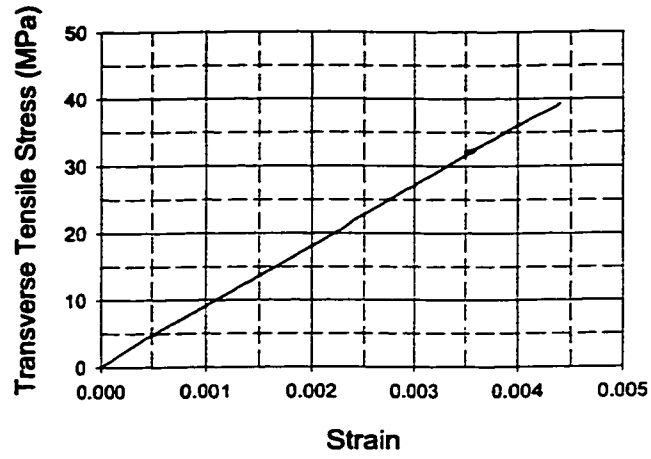


**Figure 5.4.** Typical stress-strain curve for transverse tensile specimens.

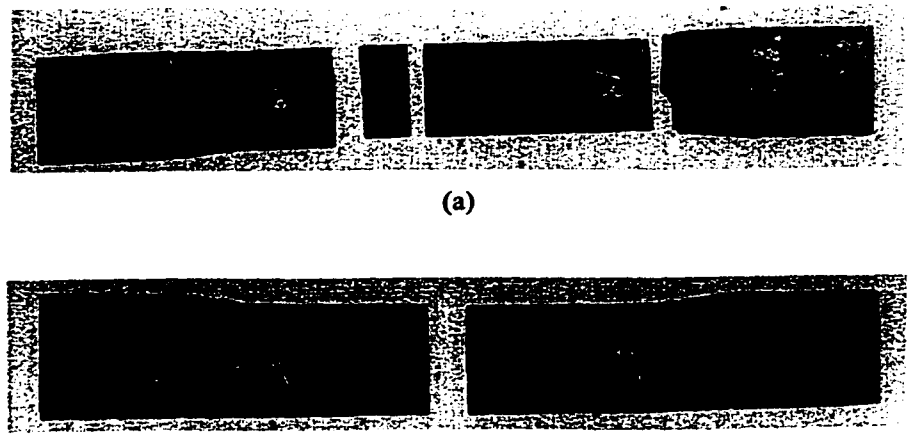


**Figure 5.5.** Fracture modes of the transverse tensile specimens; (a) failure near the tabs, and (b) failure inside specimen gage section.

The probability density function for the transverse tensile strength Yt determined by the maximum entropy technique is displayed in Figure 5.6. The probability distribution of Yt might be close to the Gaussian distribution, because most of sample values are concentrated in the middle of the lower and higher bounds. The transverse tensile strength Yt presents larger scatter, since the matrix failure is sensitive to the matrix defect due to manufacturing. The Kolmogorov-Smirnov statistic, Dn, for transverse tensile strength Yt is 0.096 and much less than the associated acceptance limit of 0.229 with respect to n = 35, thereby indicating that the probability density function of Yt obtained from the maximum entropy technique is a good candidate at a confidence level of 95%.

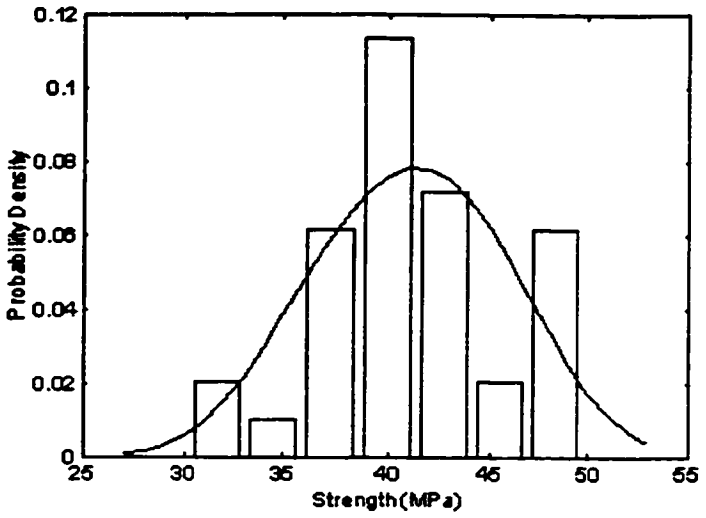


**Figure 5.6.** Probability density function for the transverse tensile strength Yt.

### 5.3.3 In-Plane Shear Strength

The stress-strain curve for the in-plane shear specimens is typically demonstrated in Figure 5.7. Different from the stress-strain relationships for the in-plane tensile specimens, non-linearity is presented by the in-plane shear specimens. The fracture mode of the in-plane shear specimens is unexpected; all of the specimens unexpectedly fail at the rail edges or under the rails rather than inside the specimen gage sections (see Figure 5.8). This is attributed to the fiber orientations in the shear specimens that are parallel to the rails. In the test, slight disturbance will be unavoidably imposed on the loading rails and make the shear specimens bend out of the in-plane. Consequently, the transverse normal stress that is perpendicular to the fiber orientations exists inside the shear specimens at the rail edges or under the rails, thereby generating the matrix cracks through the transverse stress rather than the desired in-plane shear stress. Hence, the in-plane shear specimens with the fiber orientations parallel to the rails provide the experimental values that are lower than the actual in-plane shear strengths of composite materials. The in-plane shear specimens with the fiber orientations perpendicular to the rails could generate higher experimental values. Fortunately, the in-plane shear strength is not required by the proposed *Stochastic Delamination Model*, and the purpose performing the in-plane shear test in the present experimental program is only to obtain the shear modulus.

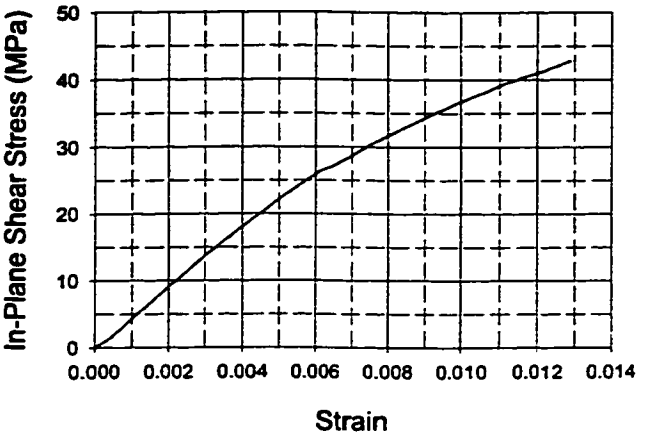


**Figure 5.7.** Typical stress-strain curve for in-plane shear specimens.

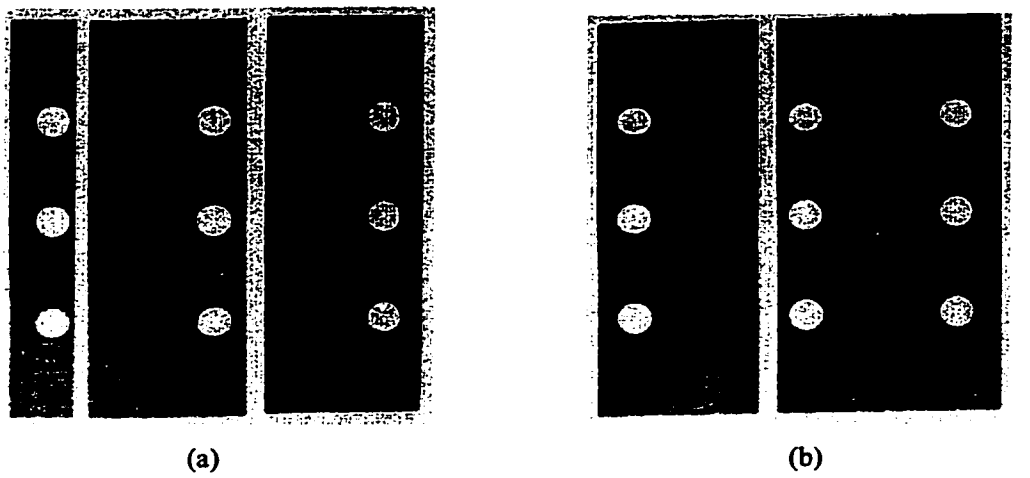


**Figure 5.8.** Fracture modes of the in-plane shear specimens; (a) two transverse matrix cracks, and (b) one transverse matrix crack.

On the basis of the 35 experimental sample values, the probability density function for the in-plane shear strength $S_{12}$ is generated through the maximum entropy technique, as displayed in Figure 5.9. The random variable $S_{12}$ seems to have a uniform distribution; the experimental sample values are quite uniformly distributed between the lower and higher bounds. The in-plane shear strength $S_{12}$ displays large scatter, because it is also sensitive to the matrix defects. The Kolmogorov-Smirnov statistic, Dn, for the shear strength has a small value of 0.089, thus demonstrating that the probability distribution of $S_{12}$ is well fitted by the probability density function from the maximum entropy technique.

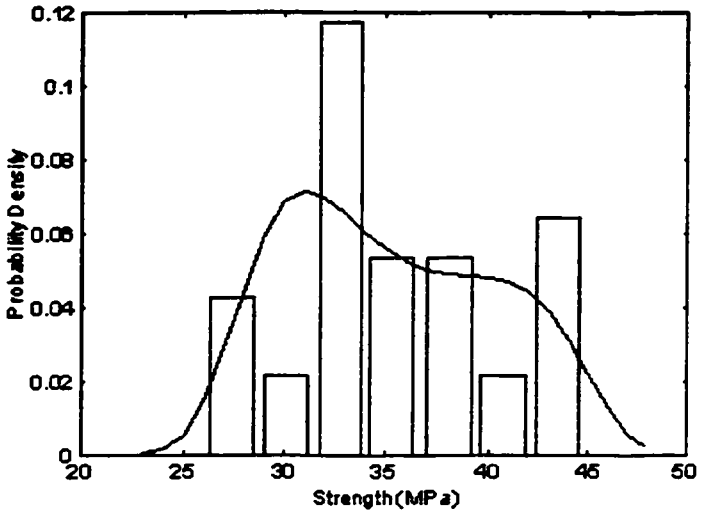


**Figure 5.9.** Probability density function for the in-plane shera strength $S_{12}$.

## 5.4 INTERLAMINAR COMPRESSIVE STRENGTHS

The unidirectional and cross-ply laminates composed of 72 plies in each case are fabricated from the G40-800/5276-1 carbon/epoxy pre-impregnated tapes and cured in an autoclave following a specified curing cycle. Three thermo-couples are inserted inside the laminates to monitor the temperature field through the laminate thickness in the curing process. The steel dams are used closely around the thick laminates to prevent the excess flowing-out of epoxy. Several bundles of glass fiber yarns are placed between the dams and the laminates and conducted to the breather, in order to form a channel to release the entrapped air and bubble out of the laminates.

The prism specimens are then cut from the laminated plates using a diamond wheel blade. Due to poor epoxy, the boundary regions of the laminated plates with a width of at least 25.4 mm are not used in order to guarantee the parallelism of specimens. The edges of the specimens are ground using sand-papers with high grit orders to remove the potential damage due to cutting. The top and bottom surfaces of specimens are lubricated by smearing some grease and the specimens are then mounted on a MTS testing machine. A compressive load is applied to the specimens by moving the plateau upward at a constant speed of 0.8 mm/min. and terminated

when the load suddenly drops down to zero. During the loading process, the relative displacements and the corresponding loads are directly recorded from the MTS testing machine.

### 5.4.1 Unidirectional Specimens

The stress-strain curves for groups 3 and 4 specimens (see Table 4.1) are typically shown in Figure 5.10. Wherein the strain is approximately obtained by dividing the crosshead movement of the testing machine, which represents the summation of the specimen deformation and the aluminum collar deformation, by the specimen thickness. The collar deformation, however, is much smaller than the specimen deformation, because the modulus of aluminum is much higher than TTH modulus of graphite/epoxy composites. In spite of the collar deformation, it can be seen that unidirectional specimens exhibit a liner stress-strain behavior in the whole loading process. Likewise stress-strain relationships are also observed from the other groups of specimens. The TTH compressive strength for each specimen is obtained by dividing the failure load by its cross-sectional area. The distribution of each individual sample value with respect to the cross-sectional area is displayed in Figure 5.11, and the mean values ($\mu$) and the coefficients of variation (Cv) for the four groups of unidirectional specimens are listed in Table 5.3. The experimental data from group 1 specimens present smaller variation, but those from the remaining groups of specimens present greater variation.

A number of transverse cracks can be observed on the sides normal to the fiber directions in each failed specimen. The cracks grow in a tree-branch way; child cracks are generated at the tips of mother cracks and their propagation directions deviate from those of the mother cracks. Consequently, the transverse cracks are found to propagate to the two side surfaces parallel to the fiber directions. Therefore, the transverse cracks are generated in the whole gage section of specimens. These evidences show that the transverse cracks grow easily in unidirectional prism specimens, because the fibers make no contributions in arresting the transverse crack propagation. Hence, the failure mechanism of the G40-800/5276-1 unidirectional composite material in the TTH compressive test is different from those reported by Goeke (1993) for woven and knit-stiched materials. Figure 5.12 displays the side view of matrix cracks with respect to one of group 3 specimens. The aforementioned fracture mode happens to all the groups of specimens.

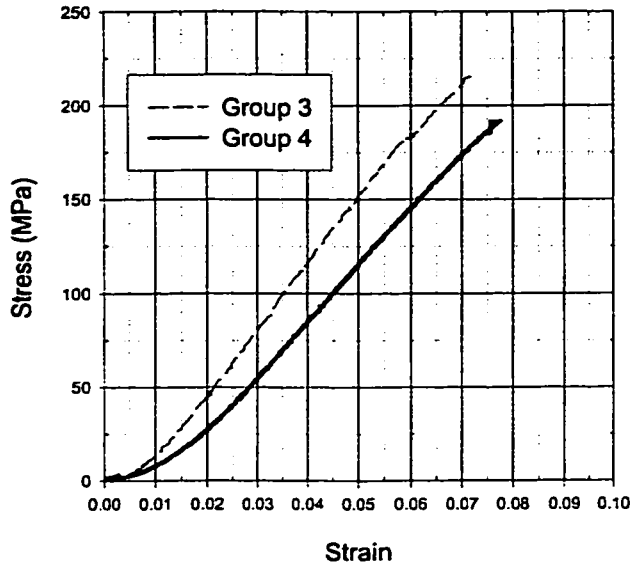


**Figure 5.10.** Typical stress-strain curve for unidirectional compressive prism specimens.

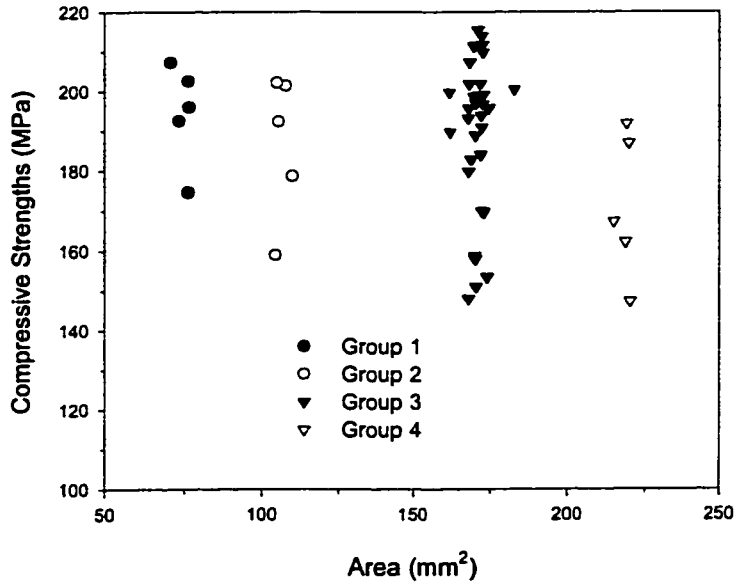


**Figure 5.11.** Sample value distribution of TTH compressive strength $Z_C$ with respect to cross-section area from unidirectional compressive prism specimens.

**Table 5.3.** Experimental results of TTH compressive strengths for G40-800/5276-1 composite material.

| | Unidirectional | | | | Cross-Ply |
|---|---|---|---|---|---|
| | Group 1 | Group 2 | Group 3 | Group 4 | |
| μ (MPa) | 194.53 | 186.62 | 189.59 | 171.10 | 1008.88 |
| Cv (%) | 6.44 | 9.73 | 10.10 | 10.71 | 5.26 |

**Figure 5.12.** Side view (from the fiber direction) of matrix cracks in unidirectional compressive prism specimens.

From the failure mode, an interesting evidence can also be obtained that the transverse cracks propagate grossly along a direction of $\theta = 10°$ with respect to the compressive loading direction (i.e., the TTH direction). The TTH compressive normal stress $\sigma_z$ can be related to the shear stress $\tau$ along the crack surfaces by

$$\sigma_z = \frac{\tau}{\sin(2\theta)} \tag{5.6}$$

If substituting the transverse interlaminar shear strength $S_{23}$ for the unidirectional specimens (see next section) for $\tau$ in the above equation, one can find that the normal stress $\sigma_z$ would be very close to the TTH compressive strength. This indicates that the transverse matrix cracks are formed when the TTH compressive load is increased to a point where the shear stress $\tau$ at the crack surfaces reaches the transverse interlaminar shear strength of the material. Therefore, it could be concluded that the TTH compressive failure of unidirectional specimens is governed by the transverse matrix cracks due to shear.

### 5.4.2 Cross-Ply Specimens

The stress-strain curve for the cross-ply specimens is typically shown in Figure 5.13, where the strain is once again approximately determined by dividing the summation of the specimen deformation and carbon steel collar deformation by the specimen thickness. Similarly, because the modulus of carbon steel is much higher than the TTH modulus of specimens, the contribution of the deformation from carbon steel collars to the TTH strain is negligible.

Therefore, it is accurate that the displayed strain in Figure 5.13 is considered to be the TTH strain of specimens. A linear stress-strain behavior is also demonstrated until the peak of the whole loading process. Larger TTH deformation is presented by the cross-ply specimens than the unidirectional specimens before the final failure. Comparing the slope of the stress-strain curves in Figures 5.10 and 5.13, it is found that the cross-ply specimens have higher TTH modulus than the unidirectional specimens. Therefore, a conclusion could be made that the fiber orientations affect the TTH modulus to some extent.

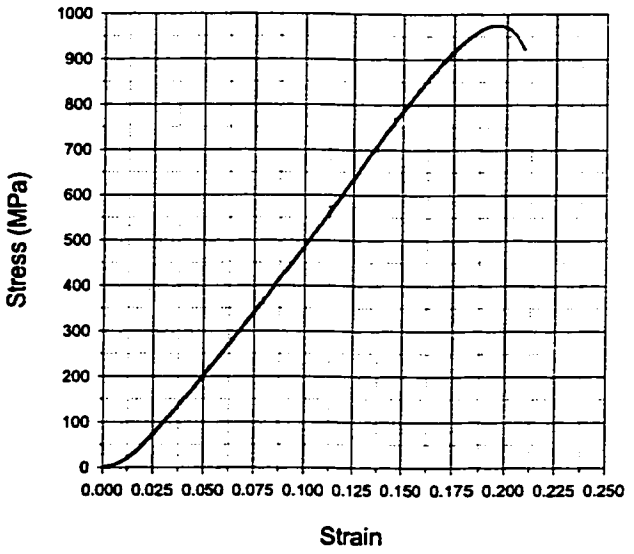


**Figure 5.13.** Typical stress-strain curve for cross-ply compressive prism specimens.

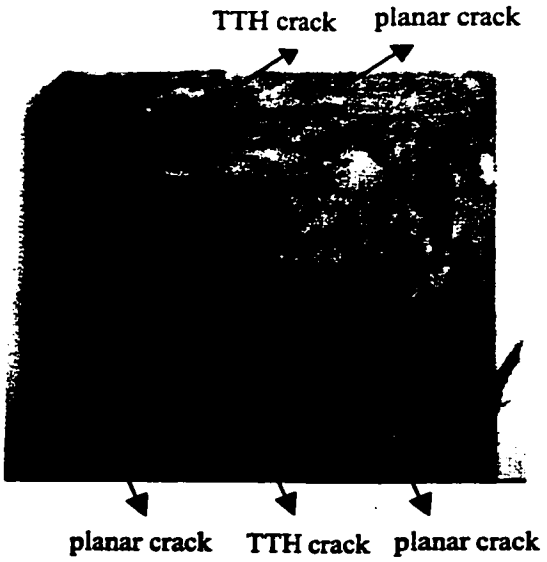


**Figure 5.14.** Front view (from the through-the-thickness direction) of fracture surfaces in cross-ply compressive prism specimens.

The mean and coefficient of variation for the TTH compressive strength are presented in Table 5.3. The TTH compressive strength of cross-ply specimens is much higher than that of unidirectional specimens, and also has much smaller coefficient of variation. The unidirectional specimens are sensitive to the matrix defects introduced in the manufacturing process; the concentrated stress due to matrix defects quickly makes the formation of macro matrix-cracks through the laminate thickness, since all the fibers in the unidirectional specimens are oriented in the same direction. The fracture surfaces of matrix defects, or the fracture surfaces of micro-cracks initiated from the matrix defects at the initial loading stage, are always parallel to the fiber direction. Along some surfaces which are slightly deviated from the loading direction, the concentrated shear stresses are large enough to make these initial matrix cracks propagate in a planar way. Therefore, the planar crack surfaces are always parallel to the fibers and slightly deviated from the loading direction for unidirectional specimens, as shown in Figure 5.12. This indicates the fibers in unidirectional specimens could not arrest the crack growth. Hence, the TTH compressive strengths from the unidirectional specimens exhibit lower value and higher scatter. In the cross-ply specimens, however, the fibers in each ply are perpendicular to the fibers in its two surrounding plies. Consequently, the fracture surfaces of matrix defects, or the fracture surfaces of initial micro-cracks in one ply, are perpendicular to the fibers of the two surrounding plies, which therefore prevent these initial matrix cracks from quickly growing through the laminate thickness. The initial matrix cracks will thus grow in two possible directions; going forward through the neighboring plies or along the fiber directions. In the first case, the fibers shall be broken in order to allow the cracks going to the neighboring plies, thereby requiring high external load. In the second case, the directions of the initial matrix cracks have to be changed and propagate in a planar way parallel to the interfaces. When subjected to the TTH compressive loading, only the nominal TTH compressive stress component is of large magnitude at the interfaces, which do not contribute much to the planar failure parallel to the interfaces. The other stress components that play dominant role in the planar failure, such as $\tau_{xz}$ and $\tau_{yz}$, are indirectly generated due to the matrix defects through deformation compatibility. Consequently, the external load must be very high in order that these stress components are large enough to form the macro-cracks. Therefore, compared with unidirectional specimens, the cross-ply specimens are not sensitive to the matrix defects, and present higher TTH compressive strength and lower scatter. The previous explanations can be verified by observing the fracture surfaces of cross-ply specimens, which are displayed in Figure 5.14. The fracture surfaces of cross-ply specimens are

not flat; accompanied with crack jumping, a number of local planar cracks parallel to the interfaces are generated at different heights in the thickness directions. The crack jumping between local planar cracks is formed through some local TTH cracks, the fracture surfaces of which are roughly normal to the interfaces. Therefore, a lot of fiber breakage can be observed at the fracture surfaces of local TTH cracks, which is attributed to the highly concentrated stress in the fiber directions at the crack tips when the cracks are growing forward.

### 5.4.3 Statistical Analysis

The so-called scale effects; i.e., whether the four groups of TTH compressive strength values form unidirectional specimens with different sizes come from the same population at a given confidence, can be judged using the rank-sum test technique (Larson, 1982). In a physical sense, the rank-sums within the confidence limits indicate that the two sets of sample values are thoroughly intermixed, thereby being viewed as sample values of a single random variable.

The test procedures are described as follows; (1) combining group 1 and other three groups and sorting the sample values, (2) summing the ranks for the two groups of sample values in each combination, (3) comparing the ranks with the confidence limits calculated from Equations (5.3) and (5.4). In the following, given $\alpha = 0.05$, the rank-sum test is performed on the three combinations of TTH compressive strength valves. The sorted sample values, the rank-sums for the three combinations and the calculated confidence limits are tabulated in Table 5.4. The rank-sums are found to be within the confidence limits for combinations 1 and 2, but out of the confidence limit for combination 3. Hence, it can be concluded that TTH compressive strength values of groups 1, 2 and 3 represent the sample values coming from the same population at a 95% confidence level, and thus the TTH compressive strength values in the first three groups can be represented by one probability function. However, the TTH compressive strength values of group 4 can not be considered to come from the same population as that of group 1 at a 95% confidence level, thereby having a different probability function from that for the sample values of groups 1, 2 and 3.

**Table 5.4.** Rank-sum test results of the sample values from different groups.

| Order | Group 1 | Group 2 | Group 3 | Group 4 |
|---|---|---|---|---|
| *1* | 174.59 | 158.88 | 148.03 | 147.28 |
| *2* | 192.48 | 178.61 | 150.97 | 162.17 |
| *3* | 195.91 | 192.27 | 153.44 | 167.27 |
| *4* | 202.50 | 201.30 | 157.98 | 186.96 |
| *5* | 207.16 | 202.04 | 158.73 | 191.85 |
| *6* | | | 169.65 | |
| *7* | | | 169.95 | |
| *8* | | | 179.83 | |
| *9* | | | 182.79 | |
| *10* | | | 183.96 | |
| *11* | | | 188.91 | |
| *12* | | | 189.72 | |
| *13* | | | 190.92 | |
| *14* | | | 193.19 | |
| *15* | | | 193.85 | |
| *16* | | | 195.62 | |
| *17* | | | 195.72 | |
| *18* | | | 196.68 | |
| *19* | | | 197.00 | |
| *20* | | | 198.59 | |
| *21* | | | 198.95 | |
| *22* | | | 199.14 | |
| *23* | | | 199.70 | |
| *24* | | | 200.43 | |
| *25* | | | 201.83 | |
| *26* | | | 201.87 | |
| *27* | | | 207.34 | |
| *28* | | | 209.79 | |
| *29* | | | 211.40 | |
| *30* | | | 211.65 | |
| *31* | | | 213.87 | |
| *32* | | | 215.42 | |
| Combination Gr 1 & Gr 2 | $W_1 = 32$, $W_2 = 23$; $t_{0.025} = 17.6$, $t_{0.975} = 37.4$; Therefore $t_{0.025} < W_2 < t_{0.975}$ | | | |
| Combination Gr 1 & Gr 3 | $W_1 = 104$, $W_3 = 599$; $t_{0.025} = 563.4$, $t_{0.975} = 652.6$; Therefore $t_{0.025} < W_3 < t_{0.975}$ | | | |
| Combination Gr 1 & Gr 4 | $W_1 = 38$, $W_4 = 17$; $t_{0.025} = 17.6$, $t_{0.975} = 37.4$; Therefore $W_4$ is out of range $[t_{0.025}, t_{0.975}]$ | | | |

Therefore, the TTH compressive strength values of groups 1, 2, and 3 are combined together and then their probability density function is estimated using the maximum entropy technique, and displayed in Figure 5.15. The mean value of the TTH compressive strength is 189.83 MPa and the coefficient of variation is 9.55% after the combination. The good-of-fit between the theoretical and sample probability distributions is evaluated by the Kolmogorov-Smirnov test technique. For the TTH compressive strength values, the Kolmogorov-Smirnov statistic Dn is found to be 0.097, which is smaller than the acceptance limit 0.209 with respect to n = 42. This indicates the TTH compressive sample values can be well fitted by the probability

distribution function generated by the maximum entropy technique. On the basis of the previous rank-sum test results, a conclusion can be made that the TTH compressive strength values from the unidirectional specimens present scale effects to some degree. However, the inherent scale effects do not seem to be apparent, because the strength values within groups 1, 2 and 3 seem to be independent of specimen sizes. Nevertheless, the investigation on size effects is not sufficient herein, because the ranges of specimen sizes tested are narrow. The size effects on the TTH compressive strength of laminated composites shall be investigated through testing a sufficiently wide range of specimen sizes.

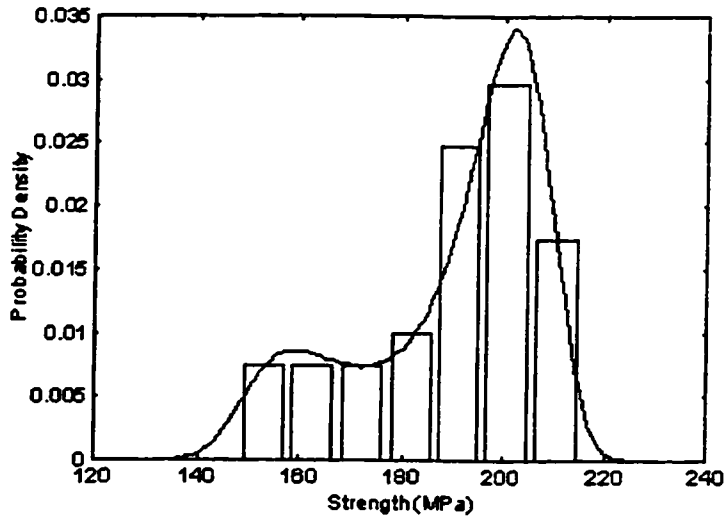


**Figure 5.15.** Probability density function for the interlaminar compressive strength Zc.

## 5.5 INTERLAMINAR SHEAR STRENGTHS

The multi-directional laminates composed of 24 plies are fabricated from the G40-800/5276-1 carbon/epoxy pre-impregnated tapes and cured in an autoclave. The quality of the manufactured laminates is examined by performing a C-Scan non-destructive examination. The half-thickness notches are cut using a diamond wheel blade with a higher grit order; the tolerance of notch depth is allowed within one ply thickness. Each cured laminate has a sufficiently large area from which at least 35 effective specimens can be cut using a diamond blade wheel. Especially, the Type II laminates have a little bit larger areas than the Type I laminates because of ineffective specimens that possibly appear in the testing. The edges of the specimens are ground using two types of sand papers with grit orders of 120 and 320 respectively to remove the

potential damage due to cutting. Each specimen inside a separate data set is numbered, which is essential for the calculation of joint moments in the stochastic modeling (see Chapter 6). The notch space and specimen width for each specimen are measured using a caliper and recorded. The specimens are then clipped into the clamp by applying a torque of 1 lbs. in. through a torque wrench, and mounted on the MTS testing machine. A compressive load is applied to the specimens by moving the steel platen upward at a constant speed of 1 mm/minute and terminated when the load suddenly drops down close to zero. During the loading process, the relative displacements and the corresponding loads are directly recorded from the MTS machine.

### 5.5.1 Fracture Mode

As expected, all Type I specimens are delaminated around the central planes. However, some Type II specimens initiate the delamination at the 0/90 or 0/(90-θ) interfaces rather than at the intended 90/(90-θ) interfaces around the central planes. These ineffective specimens are discarded and therefore more specimens are tested until the 35 effective specimens are obtained. Fortunately, only a limited number of ineffective specimens appear in testing the ILS strengths $S_{23}$ at the 0°- and 10°-interfaces, but few ineffective specimens appear with the other interfaces. The side views of the failed specimens are shown in Figure 5.16. It can be observed that the delamination cracks always cross the specimen gage section and pass the fillet regions. This observation confirms that the materials inside the fillets also make contributions to suspend the external loading, which is in agreement with the finite element results shown in Figure 4.21. Hence, the correction parameter δ in Equation (4.6) is essential to calculate the ILS strengths based on the measured ultimate loads. The load versus displacement curves for all the specimens, exhibit a linear response in the loading process, as typically shown in Figure 5.17 (the preloading procedure was not taken in the present experimental program, which results in the nonlinear potions of the curves at the initial stage of loading process). As soon as the applied loads for most of specimens reach the ultimate values, a sound is heard and then the loads quickly drop down close to zero. That means the delamination propagation is very quick once the initial delamination is formed.

a) $\theta = 20°$ b) $\theta = 60°$

**Figure 5.16.** Edge views of the failed II(θ) specimens.

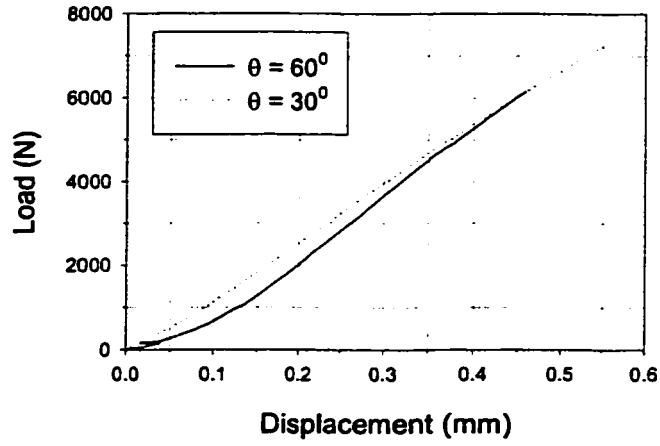


(a)

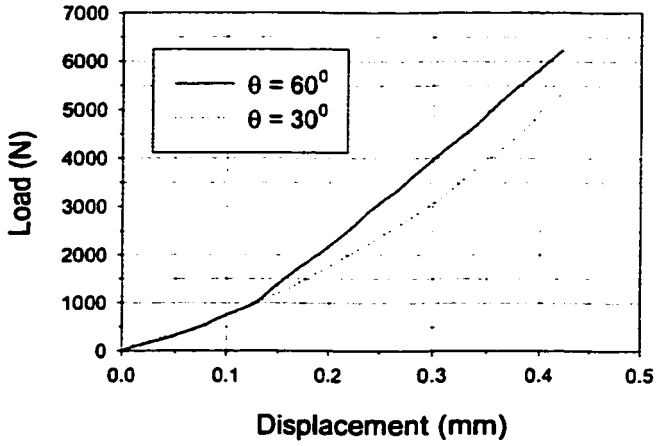


(b)

**Figure 5.17.** Load vs. displacement curves in the testing; (a) I(θ) specimens, and (b) II(θ) specimens.

In the double notch shear specimens, the initial delamination is formed at one of the notch bottoms and then propagates towards the other one. In other words, the cracks grossly propagate along the external loading direction. Therefore, the fiber orientations of the plies surrounding the interfaces play important role in determining fracture modes and ILS strengths.

If the surrounding plies are oriented away from the loading direction, e.g., for all Type II specimens, the interfaces are insensitive to the defects because transverse fibers can branch the planar cracks through crack jumping or fiber bridging. Consequently, the fracture surfaces exhibit rough morphologies and the corresponding ILS strengths have higher values and smaller scatter. In contrast, when the surrounding plies have fiber orientations close to the loading directions, such as Type I specimens with smaller values of θ, the cracks grow almost parallel to fibers that could not detour the growth of planar cracks. The corresponding specimens present smooth fracture surface morphologies, and the ILS strengths are involved with lower values and larger scatter. Hence, the effects of fiber orientations on the ILS strengths might be studied by observing the fracture surface morphologies of specimens.

#### 5.5.1.1 Type I Specimens ($S_{13}$)

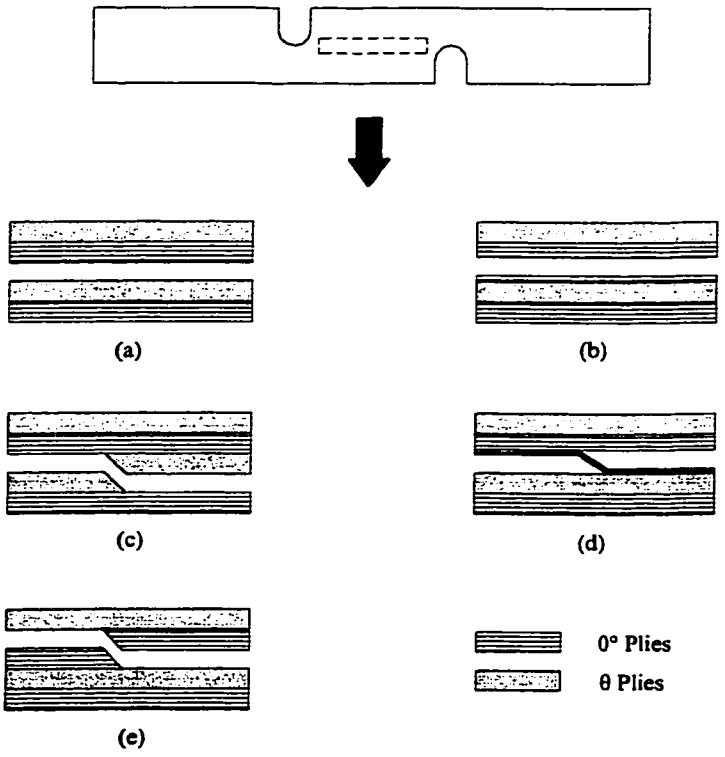


**Figure 5.18.** Schematic descriptions of five failure modes; (a) interface crack, (b) in-ply crack, (c) crack jumping, (d) fiber bridging, and (e) fiber breakage.

The post microscopic examinations discover that the fracture surfaces of specimens exhibit fairly complex morphologies. Five failure modes are observed with Type I specimens; interface crack, in-ply crack, crack jumping, fiber bridging and fiber breakage, which are

schematically shown in Figure 5.18. Even inside the specimens which yield the same experimental data set, different failure modes are also observed. The specimen numbers with respective failure modes are listed in Table 5.5.

**Table 5.5.** The numbers of specimens with each failure mode; ILS strengths $S_{13}$ at the θ-interfaces.

| θ | 0° | 10° | 20° | 30° | 40° | 50° | 60° | 70° | 80° | 90° |
|---|---|---|---|---|---|---|---|---|---|---|
| Interface crack | 7 | 15 | 27 | 22 | 21 | 20 | 19 | 29 | 12 | 16 |
| In-ply crack | 4 | 8 | 3 | 2 | | 3 | | | 23 | |
| Crack jumping | 24 | 12 | 5 | 3 | | 3 | | 4 | | 13 |
| Fiber bridging | | | | | | | 2 | 2 | | 6 |
| Fiber breakage | | | | 8 | 14 | 9 | 14 | | | |

**(1) Interface Crack**

The fracture surface morphologies of the θ-interfaces (θ = 30°, 50°, 70° and 90°) with respect to the failure mode of interface crack are demonstrated in Figure 5.19. This type of failure mode is expected because the cracks always grow along the interfaces, thereby providing the pure delamination failure. The fracture surfaces exhibit matted morphologies and distinct straight streaks along the 0° and θ directions can be observed by naked eyes. Except the specimens with 0°- and 10°-interfaces, large part of specimens with the other interfaces presents the failure mode of interface crack. In a few specimens, the interface crack occasionally deviates away from the interfaces and then enters into one of the adjacent plies. Figure 5.20 shows the corresponding fracture surface morphologies of the 20°- and 80°-interfaces, where the white areas represent the initiative interface cracks and the dark areas represent the deviated cracks (i.e., in-ply cracks) in the adjacent plies. The depth is very shallow that the cracks enter the adjacent plies and there are no transverse matrix cracks clearly observed along the transformation edges from the interface cracks to the in-ply cracks. In addition, the regions of in-ply cracks are usually not across the whole specimen gage sections. Because of these distinct features, the associated specimens are grouped into those with the failure mode of interface crack rather than those with the failure mode of crack jumping. Similar discovery was also reported by Robinson and Song (1992), and Russell and Street (1982), pertaining to the DCB specimens in the Mode I tests. The sites at which the interface cracks are initiated are found to have correlation with the notch depth to some extent. When a specimen has two overcut notches, the interface cracks are usually initiated at one notch's bottom and grow along one interface adjacent to the

central plane. However, the interface cracks are formed at the notch's bottoms and grow along the central planes, when one or two notches in a specimen are very closely cut to half the laminate thickness. In few specimens that have one undercut notch each, the initial interface cracks are generated at central planes, thereby being initiated a little bit over the overcut notch's bottom or at the more precisely cut notch's bottom. The fiber breakage is found at the sites close to the undercut notch's bottom, as shown in the right side of the picture in Figure 5.19(a). This is because the external compressive load is withstood only by less than one single ply when the interface cracks grow close to the undercut notch, therefore the extremely high stress state causes the fiber breakage. It should be clarified that the foregoing discussions on the formation of initial delamination are confined in the cases with notch depth tolerance less than one ply thickness. In Type I specimens, the interface cracks absorb more energy and thus yield higher ILS strengths, because the matted morphologies mesoscopically detour the planar crack propagation.

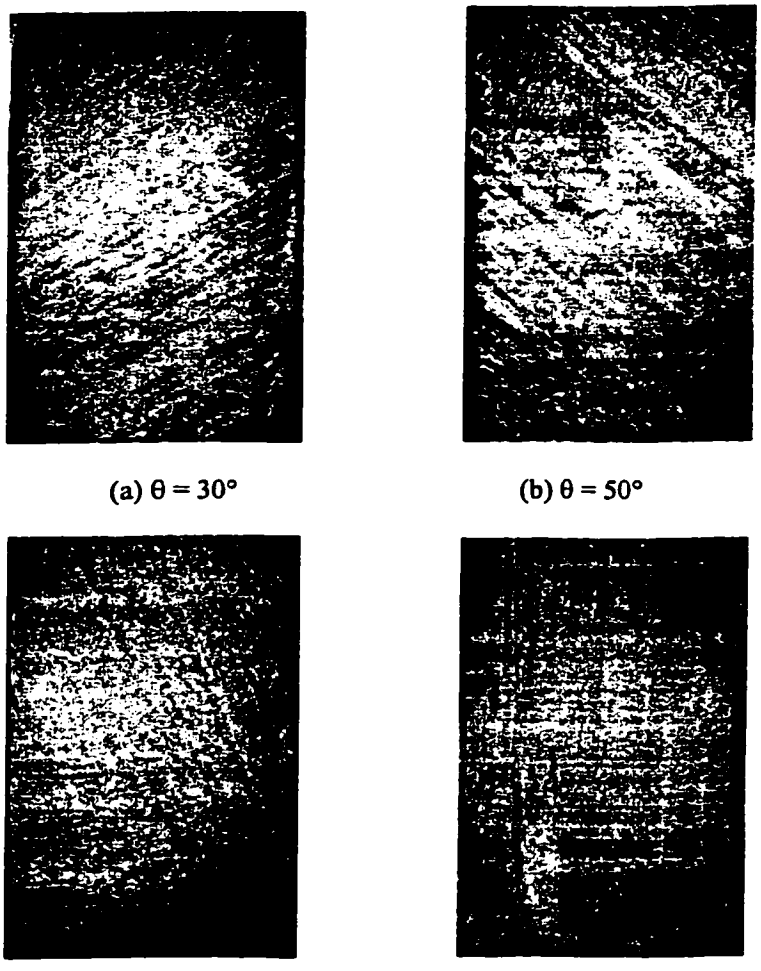

(a) $\theta = 30°$ (b) $\theta = 50°$

(c) $\theta = 70°$ (d) $\theta = 90°$

**Figure 5.19.** Fracture surface morphologies of I($\theta$) specimens; the failure mode of interface crack.

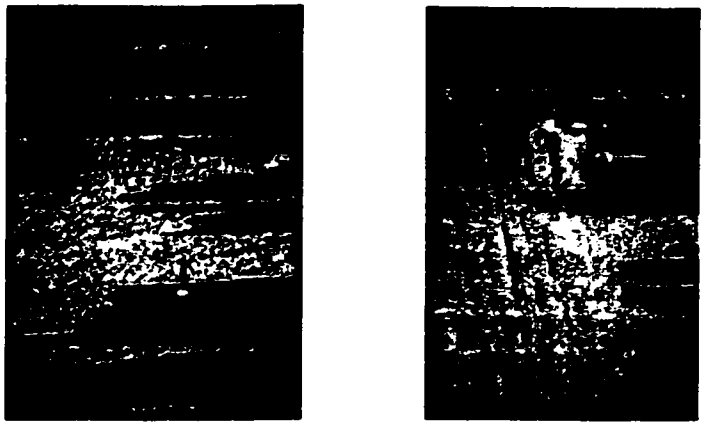

(a) $\theta = 10°$ (b) $\theta = 80°$

**Figure 5.20.** Fracture surface morphologies of I(θ) specimens; locally deviated interface crack.

### (2) In-Ply Crack

The failure mode of in-ply crack defines the cracks that propagate within one single ply almost parallel to the interfaces. Figure 5.21(a) and (b) presents the fracture surface morphologies with respect to this type of failure mode happening to the I(10) and I(80) specimens. The in-ply cracks are always found to be generated in the 0° plies, and mainly happen to the I(10) and I(80) specimens. It can be seen by naked eyes that the fracture surfaces exhibit glossary morphologies. However, the microscopic examinations reveal that the fracture surface morphologies are not smooth, but of fairly rugged and rough shape. In most cases, the in-ply cracks are formed at the locations very close to the interfaces so that narrow interface strips are still observed, as shown by the white line in Figure 5.21(a). The mechanism why the in-ply cracks are formed within the 0° plies is complex. The first reason that one may naturally think about is because the notch's bottoms are cut right inside the 0° plies. The microscopic examinations indeed show that some specimens with the failure mode of in-ply cracks have the notches bottomed inside the 0° plies, and the in-ply cracks are initiated at these notches' bottoms. However, if this argument were correct, how could one explain the fact that some specimens with similar notches exhibit the other types of failure modes? In fact, it is extremely difficult to cut the notch bottoms precisely at the central planes. In order to clarify whether the locations of notch's bottoms have influence on the failure modes, a statistical judgment based on the rank-sum test is performed on the experimental data set from the I(10) and II(80) specimens respectively. The mathematical procedures and results of the rank-sum test will be demonstrated in the next section. The results indicate that the sample values related to different failure modes

come from the same population in each experimental data set, thereby clarifying that the notch depth does not determine the failure modes and therefore does not have apparent influence on the measured ILS strengths. The failure mode of in-ply crack, in the author' opinion, is likely attributed to the residual shear stresses at the matrix-fiber interfaces generated during the curing cycle. This argument comes from the fact that on almost all the fracture surfaces of in-ply cracks in the 0° plies, a number of strips with different degrees of darkness are seen along the θ directions by naked eyes. These strips might represent the disturbance of fibers in the θ plies on the fibers in the 0° plies during the curing cycle, which would make the fibers in the 0° plies wavy. The wavy fibers would induce the residual shear stresses with higher magnitudes at the fiber-matrix interfaces when the composites cool down from the dwell temperature to the room temperature [Zhang and Yeh, 1998(b)]. Therefore, the residual shear stress in combination with the mechanical shear stress due to the external load at the fiber-matrix interface could generate the interface debonding, thereby forming the in-ply cracks rather than the desired interface cracks. The specimens with this type of failure mode presents lower ILS strengths because the in-ply cracks inside the 0° plies propagate exactly parallel to the fiber directions.

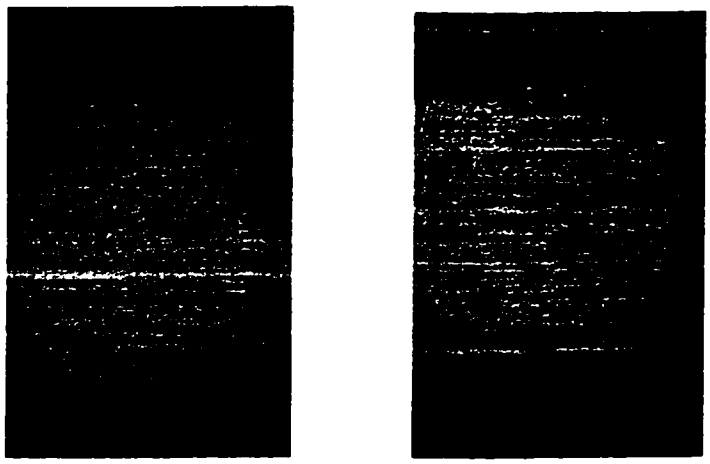

(a) θ = 20° (b) θ = 80°

**Figure 5.21.** Fracture surface morphologies of I(θ) specimens; the failure mode of in-ply crack.

### (3) Crack Jumping

Crack jumping is an important failure mode due to the interlaminar stress state, and usually observed in delamination failure (Chou *et al.*, 1995, Tao and Sun, 1998). Formed through matrix cracks parallel to the fiber directions, and always accompanied by the failure mode of

interface crack or in-ply crack, crack jumping can not uniquely exist. This type of failure mode mainly happens to the specimens with the θ-interfaces (θ = 0°, 10°, 20° and 90°) in the present experimental program. However, the mechanisms behind crack jumping are different at the 0°-, 10°-, and 20°-interfaces and the 90°-interfaces. In the former cases, the matrix cracks are almost parallel to the loading directions, therefore the crack jumping does not roughen the fracture surfaces and not increase ILS strengths. In the latter cases, the matrix cracks are perpendicular to the loading directions, therefore the crack jumping increase the ILS strengths through tearing-out the fibers. The corresponding fracture surface morphologies are shown in Figure 5.22; (a) transverse matrix cracks across a number of 0° plies and partially two 0° plies (i.e., from in-ply crack to in-ply crack), (b) transverse matrix cracks across the 0° and partially 10° plies (i.e., from interface crack to in-ply crack), (c) transverse matrix cracks across the 0° and 20° plies (i.e., from interface crack to interface crack), and (d) transverse matrix cracks across the 90° ply (i.e., from interface crack to interface crack). The locations of matrix cracks are hereafter indicated by arrows in figures. In the I(0) specimens, the fracture surfaces with the failure mode of crack jumping present very rugged morphologies; most of the interface and in-ply cracks shift into the remote plies across a number of 0° plies. The crack jumping in the I(10) specimens is formed mostly through the matrix cracks in the 0° plies, and lesser in the 10° plies. Furthermore, in most cases, the interface cracks shift into their adjacent plies and then are transformed into in-ply cracks, that is, the matrix cracks do not go through one single ply. Unlike the failure mode of interface cracks with locally shallow deviation mentioned above, the regions of these in-ply cracks are across the whole specimen gage sections (i.e., from one notch to another notch) and there are matrix cracks clearly observed along the transformation edges between the interface cracks and the in-ply cracks. Considering these distinct features, the related specimens are grouped into those with the failure mode of crack jumping. In the I(20) specimens with the failure mode of crack jumping, the matrix cracks go through the 20° ply or both 0° and 20° plies [see Figure 5.22(c)]. All the cracks are initiated and propagate along the interfaces. The failure mode of cracking jumping only happens to four I(70) specimens, where two specimens have the crack jumping from interface to interface through the transverse matrix cracks across the 70° ply but the other two specimens have the crack jumping shifting from the interface into the 0° ply. The crack jumping in the I(90) specimens is formed by the transverse matrix cracks in one 90° ply accompanied by the interface cracks at two adjacent interfaces. Furthermore, fiber tearing-

out is generated at the matrix crack surfaces [see Figure 5.22(d)], which indicates why the crack jumping in I(90) specimens increases the ILS strengths. By examining the failure mode of crack jumping and the notch depth, no correlations are found between them.

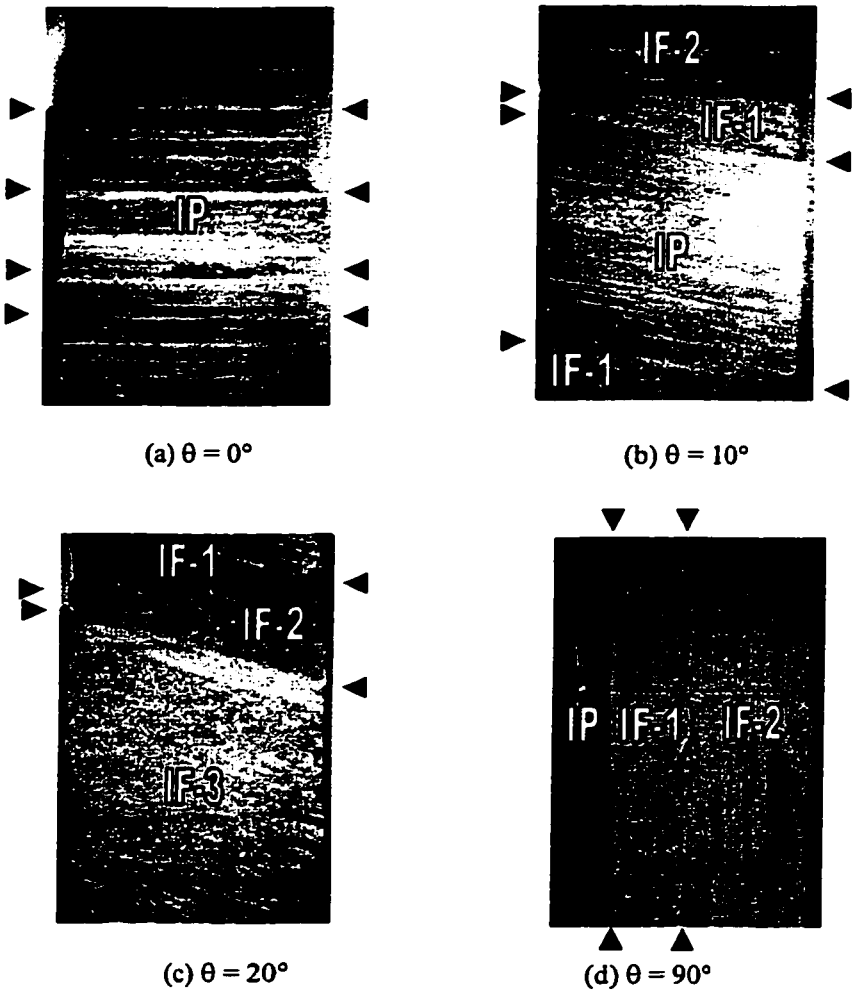


**Figure 5.22.** Fracture surface morphologies of I(θ) specimens; the failure mode of crack jumping (herein "IP" denotes in-ply cracks and "IF" interface cracks, and the digital numbers indicate the interface cracks located different interfaces).

### (4) Fiber Bridging

The fiber bridging is also an important failure mode generated by the interlaminar stress state, and frequently observed in the delamination failure (Chou *et al.*, 1995). The fiber bridging between the adjacent fracture surfaces could increase the ILS strengths (Chou *et al.*, 1995) because the tearing-out of fibers from the matrix. Sometimes, the fiber breakage happens if the external load is suspended by the bridged fibers before the final failure, which is thus a mark of fiber bridging (Chou *et al.*, 1995). Therefore, there is no fiber breakage at the initiation of

delamination. As a matter of fact, the principal stress component along the fiber direction, which could result in the fiber breakage, is assumed not to affect the matrix failure of composite materials, thereby usually being neglected in the matrix failure criteria (Hashin, 1980). Figure 5.23 displays the fiber breakage found in the specimens with θ-interfaces (θ = 30°, 40°, 50° and 60°). It can be seen that the fiber breakage is accompanied by the crack jumping across one θ ply, and always occurs in the θ plies. The broken fiber edges are found to be neat and normal to the fiber directions. It is likely that the two partial transverse matrix cracks would generate fiber bridging by shifting the interface crack from interface to interface. Consequently, the external load is withdrawn only by the cross section of the singe ply within the two matrix cracks in a compressive way before final failure. The principal stress in the fiber direction is thus large enough to break the fibers. Hence, the ILS strengths $S_{13}$ are higher at the 30°-, 40°-, 50°- and 60°-interfaces as well as the 90°-interfaces, because a number of the associated specimens exhibit the failure mode of fiber bridging, or fiber breakage.

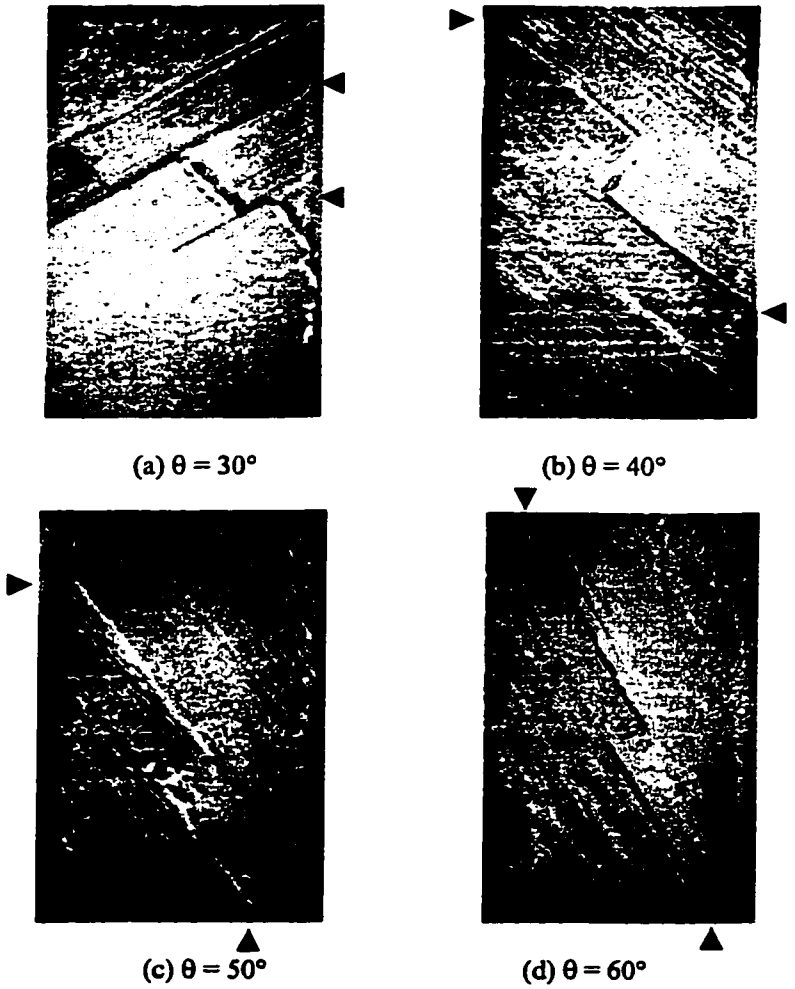


**Figure 5.23.** Fracture surface morphologies of I(θ) specimens; the failure mode of fiber breakage.

### 5.5.1.2 Type II Specimens ($S_{23}$)

Different from the failure modes involved in Type I specimens, there are only three failure modes with Type II specimens; i.e., interface crack, crack jumping and fiber bridging, as shown in Table 5.6. Also, the ILS strengths $S_{23}$ present smaller coefficients of variation. Except for the II(20) and II(80) specimens, the other specimens almost fail only in the failure modes of crack jumping or fiber bridging.

**Table 5.6.** The numbers of specimens with each failure mode; ILS strengths $S_{23}$ at the θ-interfaces.

| θ | 0° | 10° | 20° | 30° | 40° | 50° | 60° | 70° | 80° | 90° |
|---|---|---|---|---|---|---|---|---|---|---|
| Interface crack | | | 2 | | | 1 | | 13 | 16 | 16 |
| Crack jumping | 14 | 11 | 15 | 20 | 12 | 18 | 11 | 10 | 11 | 13 |
| Fiber bridging | 21 | 24 | 18 | 15 | 23 | 16 | 24 | 12 | 8 | 6 |

**(1) Interface Crack**

The fracture surface morphologies of the 20°- and 80°-interfaces with respect to the failure mode of interface crack are displayed in Figure 5.24. The straight streaks along the 90° and (90° – θ) directions are also apparent, which are thus symbols of the adjacent 90° and (90° – θ) plies. It might be concluded that the interface cracks be possible, provided that at least one of the two plies surrounding the interface has the fiber orientation close to the loading direction. Within II(70), II(80) and II(90) specimens, the 20°, 10° and 0° plies take the responsibility to yield the interface cracks (the loading direction is 0°). Similarly, it is because of the 0° plies that so many Type I specimens fail in the failure mode of interface crack.

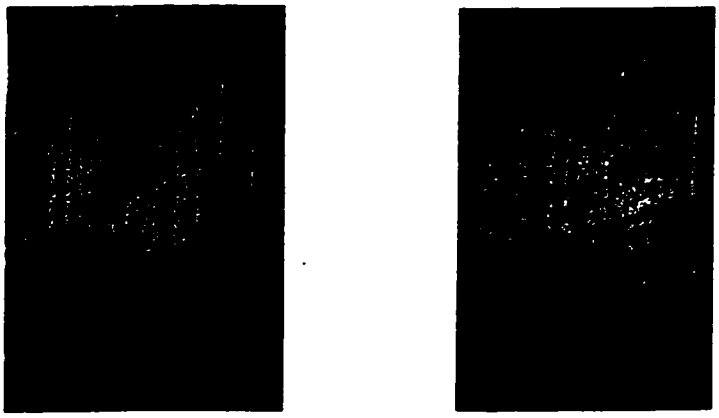

(a) θ = 20° (b) θ = 70°

**Figure 5.24.** Fracture surface morphologies of II(θ) specimens; the failure mode of interface crack.

**(2) Crack Jumping**

Figure 5.25 demonstrates the fracture surface morphologies for eight types of interfaces with respect to the crack jumping; the white areas represent the interface cracks and the dark areas represent the in-ply cracks from (c) to (g). Similarly, in some specimens the interface cracks are deviated into one of the adjacent plies and thus transformed into the in-ply cracks. Because the regions of the in-ply cracks are across the whole specimen gage sections, these specimens are grouped into those with the failure mode of crack jumping. In the II(0), II(10) and II(20) specimens, the crack jumping usually takes place through the transverse matrix cracks which grow across a number of plies [i.e., both the 90° and (90° – θ) plies], as shown in Figure 5.25(a) and (b). The failure mode of crack jumping in most of II(30) and II(50) specimens is formed with the interface cracks deviated into the adjacent (90° – θ) plies, while in few specimens, with the interface cracks deviated into the adjacent 90° plies or with the transverse matrix cracks going through the 90° plies. The fracture surfaces of the II(40) and II(60) specimens with respect to the failure mode of cracking jumping present simple morphologies, i.e., the initial interface cracks shift into the adjacent (90° – θ) plies. The crack jumping happens to the II(70) specimens either through the transverse matrix cracks across the 70° plies or through the deviation of interface cracks into the 70° plies. The transverse matrix cracks in one single 90° ply make the crack jumping from interface to interface in the II(10) specimens. Therefore, the failure mode of crack jumping in Type II specimens involves at least one interface; growing from interface cracks to interface cracks accompanied with the transverse matrix cracks across the adjacent plies or deviation form interface cracks to in-ply cracks.

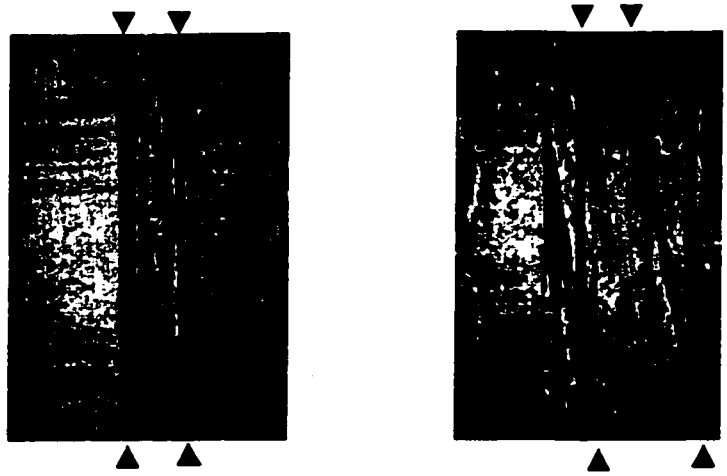

(a) θ = 0° (b) θ = 10°

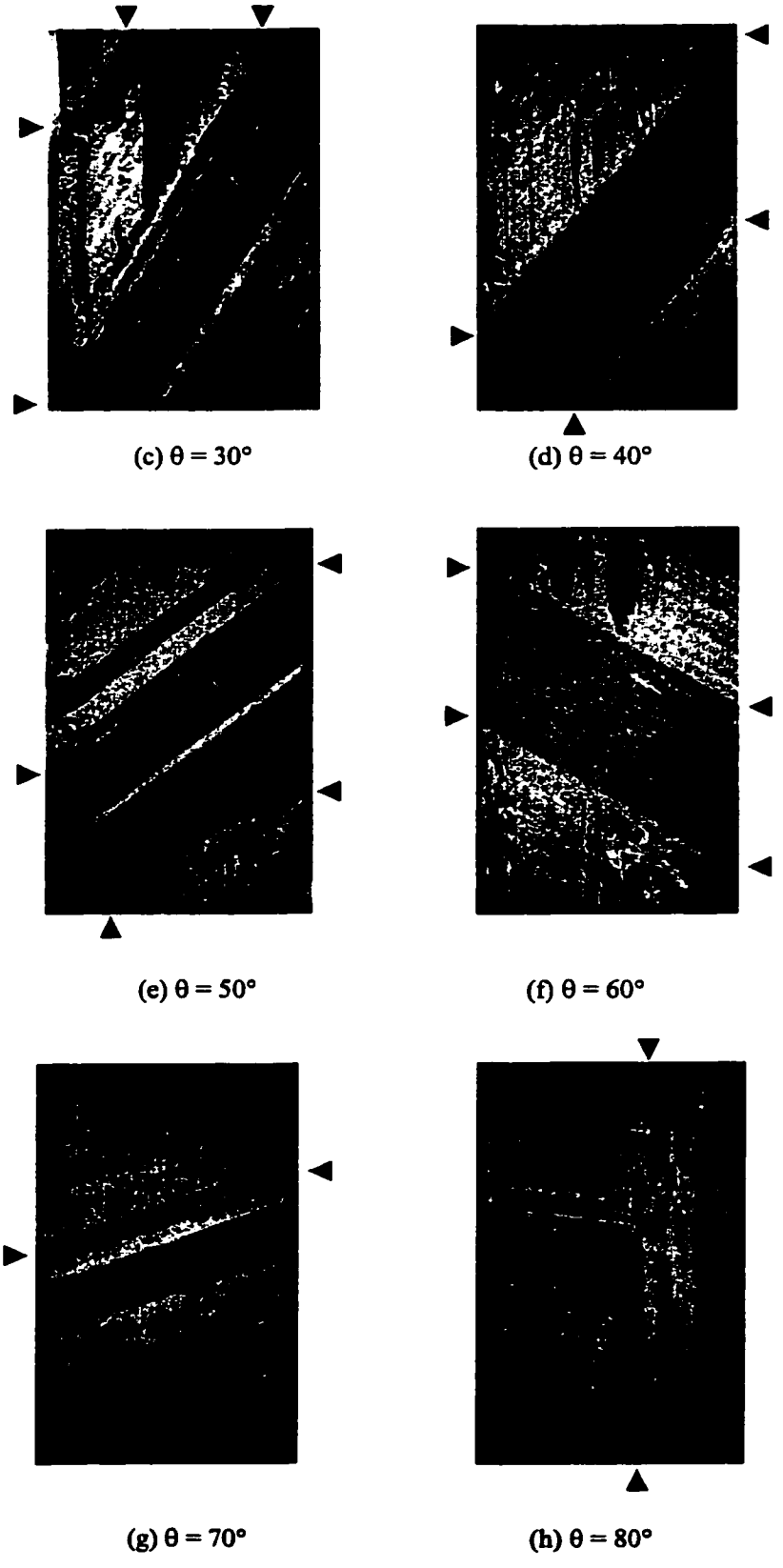

(c) θ = 30° (d) θ = 40°

(e) θ = 50° (f) θ = 60°

(g) θ = 70° (h) θ = 80°

**Figure 5.25.** Fracture surface morphologies of II(θ) specimens; the failure mode of crack jumping.

**(3) Fiber Bridging**

Large number of specimens with each specified interface presents the failure mode of fiber bridging. This could be attributed to the contribution of 90° plies in the specimens. Because the 90° plies give an obstacle to delamination propagation as mentioned above, the fiber bridging is apt to occur and thus increase the ILS strengths $S_{23}$. Furthermore, the fiber bridging usually accompanied with the crack jumping would make delamination tend to propagate around the 90° plies, therefore promoting the delamination growth along two separate interfaces (Chou *et al.*, 1995). In Figure 20, shown are the 90° fibers bridging cross the adjacent fracture surfaces in the II(40) and II(60) specimens.

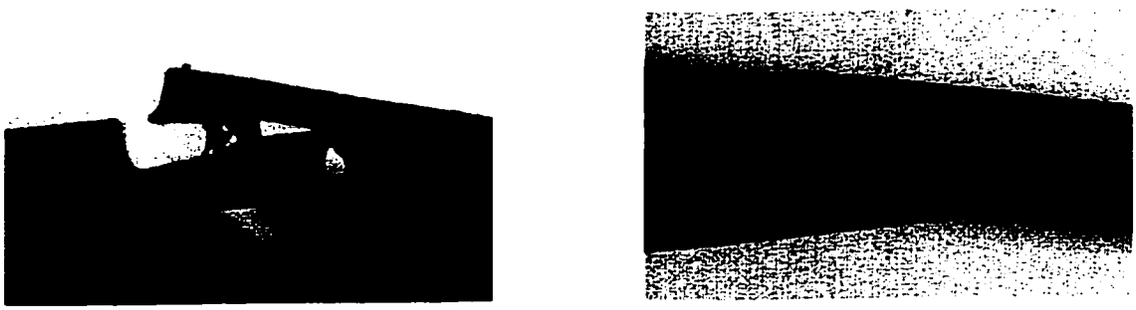

(a) $\theta = 40°$ (b) $\theta = 60°$

**Figure 5.26.** Edge views of II(θ) specimens; the failure mode of fiber bridging.

### 5.5.2 Statistical Analysis

In the present experimental program, 20 experimental date sets are obtained in each case by a sample with 35 specimens, which could be large enough to demonstrate the probabilistic characteristics involved in the ILS strengths. By performing the statistical analysis, the probabilistic characteristics of ILS strengths at the 10 specified θ-interfaces are given as follows.

#### 5.5.2.1 Means and Variances

The mean values and coefficients of variation for the ILS strengths $S_{13}$ at the 10 specified θ-interfaces are tabulated in Table 5.7. Also, the mean values and standard deviations, represented by the bars and error bars, are shown in Figure 5.27. It is apparent that both the mean values and coefficients of variation depend on the FOD angle θ. The ILS strengths $S_{13}$ reach the maximum around $\theta = 60°$ and the minimum around $\theta = 80°$; the maximum value is 69.3% larger

than the minimum value. Within the range from $\theta = 0°$ to $\theta = 60°$, the ILS strengths $S_{13}$ increase with the increment of $\theta$; the value at $\theta = 60°$ is 26.9% higher than that at $\theta = 0°$. The coefficients of variation are found to be larger except for at $\theta = 60°$ and 90°, compared with the typical scatter of no more than 10-15% for the in-plane strengths of advanced composite materials (Hiel *et al.*, 1991).

**Table 5.7.** The mean values and coefficients of variation for the strength components $S_{13}$ at the $\theta$-interfaces.

| $\theta$ | 0° | 10° | 20° | 30° | 40° | 50° | 60° | 70° | 80° | 90° |
|---|---|---|---|---|---|---|---|---|---|---|
| Mean Value (MPa) | 44.75 | 48.25 | 52.63 | 55.48 | 60.51 | 60.53 | 61.20 | 51.09 | 36.16 | 58.63 |
| Coefficient of Variation (%) | 20.73 | 18.49 | 19.11 | 16.96 | 14.44 | 14.11 | 9.13 | 19.40 | 17.19 | 9.03 |

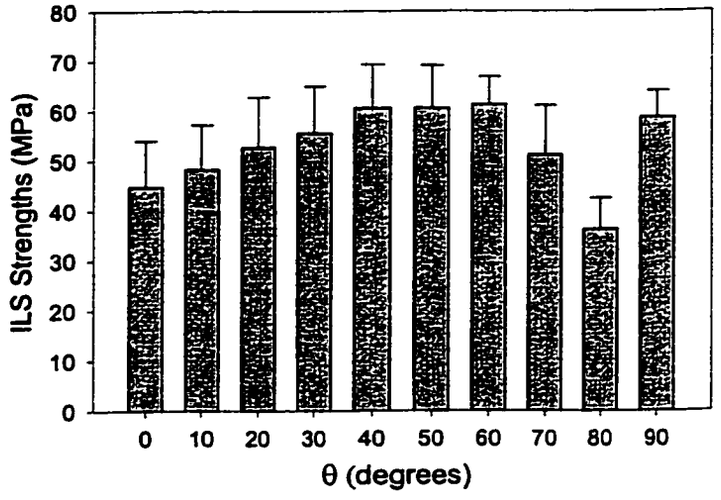


**Figure 5.27.** Experimental results of the ILS strengths $S_{13}$ at the 10 specified $\theta$-interfaces.

The mean values, coefficients of variation, and standard deviations for the measured ILS strengths $S_{23}$ at the 10 specified $\theta$-interfaces are shown in Table 5.8 and Figure 5.28 respectively. Compared with the ILS strengths $S_{13}$, the $\theta$-dependence of these probabilistic parameters for the ILS strengths $S_{23}$ is not so strong. The ILS strengths $S_{23}$ reach the maximum around $\theta = 40°$ and the minimum around $\theta = 70°$; the maximum value is 30.7% larger than the minimum value. The coefficients of variation for the ILS strengths $S_{23}$ are found to be smaller, and their mean values are higher than those for the ILS strengths $S_{13}$ except for at $\theta = 60°$. As mentioned earlier, the 90° plies form an obstacle against the delamination growth, thus increasing the ILS strengths $S_{23}$ and decreasing the coefficients of variation.

**Table 5.8.** The mean values and coefficients of variation for the strength components $S_{23}$ at the θ-interfaces.

| θ | 0° | 10° | 20° | 30° | 40° | 50° | 60° | 70° | 80° | 90° |
|---|---|---|---|---|---|---|---|---|---|---|
| Mean Value (MPa) | 61.68 | 62.00 | 63.14 | 67.53 | 69.11 | 64.72 | 58.70 | 52.87 | 57.03 | 58.63 |
| Coefficient of Variation (%) | 9.76 | 10.66 | 7.87 | 6.80 | 6.01 | 8.38 | 7.96 | 14.14 | 8.86 | 9.03 |

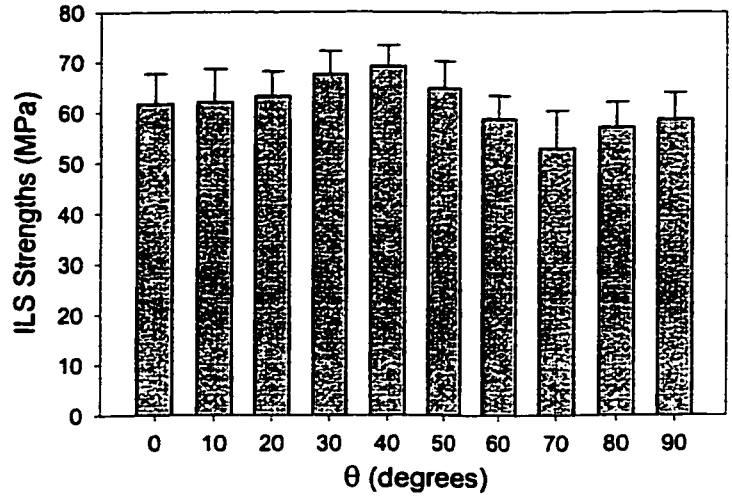


**Figure 5.28.** Experimental results of the ILS strengths $S_{23}$ at the 10 specified θ-interfaces.

For both ILS strength components, the variation tendency with respect to θ demonstrated by their mean values can also be observed in Figures 5.27 and 5.28 even though the standard deviations are included. Therefore, in spite of the fact that the experimental results present quite large scatter, the θ-dependence of ILS strengths is not masked because the larger samples with 35 specimens are used in the present experimental program. It is an interesting observation that the mean values even including the associated standard deviations for the two ILS strength components have a similar variation tendency.

It is important to notice that the two ILS strength components $S_{13}$ and $S_{23}$ exhibit different magnitudes at each θ-interface. This indicates that the ILS strengths at a given interface also have the physical characteristic of directional dependence. Or in other words, like the in-plane and normal (tensile and compressive) strengths, the ILS strength components present different values when considered in different coordinate systems. Form this point of view, it must be careful to properly select the coordinate system for predicting delamination failure of laminated composites using the stress-based criteria. Perhaps, there are two approaches towards

the delamination evaluation; one using the failure criteria only in terms of the principal strengths likewise Azzi-Tsai, or Hoffman empirical criteria (Azzi and Tsai, 1965, Hoffman, 1967); and the other using the failure criteria with the capability of strength tensor transformation likewise Tsai-Wu criterion (Tsai and Wu, 1971). With principal directions of interfaces fixed, the ILS strength components along the principal directions should be experimentally measured and then the mathematical operations would be performed in the principal coordinate system. Otherwise, with the couple of ILS strength components at an arbitrary direction experimentally obtained, the mathematical operation could be performed in any coordinate system based on strength tensor transformation relationships. The second approach is obviously advantageous, because one can find the optimum directions to measure the ILS strength components, as done in the present experimental program.

#### 5.5.2.2 Rank-Sum Test

From the preceding discussions, it can be seen that the ILS strengths present larger scatter, especially for Type I specimens, and even the specimens yielding the same experimental data set demonstrate different failure modes. Therefore, some interesting questions come out: (1) Are there any direct relationships between larger variations of ILS strengths and multiple failure modes? (2) Can the sample values in each data set be considered to come from the same population (i.e., with a same probability distribution)? These questions should be clarified, before performing further statistical analyses on the experimental data sets, such as the determination of probability density functions.

Using the rank-sum test technique, one can make a judgement on whether the ILS strength values in each data set with different failure modes come from the same population. The test procedures are described as follows; (1) separating the 35 specimens in each data set into groups corresponding to each different failure mode, (2) combining every two groups and sorting the strength values, (3) summing the ranks for the two groups of ILS strength values respectively, (4) comparing the ranks with the confidence limits calculated from Equations (5.3) and (5.4). In the following, given $\alpha = 0.05$, the rank-sum test is typically performed on the experimental data sets $S_{13}$ at 10°-, 40°- and 80°-interfaces because of their larger scatter.

**Table 5.9.** Rank-sum test for sample values of $S_{13}$ at the 10°-interface.

| Order | Group 1 | Group 2 | Group 3 |
|---|---|---|---|
| *1* | 42.69 | 32.83 | 29.50 |
| *2* | 45.00 | 35.80 | 37.41 |
| *3* | 46.47 | 36.89 | 41.00 |
| *4* | 46.52 | 40.15 | 46.78 |
| *5* | 46.77 | 40.21 | 47.42 |
| *6* | 47.14 | 40.35 | 49.15 |
| *7* | 47.58 | 41.77 | 53.70 |
| *8* | 47.83 | 53.73 | 54.36 |
| *9* | 51.34 | 55.52 | |
| *10* | 52.71 | 61.12 | |
| *11* | 53.09 | 64.08 | |
| *12* | 55.89 | 65.75 | |
| *13* | 56.23 | | |
| *14* | 59.64 | | |
| *15* | 62.17 | | |
| Mean Values | 50.75 | 47.35 | 44.91 |
| Combination of Gr.1 & Gr. 2 | $W_1 = 234$, $W_2 = 144$, $t_{0.025} = 127$, $t_{0.975} = 208$ Therefore $t_{0.025} < W_2 < t_{0.975}$ | | |
| Combination of Gr. 1 & Gr. 3 | $W_1 = 199$, $W_3 = 77$, $t_{0.025} = 65$, $t_{0.975} = 127$ Therefore $t_{0.025} < W_3 < t_{0.975}$ | | |

Group 1 – interface crack
Group 2 – crack jumping
Group 3 – in-ply crack

**Table 5.10.** Rank-sum test for sample values of $S_{13}$ at the 40°-interface.

| Order | Group 1 | Group 2 | Order | Group 1 | Group 2 |
|---|---|---|---|---|---|
| *1* | 45.10 | 48.81 | *12* | 61.19 | 70.87 |
| *2* | 46.18 | 53.12 | *13* | 62.61 | 73.82 |
| *3* | 46.37 | 54.22 | *14* | 63.10 | 74.62 |
| *4* | 49.41 | 57.00 | *15* | 65.08 | |
| *5* | 50.20 | 57.26 | *16* | 65.56 | |
| *6* | 51.22 | 57.59 | *17* | 67.20 | |
| *7* | 54.40 | 59.90 | *18* | 67.65 | |
| *8* | 56.22 | 63.84 | *19* | 72.23 | |
| *9* | 56.31 | 65.66 | *20* | 73.12 | |
| *10* | 56.59 | 67.23 | *21* | 74.17 | |
| *11* | 60.38 | 69.65 | | | |
| Mean Values | | | | 59.25 | 62.40 |
| Combination of Gr.1 and Gr. 2 | $W_1 = 346$, $W_2 = 284$, $t_{0.025} = 193$, $t_{0.975} = 311$ Therefore $t_{0.025} < W_2 < t_{0.975}$ | | | | |

Group 1 – interface crack
Group 2 – fiber breakage

The sorted strength values corresponding to each failure mode, the rank-sums for the combination of every two groups, and the calculated confidence limits are tabulated in Tables 5.9 to 11. All the rank-sums are found to be within the confidence limits. Therefore, it can be concluded that all the ILS strength values in each experimental data set represent the sample

values coming from the same population at a 95% confidence level, although the specimens present different failure modes. In a physical sense, the rank-sums within the confidence limits indicate that the ILS strength values from every two groups with different failure modes are thoroughly intermixed, thereby being viewed as sample values of a single random variable. The ILS strength values in each data set can be represented by one probability density function.

**Table 5.11.** Rank-sum test for sample values of $S_{13}$ at the 80°-interface.

| Order | Group 1 | Group 2 | Order | Croup 1 | Croup 2 |
|---|---|---|---|---|---|
| *1* | 22.61 | 29.08 | *13* | 37.19 | |
| *2* | 26.23 | 30.69 | *14* | 37.87 | |
| *3* | 29.37 | 31.59 | *15* | 37.89 | |
| *4* | 30.17 | 34.81 | *16* | 37.99 | |
| *5* | 30.74 | 36.34 | *17* | 38.56 | |
| *6* | 31.03 | 37.36 | *18* | 40.81 | |
| *7* | 31.03 | 38.16 | *19* | 41.74 | |
| *8* | 32.41 | 38.39 | *20* | 42.15 | |
| *9* | 32.51 | 39.25 | *21* | 42.82 | |
| *10* | 32.92 | 42.28 | *22* | 43.14 | |
| *11* | 32.97 | 53.15 | *23* | 44.06 | |
| *12* | 33.48 | | *24* | 45.74 | |
| Mean Values | | | | 35.64 | 37.37 |
| Combination of Gr. 1 and Gr. 2 | $W_1$ =420, $W_2$ = 210, $t_{0.025}$ = 143, $t_{0.975}$ = 253 Therefore $t_{0.025} < W_2 < t_{0.975}$ | | | | |

Group 1 – in-ply crack
Group 2 – interface crack

Moreover, the means of sample values for each group are also presented in Tables 5.9 to 5.11. For the ILS strength $S_{13}$ at the 10-interface, the mean value from the first group is found to be higher than that from the second and third groups. As mentioned previously, the failure mode of interface crack present the matted surface morphologies and absorbs more energy than the failure modes of crack jumping and in-ply crack in Type I specimens with smaller values of θ, therefore the specimens with interface cracks present higher ILS strength values. Likewise, higher mean value is obtained from the group with interface cracks than the group with in-ply cracks at the 80°-interface. For the ILS strength $S_{13}$ at the 40°-interface, the mean of the sample values with the failure mode of fiber breakage is higher than that with the failure mode of interface crack, because fiber breakage (i.e., the symbol of fiber bridging) absorbs more energy (Chou *et al.*, 1995). Although different failure modes at a specified θ-interface present different ILS strength values, the sample values can still be considered to come from the same random variable, as shown by the rank-sum test. The sample values within different failure modes are

uniformly intermixed, therefore there are no direct relationships between considerable scatter of sample values and multiple failure modes of specimens.

### 5.5.2.3 Individual Probability Density Functions

The sample values in each experimental data set have been proved to come from the same population, therefore the ILS strength at any given θ-interface could be viewed as a random variable. Let S denotes the random variable at a given θ-interface and $s_1$, ..., $s_{35}$ denote the 35 sample values in the associated experimental data set. The probability density function of S can thus be estimated from the sample values $s_1$, ..., $s_{35}$. Herein the individual probability density functions (or distribution functions) for each data set are represented using a general distribution instead of standard distributions such as Gaussian or Weibull, because the histograms of the ILS strength values demonstrate that sometimes their random behaviors do not fit these standard distributions very well.

Figure 5.29 display the histograms and the individual probability density functions for the ILS strengths $S_{13}$ at the 10 specified θ-interfaces. Apparent differences are observed between the individual probability density functions at each of specified interfaces. The strengths $S_{13}$ at θ = 10° and 80° present the probability distributions that are close to the Gaussian distributions; most of the sample values in each date set are located in the middle of the data ranges. The ILS strength $S_{13}$ at θ = 0° might have a two-parameter Weibull distribution because the more experimental data are concentrated towards the lower bound. The individual probability density functions at θ = 40° and 60° have a hump shape in each case, which would be close to the uniform distributions. That is, the experimental data are rather uniformly distributed inside the data ranges. In the remaining data sets, the probability distributions of the ILS strengths have a tendency towards the higher bounds, which are also close to Weibull distributions. Especially, the ILS strength $S_{13}$ at θ = 70° has a rising-up tail near the lower bound, because a few of sample values are concentrated near the lower bound and discretely distributed away from the cluster of other sample values in the histogram. The Kolmogorov-Smirnov statistics Dn for the 10 experimental data sets are also tabulated in Table 5.12. The small magnitude of Dn indicates that the ILS strengths $S_{13}$ are well described by the probability distribution given in Equation (5.1).

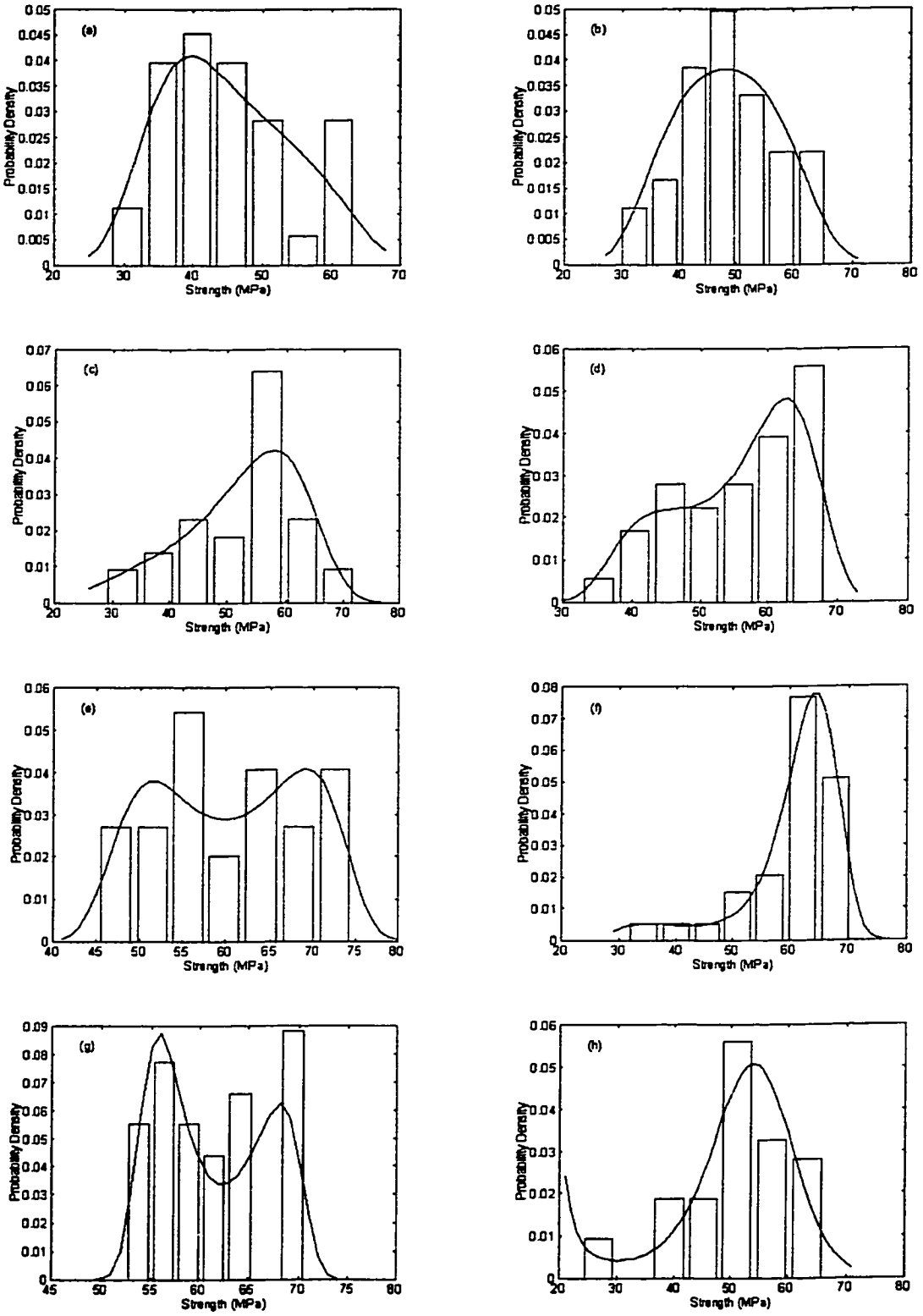


**Figure 5.29.** Histograms and individual probability density functions of the ILS Strengths $S_{13}$ at 10 specified θ-interfaces; (a) θ = 0°, (b) θ = 10°, (c) θ = 20°, (d) θ = 30°, (e) θ = 40°, (f) θ = 50° (g) θ =60°, (h) θ = 70°, (i) θ = 80° and (j) θ = 90°.

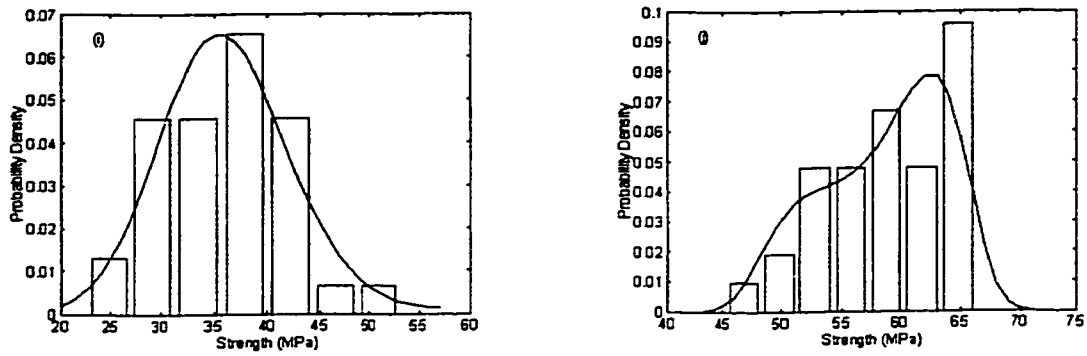


**Figure 5.29.** Histograms and individual probability density functions of the ILS Strengths $S_{13}$ at 10 specified θ-interfaces; (a) θ = 0°, (b) θ = 10°, (c) θ = 20°, (d) θ = 30°, (e) θ = 40°, (f) θ = 50° (g) θ =60°, (h) θ = 70°, (i) θ = 80° and (j) θ = 90° (*continued*).

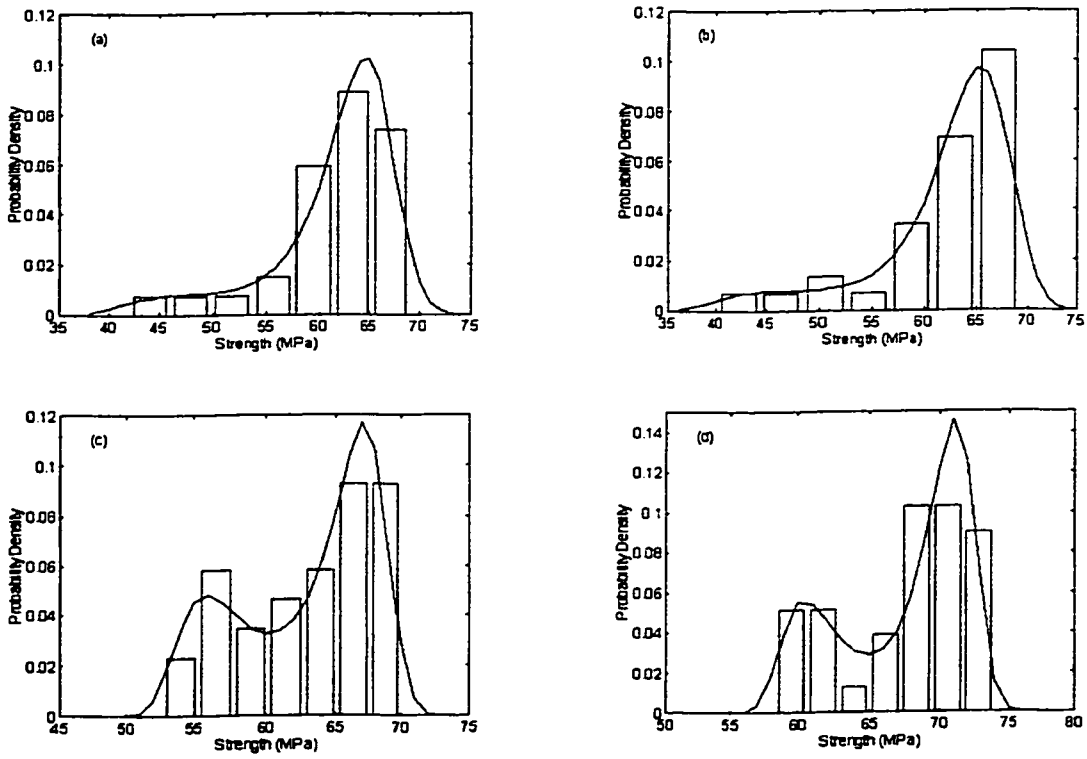


**Figure 5.30.** Histograms and individual probability density functions for the ILS Strengths $S_{23}$ at 10 specified θ-interfaces; (a) θ = 0°, (b) θ = 10°, (c) θ = 20°, (d) θ = 30°, (e) θ = 40°, (f) θ = 50° (g) θ =60°, (h) θ = 70°, (i) θ = 80°, and (j) θ = 90°.

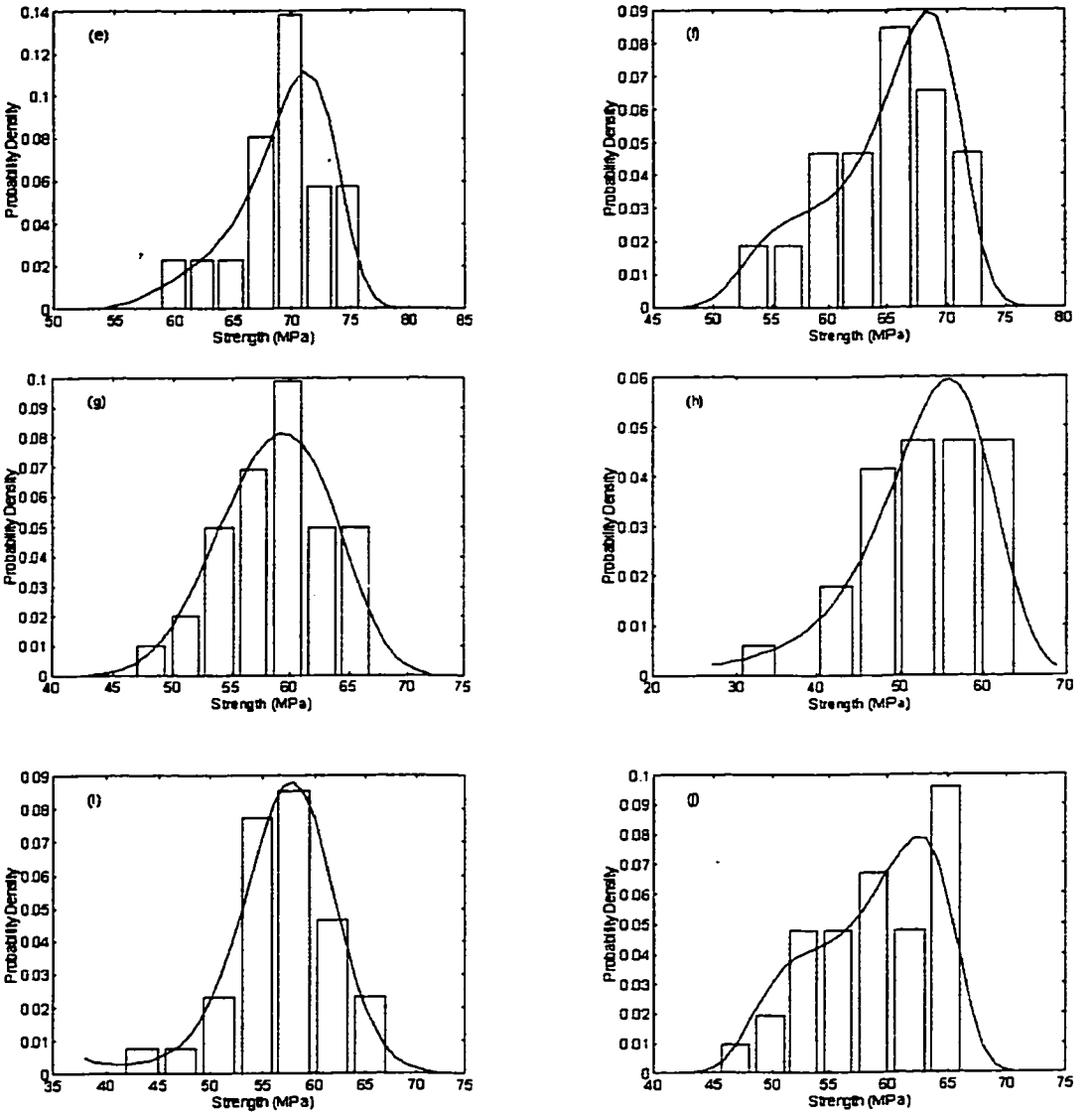


**Figure 5.30.** Histograms and individual probability density functions of the ILS Strengths $S_{23}$ at 10 specified θ-interfaces; (a) θ = 0°, (b) θ = 10°, (c) θ = 20°, (d) θ = 30°, (e) θ = 40°, (f) θ = 50° (g) θ =60°, (h) θ = 70°, (i) θ = 80°, and (j) θ = 90° (*continued*).

**Table 5.12.** The Kolmogorov-Smirnov statistics for ILS strengths $S_{13}$.

| θ | 0° | 10° | 20° | 30° | 40° | 50° | 60° | 70° | 80° | 90° |
|---|---|---|---|---|---|---|---|---|---|---|
| Dn | 0.0884 | 0.0863 | 0.0867 | 0.0590 | 0.0691 | 0.0682 | 0.0767 | 0.0976 | 0.0863 | 0.0681 |

Acceptance limit $1.36/\sqrt{n} = 0.229$ (here n = 35)

**Table 5.13.** The Kolmogorov-Smirnov statistics for ILS strengths $S_{23}$.

| θ | 0° | 10° | 20° | 30° | 40° | 50° | 60° | 70° | 80° | 90° |
|---|---|---|---|---|---|---|---|---|---|---|
| Dn | 0.0696 | 0.1215 | 0.0475 | 0.0842 | 0.1018 | 0.0701 | 0.0829 | 0.0689 | 0.0607 | 0.0681 |

Acceptance limit $1.36/\sqrt{n} = 0.229$ (here n = 35)

The histograms and the individual probability density functions for the ILS strengths $S_{23}$ at the 10 specified θ-interfaces are displayed in Figure 5.30. The apparent θ-dependence of the probability distribution forms can also be observed in these plots. The ILS strengths $S_{23}$ only at $\theta = 60°$ and 80° exhibit the probability distribution that are close to the Gaussian distributions. In all the remaining interfaces, however, the experimental data are tended towards their higher bounds and thus close to the Weibull distributions. The probability distributions are found to have similar forms for the paired ILS strengths $S_{23}$ at $\theta = 0°$ and 10°, at $\theta = 20°$ and 30° (hump shapes), and at $\theta = 40°$ and 50°. The results of Kolmogorov-Smirnov good-of-fit test given in Table 5.13 also show that the statistics Dn are smaller than the acceptance limit, and thus the probability distributions in Equation (5.1) describe the random ILS strength $S_{23}$ well.

## 5.6 SUMMARY

The TTH compressive test based on the end-loaded prism specimens has been demonstrated to be an effective test technique towards the TTH compressive strengths of laminated composites in the present experimental program. The experimental results show that the TTH compressive strengths of laminated composites strongly depend on the lay-ups; the value for cross-ply specimens is five times as much as that for unidirectional specimens. Also, the TTH compressive strengths present scale effects to some degree which is however under the Weibull scale law. Compared with the other matrix-dominated strengths, the TTH compressive strength demonstrates smaller scatter, and the inherent randomness can be well represented by the two-parameter Weibull probability functions.

The effects of fiber orientations on the ILS strengths in graphite/epoxy laminated composites are experimentally quantified through the double notch shear test. It appears to be quite difficult to obtain the pure delamination failure (i.e., interface crack) inside the whole specimen gage section in the test, which designate the planar cracks propagating along the interfaces between plies in laminated composites. Other failure modes, such as in-ply crack, crack jumping, fiber bridging and fiber breakage, always exist when performing the intended delamination test. However, the local interface cracks can be observed in most cases, although they are subsequently followed by other failure modes. It is found that the failure mode of fiber bridging makes apparent contributions to increasing the ILS strengths. The effects of fiber

orientations on the ILS strengths are apparent. The interfaces surrounded by differently-oriented plies present different ILS strengths not only in mean values but in the forms of probability distribution as well. Different fracture surface morphologies are also displayed with the interfaces when the FOD angle of the surrounding plies is changed. Since the ILS strengths depend on the FOD angles, new failure criteria are essential which are capable of taking into account the effects of FOD angles on delamination failure.

# CHAPTER 6

# STOCHASTIC MODELING OF INTERLAMINAR SHEAR STRENGTHS

This chapter presents the analytical investigation performed to study the probabilistic characteristics regarding effects of fiber orientations on the interlaminar shear (ILS) strengths in laminated composites. A stochastic simulation model is proposed, in which the probabilistic dependence of ILS strengths on the fiber orientation difference angles $\theta$ is simulated as a non-Gaussian nonstationary stochastic process within the bounded interval $[0, \pi/2]$. The random trigonometric polynomials with unknown correlated random parameters are employed to approximately represent this type of stochastic process. The correlated random parameters are then determined based on the probabilistic characteristics of the experimental sample data sets at 10 particular values of $\theta$ at which the experiments are performed. With the generated stochastic process, the individual probability density functions and the other probabilistic characteristics of the ILS strengths can be obtained at any particular values of $\theta$ at which experiments are not performed.

## 6.1 INTRODUCTION

Experimental results (see Chapter 5) clearly demonstrate that the interlaminar shear (ILS) strengths of fiber-reinforced laminated composites have two distinct characteristics; (1) the strength values present considerable scatter, and (2) the mean values and probability distributions apparently depend on the magnitude of the fiber orientation difference (FOD) angle $\theta$ between the two adjacent plies of the interface. These probabilistic characteristics need to be thoroughly investigated in order to have adequate information on the ILS strength components that is essential for the design of laminated composite structures on the basis of the reliability-based methodology. However, what one can obtain from the experiments is only the estimation of these probabilistic

characteristics at a limited number of discrete FOD angles, but not in the whole domain of the FOD angles (i.e., $0 \leq \theta \leq \pi/2$). Therefore, the analytical modeling becomes imperative in order to provide the adequate information involved in the θ-dependent ILS strengths. The stochastic simulation technique, in which each ILS strength component is simulated as a stochastic process with respect to θ in the whole domain, could be an efficient method to attempt this investigation. The purpose of the present chapter is to establish the stochastic simulation model in order to obtain the stochastic processes that can adequately represent all the probabilistic characteristics of the experimental sample data sets at the tested values of θ. Thus the probabilistic characteristics at the FOD angles at which the experiments are not performed could be estimated.

The simulation of stochastic fields in uncertain structural systems is an important branch in engineering mechanics and structural engineering, to which engineers and researchers have devoted enormous efforts in the last thirty years. So far, numerous digital simulation approaches have been well established towards some special types of stochastic processes with the aid of the so-called Monte Carlo techniques, such as spectral representation technique, time series representation technique, and white noise filter technique, just to name a few. In the spectral representation technique, the most remarkable contribution was made by Shinozuka (1970) to simulate the multivariate and multidimensional Gaussian stationary processes with specified cross-spectral density. The stochastic processes are simulated in terms of the sum of cosine functions with weighted amplitudes, random frequencies and random phase angles. This simulation technique has then been extended to the problem of Gaussian non-stationary stochastic processes in conjunction with the Priestley's evolutionary power spectra theory (Priestley, 1967) by Shinozuka and Jan (1972), Shinozuka (1974), and Deodatis and Shinozuka (1989). In the time series representation technique, the stochastic processes are simulated by the ARMA (auto-regressive moving-average) time series; the stationary ones with time-independent coefficients (Deodatis and Shinozuka, 1988, Hoshiya *et al.*, 1984) and the nonstationary ones with time-dependent parameters (Naganuma *et al.*, 1987, Samaras *et al.* 1985). These coefficients are determined from the prescribed autocorrelation functions. Because the time series theory usually deals with the response of a stochastic system to independent Gaussian white noise input, this simulation technique is only restricted to the Gaussian stochastic processes. The white noise filter technique simulates the stochastic processes through the output which is generated by filtering the white noise (Amin and Ang, 1968, Ruiz and Penzien, 1971).

Compared with the spectral and time series representation techniques, this simulation technique is less effective and was mainly used two or three decades ago.

The literature search for stochastic simulation approaches leaves a feeling that the digital simulation of non-Gaussian nonstationary stochastic processes has so far been dealt with to a lesser extent, and therefore very few papers are available. Yamazaki and Shinozuka (1988) developed a simulation approach in which the Gaussian nonstationary stochastic processes are digitally generated using the technique presented by Shinozuka and Jan (1972) and Shinozuka (1974) and then mapped into the non-Gaussian nonstationary processes with the aid of an iterative procedure. Also, Ammon (1990) proposed a simulation method by which the Gaussian or non-Gaussian stationary stochastic processes with prescribed spectral densities and probability density functions can be generated. The theoretical background is related to combining a linear dynamic filter system under white noise to generate the Gaussian processes, and a static polynomial transform to adapt the non-Gaussian processes with prescribed probability distribution functions. In these two simulation techniques, the probability distribution functions for the non-Gaussina processes, however, are not allowed to change with respect to the spatial or time variables. The probabilistic θ-dependence of ILS strengths obtained from the double notch shear experimental program (see Chapter 5) presents a very general non-Gaussian nonstationary stochastic process; the individual probability distribution forms vary with respect to θ. Hence, it is impractical to employ the aforementioned simulation approaches to represent the stochastic process involving ILS strengths.

In addition, Hasofer (1982) and Grigoriu (1993) proposed an alternative stochastic simulation technique, namely random parametric approach, to simulate Gaussian stationary and non-stationary stochastic processes with prescribed autocovariance functions within the bounded intervals. Wherein, the target stochastic processes are simulated using the random trigonometric polynomials in terms of correlated random Gaussian coefficients. The autocovariance functions of the random trigonometric polynomials can thus be written in terms of the second-order joint moments of the random Gaussian coefficients, which are then determined by equating these coefficients to the Fourier expansion coefficients of the prescribed autocovariance functions of the target stochastic processes. Therefore, the high simulation degree of accuracy can be obtained provided that the order of the random trigonometric polynomials is sufficiently large.

This simulation technique, albeit with a limitation to the second-order stochastic processes in the work of Hasofer (1982) and Grigoriu (1993), is convenient and physically straightforward, if employed to represent the stochastic processes on the basis of the experimental sample data sets at limited number of discrete spatial or time variables.

The present investigation extends the random parametric approach (Hasofer, 1982, Grigoriu, 1993) to the case of the non-Gaussian nonstationary stochastic processes with very general stochastic characteristics, as those involved in the probabilistic θ-dependent ILS strengths. This attempt is implemented by utilizing the correlated non-Gaussian random parameters in the random trigonometric polynomials instead of the Gaussian ones. Therefore, higher than the second-order moments are necessary to represent the general probabilistic characteristics of the non-Gaussian random parameters, or in other words, those of the simulated stochastic processes. In the present stochastic simulation model, the moments up to the fourth-order are evaluated because the individual probability density functions based the maximum entropy technique make certain that such orders of moments are adequate to demonstrate the probabilistic characteristics involved in the θ-dependent ILS strengths (see Chapter 5).

## 6.2 METHODOLOGY OF THE APPROACH

The stochastic processes involving the probabilistic θ-dependence of the ILS strengths are simulated by the random trigonometric polynomials in terms of the correlated random parameters. Therefore, the analytical expressions for various orders of joint moments of the simulated stochastic process can be derived in terms of the joint moments of the random parameters. The random parameters and then their joint moments are determined by the experimental sample data sets at 10 discrete FOD angles at which experiments are performed. Hence, the simulated stochastic process can be obtained, which can satisfy all the probabilistic characteristics of the ILS strengths at the 10 tested FOD angles.

Besides the higher order joint moments, the lower and higher bounds of the stochastic processes involving the ILS strengths are essential to evaluate the individual probability density functions. It would not be physically acceptable to assume that random strength values are distributed within the infinite ranges, such as in the Gaussian or Weibull distributions, because

the ILS strengths experimentally obtained from composite specimens are neither infinite nor close to zero. In the present stochastic simulation model, an estimation approach is also developed based on the time series theory (Papoulis, 1984, Jenkins and Watts, 1968). That is, all the bound (lower or higher) data are assumed to form a single stationary time series with respect to θ, and thus the mean value and the autocorrelation function can be estimated following the Ergodic Theorem in the Mean and in the Correlation Function (Jenkins and Watts, 1968). The terminology "time series" is still employed in the present chapter due to the fact that many textbooks derive the involved theories in the domain of time variables, although the ILS strengths are probabilistically changed with respect to the FOD angles θ. The lower and higher bounds are determined at any values of θ by performing the stochastic interpolation on the basis of the estimated autocorrelation functions.

The individual probability density functions at any particular values of the FOD angles are of significant interest in the reliability-based structural design. In most of the probabilistic analyses, the probability distribution functions of the strengths are assumed to be one of the standard distribution forms, such as the Gaussian and Weibull distributions (i.e., second-order). Then the parameters in these standard distribution functions are obtained by the method of moments, the method of maximum likelihood and so on. In the present stochastic simulation model, however, the individual density functions of the random ILS strengths are of higher order and thus determined using the maximum entropy technique (Siddall 1983). The individual density functions are written in a general form as

$$f(s) = \exp[\lambda_0 + \sum_{i=1}^{4} \lambda_i s^i] \tag{6.1}$$

where the five parameters $\lambda_i$'s, are evaluated by the first four moments of the random variables and the corresponding bounds. It has already been shown that the individual density functions evaluated from the first four moments can accurately characterize the probability distributions of the random ILS strengths (see Chapter 5).

## 6.3 RANDOM TRIGONOMETRIC SERIES REPRESENTATION

Suppose that X(t) is a non-Gaussian nonstationary stochastic process within the interval [0, T], and the first four statistical moments, i.e., $E[X(t)] = \mu(t)$, $E[X^2(t)] = k(t, t)$, $E[X^3(t)] = k(t, t, t)$ and $E[X^4(t)] = k(t, t, t, t)$, are finite inside the interval. From this point of view, X(t) is a fourth-order stochastic process and its probabilistic characteristics up to the fourth-order are of concern. Then a simulated stochastic process X'(t) is defined in terms of the random trigonometric series,

$$X'(t) = \frac{A_0}{2} + \sum_{i=1}^{\infty} A_i \cos\omega_i t \tag{6.2}$$

where $\omega_i = i\pi/T$ and $A_i$'s are correlated random parameters which are relevant to the target stochastic process X(t) according to

$$A_i = \frac{2}{T}\int_0^T X(t)\cos\omega_i t dt \tag{6.3}$$

At the first glance, the simulated stochastic process looks like the Fourier cosine expansion of the target process inside [0, T]. However, Equation (6.3) presents a stochastic integration rather than a deterministic integration. The calculus involving the Fourier expansion has been well established only for the deterministic functions and thus can not be directly applied to the stochastic processes. The convergence and the other characteristics of the random trigonometric series defined in Equations (6.2) and (6.3) need to be proved using the calculus associated with the stochastic processes, such as limiting sums, derivatives and integrals, etc. (Soong, 1973).

At present the stochastic calculus available is the so-called mean square calculus, because it is developed only based on the moments up to the second-order (Soong, 1973). Following the work of Grigoriu (1993), it can be proved that in mean square sense: (1) The random parameters $A_i$'s, or the stochastic integration in Equation (6.3), exist; (2) The random trigonometric series converges to the target stochastic process, i.e., the mean square error between X(t) and X'(t) is

equal to zero. Furthermore, it can be proved that the joint moments up to the fourth-order of the random parameters $A_i$'s have the forms as

$$E[A_i] = \frac{2}{T}\int_0^T \mu(t)\cos\omega_i t\,dt \tag{6.4.a}$$

$$E[A_i A_j] = \left(\frac{2}{T}\right)^2 \int_0^T dt \int_0^T k(t,s)\cos\omega_i t\cos\omega_j s\,ds \tag{6.4.b}$$

$$E[A_i A_j A_k] = \left(\frac{2}{T}\right)^3 \int_0^T dt \int_0^T ds \int_0^T k(t,s,\tau)\cos\omega_i t\cos\omega_j s\cos\omega_k \tau\,d\tau \tag{6.4.c}$$

$$E[A_i A_j A_k A_l] = \left(\frac{2}{T}\right)^4 \int_0^T dt \int_0^T ds \int_0^T d\tau \int_0^T k(t,s,\tau,\sigma)\cos\omega_i t\cos\omega_j s\cos\omega_k \tau\cos\omega_l \sigma\,d\sigma \tag{6.4.d}$$

where k(t, s) = E[X(t)X(s)], k(t, s, τ) = E[X(t)X(s)X(τ)] and k(t, s, τ, σ) = E[X(t)X(s)X(τ)X(σ)] are the joint moments of the target stochastic process. And the joint moments of the random trigonometric series equal to the Fourier expansion of the target joint moments and thus converge to the joint moments of the target stochastic process.

**Proof.** The joint moments of $A_i$'s in Equation (6.4) can be directly derived from the definition in Equation (6.3). The joint moments of X(t) are deterministic functions, and thus can be expanded into the Fourier cosine series inside the interval [0, T] directly following the associated calculus (Sneddon, 1951), provided that they satisfy the Dirichlet's conditions. For the first-order moment (or mean value)

$$u(t) = \sum_{i=0}^{\infty} \lambda_i a_i \cos\omega_i t \tag{6.5.a}$$

where $\lambda_0 = 1/2$, $\lambda_i = 1$ for $i \geq 1$ and the Fourier coefficients are written as

$$a_i = \frac{2}{T}\int_0^T \mu(t)\cos\omega_i t\,dt \tag{6.5.b}$$

For the second-order joint moment (or autocorrelation function)

$$k(t,s) = \sum_{i=0}^{\infty}\sum_{j=0}^{\infty}\lambda_{ij}a_{ij}\cos\omega_i t\cos\omega_j s \tag{6.6.a}$$

in which $\lambda_{00} = 1/4$, $\lambda_{0i} = \lambda_{i0} = 1/2$ for $i \geq 1$, and $\lambda_{ij} = 1$ for $i \geq 1$ and $j \geq 1$. The second-order Fourier coefficients are defined as

$$a_{ij} = \left(\frac{2}{T}\right)^2 \int_0^T dt \int_0^T k(t,s)\cos\omega_i t\cos\omega_j s ds \tag{6.6.b}$$

For the third-order joint moment

$$k(t,s,\tau) = \sum_{i=0}^{\infty}\sum_{j=0}^{\infty}\sum_{k=0}^{\infty}\lambda_{ijk}a_{ijk}\cos\omega_i t\cos\omega_j s\cos\omega_k \tau \tag{6.7.a}$$

in which $\lambda_{000} = 1/8$, $\lambda_{i00} = \lambda_{0i0} = \lambda_{00i} = 1/4$ for $i \geq 1$, $\lambda_{0ij} = \lambda_{i0j} = \lambda_{ij0} = 1/2$ for $i, j \geq 1$, and $\lambda_{ijk} = 1$ for $i, j, k \geq 1$. The third-order Fourier coefficients are defined as

$$a_{kjk} = \left(\frac{2}{T}\right)^3 \int_0^T dt \int_0^T ds \int_0^T k(t,s,\tau)\cos\omega_i t\cos\omega_j s\cos\omega_k \tau d\tau \tag{6.7.b}$$

For the fourth-order joint moment

$$k(t,s,\tau,\sigma) = \sum_{i=0}^{\infty}\sum_{j=0}^{\infty}\sum_{k=0}^{\infty}\sum_{l=0}^{\infty}\lambda_{ijkl}a_{ijkl}\cos\omega_i t\cos\omega_j s\cos\omega_k \tau\cos\omega_l \sigma \tag{6.8.a}$$

where $\lambda_{0000} = 1/16$, $\lambda_{000i} = \lambda_{00i0} = \lambda_{0i00} = \lambda_{i000} = 1/8$ for $i \geq 1$, $\lambda_{00ij} = \lambda_{0i0j} = \lambda_{0ij0} = \lambda_{i00j} = \lambda_{i0j0} = \lambda_{ij00} = 1/4$ for $i, j \geq 1$, $\lambda_{0ijk} = \lambda_{i0jk} = \lambda_{ij0k} = \lambda_{ijk0} = 1/2$ for $i, j, k \geq 1$, and $\lambda_{ijkl} = 1$ for $i, j, k, l \geq 1$. The fourth-order Fourier coefficients are written as

$$a_{ijkl} = \left(\frac{2}{T}\right)^4 \int_0^T dt \int_0^T ds \int_0^T d\tau \int_0^T k(t,s,\tau,\sigma)\cos\omega_i t\cos\omega_j s\cos\omega_k \tau\cos\omega_l \sigma d\sigma \tag{6.8.b}$$

The joint moments of X'(t) can be directly derived from the definitions in Equations (6.2) and (6.3), and the moment definition of stochastic processes; i.e.,

$$u'(t) = \sum_{i=0}^{\infty} \lambda_i E[A_i] \cos\omega_i t \tag{6.9}$$

$$k'(t,s) = \sum_{i=0}^{\infty}\sum_{j=0}^{\infty} \lambda_{ij} E[A_i A_j] \cos\omega_i t \cos\omega_j s \tag{6.10}$$

$$k'(t,s,\tau) = \sum_{i=0}^{\infty}\sum_{j=0}^{\infty}\sum_{k=0}^{\infty} \lambda_{ijk} E[A_i A_j A_k] \cos\omega_i t \cos\omega_j s \cos\omega_k \tau \tag{6.11}$$

$$k'(t,s,\tau,\sigma) = \sum_{i=0}^{\infty}\sum_{j=0}^{\infty}\sum_{k=0}^{\infty}\sum_{l=0}^{\infty} \lambda_{ijkl} E[A_i A_j A_k A_l] \cos\omega_i t \cos\omega_j s \cos\omega_k \tau \cos\omega_l \sigma \tag{6.12}$$

Comparing the target joint moments in Equations (6.5) to (6.8) with the simulated joint moments in Equations (6.9) to (6.12) and considering the relationships specified in Equation (6.4), one can find that they are equal to each other. Consequently, it can be concluded that the joint moments of the random trigonometric series converge to those of the target stochastic process.

## 6.4 RANDOM PARAMETRIC SIMULATION ALGORITHM

In the above section, it has been proved that the simulated stochastic process X'(t) in terms of random trigonometric series exists and converges to the target stochastic process X(t) in mean square sense. Furthermore, the simulated joint moments are identical to the target joint moments. Therefore, one can truncate a finite number of terms in random trigonometric series to approximate the target stochastic process inside [0, T]; the accuracy would depend on the number of the truncated terms and the probabilistic characteristics of the target stochastic processes. The determination of the simulated stochastic process, in fact, is deduced to determine a number of the correlated random parameters $A_i$'s based on the probabilistic characteristics of X(t). For example, if the first four joint moments of X(t) are prescribed, then the terms as many as expected can be truncated and the joint moments of the corresponding random parameters $A_i$'s can be directly determined from Equation (6.4), such as in the work of Grigoriu (1993).

For the stochastic process $S(\theta)$ [hereafter $S(\theta)$ represents the two stochastic processes $S(\theta)_{13}$ and $S(\theta)_{23}$ corresponding to the two ILS strength components] involving the ILS strengths, however, all the available information is the experimental sample data sets $S(\theta_i)$ at 10 discrete FOD angles $\theta_i$. Or in other words, the target stochastic process is not known yet; either sample data or joint moments in the whole domain. The purpose of the developed stochastic simulation algorithm is thus to look for the simulated stochastic process, which can satisfy all the probabilistic characteristics up to the fourth order at the 10 tested FOD angles. That is, the simulated stochastic process can "pass through" the experimental sample data sets at 10 tested FOD angles. Based on the theoretical background in the above section, the simulated stochastic process in terms of random trigonometric series is known to exist, and converges to the target stochastic process if the number of experimental sample data sets is large enough. However, this would need a large number of specimens, and thus be impractical due to the high cost and unnecessary because the required accuracy can be available from an appropriate sampling interval. In the present experimental program, it could be adequate to demonstrate the probabilistic θ-dependence of the ILS strengths that the interval $[0, \pi/2]$ is divided into 9 uniform sampling intervals (i.e., $\Delta = \pi/18$). Suppose that the nonstationary stochastic process $S(\theta)$ can be approximately represented by a simulated stochastic process in terms of a $10^{th}$ order of Fourier cosine polynomial in Equation (6.2) within the interval $[0, \pi/2]$,

$$S'(\theta) = \frac{A_0}{2} + \sum_{i=1}^{9} A_i \cos(2i)\theta \tag{6.13}$$

where the order is determined by the number of discrete FOD angles at which experiments are performed. The unknown random parameters $A_i$'s need to be determined in order to make $S'(\theta_i) = S(\theta_i)$. However, it is difficult to digitally generate the sample data for the fourth-order random parameters $A_i$'s due to the strong correlation between them. Furthermore, the individual probability density functions at each value of θ, which are determined by the moments (and the bounds) using the maximum entropy technique (Siddall, 1983), are one of the most interesting probabilistic characteristics. Hence, the present simulation algorithm is focused on the generation of the joint moments of the simulated stochastic process rather than the digital generation of the sample data. After introducing the random parameters

$$B_i = A_i - E(A_i) \tag{6.14}$$

the analytical expressions of the mean and joint central moments involving the simulated stochastic process S'(θ) are rewritten from Equations (6.9) to (6.12), as

$$\mu'(t) = E[S(t)] = \sum_{i=0}^{9} \lambda_i E(A_i) \cos\omega_i t \tag{6.15}$$

$$c'(t,s) = \sum_{i=0}^{9} \lambda_i E[B_i^2] \cos\omega_i t \cos\omega_i s + \sum_{i=0}^{8} \sum_{j=i}^{9} \lambda_{ij} E[B_i B_j](\cos\omega_i t \cos\omega_j s + \cos\omega_i s \cos\omega_j t) \tag{6.16}$$

$$\begin{aligned} c'(t,s,\sigma) = {} & \sum_{i=0}^{9} \lambda_i E[B_i^3] \cos\omega_i t \cos\omega_i s \cos\omega_i \tau + \sum_{i=0}^{9} \sum_{j=0}^{9} \lambda_{iij} (1-\delta_{ij}) E[B_i^2 B_j] \cos\omega_i t \cos\omega_j s \cos\omega_k \tau \\ & + \sum_{i=0}^{7} \sum_{j=i+1}^{8} \sum_{k=j+1}^{9} \lambda_{ijk} E[B_i B_j B_k](\cos\omega_i t \cos\omega_j s \cos\omega_k \tau + \cos\omega_i t \cos\omega_k s \cos\omega_j \tau \\ & + \cos\omega_j t \cos\omega_i s \cos\omega_k \tau + \cos\omega_j t \cos\omega_k s \cos\omega_i \tau + \cos\omega_k t \cos\omega_i s \cos\omega_j \tau \\ & + \cos\omega_k t \cos\omega_j s \cos\omega_i \tau) \end{aligned} \tag{6.17}$$

$$\begin{aligned} c'(t,s,\tau,\sigma) = {} & \sum_{i=0}^{9} \lambda_{iiii} E[B_i^4] \cos\omega_i t \cos\omega_i s \cos\omega_i \tau \cos\omega_i \sigma \\ & + \sum_{i=0}^{9} \sum_{j=0}^{9} \lambda_{iiij} (1-\delta_{ij}) E[B_i^3 B_j](\cos\omega_i t \cos\omega_i s \cos\omega_i \tau \cos\omega_j \sigma + \\ & \cos\omega_i t \cos\omega_i s \cos\omega_j \tau \cos\omega_i \sigma + \cos\omega_i t \cos\omega_j s \cos\omega_i \tau \cos\omega_i \sigma \\ & + \cos\omega_j t \cos\omega_i s \cos\omega_i \tau \cos\omega_i \sigma) \\ & + \sum_{i=0}^{8} \sum_{j=i+1}^{9} \lambda_{iijj} E[B_i^2 B_i^2](\cos\omega_i t \cos\omega_i s \cos\omega_j \tau \cos\omega_j \sigma \\ & + \cos\omega_i t \cos\omega_j s \cos\omega_i \tau \cos\omega_j \sigma + \cos\omega_i t \cos\omega_j s \cos\omega_j \tau \cos\omega_i \sigma \\ & + \cos\omega_j t \cos\omega_j s \cos\omega_i \tau \cos\omega_i \sigma + \cos\omega_j t \cos\omega_i s \cos\omega_j \tau \cos\omega_i \sigma \\ & + \cos\omega_j t \cos\omega_i s \cos\omega_i \tau \cos\omega_j \sigma) \\ & + \sum_{i=0}^{9} \sum_{j=0}^{9} \sum_{k=j+1}^{9} \lambda_{iijk} (1-\delta_{ij})(1-\delta_{ik}) E[B_i^2 B_j B_k](\cos\omega_i t \cos\omega_i s \cos\omega_j \tau \cos\omega_k \sigma \\ & + \cos\omega_i t \cos\omega_j s \cos\omega_i \tau \cos\omega_k \sigma + \cos\omega_i t \cos\omega_j s \cos\omega_k \tau \cos\omega_i \sigma \\ & + \cos\omega_i t \cos\omega_k s \cos\omega_j \tau \cos\omega_i \sigma + \cos\omega_i t \cos\omega_j s \cos\omega_i \tau \cos\omega_k \sigma \\ & + \cos\omega_i t \cos\omega_k s \cos\omega_i \tau \cos\omega_j \sigma + \cos\omega_j t \cos\omega_i s \cos\omega_i \tau \cos\omega_k \sigma \end{aligned}$$

$$
\begin{aligned}
&+\cos\omega_j t\cos\omega_i s\cos\omega_k\tau\cos\omega_i\sigma+\cos\omega_j t\cos\omega_k s\cos\omega_i\tau\cos\omega_i\sigma\\
&+\cos\omega_k t\cos\omega_j s\cos\omega_i\tau\cos\omega_i\sigma+\cos\omega_k t\cos\omega_i s\cos\omega_j\tau\cos\omega_i\sigma\\
&+\cos\omega_k t\cos\omega_i s\cos\omega_i\tau\cos\omega_j\sigma)\\
&+\sum_{i=0}^{6}\sum_{j=i+1}^{7}\sum_{k=j+1}^{8}\sum_{l=k+1}^{9}E[B_iB_jB_kB_l](\cos\omega_i t\cos\omega_j s\cos\omega_k\tau\cos\omega_l\sigma\\
&+\cos\omega_i t\cos\omega_j s\cos\omega_l\tau\cos\omega_k\sigma+\cos\omega_i t\cos\omega_k s\cos\omega_j\tau\cos\omega_l\sigma\\
&+\cos\omega_i t\cos\omega_k s\cos\omega_l\tau\cos\omega_j\sigma+\cos\omega_i t\cos\omega_l s\cos\omega_j\tau\cos\omega_k\sigma\\
&+\cos\omega_i t\cos\omega_l s\cos\omega_k\tau\cos\omega_j\sigma+\cos\omega_j t\cos\omega_i s\cos\omega_k\tau\cos\omega_l\sigma\\
&+\cos\omega_j t\cos\omega_i s\cos\omega_l\tau\cos\omega_k\sigma+\cos\omega_j t\cos\omega_k s\cos\omega_i\tau\cos\omega_l\sigma\\
&+\cos\omega_j t\cos\omega_k s\cos\omega_l\tau\cos\omega_i\sigma+\cos\omega_j t\cos\omega_l s\cos\omega_i\tau\cos\omega_k\sigma\\
&+\cos\omega_j t\cos\omega_l s\cos\omega_k\tau\cos\omega_i\sigma+\cos\omega_k t\cos\omega_i s\cos\omega_j\tau\cos\omega_l\sigma\\
&+\cos\omega_k t\cos\omega_i s\cos\omega_l\tau\cos\omega_j\sigma+\cos\omega_k t\cos\omega_j s\cos\omega_i\tau\cos\omega_l\sigma\\
&+\cos\omega_k t\cos\omega_j s\cos\omega_l\tau\cos\omega_i\sigma+\cos\omega_k t\cos\omega_l s\cos\omega_i\tau\cos\omega_j\sigma\\
&+\cos\omega_k t\cos\omega_l s\cos\omega_j\tau\cos\omega_i\sigma+\cos\omega_l t\cos\omega_i s\cos\omega_j\tau\cos\omega_k\sigma\\
&+\cos\omega_l t\cos\omega_i s\cos\omega_k\tau\cos\omega_j\sigma+\cos\omega_l t\cos\omega_j s\cos\omega_i\tau\cos\omega_k\sigma\\
&+\cos\omega_l t\cos\omega_j s\cos\omega_k\tau\cos\omega_i\sigma+\cos\omega_l t\cos\omega_k s\cos\omega_i\tau\cos\omega_j\sigma\\
&+\cos\omega_l t\cos\omega_k s\cos\omega_j\tau\cos\omega_i\sigma)
\end{aligned}
\tag{6.18}
$$

In the above, $\delta_{ij}$ is the Delta function and defined by

$$
\delta_{ij}=\begin{cases}1 & i=j\\ 0 & i\neq j\end{cases}
\tag{6.19}
$$

The joint central moments of the stochastic process are evaluated because the distribution forms of the individual density functions are directly related to the central moments at particular values of θ. Therefore, the analytical expressions of joint central moments of the simulated stochastic process inside [0, π/2] are only in terms of the joint moments of the random parameters $B_i$'s. The joint central moments of S(θ) between the ILS strengths at the 10 tested FOD angles can be estimated from the experimental sample data sets respectively; for the first order moments (or mean values)

$$
ES(\theta_i)=\frac{1}{35}\sum_{n=1}^{35}S_n(\theta_i)
\tag{6.20}
$$

for the second-order joint central moments (or autocovariance)

$$c(\theta_i,\theta_j)=\frac{1}{34}\sum_{n=1}^{35}\{[S_n(\theta_i)-ES(\theta_i)][S_n(\theta_j)-ES(\theta_j)]\} \tag{6.21}$$

for the third-order joint central moments

$$c(\theta_i,\theta_j,\theta_k)=\frac{1}{35}\sum_{n=1}^{35}\{[S_n(\theta_i)-ES(\theta_i)][S_n(\theta_j)-ES(\theta_j)][S_n(\theta_k)-ES(\theta_k)]\} \tag{6.22}$$

and for the fourth-order joint central moments

$$\begin{aligned}&c(\theta_i,\theta_j,\theta_k,\theta_l)=\\&\frac{1}{35}\sum_{n=1}^{35}\{[S_n(\theta_i)-ES(\theta_i)][S_n(\theta_j)-ES(\theta_j)][S_n(\theta_k)-ES(\theta_k)][S_n(\theta_l)-ES(\theta_l)]\}\end{aligned} \tag{6.23}$$

where i, j, k, l = 0, ..., 9 and n denotes the sequence number of each sample data. The simulated joint central moments must be equal to the target joint central moments at or between the 10 tested values of θ. Therefore four sets of linear equations are established; one regarding the mean values of $A_i$'s and three regarding the joint moments of $B_i$'s up to the fourth order. Equations (6.15) and (6.20) form a $10^{th}$ order equation set involving 10 terms of $E[A_i]$ (i = 0, ..., 9). Equations (6.16) and (6.21) form a $55^{th}$ order equation set which involves 10 terms of $E[B_i^2]$ (i = 0, ..., 9) and 45 terms of $E[B_iB_j]$ (i = 0, ..., 9; and j = i+1, ... 9). Equations (6.17) and (6.22) are combined to generate a $220^{th}$ order equation set which has 10 terms of $E[B_i^3]$ (i = 1, ..., 9), 90 terms of $E[B_i^2B_j]$ (i = 0, ..., 9; and j = 0, ..., 9 but ≠ i) and 120 terms of $E[B_iB_jB_k]$ (i = 0, ..., 9; j = i+1, ... 9; and k = j+1, ..., 9). Equations (6.18) and (6.23) are combined to generate a $715^{th}$ order equation set which has 10 terms of $E[B_i^4]$ (i = 0, ..., 9), 90 terms of $E[B_i^3B_j]$ (i = 0, ..., 9; and j = 0, ..., 9 but ≠ i), 45 terms of $E[B_i^2B_j^2]$ (i = 0, ..., 9; and j = i+1, ..., 9), 360 terms of $E[B_i^2B_jB_k]$ (i = 0, ..., 9; j = 0, ..., 9 but ≠ i; and k = j+1 but ≠ i) and 210 terms of $E[B_iB_jB_kB_l]$ (i = 0, ... 9; j = i+1, ..., 9; k = j+1, ..., 9; and l = k+1, ..., 9). The mean values of $A_i$'s and the joint moments of $B_i$'s are thus obtained by solving the four equation sets. To this point, the analytical

expressions of the simulated joint moments are obtained and thus the joint moments at any particular values of θ can be determined.

## 6.5 BOUND ESTIMATION

The lower and higher bounds of the stochastic process S(θ) in the whole domain are essential to evaluate the individual probability density functions using the maximum entropy technique (Siddall, 1983). Once again, the bound data that can be available are those at the 10 tested values of θ from the present experimental program; therefore there are 10 sample data in each bound. Simply, the bound can be estimated inside [0, π/2] using some deterministic interpolation techniques, for example, linear interpolation, Gaussain interpolation and so on. However, since the badly selected bounds would generate the false rising tails on the maximum entropy distributions (Siddall, 1983), more accurate techniques, such as the stochastic interpolation, are necessary in order that the randomness of the bounds can be taken into account.

In the present stochastic simulation model, an estimation approach is also developed based on the time series theory to estimate the bounds in the whole domain. Each bound sample data are assumed to form a stationary time series u with respect to θ; therefore there are only 10 sample data uniformly distributed at the 10 tested FOD angles $\theta_i$ in each time series u(θ). It is reasonable that the four sets of sample data are viewed as the stationary time series, because they are located within a sufficiently short interval [0, π/2] (Jenkins and Watts, 1968). In Figures 6.1 and 6.2, the sample data in the lower bound series and higher bound series of the stochastic processes $S_{13}(\theta)$ and $S_{23}(\theta)$ are presented by the symbols in each case. Wherein the sample data of lower bounds equal to 0.92 minimum experimental strength values and the values of higher bounds to 1.08 maximum experimental strength values at the 10 tested FOD angles.

On the basis of the time series theory (Papoulis, 1984), the mean square estimation towards the value $u(\theta_k+\Delta\theta)$ in the time series can be obtained in terms of the (2N+1) sample data that are nearest to $\theta_k+\Delta\theta$,

$$\hat{u}(\theta_k + \Delta\theta) = \sum_{i=k-N}^{k+N} h_i u(\theta_i) \tag{6.24}$$

where $h_i$'s are undetermined deterministic parameters. The so-called orthogonality principle (Papoulis, 1984) demonstrates that the optimum mean square estimation in Equation (6.24) is such that the estimation error $(u - \hat{u})$ is orthogonal to each data $u(\theta_i)$. That is,

$$E\left\{\left[u(\theta_k + \Delta\theta) - \sum_{i=k-n}^{k+n} h_i u(\theta_i)\right] u(\theta_j)\right\} = 0 \qquad k-N \le j \le k+N \tag{6.25}$$

This is a fundamental principle in the mean square estimation with extensive applications. Therefore, one can directly derive that

$$\sum_{i=k-N}^{k+N} h_i R(\theta_i - \theta_j) = R(\theta_k + \Delta\theta - \theta_j) \qquad k-N \le j \le k+N \tag{6.26}$$

Thus, $h_i$'s could be determined by the (2N+1)th order linear equation set provided that the autocorreleation function $R(\tau)$ is known.

The autocorrelation function can be estimated from the sample data based on the spectral theory (Jenkins and Watts, 1968). First of all, the mean and autocovariance of the time series $u(\theta)$ can be estimated by

$$\mu = \frac{1}{10} \sum_{i=1}^{10} u(\theta_i) \tag{6.27}$$

$$c(k\Delta) = \frac{1}{10} \sum_{i=1}^{10-k} [u(\theta_i) - \mu][u(\theta_{i+k}) - \mu] \tag{6.28}$$

where $c(k\Delta)$ denotes the autocovariance with a lag of $k\Delta$. The above estimations are based on the Ergodic Theorem in the Mean and in the Correlation Function; i.e., the average over one realization (time series) is equivalent to an ensemble average in the stationary stochastic processes (Jenkins and Watts, 1968, Soong, 1973). The estimation error is said to be arbitrarily

small from the sufficiently long realization. Therefore, the estimation in Equations (6.27) and (6.28) is not accurate because only 10 sample data with the time series u(θ) are available inside [0, π/2]. The estimation accuracy could be improved by introducing the lag window in the sample spectrum, as shown immediately. The sample spectrum s(ω) can thus be written in terms of the estimated covariance.

$$s(\omega) = \Delta[c(0) + 2\sum_{i=1}^{L-1} w(i)c(i\Delta)\cos(2\pi\omega i\Delta)] \quad -1/(2\Delta) \le \omega \le 1/(2\Delta) \tag{6.29}$$

where w(i) is the lag window through which the spectrum estimations would have smaller variance (Jenkins and Watts, 1968), and L = 2N+1. There are a number of lag windows in the spectrum estimation, and the commonly used Bartlett lag window is selected.

$$w(i) = \begin{cases} (1 - \frac{i}{L}) & 0 \le i \le L-1 \\ 0 & i \ge L \end{cases} \tag{6.30}$$

From the inverse Fourier transform of the spectrum,one can obtain the estimation of the continuous autocorrelation function.

$$\begin{aligned} R(\tau) &= \int_{-1/2\Delta}^{1/2\Delta} s(\omega)\cos(2\pi\omega\tau)d\omega + \mu \\ &= \frac{\sin(18\tau)}{18\tau}c(0) + \sum_{i=1}^{L-1}(1 - \frac{i}{L})c(i\Delta)[\frac{\sin(i\pi + 18\tau)}{(i^2\pi + 18\tau)} + \frac{\sin(i\pi - 18\tau)}{(i^2\pi - 18\tau)}] + \mu \end{aligned} \tag{6.31}$$

It is obvious that more terms (or higher values of N) would be preferable so as to yield a better estimation in Equation (6.24). Right here only the five nearest sample data are employed (i.e., N = 2), because higher values of N mean that the autocovariances with bigger lag are required in Equation (6.28). However, it makes no physical sense that the autocovariances with the bigger lag are estimated by a time series only with 10 sample data. Consequently, the autocovarince function inside a range of 4Δ is needed, thereby designating L = 5 in Equation (6.29).

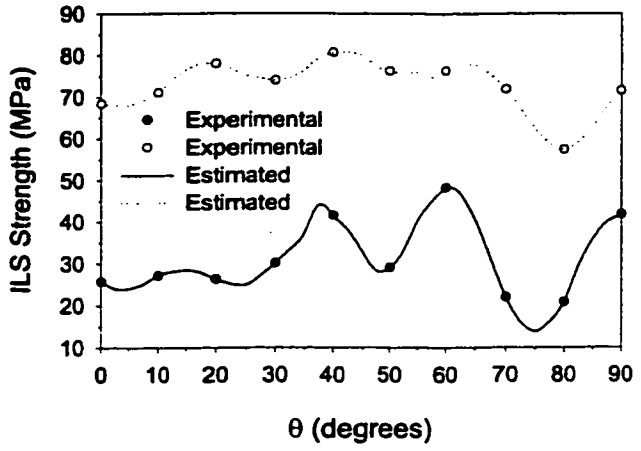


**Figure 6.1.** The lower and higher bounds for the stochastic process $S_{13}(\theta)$; the symbols denote the experimental data, and the curves denote the estimated values.

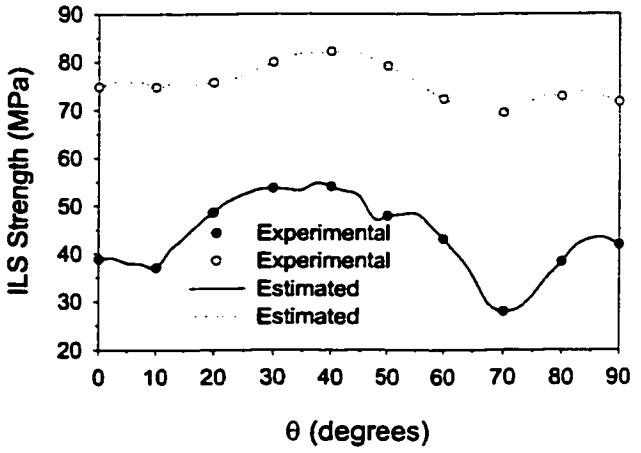


**Figure 6.2.** The lower and higher bounds for the stochastic process $S_{23}(\theta)$; the symbols denote the experimental data, and the curves denote the estimated values.

The estimated bounds for the stochastic processes $S_{13}(\theta)$ and $S_{23}(\theta)$ are presented through the curves in Figures 6.1 and 6.2. It can be observed that the higher bounds of the two stochastic processes present a similar θ-dependent tendency to their mean values in each case. This is an interesting evidence that can confirm in another way that the ILS strengths do depend on the FOD angles between the two surrounding plies of interfaces. The random distribution of defects inside composite materials could be considered as the origin of considerable scatter and lower mean values involving the ILS strengths. Under a specified manufacturing level, the higher bounds in the sample data sets represent the inherent behavior of a particular material, and thus are close to the idealistic strength values which could be presented by the specimens with the

"best quality". In other words, at least one specimen, the quality of which is close to the best, could be obtained from a large number of specimens in a single sample data set. In the present experimental program, the sample data sets with a sample size of 35 can thus reveal the θ-dependence of the ILS strengths not only in the mean values but in the higher bounds as well. Therefore one can conclude that the higher bounds of $S_{13}(\theta)$ and $S_{23}(\theta)$ determined by the developed estimation approach are of satisfactory accuracy, and close to the idealistic ones. In contrast, the time series representing the lower bounds of $S_{13}(\theta)$ and $S_{23}(\theta)$ pose high degree of randomness, as shown in Figures 1 and 2, because the values of the lower bounds are determined by the quantity and location of defects inside specimens. Although the quality of all the specimens is examined by the C-scan nondestructive technique, one could not define a minimum acceptable level corresponding to the quantity and location of defects. What can be done is only to discard the specimens with apparent defects detected. Consequently, it is very difficult, if not impossible, to accurately estimate the lower bounds of $S_{13}(\theta)$ and $S_{23}(\theta)$. And the estimated lower bounds shown in Figures 6.1 and 6.2 can not be directly employed to estimate the individual probability density function based the maximum entropy technique.

## 6.6 MODEL VERIFICATION

Before the simulation algorithm developed in the present chapter is applied to study the stochastic processes involving the probabilistic θ-dependent ILS strengths, its validity needs to be substantiated through the available stochastic processes by comparing the target and simulated joint moments. Ideally the present simulation algorithm should be verified by the fourth-order stochastic processes towards that it is originally developed. However, all the previous research, to the author' knowledge, only deals with the second-order stochastic processes, and thus such verification can not be available. Herein, two Gaussian nonstationary stochastic processes are selected and only the target and simulated autocorrelation functions (second-order) are respectively compared; one is the Ornstein-Uhlenbeck process (Grigoriu, 1993), and the other is the process that represents the South-North component recorded during the earthquake happening in El Centro, California in December 30, 1934 (Liu, 1970). Because of their complicated autocorrelation functions, these two stochastic processes are selected so that an effective verification could be attempted. The analytical expression of the autocorrelation function for the Ornstein-Uhlenbeck process has the form

$$k(t,s) = \alpha e^{-\kappa(t+s)} + e^{2\kappa \min\{t,s\}} e^{-\kappa(t+s)} \qquad t, s \geq 0 \tag{6.32}$$

and the two parameters are selected as $\alpha = -1$ and $\kappa = 0.6$ (Grigoriu, 1993). The autocorrelation function of the El Centro earthquake process is derived from the power spectrum estimated by Liu (1970), with the following form (Deodatis and Shinozuka, 1988):

$$k(t,s) = \frac{[\exp(-at) - \exp(-bt)]}{\max[\exp(-at) - \exp(-bt)]} \bullet \frac{[\exp(-as) - \exp(-bs)]}{\max[\exp(-as) - \exp(-bs)]} \bullet \frac{\pi S_0 \omega_g}{2\zeta_g} \exp[-\zeta_g \omega_g (s-t)]$$
$$\bullet \{(1+4\zeta_g^2)\cos[\sqrt{1-\zeta_g^2}\,\omega_g (s-t)] + (1-4\zeta_g^2)\frac{\zeta_g}{\sqrt{1-\zeta_g^2}}\sin[\sqrt{1-\zeta_g^2}\,\omega_g (s-t)]\} \tag{6.33}$$

where the expression is valid only when $s \geq t$. The following values are employed for the parameters (Deodatis and Shinozuka, 1988): $a = 0.25$ sec$^{-1}$; $b = 0.50$ sec$^{-1}$; $\omega_g = 15.0$ rad/sec; $\zeta_g = 0.25$; $S_0 = 0.1$ cm$^2$/sec$^3$.

In order to coincide with the present simulation algorithm, only the parts of the two stochastic processes during the duration [0, 3] are considered (i.e., $T = 3$). Thus the argument variables t and s in the autocorrelation functions are bounded within $[0, 3] \times [0, 3]$. The duration [0, 3] is uniformly divided into 9 sampling intervals ($\Delta = 1/3$) and then the 55 discrete values regarding k(t, s) at $t = i\Delta$ and $s = k\Delta$ ($i = 0, \ldots, 9$; and $k = i, \ldots, 9$) are obtained by sampling the autocorrelation functions in Equations (6.32) and (6.33) at space $\Delta$. By substituting the 55 discrete values into Equation (6.16), one can obtain an equation set which governs the second-order joint moments of random parameters $A_i$'s and subsequently the associated solutions. It should be noted that Equation (6.16) is written for the autocovariance functions in terms of $B_i$'s, but it still works for the autocorrelation functions if one replaces c'(t, s) by k'(t, s) at left-hand side and $B_i$'s by $A_i$'s in the right-hand side. In this way, the analytical expressions of simulated autocorrelation functions are also determined through Equation (6.16).

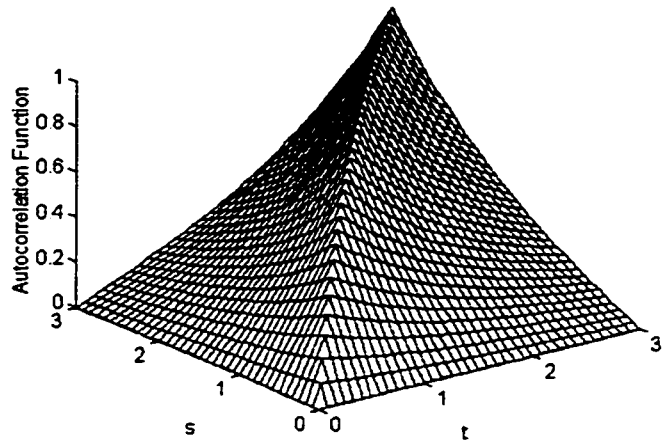


(a) k(t, s)

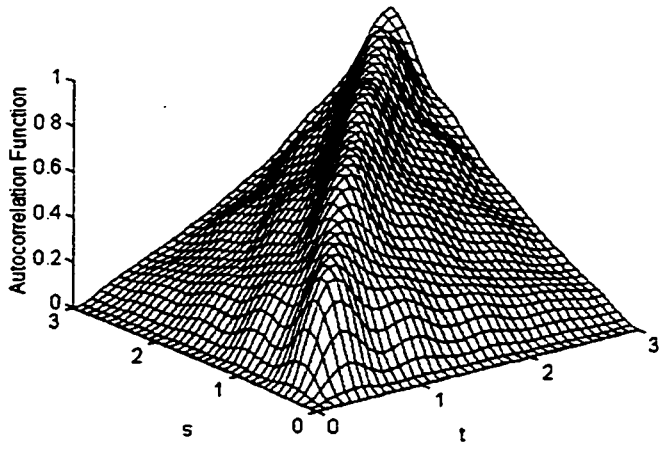


(b) k'(t, s)

**Figure 6.3.** The target and simulated autocorrelation functions of the Ornstein-Uhlenbeck stochastic process (Grigoriu, 1993).

The target and simulated autocorrelation functions within the domain [0, 3] × [0, 3] are shown in Figures 6.3 and 6.4 for the two Gaussian nonstationary stochastic processes. The simulation is found to be good for the Ornstein-Uhlenbeck process, but not satisfactory for the El Centro earthquake process because of the large oscillation of the simulated autocorrelation function from one sampling space to another. Comparing the two stochastic processes, different probabilistic characteristics can be observed inside the duration [0, 3]. The Ornstein-Uhlenbeck process presents a quite strong correlation between the larger time lag [i.e., (s – t)], however the El Centro earthquake process has no correlation between the larger time lag except for a narrow

time lag strip. These probabilistic characteristics would determine the accuracy of the present simulation algorithm, because in the solutions of the linear equation sets the random parameters $A_i$'s usually present quite strong correlation which is represented by quite high values of $E[A_iA_j]$ ($i \neq j$). Therefore, when the target stochastic process has quite strong correlation within the duration [0, T], the high accuracy of the present simulation algorithm can be expected only through keeping a few terms in the random trigonometric series in Equation (6.2). In the case of simulating the Ornstein-Uhlenbeck process, for example, the satisfactory accuracy is obtained by truncating only 10 terms. However, the present simulation algorithm still can efficiently simulate the stochastic processes that have very weak correlation within the duration [0, T]. In these cases, there are two solutions to attempt higher simulation accuracy: (1) without changing the time duration, to employ more terms in the random trigonometric polynomial (i.e., narrowing the sampling interval Δ); and (2) without changing the sampling interval Δ, to reduce the time duration inside which only the strong correlation exists. The first solution would generate the higher order linear equation sets, thus requiring the huge computer memory. The second solution is practicably accepted, because one can periodically simulate the target stochastic processes that are only correlated within the narrow time lag. In fact, the very good simulation is presented for the El Centro earthquake process if one narrow the time duration into [0, 1] (i.e., T = 1), inside which the autocorrelation functions have higher values.

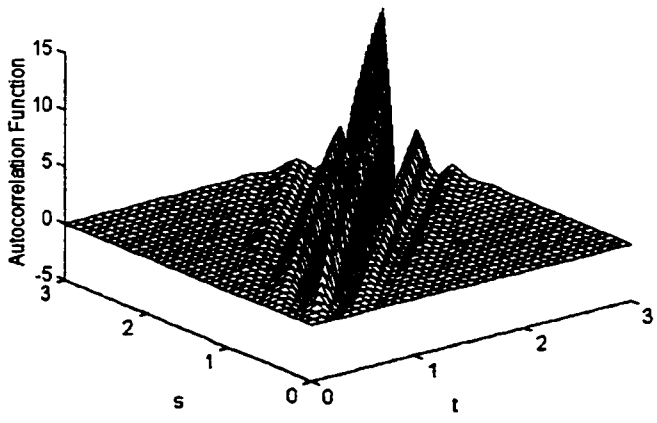


(a) k(t, s)

**Figure 6.4.** The target and simulated autocorrelation functions of the El Centro earthquake stochstic process (Liu, 1970).

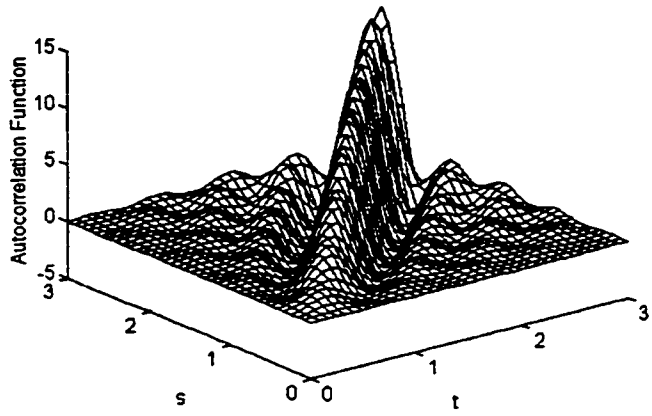


(b) k′(t, s)

**Figure 6.4.** The target and simulated autocorrelation functions of the El Centro earthquake stochstic process (Liu, 1970) (*continued*).

## 6.7 NUMERICAL RESULTS

All the probabilistic characteristics up to the fourth-order for the two stochastic processes $S_{13}(\theta)$ and $S_{23}(\theta)$ regarding the two ILS strength components can be calculated following the developed simulation algorithm. The variations of moments and individual probability density functions with respect to the FOD angles θ are demonstrated onwards, because both of them can be used to define the random nature of the ILS strengths at particular values of θ. The symbol (′) which designates the simulated stochastic processes and the involving probabilistic characteristics is omitted for reasons of clarity, however all the following numerical results presented are calculated from the simulated stochastic processes.

### 6.7.1. Probabilistic Moments

The first four moments are the important probabilistic parameters, from which one can directly figure out the shape of individual probability density functions. Besides the first two moments (mean value and variance) commonly used, for example, the third-order central moments can reveal the skewness and the fourth-order central moments the kurtosis of density functions.

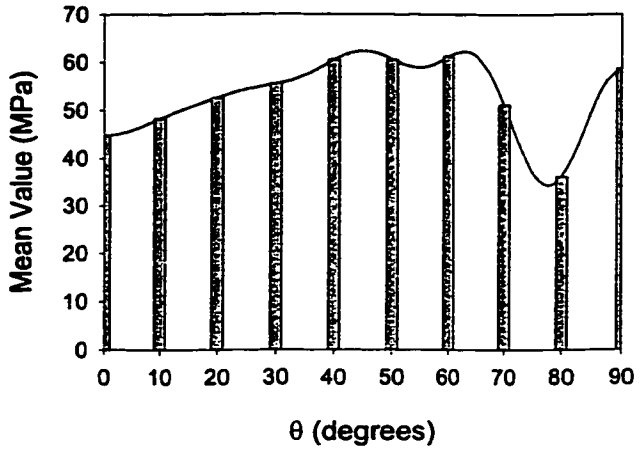


(a) $\mu(\theta)$

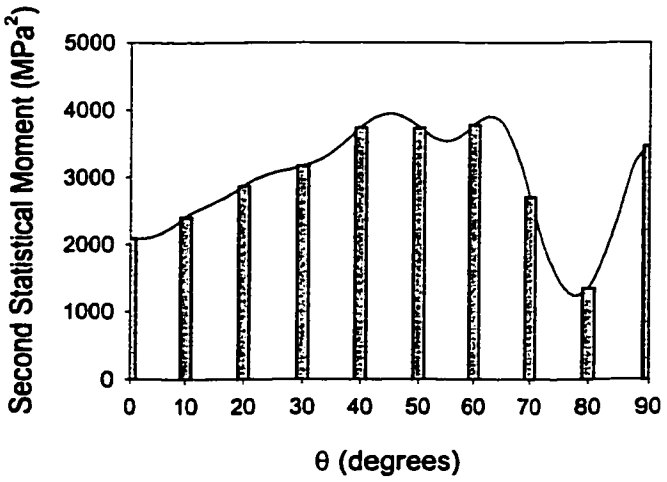


(b) $k(\theta, \theta)$

**Figure 6.5.** The probabilistic moments of the stochastic process $S_{13}(\theta)$; (a) mean value, and (b) second-order statistical moment.

Figures 6.5 and 6.6 demonstrate these probabilistic parameters involved in the stochastic processes $S_{13}(\theta)$. Hereafter, the vertical bars represent the experimental results, and the continuous curves and surfaces the calculated results from the present simulation algorithm. Its first-order and second-order original moments, $\mu(\theta)$ and $k(\theta, \theta)$, in Figure 6.5 are strongly dependent on the FOD angles $\theta$ and smoothly distributed over the bound $[0, \pi/2]$, thereby indicating that the simulation accuracy is satisfactory. It is noteworthy that the second-order moment $k(\theta, \theta)$ is not a function which only satisfy the single moments of the experimental sample data sets at the 10 tested FOD angles, but a particular case of the autocorrelation function

k(t, s) which can satisfy all the joint moments between the 10 data sets. The higher simulation accuracy is attributed to the correlation to some extent between the 10 experimental sample data sets. The correlation degree can be quantified by the correlation coefficient function ρ(t, s), as defined by

$$\rho(t,s) = \frac{c(t,s)}{\sqrt{c(t,t)c(s,s)}} \tag{6.34}$$

and for the stochastic process $S_{13}(\theta)$ is shown in Figure 6.6(a). The values of the function ρ(t, s) between some experimental data sets are ranged from 0.1 to 0.5, which can thus be considered to represent a weak correlation. Once again, the higher order central moments c(θ, θ), c(θ, θ, θ) and c(θ, θ, θ, θ) are particular cases of the corresponding joint central moments that satisfy all the probabilistic characteristics up to the fourth-order between the 10 experimental sample data sets. Therefore the central moments, which determine the individual probability density functions at any particular values of θ, present a sharp variation tendency with respect to the FOD angles θ in each case. Consequently, the forms of individual density functions would strongly depend on the values of θ, thus indicating the nonstationarity of the stochastic process $S_{13}(\theta)$. In Figure 6.6(c), the third-order central moments have relatively higher and positive values only near θ = 0°, but the values in the remaining range either close to zero or highly negative. That means the individual density functions are of left-deviated distribution in a very small range around θ = 0°, but almost symmetric distribution with respect to the mean values, or of right-deviated distribution in a wide range. The fourth-order central moments in Figure 6.6(d) exhibit higher values at most values of θ, which indicates the individual density functions are of wide-bound-range distributions. Around θ = 65° and 85°, very small and negative values are presented in Figure 6.6(d) which is unacceptable in a physical sense. This could be viewed as an estimation error there, because in the present simulation algorithm the simulated stochastic processes only satisfy all the probabilistic characteristics up to the fourth-order at the 10 tested FOD angles. However, in spite of the estimation error, one can make certain that the target fourth-order central moments are of very small values around θ = 65° and 85°.

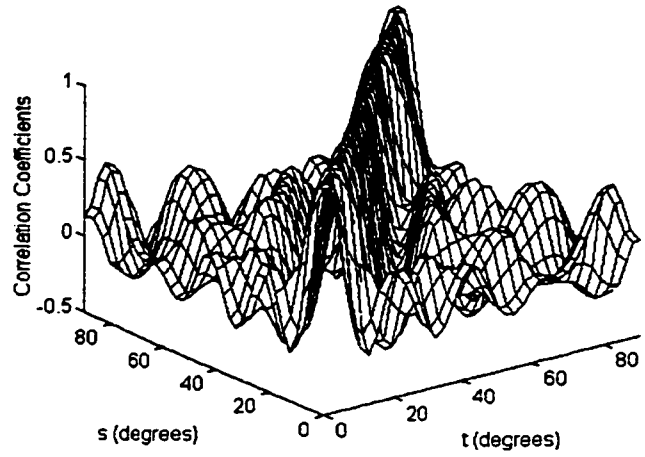


(a) ρ(t, s)

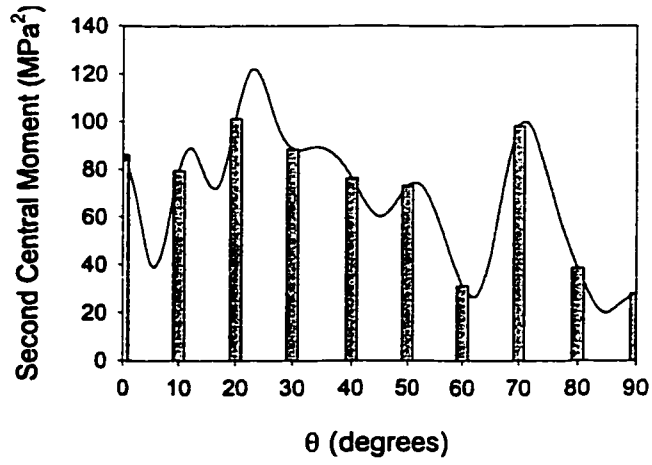


(b) c(θ, θ)

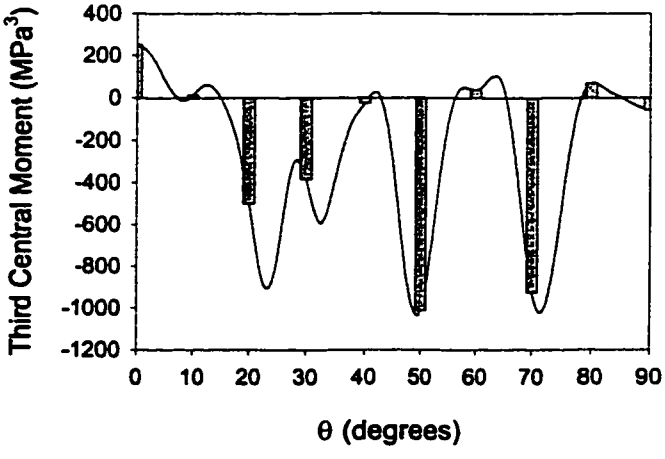


(c) c(θ, θ, θ)

**Figure 6.6.** The probabilistic moments of the stochastic process $S_{13}(\theta)$; (a) correlation coefficient function, (b) second-order central moment, (c) third-order central moment, and (d) fourth-order central moment.

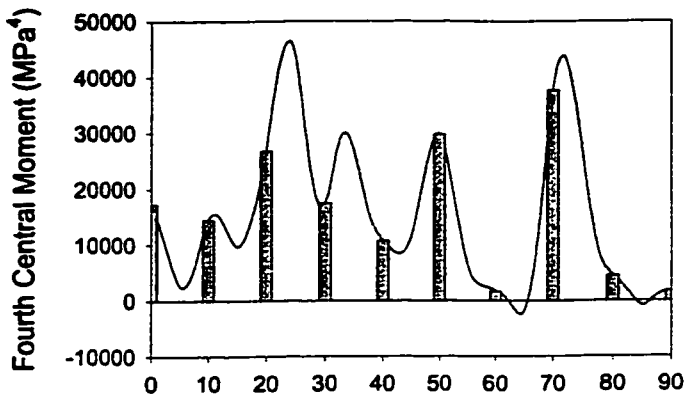


(d) $c(\theta, \theta, \theta, \theta)$

**Figure 6.6.** The probabilistic moments of the stochastic process $S_{13}(\theta)$; (a) correlation coefficient function, (b) second-order central moment, (c) third-order central moment, and (d) fourth-order central moment (*continued*).

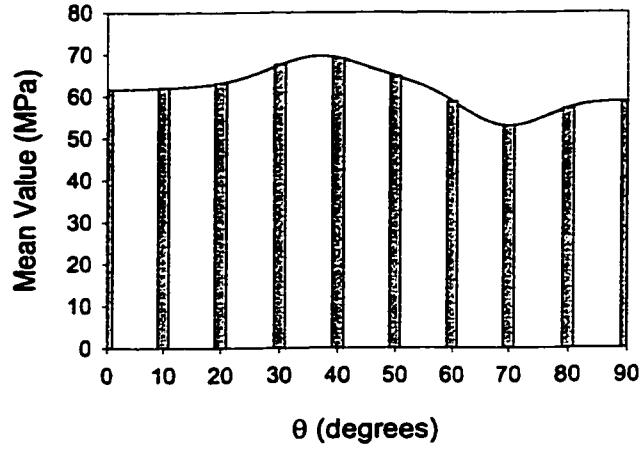


(a) $\mu(\theta)$

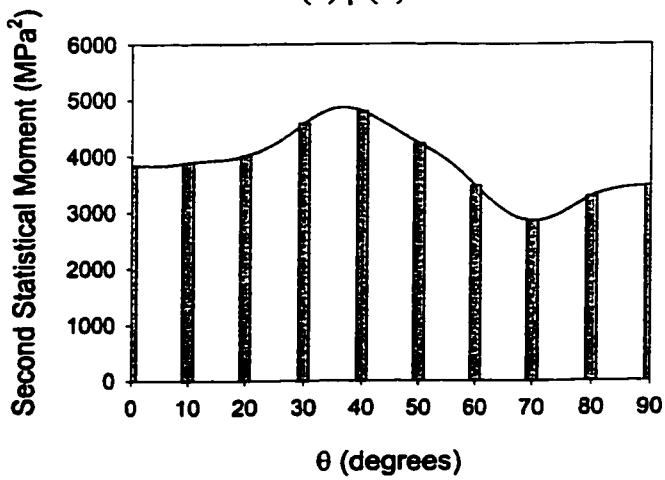


(b) $k(\theta, \theta)$

**Figure 6.7.** The probabilistic moments of the stochastic process $S_{23}(\theta)$; (a) mean value, and (b) second-order statistical moments.

The probabilistic characteristics involved in the stochastic process $S_{23}(\theta)$ are shown in Figures 6.7 and 6.8. From the smooth distribution of the first- and second-order original moments in Figure 6.7, one can make a conclusion that the estimation has a satisfactory accuracy. The nonstationarity of the stochastic process $S_{23}(\theta)$ is also presented because of the dependence of the two original moments on the FOD angles θ. The correlation coefficient function ρ(t, s) shown in Figure 6.8(a) demonstrate that the correlation degree between the 10 experimental sample data sets in the process $S_{23}(\theta)$ has almost the same level as that in the process $S_{13}(\theta)$, thereby also indicating a weak correlation. Because the ILS strength component $S_{23}$ presents smaller scatter than the strength component $S_{13}$ (see Chapter 5), the central moments in Figure 6.8 have much lower values. The third-order central moments are of negative values or close to zero within [0, π/2], therefore the individual probability density functions have also symmetric distribution with respect to the mean values, or right-deviated distributions. The lower values of the fourth-order central moments specify that the individual density functions have the narrow-bound-range distributions.

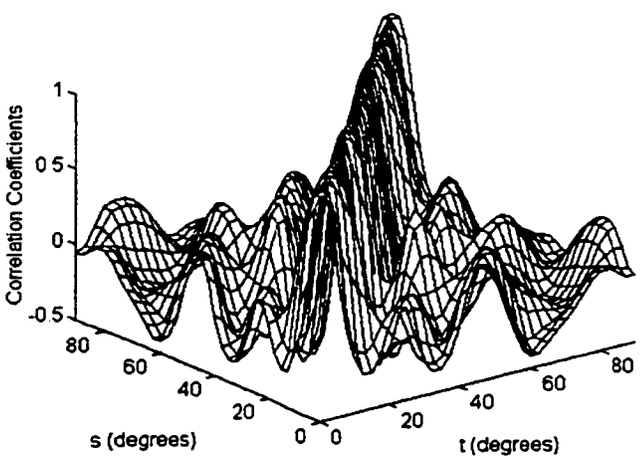


(a) ρ(t, s)

**Figure 6.8.** The probabilistic moments of the stochastic process $S_{23}(\theta)$; (a) correlation coefficient function, (b) second-order central moment, (c) third-order central moment, and (d) fourth-order central moment.

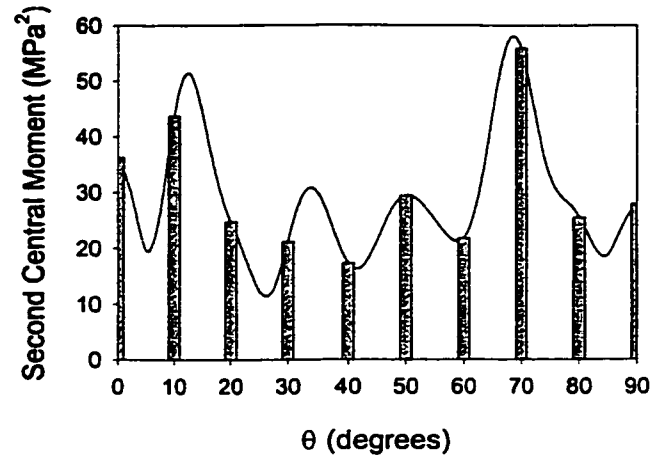


(b) c(θ, θ)

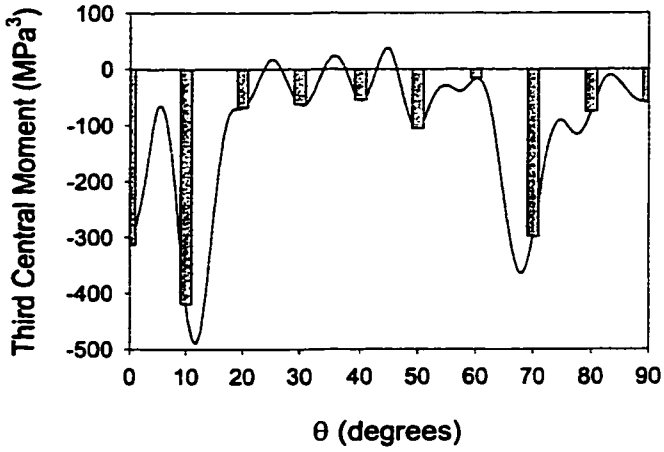


(c) c(θ, θ, θ)

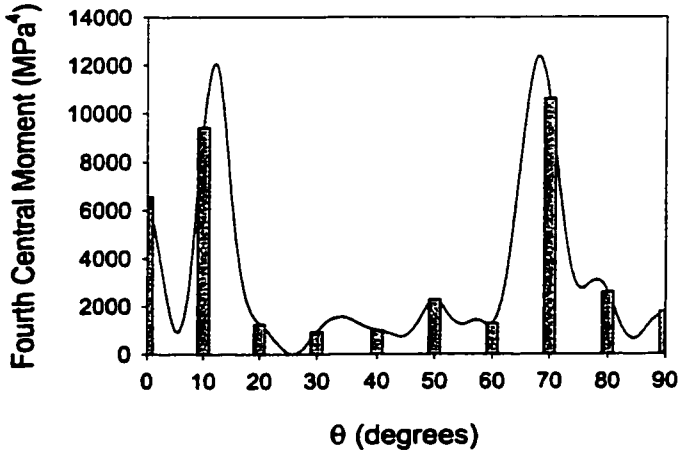


(d) c(θ, θ, θ, θ)

**Figure 6. 8.** The probabilistic moments of the stochastic process $S_{23}(\theta)$; (a) correlation coefficient functions, (b) second-order central moment, (c) third-order central moment, and (d) fourth-order central moment (*continued*).

### 6.7.2 Individual Probability Density Functions

The individual probability density functions for the two stochastic processes $S_{13}(\theta)$ and $S_{23}(\theta)$ at particular values of $\theta$ are evaluated by looking for the solutions to the five parameters $\lambda_i$'s in Equation (6.1) using the computer code (Siddall, 1983), which executes the mathematical operations based on the maximum entropy technique. The mean values, second-, third- and fourth-order central moments estimated using the present simulation algorithm are acted as the input data to the computer code.

The bounds of the two stochastic processes are also essential as the input data to the computer code. As mentioned above, the higher bounds estimated from the sample data are of satisfactory accuracy, because they have almost the same variation tendency with respect to $\theta$ as the mane values in each case. Hence, the estimated higher bounds are directly employed without any adjustment. The estimated lower bounds, however, need to be subjectively adjusted based on a judgement when employed to evaluate the density functions. This is because it is difficult to make a decision whether the estimated lower bounds do really represent the physical basis, and then whether one can accept them. Fortunately, the subjective adjustment is allowed, since it is believed that the difference in maximum entropy density functions caused by different bounds would not be a matter of concern (Siddall, 1983). The adjustment in the present work is accomplished by performing an iterative procedure; i.e, starting at the estimated lower bounds and then stretching out or shrinking in based on the tail shapes on maximum entropy distributions. Furthermore, the bounds have relations to some extent with the fourth-order central moments and this also can be used in judgement; the smaller the moments, the narrower the bound ranges (i.e., the distance between the lower bounds and higher bounds) are.

Figure 6.9 displays the individual probability density functions involving the stochastic process $S_{13}(\theta)$ at a number of FOD angles $\theta$, at which experiments are not performed. The adjusted lower bounds at the corresponding FOD angles are tabulated in Table 6.1, in which four bounds are not adjusted, two bounds are stretched out and the other three bounds are shrunk in. At $\theta = 5°$, the solutions to the five parameters $\lambda_i$'s would not be available from the computer code (Siddall, 1983) without adjusting the lower bounds. At the other FOD angles, the lower bounds are adjusted to modify the tail distributions. The individual density functions at $\theta = 5°$,

15° and 55° have hump shapes, because the corresponding fourth-order central moments are of lower values and the bound ranges are narrower. In contrast, the fourth-order central moments are higher and the corresponding bound ranges are wider at θ = 25°, 35°, 45° and 75°, the individual density functions present single-wave distributions over the wide ranges. A rising tail arises with the individual density function at θ = 75°, which would coincide with that at θ = 80° evaluated from the experimental sample data. Special attention should be paid to the evaluation of density functions at θ = 65° and 85°. Because the fourth-order central moments calculated from the present simulation algorithm are of negative values, the density functions at these FOD angles are evaluated using the central moments only up to the third-order and thus disregarding the fourth-order central moments. The involved problem is that the generated density functions only present single-waved distributions over narrow range. The tentative calculations do discover that the density functions of the experimental sample data sets always have single-waved distributions, if calculated using the central moments up to the third-order. On the basis of the experience in the evaluation of density functions at θ = 5°, 15° and 55°, the density functions at θ = 65° and 85° probably have hump-type distributions according to the characteristics of their fourth-order central moments and bound ranges. The estimation errors, therefore, might be yielded in the density functions at θ = 65° and 85° following the estimation errors in the fourth-order central moments. A possible method to remove the estimation error would be to perform additional experiments at these FOD angles, which is not covered in the present chapter. Even so, the density functions evaluated from the first three moments are still more accurate than those from the first two moments, e.g., Gaussian or Weibull distributions.

**Table 6.1.** The estimated and adjusted lower bounds at the specified FOD angles for the stochastic process $S_{13}(\theta)$.

| θ | 5° | 15° | 25° | 35° | 45° | 55° | 65° | 75° | 85° |
|---|---|---|---|---|---|---|---|---|---|
| Estimated | 24.1 | 28.5 | 25.0 | 37.4 | 32.7 | 40.5 | 40.6 | 13.7 | 35.6 |
| Adjusted | 35.0 | no | 19.3 | 22.1 | no | no | 46.0 | 11.1 | no |

Figure 6.10 displays the individual probability density functions involving the stochastic process $S_{23}(\theta)$ at the 9 corresponding FOD angles. The lower bounds are adjusted as shown in Table 2; the bounds at θ = 5° and 45° are stretched out in order to obtain the solutions to the five parameters $\lambda_i$'s, and at θ = 25° and 35° are shrunk in order to modify the tail distributions. The

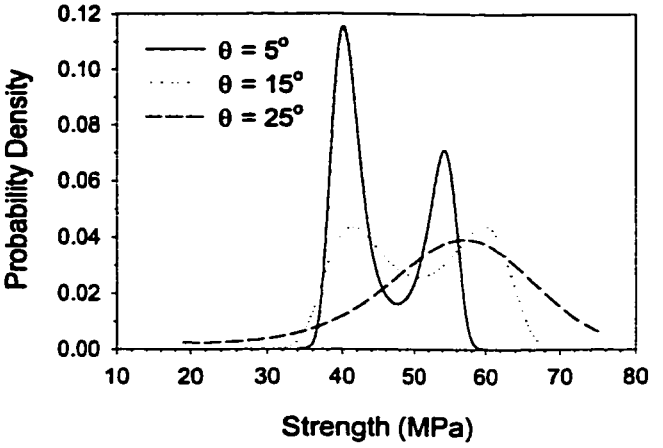


(a)

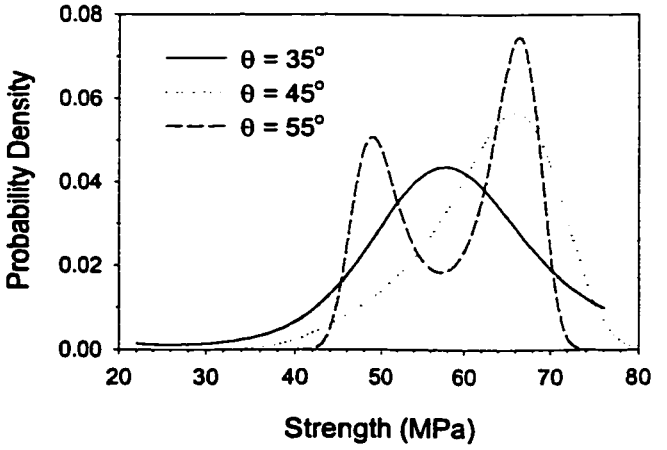


(b)

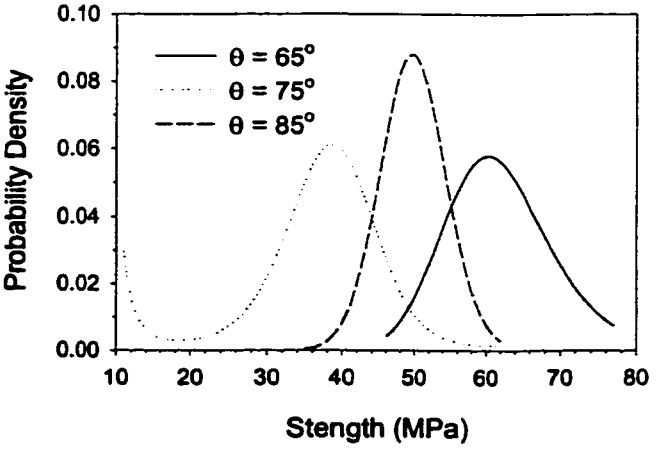


(c)

**Figure 6.9.** The individual probability density functions of the stochastic process $S_{13}(\theta)$ at the specified FOD angles (i.e., at the θ-interfaces) calculated by the stochastic simulation algorithm; (a) θ = 5°, 15° and 25°, (b) θ = 35°, 45° and 55°, and (c) θ = 65°, 75° and 85°.

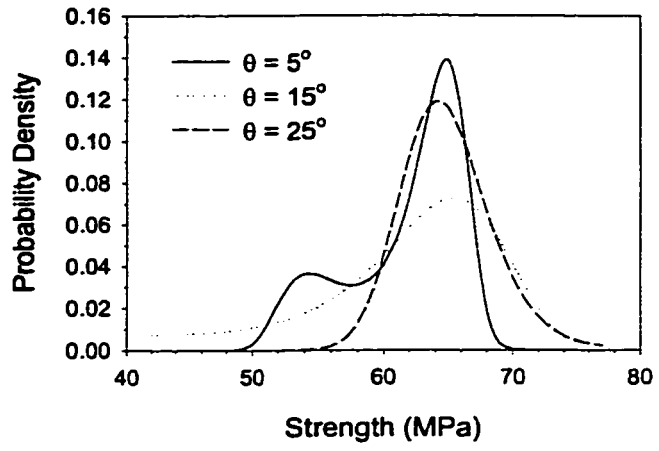


(a)

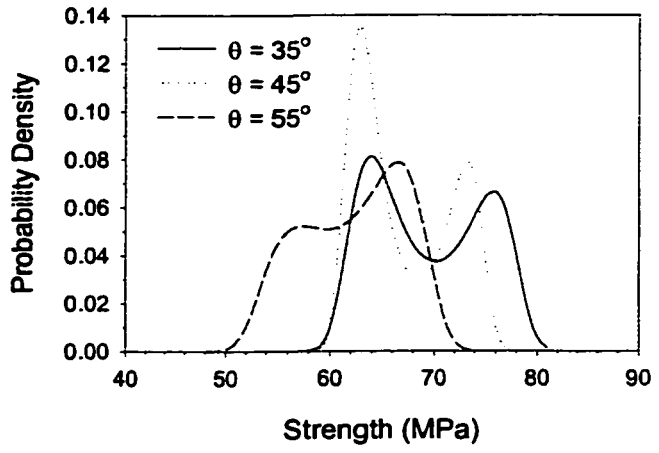


(b)

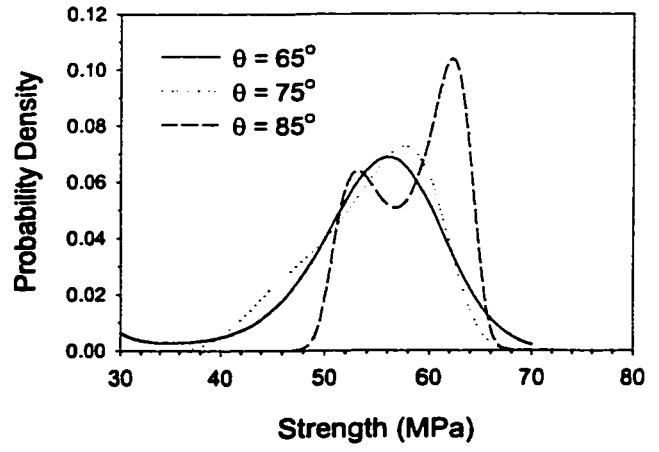


(c)

**Figure 6.10.** The individual probability density functions of the stochastic process $S_{23}(\theta)$ at the specified FOD angles [i.e., at the θ-interfaces] calculated by the stochastic simulation algorithm; (a) θ = 5°, 15° and 25°, (b) θ = 35°, 45° and 55°, and (c) θ = 65°, 75° and 85°.

individual density functions at θ = 5°, 35°, 45°, 55° and 85° present hump distributions in order to response the lower fourth-order central moments and narrower bound ranges. At θ = 15°, 65° and 75°, the density functions present single-waved distributions because of the higher fourth-order central moments and wider bound ranges. Once again, special attentions should be addressed to the density function at θ = 25°, which is evaluated only using the central moments up to the third-order. The fourth-order central moment estimated by the present simulation algorithm is of positive but small value at θ = 25°, where in fact the moments reach the minimum. However, if the central moments up to the fourth-order are employed, the solutions to the five parameters $\lambda_i$'s are not available from the computer code (Siddall, 1983) no matter what bound ranges are selected. The density function at θ = 25° shown in Figure 6.10(a) consequently presents a single-waved distribution over a narrow bound ranges. Similarly, the estimation error exists there to some extent, because the density function probably have a hump distribution according to the moment characteristics. By the way, it is found that the computer code (Siddall, 1983) always yields solutions to the four parameters $\lambda_i$'s (i = 0, ..., 3) for the experimental sample data sets involved in the two stochastic processes $S_{13}(\theta)$ and $S_{23}(\theta)$, if one only uses the central moments up to the third-order. In this case, the bound ranges only affect the distribution tails, but do not affect the solution existence.

**Table 6.2.** The estimated and adjusted lower bounds at the specified FOD angles for the stochastic process $S_{23}(\theta)$.

| θ | 5° | 15° | 25° | 35° | 45° | 55° | 65° | 75° | 85° |
|---|---|---|---|---|---|---|---|---|---|
| Estimated | 38.0 | 43.2 | 52.3 | 53.3 | 51.7 | 48.3 | 35.3 | 31.3 | 43.1 |
| Adjusted | 46.9 | 42.3 | no | no | 57.0 | no | 30.4 | no | no |

## 6.8 SUMMARY

This chapter implemented the analytical investigation on the probabilistic θ-dependent ILS strengths based on a proposed stochastic simulation algorithm. This simulation algorithm provides a feasible approach to simulate the general non-Gaussian nonstationary stochastic processes within a bounded interval, or in other words, to execute the stochastic interpolation based on experimental sample data that are discretely distributed. It can be seen that this simulation algorithm is efficient to investigate the probabilistic characteristics involved in the θ-dependent ILS strengths obtained from the double notch shear experimental program.

The stochastic simulation algorithm developed would provide a powerful mathematical tool to treat the experimental sample data with considerable scatter, in which certain variation tendencies with respect to physical variables are included. Traditionally, the variation tendencies in the experimental data are judged and then are best fitted by the least square estimate or maximum likelihood estimate techniques. However, when the experimental data have considerable scatter, such as the strengths of composite materials, these deterministic fitting techniques do not work any more because the variation tendency in a deterministic sense would be possibly masked by the scatter. The stochastic simulation techniques, therefore, are essential to uncover the effects of the physical variables on the intended physical phenomena. Moreover, the stochastic simulation techniques can draw more information from the experimental sample data. The probabilistic characteristics, such as the individual probability density functions, in the whole domain of the physical variables can be obtained on the basis of the experimental sample data yielded from a limited number of specimens at discrete physical variables. These results are important because they are the imprimitive input data to the reliability-based structural design. From this point of view, the present simulation algorithm can also be called as a stochastic interpolation technique.

However, the disadvantages of the developed simulation algorithm are apparent. That is, if the numbers of experimental sample data sets are quite large and they are correlated to some degree, then the orders of linear equation sets that govern the joint moments of the random parameters $A_i$'s would become huge and thus be difficult to solve for the solutions. In this circumstance, one could probably use the so-called sample theorem (Grigoriu, 1993) to develop the stochastic simulation algorithm, from which the simulated stochastic process X'(t) could be written as

$$X'(\theta) = \sum_{i=-n}^{n} X(i\Delta)\frac{\sin[\pi(t-i\Delta)/\Delta]}{\pi(t-i\Delta)/\Delta} \tag{6.35}$$

where X(iΔ) is the experimental sample data. The only limitation in Equation (6.35) is that the target stochastic processes must be band-limited. The simulation algorithm based on the sample theorem is outside the scope of this chapter.

## APPENDIX 6.1: EXPERIMENTAL SAMPLE DATA SETS

The experimental sample data sets for the ILS strengths $S_{13}$ and $S_{23}$, which are obtained from the double notch shear experimental program (see Chapter 5), are tabulated in Tables 6.A and 6.B respectively. These sample data sets are used to estimate the joint moments up the fourth-order between the 10 tested FOD angles in the present stochastic simulation model.

**Table 6.A.** Experimental sample data sets of the ILS strength $S_{13}$ at the θ-interfaces (MPa).

| θ | 0° | 10° | 20° | 30° | 40° | 50° | 60° | 70° | 80° | 90° |
|---|---|---|---|---|---|---|---|---|---|---|
| 1 | 46.89 | 64.08 | 61.55 | 61.09 | 50.20 | 62.94 | 57.28 | 61.17 | 32.51 | 59.20 |
| 2 | 50.11 | 37.41 | 55.15 | 58.40 | 57.26 | 61.32 | 57.58 | 44.35 | 29.37 | 57.73 |
| 3 | 46.43 | 46.52 | 58.72 | 67.31 | 67.23 | 64.63 | 69.46 | 23.82 | 26.23 | 54.01 |
| 4 | 27.93 | 53.09 | 57.95 | 66.72 | 67.65 | 69.50 | 70.62 | 58.19 | 34.81 | 54.59 |
| 5 | 38.99 | 62.17 | 56.86 | 54.42 | 60.38 | 69.61 | 62.95 | 51.48 | 37.19 | 45.38 |
| 6 | 63.29 | 56.23 | 48.99 | 52.95 | 74.17 | 56.16 | 61.73 | 56.98 | 36.34 | 50.87 |
| 7 | 62.30 | 45.00 | 55.60 | 59.87 | 67.20 | 68.68 | 61.10 | 57.42 | 53.15 | 53.55 |
| 8 | 34.62 | 47.83 | 52.71 | 56.56 | 65.66 | 62.42 | 57.31 | 40.69 | 29.08 | 61.07 |
| 9 | 35.42 | 46.78 | 39.09 | 66.71 | 73.82 | 68.33 | 60.70 | 36.59 | 32.92 | 57.27 |
| 10 | 48.19 | 47.42 | 65.28 | 58.36 | 59.90 | 65.65 | 69.97 | 39.72 | 40.81 | 60.59 |
| 11 | 33.39 | 49.15 | 66.35 | 65.95 | 45.10 | 64.20 | 53.85 | 64.94 | 42.15 | 52.50 |
| 12 | 37.36 | 47.14 | 65.74 | 65.84 | 46.18 | 70.59 | 58.50 | 49.22 | 37.87 | 51.39 |
| 13 | 42.64 | 51.34 | 32.81 | 48.86 | 57.59 | 31.54 | 64.13 | 54.47 | 30.03 | 57.51 |
| 14 | 38.59 | 55.89 | 41.77 | 60.58 | 63.84 | 44.91 | 56.23 | 40.61 | 30.17 | 61.17 |
| 15 | 37.62 | 65.75 | 36.54 | 40.04 | 74.62 | 60.65 | 68.16 | 24.50 | 22.61 | 50.78 |
| 16 | 43.03 | 61.12 | 53.89 | 50.79 | 69.65 | 68.24 | 69.05 | 49.96 | 32.41 | 62.22 |
| 17 | 38.66 | 52.71 | 62.07 | 55.11 | 65.56 | 61.60 | 53.45 | 49.70 | 32.97 | 54.64 |
| 18 | 43.29 | 32.83 | 54.35 | 45.47 | 53.12 | 59.28 | 53.30 | 53.92 | 33.48 | 64.97 |
| 19 | 52.99 | 47.58 | 53.82 | 67.84 | 49.41 | 65.19 | 65.34 | 52.70 | 38.39 | 63.40 |
| 20 | 42.07 | 42.69 | 41.73 | 46.88 | 57.00 | 53.14 | 58.58 | 64.37 | 37.36 | 52.37 |
| 21 | 34.76 | 41.77 | 28.51 | 51.20 | 61.19 | 64.33 | 68.35 | 55.79 | 42.28 | 65.31 |
| 22 | 42.89 | 35.80 | 42.74 | 68.44 | 56.31 | 67.46 | 60.17 | 51.25 | 30.74 | 59.62 |
| 23 | 49.86 | 46.77 | 54.26 | 54.27 | 62.61 | 61.23 | 55.27 | 51.59 | 42.82 | 65.59 |
| 24 | 28.53 | 54.36 | 38.96 | 55.48 | 54.40 | 57.19 | 64.77 | 63.22 | 31.03 | 57.94 |
| 25 | 42.81 | 36.89 | 51.21 | 47.27 | 56.22 | 53.46 | 69.19 | 59.56 | 30.69 | 55.32 |
| 26 | 44.88 | 40.15 | 54.53 | 45.30 | 54.22 | 38.98 | 58.70 | 52.07 | 38.16 | 66.23 |
| 27 | 35.14 | 41.00 | 46.19 | 64.41 | 51.22 | 62.50 | 54.97 | 55.91 | 31.59 | 60.11 |
| 28 | 59.18 | 53.70 | 72.17 | 60.25 | 72.23 | 64.42 | 68.89 | 60.76 | 41.74 | 60.82 |
| 29 | 44.94 | 29.50 | 57.65 | 44.57 | 70.87 | 58.81 | 55.14 | 52.45 | 39.25 | 64.98 |
| 30 | 60.62 | 46.47 | 52.30 | 58.45 | 48.81 | 49.36 | 56.80 | 52.64 | 43.14 | 63.89 |
| 31 | 59.35 | 40.21 | 58.25 | 41.88 | 63.10 | 64.34 | 60.60 | 51.65 | 38.56 | 59.19 |
| 32 | 46.15 | 53.73 | 59.31 | 32.70 | 46.37 | 60.38 | 52.46 | 66.54 | 37.99 | 65.52 |
| 33 | 48.06 | 59.64 | 45.17 | 63.45 | 65.08 | 59.60 | 65.41 | 46.15 | 37.89 | 63.91 |
| 34 | 56.38 | 40.35 | 59.13 | 64.24 | 73.12 | 61.95 | 58.81 | 46.80 | 45.74 | 54.99 |
| 35 | 48.76 | 55.52 | 60.62 | 40.19 | 56.59 | 65.81 | 63.24 | 46.93 | 44.06 | 63.34 |

**Table 6.B.** Experimental sample data sets of the ILS strength $S_{23}$ at the θ-interfaces (MPa).

| θ | 0° | 10° | 20° | 30° | 40° | 50° | 60° | 70° | 80° | 90° |
|---|---|---|---|---|---|---|---|---|---|---|
| 1 | 64.90 | 62.08 | 66.63 | 71.10 | 74.35 | 51.92 | 53.89 | 41.12 | 62.68 | 59.20 |
| 2 | 60.20 | 62.57 | 67.81 | 58.34 | 72.64 | 69.11 | 62.56 | 54.98 | 58.11 | 57.73 |
| 3 | 67.32 | 68.90 | 69.04 | 59.41 | 70.03 | 67.53 | 57.94 | 56.96 | 55.76 | 54.01 |
| 4 | 58.18 | 67.24 | 70.07 | 61.36 | 70.88 | 66.69 | 61.58 | 48.26 | 53.18 | 54.59 |
| 5 | 60.91 | 60.98 | 69.35 | 67.39 | 67.92 | 72.50 | 59.46 | 52.78 | 51.68 | 45.38 |
| 6 | 65.88 | 61.10 | 64.68 | 69.09 | 73.53 | 63.60 | 59.10 | 47.12 | 54.94 | 50.87 |
| 7 | 68.97 | 55.03 | 59.61 | 68.59 | 72.02 | 66.67 | 55.47 | 62.78 | 61.57 | 53.55 |
| 8 | 69.15 | 51.51 | 65.61 | 61.26 | 74.58 | 66.88 | 51.62 | 62.50 | 54.93 | 61.07 |
| 9 | 66.58 | 59.96 | 61.62 | 70.72 | 68.27 | 67.71 | 52.10 | 60.98 | 51.11 | 57.27 |
| 10 | 60.10 | 58.55 | 68.36 | 70.13 | 69.38 | 70.90 | 55.17 | 54.78 | 64.42 | 60.59 |
| 11 | 64.33 | 40.21 | 64.67 | 67.49 | 67.37 | 69.98 | 58.31 | 58.83 | 61.05 | 52.50 |
| 12 | 64.51 | 62.58 | 59.18 | 65.24 | 64.79 | 65.30 | 66.27 | 61.39 | 57.39 | 51.39 |
| 13 | 55.99 | 51.35 | 58.40 | 71.95 | 69.21 | 57.25 | 62.43 | 49.28 | 47.96 | 57.51 |
| 14 | 46.63 | 61.61 | 66.01 | 72.61 | 75.60 | 52.29 | 65.80 | 59.26 | 54.50 | 61.17 |
| 15 | 61.81 | 58.06 | 52.89 | 72.16 | 70.22 | 59.38 | 66.92 | 60.40 | 55.17 | 50.78 |
| 16 | 62.23 | 68.03 | 65.80 | 73.91 | 72.04 | 73.18 | 57.07 | 55.93 | 62.08 | 62.22 |
| 17 | 42.12 | 67.05 | 61.04 | 72.10 | 68.96 | 67.09 | 66.14 | 64.17 | 56.89 | 54.64 |
| 18 | 62.27 | 68.18 | 68.18 | 70.49 | 71.94 | 63.33 | 66.14 | 50.09 | 59.17 | 64.97 |
| 19 | 66.50 | 68.15 | 67.85 | 67.99 | 67.45 | 61.85 | 60.14 | 50.91 | 41.53 | 63.40 |
| 20 | 58.55 | 68.23 | 57.39 | 71.49 | 75.99 | 66.47 | 58.39 | 42.15 | 50.13 | 52.37 |
| 21 | 55.30 | 62.77 | 55.88 | 71.71 | 67.50 | 69.63 | 62.13 | 52.66 | 67.36 | 65.31 |
| 22 | 58.63 | 65.99 | 65.33 | 67.72 | 61.79 | 66.78 | 60.20 | 59.59 | 60.56 | 59.62 |
| 23 | 58.69 | 57.40 | 63.54 | 66.65 | 71.92 | 62.02 | 55.82 | 60.70 | 53.41 | 65.59 |
| 24 | 63.27 | 46.26 | 52.81 | 67.15 | 70.73 | 58.80 | 59.78 | 47.79 | 65.41 | 57.94 |
| 25 | 65.06 | 62.72 | 55.43 | 70.46 | 69.16 | 66.11 | 60.49 | 45.15 | 58.16 | 55.32 |
| 26 | 67.57 | 65.46 | 62.18 | 59.31 | 61.59 | 70.16 | 60.36 | 53.51 | 56.21 | 66.23 |
| 27 | 67.14 | 60.58 | 67.53 | 59.82 | 67.64 | 63.64 | 46.74 | 30.27 | 58.95 | 60.11 |
| 28 | 64.77 | 63.87 | 63.20 | 61.42 | 70.10 | 70.81 | 61.64 | 42.67 | 54.57 | 60.82 |
| 29 | 50.30 | 62.63 | 66.22 | 64.87 | 67.22 | 60.51 | 53.32 | 55.34 | 54.89 | 64.98 |
| 30 | 59.50 | 69.12 | 66.77 | 60.66 | 65.85 | 64.82 | 53.66 | 51.39 | 60.18 | 63.89 |
| 31 | 62.00 | 66.75 | 68.13 | 68.96 | 70.85 | 58.05 | 60.37 | 54.43 | 58.15 | 59.19 |
| 32 | 66.70 | 65.84 | 60.54 | 73.42 | 69.82 | 55.81 | 54.90 | 47.17 | 57.38 | 65.52 |
| 33 | 64.68 | 65.63 | 57.54 | 67.98 | 69.69 | 60.82 | 55.78 | 59.00 | 59.31 | 63.91 |
| 34 | 65.50 | 67.90 | 64.93 | 70.59 | 58.65 | 68.93 | 57.17 | 50.17 | 57.33 | 54.99 |
| 35 | 62.57 | 65.54 | 55.70 | 70.02 | 59.22 | 68.81 | 55.60 | 45.88 | 59.98 | 63.34 |

# CHAPTER 7

# FAILURE CRITERIA AND PROBABILISTIC EVALUATION OF DELAMINATION INITIATION

In this chapter, two innovative delamination criteria in terms of quadratic and cubic polynomials in each case, are developed based on the Malmeister strength theory and Hashin assumption. The intent of the developed criteria is to include the effects of θ-dependent and directionally-dependent interlaminar strength components into the failure evaluation of laminated composites, as demonstrated in Chapter 5. This intent is achieved by introducing the capabilities of strength tensor transformation to the delamination criteria. The effectiveness of the two developed criteria is verified through evaluating the random delamination failure induced by the straight edge effect interlaminar stresses in two types of laminated composites under uniaxial tension. Herein the Monte Carlo simulation technique is employed and the input data to the delamination criteria, i.e., the probabilistic strength tensors, are obtained from the stochastic simulation algorithm in Chapter 6.

## 7.1 INTRODUCTION

Delamination failure of fiber-reinforced laminated composites can be predicted by two distinct methodologies; one is based on fracture mechanics (O'Brien, 1982 and 1984), and the other is based on mechanics of materials (Sun and Zhou, 1988, Brewer and Lagace, 1988). Among the stress-based delamination criteria, the quadratic one is most frequently employed towards the delamination failure of laminated composites (Sun and Zhou, 1988, Brewer and Lagace, 1988), with the following form:

$$(\frac{\sigma_z}{Z_t})^2+(\frac{\tau_{1z}}{S_{13}})^2+(\frac{\tau_{2z}}{S_{23}})^2=1 \tag{7.1}$$

where $\sigma_z$, $\tau_{1z}$ and $\tau_{2z}$ are the three interlaminar stress components at the interfaces, and $Z_t$, $S_{13}$ and $S_{23}$ are the corresponding strength components. With the z axis fixed in the laminate thickness direction, the directions of the 1 and 2 axes at the interfaces are arbitrary, or in other words, no special coordinate system is required for the mathematical operation on this quadratic delamination criterion. For example, when this criterion is used to evaluate the delamination failure generated by edge effect interlaminar stresses, the 1 axis is usually selected to be parallel to the tangential direction of the straight or curved edges. Moreover, it is usually assumed that the two interlaminar shear (ILS) strength components are directionally independent in this criterion in order to make $S_{13} = S_{23}$ (Sun and Zhou, 1988, Brewer and Lagace, 1988).

It is apparent that the quadratic criterion in Equation (7.1) is empirically developed through the square root of the sum of the squares of the contribution from individual interlaminar stress component to the delamination failure, thereby neglecting the interactive effects between different interlaminar stress components. Furthermore, this criterion can not distinguish the functions of positive or negative interlaminar normal stresses with the associated term only being quadratic. Consequently, both negative and positive interlaminar normal stresses tend to promote the generation of delamination failure. This is not physically acceptable since it is well known that the negative (compressive) interlaminar normal stress lower than the interlaminar compressive strength could constrain the delamination failure to some extent.

Also, the assumption of directionally independent ILS strengths in the quadratic criterion in Equation (7.1) is in contrast to the experimental discovery in Chapter 5 that the ILS strengths are directionally dependent material properties. Like unidirectional plies, the interfaces between two adjacent plies with different fiber orientations also have the *so-called* principal material directions from the viewpoint of ILS strengths, which are along the symmetric axes of the fiber orientations in the two adjacent plies; i.e., the 1′ and 2′ axes in Figure 7.1. This means that the identical ILS strengths are obtained if one performs the shear tests along two directions symmetric with respect to the 1′ axis or the 2′ axis in each case. Usually the mathematical operations on the quadratic criterion in Equation (7.1) are performed in an arbitrary coordinate

system rather than in the principal material coordinate system, because in most cases, the edges of laminated composites are not along the principal material directions of the interfaces. The assumption of directionally independent ILS strengths thus becomes essential for the quadratic criterion in Equation (7.1), so that it can be functional in any coordinate systems along the non-principal material directions, as explained below. In Figure 7.1, the 1 and 2 axes are supposed to be the arbitrary directions deviated from the principal material directions with an angle $\phi$. The transformation relations of the ILS stresses in the two individual coordinate systems are

$$\tau_{1z} = \tau_{1'z}\cos\phi + \tau_{2'z}\sin\phi \tag{7.2.a}$$

$$\tau_{2z} = -\tau_{1'z}\sin\phi + \tau_{2'z}\cos\phi \tag{7.2.b}$$

and the identical relationship can then be found that

$$\tau_{1z}^{\,2} + \tau_{2z}^{\,2} = \tau_{1'z}^{\,2} + \tau_{2'z}^{\,2} \tag{7.3}$$

Because it is assumed that the ILS strengths are directionally independent ($S_{13} = S_{23}$) in any arbitrary directions, the quadratic criterion in Equation (7.1) can predict the invariant failure strengths governed by the delamination failure in any coordinate systems with the identical relationship in Equation (7.3); this is a fundamental physical requirement for any failure criteria.

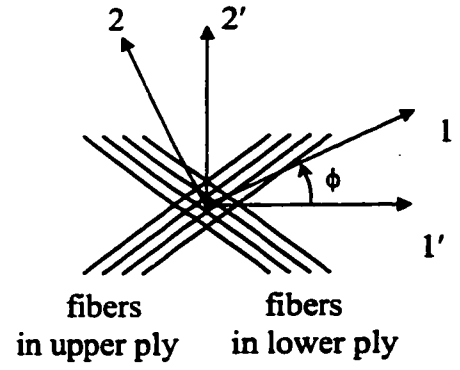


**Figure 7.1.** Coordinate systems in which the delamination criteria are considered; the z axis is not shown for clarity, however, a right-hand coordinate system is formed of the 1, 2 and z axes or the 1', 2' and z axes.

The shortcomings of the quadratic delamination criterion in Equation (7.1) are thus apparent, because the experimental results in Chapter 5 clearly show that $S_{13} \neq S_{23}$ (more generally, $S_{13}$ and $S_{23}$ depend on the FOD angle of surrounding plies). From this point of view, the criteria without the capability of strength tensor transformation, such as in Equation (7.1), could not take into account the directionally-dependent ILS strength components. Generally, in the failure criteria with the capability of strength tensor transformation, the strength tensors in term of the strength components would be changed with respect to different coordinate systems (Tsai and Wu, 1971), with each stress component simultaneously changed according to the transformation relationships, e.g., in Equation (7.2). For instance, in the Tsai-Wu quadratic criterion (Tsai and Wu, 1971), the complete sets of the strength tensor transformation relationships are already derived. In this regard, the failure criteria could predict invariant failure strengths no matter which coordinate system the mathematical operation is performed. Moreover, if the failure criteria are not written in the principal material coordinate system, the interactive terms between different shear stresses will appear (Tsai and Wu, 1971), because the sign change of one shear stress in the couple would affect the failure strength of laminated composites in this case.

The intent of this chapter is thus to develop two innovative delamination criteria, which can overcome all the shortcomings involved in the quadratic delamination criterion in Equation (7.1). These two delamination criteria are developed based on Malmeister strength theory (Malmeister, 1967) and Hashin assumption (Hashin, 1980), and in terms of second-order (quadratic) and third-order (cubic) polynomials respectively. Wherein all of the second- and fourth-rank strength tensors in any arbitrary directions at given interfaces are determined by the interlaminar strength components experimentally characterized in one arbitrary direction. In the cubic criterion, however, the sixth-rank strength tensors characterizing the interaction between the ILS and normal stress components should be experimentally determined using the interlaminar tension-shear or compression-shear combined loading tests. Therefore, comparing the two developed criteria, one would find the quadratic criterion is more convenient to evaluate the delamination failure without the additional combined loading tests required, but the cubic criterion is more flexible to best fit the experimental results through adjusting the sixth-rank strength tensors. The analytical determination of the value ranges for the sixth-rank strength tensors is also given in this chapter.

## 7.2 THEORETICAL BACKGROUND

Fiber-reinforced composite materials usually exhibit complicated failure mechanisms due to the significant difference of their constituents in material properties, which include the fundamental failure modes of matrix crack, fiber breakage and fiber/matrix debonding, or the simultaneous occurrence of these failure modes. Therefore, it is extremely complex to evaluate the failure of composite materials under combined stress state on the basis of micro-mechanics approaches due to the difficulties in distinguishing the fundamental failure modes and performing micro-mechanics stress analysis. Up to now the associated investigations are only limited to unidirectional composite materials. On the other hand, the failure evaluation of composite materials on the basis of macro-mechanics approaches is relatively convenient, which treat composite materials to be anisotropic homogeneous and employ the macro-variables, i.e., average stresses and strains. The macro-mechanics failure criteria are usually written in terms of polynomials (Hoffman, 1967, Tsai and Wu, 1971) and the inherent non-interactive strength tensors could be determined by the strength components along the principle material directions obtained from uniaxial loading tests. Thus these failure criteria are phenomenological in nature, because they only predict the failure appearance in an average sense but do not explain the failure mechanisms.

An efficient phenomenological failure criterion towards the failure of composite materials should have the following characteristics (Wu, 1973):

(1) It should be of operational simplicity and mathematical rationality;
(2) It should be invariant, or in other words, predict identical failure strength in any arbitrary coordinate systems;
(3) It should be sufficiently flexible to model any failure modes without presumption on the mechanisms of failure;
(4) It should yield two effective distinct roots for two colinear loading paths;
(5) It should be piecewise continuous without singularity in the stress space;

It is apparent that the empirically developed failure criteria can not satisfy all of the above requirements, which usually are functional in the coordinate systems specially consistent with the principal material directions of composite materials.

The Malmeister strength theory (Malmeister, 1967), to the author's knowledge, is the unique phenomenological stress-based failure criterion for anisotropic materials, which satisfies all the aforementioned requirements. Its extensive application in the failure evaluation of fiber-reinforced composite materials can be found in numerous published papers (Tsai and Wu, 1971, Wu, 1973, Wu and Scheublein, 1975, Tennyson *et al.*, 1978). In this chapter, the two innovative delamination criteria are developed based on the Malmeister strength theory in conjunction with the Hashin assumption (Hashin, 1980). The purpose of the Hashin assumption (Hashin, 1980) is to simplify the delamination criteria due to the fact that the directions of fracture planes for the delamination failure is always known in advance. Furthermore, the aforementioned principal material directions of the θ-interfaces, which is a new concept introduced in this chapter, play a significant role in developing the two innovative delamination criteria.

### 7.2.1 Malmeister Strength Theory

In an arbitrary three-dimensional (3D) Cartesian coordinate system, the Malmeister strength theory assumes that the failure criterion for an anisotropic body has a general form as

$$k_i \sigma_i + k_{ij} \sigma_i \sigma_j + k_{ijk} \sigma_i \sigma_j \sigma_k + \ldots = 1 \tag{7.4}$$

where $k_i$, $k_{ij}$, $k_{ijk}$, ..., are the second-, the fourth- and the sixth-, ..., rank strength tensors, and $\sigma_i$, $\sigma_j$, $\sigma_k$, ..., are the stress components in the arbitrarily designated coordinate system. This failure criterion is versatile and convenient to characterize the failure of fiber-reinforced composite materials. It can be considered in any Cartesian coordinate systems, thus presenting the potential capabilities of strength tensor transformation. Also, it encompasses all of the empirical stress-based criteria by setting some strength tensors to be zero.

### 7.2.2. Hashin Assumption

The failure criterion in Equation (7.4) shows that all the six stress components usually appear in any arbitrary Cartesian coordinate systems. However, if the directions of fracture

planes can be identified *a priori* and the stress state is considered in a deliberate coordinate system, one of the three planes of which is parallel to the fracture planes, then the contribution of each stress component to the material failure is different. The out-of-plane stress components play a dominant role in generating the failure in comparison with the in-plane stress components. Therefore, Hashin (1980) assumed that the failure is only produced by the out-of plane stress components (i.e., normal and shear stresses on the fracture planes) and thus the in-plane stress components should drop out of the failure criteria. The intent of this assumption is to simplify the failure criteria that can be in terms of only three stress components. On the basis of this assumption, Hashin (1980) proposed an empirical failure criterion applicable to the principal material coordinate system, which can differentiate two primary failure modes for fiber-reinforced composite materials: fiber breakage and matrix crack. It is noteworthy that the quadratic delamination criterion in Equation (7.1) intuitively made use of the Hashin assumption.

### 7.2.3 Principal Material Directions of Interfaces

From the viewpoint of ILS strengths, the symmetric axes of the fiber orientations of the surrounding plies (1′ and 2′ axes in Figure 7.1) are the principal material directions of the interfaces. This is because the ILS strengths are equal to each other along two arbitrary directions which are symmetric with respect to 1′ or 2′ axis. For instance, the ILS strengths are identical along two directions that are parallel to or perpendicular to the fiber orientations of the surrounding plies in Figure 7.1. Therefore, usually the principal material directions of the interfaces are not parallel or normal to the fiber orientations of the surrounding plies. It is well recognized that the sign change of single shear does not change the failure strengths of composite materials. In one arbitrary coordinate system, if the signs of the two ILS stresses $\tau_{1z}$ and $\tau_{2z}$ are changed simultaneously, the direction of the vector sum of them will be reversed and thus the failure strengths will remain invariant. The failure strengths will be changed if the sign of only one ILS stress is changed, since the direction of the vector sum of $-\tau_{1z}$ and $\tau_{2z}$ or $\tau_{1z}$ and $-\tau_{2z}$ will be deviated from the original direction of the vector sum of $\tau_{1z}$ and $\tau_{2z}$. In the principal material coordinate systems of any interfaces, the directions of the vector sum of $\tau_{1z}$ and $\tau_{2z}$, and the vector sum of $-\tau_{1z}$ and $\tau_{2z}$ or $\tau_{1z}$ and $-\tau_{2z}$ are symmetric with respect to the principal material directions. Therefore, the failure strengths remain invariant if the sign of only one ILS stress is

changed in the principal material directions of the interfaces, because of the symmetry of ILS strengths.

## 7.3 DEVELOPMENT OF INNOVATIVE DELAMINATION CRITERIA

The innovative quadratic and cubic delamination criteria are developed on the basis of the Malmeister strength theory shown in Equation (7.4); higher than second-order terms are truncated off in the quadratic one and higher than third-order terms are off in the cubic one in each case. After the truncation of the higher order terms, a lot of strength tensors still remain there; 6 second-rank strength tensors $F_i$, 36 fourth-rank strength tensors $F_{ij}$ and 216 sixth-rank strength tensors $F_{ijk}$, as follows:

$$F_i = \begin{bmatrix} F_1 \\ F_2 \\ F_3 \\ F_4 \\ F_5 \\ F_6 \end{bmatrix}; \; F_{ij} = \begin{bmatrix} F_{11} & F_{12} & F_{13} & F_{14} & F_{15} & F_{16} \\ F_{21} & F_{22} & F_{23} & F_{24} & F_{25} & F_{26} \\ F_{31} & F_{32} & F_{33} & F_{34} & F_{35} & F_{36} \\ F_{41} & F_{42} & F_{43} & F_{44} & F_{45} & F_{46} \\ F_{51} & F_{52} & F_{53} & F_{54} & F_{55} & F_{56} \\ F_{61} & F_{62} & F_{63} & F_{64} & F_{65} & F_{66} \end{bmatrix} \tag{7.5}$$

$$F_{1jk} = \begin{bmatrix} F_{111} & F_{112} & F_{113} & F_{114} & F_{115} & F_{116} \\ F_{121} & F_{122} & F_{123} & F_{124} & F_{125} & F_{126} \\ F_{131} & F_{132} & F_{133} & F_{134} & F_{135} & F_{136} \\ F_{141} & F_{142} & F_{143} & F_{144} & F_{145} & F_{146} \\ F_{151} & F_{152} & F_{153} & F_{154} & F_{155} & F_{156} \\ F_{161} & F_{162} & F_{163} & F_{164} & F_{165} & F_{166} \end{bmatrix}; \; F_{2jk} = \begin{bmatrix} F_{211} & F_{212} & F_{213} & F_{214} & F_{215} & F_{216} \\ F_{221} & F_{222} & F_{223} & F_{224} & F_{225} & F_{226} \\ F_{231} & F_{232} & F_{233} & F_{234} & F_{235} & F_{236} \\ F_{241} & F_{242} & F_{243} & F_{244} & F_{245} & F_{246} \\ F_{251} & F_{252} & F_{253} & F_{254} & F_{255} & F_{256} \\ F_{261} & F_{262} & F_{263} & F_{264} & F_{265} & F_{266} \end{bmatrix};$$

$$F_{3jk} = \begin{bmatrix} F_{311} & F_{312} & F_{313} & F_{314} & F_{315} & F_{316} \\ F_{321} & F_{322} & F_{323} & F_{324} & F_{325} & F_{326} \\ F_{331} & F_{332} & F_{333} & F_{334} & F_{335} & F_{336} \\ F_{341} & F_{342} & F_{343} & F_{344} & F_{345} & F_{346} \\ F_{351} & F_{352} & F_{353} & F_{354} & F_{355} & F_{356} \\ F_{361} & F_{362} & F_{363} & F_{364} & F_{365} & F_{366} \end{bmatrix}; \; F_{4jk} = \begin{bmatrix} F_{411} & F_{412} & F_{413} & F_{414} & F_{415} & F_{416} \\ F_{421} & F_{422} & F_{423} & F_{424} & F_{425} & F_{426} \\ F_{431} & F_{432} & F_{433} & F_{434} & F_{435} & F_{436} \\ F_{441} & F_{442} & F_{443} & F_{444} & F_{445} & F_{446} \\ F_{451} & F_{452} & F_{453} & F_{454} & F_{455} & F_{456} \\ F_{461} & F_{462} & F_{463} & F_{464} & F_{465} & F_{466} \end{bmatrix};$$

$$F_{5jk} = \begin{bmatrix} F_{511} & F_{512} & F_{513} & F_{514} & F_{515} & F_{516} \\ F_{521} & F_{522} & F_{523} & F_{524} & F_{525} & F_{526} \\ F_{531} & F_{532} & F_{533} & F_{534} & F_{535} & F_{536} \\ F_{541} & F_{542} & F_{543} & F_{544} & F_{545} & F_{546} \\ F_{551} & F_{552} & F_{553} & F_{554} & F_{555} & F_{556} \\ F_{561} & F_{562} & F_{563} & F_{564} & F_{565} & F_{566} \end{bmatrix}; \; F_{6jk} = \begin{bmatrix} F_{611} & F_{612} & F_{613} & F_{614} & F_{615} & F_{616} \\ F_{621} & F_{622} & F_{623} & F_{624} & F_{625} & F_{626} \\ F_{631} & F_{632} & F_{633} & F_{634} & F_{635} & F_{636} \\ F_{641} & F_{642} & F_{643} & F_{644} & F_{645} & F_{646} \\ F_{651} & F_{652} & F_{653} & F_{654} & F_{655} & F_{656} \\ F_{661} & F_{662} & F_{663} & F_{664} & F_{665} & F_{666} \end{bmatrix}; \tag{7.6}$$

The number of strength tensors can be further reduced by imposing some constraints due to the inherent characteristics of fiber-reinforced composite materials (Wu and Scheublein, 1975).

If the failure of composite materials is assumed to be independent of loading paths, one can derive the symmetry conditions; $F_{ij} = F_{ji}$, and $F_{ijk} = F_{ikj} = F_{jik} = F_{jki} = F_{kij} = F_{kji}$. Thus there are left 21 independent fourth-rank strength tensors and 56 independent sixth-rank strength tensors, i.e.,

$$F_i = \begin{bmatrix} F_1 \\ F_2 \\ F_3 \\ F_4 \\ F_5 \\ F_6 \end{bmatrix}; \; F_{ij} = \begin{bmatrix} F_{11} & F_{12} & F_{13} & F_{14} & F_{15} & F_{16} \\ & F_{22} & F_{23} & F_{24} & F_{25} & F_{26} \\ & & F_{33} & F_{35} & F_{35} & F_{36} \\ & & & F_{44} & F_{45} & F_{46} \\ & & & & F_{55} & F_{56} \\ & & & & & F_{66} \end{bmatrix} \tag{7.7}$$

$$F_{1jk} = \begin{bmatrix} F_{111} & F_{112} & F_{113} & F_{114} & F_{115} & F_{116} \\ & F_{122} & F_{123} & F_{124} & F_{125} & F_{126} \\ & & F_{133} & F_{134} & F_{135} & F_{136} \\ & & & F_{144} & F_{145} & F_{146} \\ & & & & F_{155} & F_{156} \\ & & & & & F_{166} \end{bmatrix}; \; F_{2jk} \begin{bmatrix} F_{222} & F_{223} & F_{224} & F_{225} & F_{226} \\ & F_{233} & F_{234} & F_{235} & F_{236} \\ & & F_{244} & F_{245} & F_{246} \\ & & & F_{255} & F_{256} \\ & & & & F_{266} \end{bmatrix};$$

$$F_{3jk} = \begin{bmatrix} F_{333} & F_{334} & F_{335} & F_{336} \\ & F_{344} & F_{345} & F_{346} \\ & & F_{355} & F_{356} \\ & & & F_{366} \end{bmatrix}; \; F_{4jk} = \begin{bmatrix} F_{444} & F_{445} & F_{446} \\ & F_{455} & F_{456} \\ & & F_{466} \end{bmatrix}$$

$$F_{5jk} = \begin{bmatrix} & & \\ & & \\ & F_{555} & F_{556} \\ & & F_{566} \end{bmatrix}; \; F_{6jk} = \begin{bmatrix} & & \\ & & \\ & & \\ & & F_{666} \end{bmatrix}; \tag{7.8}$$

If composite materials are assumed to exhibit identical strengths for the positive and negative shear, the following strength tensors will disappear; $F_i = 0$ (i = 4, 5, 6), $F_{ij} = 0$ (i = 1, 2, 3, j = 4, 5, 6), $F_{ijk} = 0$ (i = 4, 5, 6, j = i, ..., 6, k = j, ..., 6, and i = 1, 2, 3, j = i, ..., 3, k = 4, 5, 6). Therefore, the number of independent second-rank strength tenors is reduced to 3, fourth-rank strength tensors to 12, and sixth-rank strength tensors to 28. It is noteworthy that the simultaneous sign change in the two combined shear stresses does not change the failure strength, but the sign change of one shear stress in the non-principal material coordinate systems will do. Furthermore, the sixth-rank strength tensors $F_{iii} = 0$ (i = 1, 2, 3), because they are redundant and not admissible in polynomial failure criteria (Wu, 1973).

$$F_i = \begin{bmatrix} F_1 \\ F_2 \\ F_3 \end{bmatrix}; \; F_{ij} = \begin{bmatrix} F_{11} & F_{12} & F_{13} & & & \\ & F_{22} & F_{23} & & & \\ & & F_{33} & & & \\ & & & F_{44} & F_{45} & F_{46} \\ & & & & F_{55} & F_{56} \\ & & & & & F_{66} \end{bmatrix} \tag{7.9}$$

$$F_{1jk} = \begin{bmatrix} F_{112} & F_{113} & & & & \\ F_{122} & F_{123} & & & & \\ & F_{133} & & & & \\ & & F_{144} & F_{145} & F_{146} \\ & & & F_{155} & F_{156} \\ & & & & F_{166} \end{bmatrix}; \; F_{2jk} = \begin{bmatrix} & F_{223} & & & & \\ & F_{233} & & & & \\ & & F_{244} & F_{245} & F_{246} \\ & & & F_{255} & F_{256} \\ & & & & F_{266} \end{bmatrix};$$

$$F_{3jk} = \begin{bmatrix} & & & & \\ & & & & \\ & F_{344} & F_{345} & F_{346} \\ & & F_{355} & F_{356} \\ & & & F_{366} \end{bmatrix}; \; F_{4jk} \equiv 0; \; F_{5jk} \equiv 0; \; F_{6jk} \equiv 0 \tag{7.10}$$

The above two assumptions are generally acceptable for the failure of fiber-reinforced composite materials; therefore, 3 second-rank strength tensors, 12 fourth-rank strength tensors and 25 sixth-rank strength tensors are essential to the failure evaluation of composite materials with 3D stress state based on the polynomial failure criteria. Especially, for the delamination failure, all the strength tensors related to the in-plane stress components $\sigma_1$, $\sigma_2$ and $\sigma_6$ shall be equal to zero by imposing the Hashin assumption. Thus there are only one second-rank strength tensor, 4 fourth-rank strength tensors and 3 sixth-rank strength tensors that are left out;

$$F_i = \begin{bmatrix} F_3 \end{bmatrix}; \; F_{ij} = \begin{bmatrix} F_{33} & & \\ & F_{44} & F_{45} \\ & & F_{55} \end{bmatrix} \tag{7.11}$$

$$F_{1jk} \equiv 0; F_{2jk} \equiv 0;$$

$$F_{3jk} = \begin{bmatrix} & & \\ & F_{344} & F_{345} \\ & & F_{355} \end{bmatrix}; \; F_{4jk} \equiv 0; \; F_{5jk} \equiv 0; \; F_{6jk} \equiv 0 \tag{7.12}$$

The reduced number of strength tensors in Equation (7.11) and (7.12) allows it possible to employ the polynomial failure criteria up to the third-order to characterize the delamination failure. The non-interactive strength tensors can be conveniently determined by failure strengths from the uniaxial loading tests, and the interactive ones by the failure strengths from the combined loading tests in one arbitrary coordinate system. The polynomial failure criteria are written in any arbitrary coordinate systems, thereby providing the capabilities of strength tensor transformation through the complete set of non-interactive and interactive strength tensors. Also, these criteria are applicable to the delamination failure at any arbitrary θ-interfaces, because the θ-dependent and directionally-dependent interlaminar strength components can be taken into account by the corresponding strength tensors.

### 7.3.1 Quadratic Delamination Criterion

On the basis of Equation (7.11), the quadratic criterion (up to the second-order) with respect to a θ-interface in the arbitrary 1-2-z coordinate system (see Figure 7.1) can be written as

$$F_3\sigma_z + F_{33}\sigma_z^2 + F_{44}\tau_{1z}^2 + F_{55}\tau_{2z}^2 + 2F_{45}\tau_{1z}\tau_{2z} = 1 \tag{7.13}$$

Substituting Equation (7.2) into Equation (7.13) and expressing the quadratic criterion in terms of stress components in the 1′-2′-z coordinate system, one can obtain the quadratic criterion in principal material coordinate system, i.e.,

$$\begin{aligned} F_3\sigma_z + F_{33}\sigma_z^2 &+ (F_{44}\cos^2\phi + F_{55}\sin^2\phi - 2F_{45}\sin\phi\cos\phi)\tau_{1'z}^2 \\ &+ (F_{44}\sin^2\phi + F_{55}\cos^2\phi + 2F_{45}\sin\phi\cos\phi)\tau_{2'z}^2 \\ &+ [(F_{44} - F_{55})\sin 2\phi + 2F_{45}\cos 2\phi]\tau_{1'z}\tau_{2'z} = 1 \end{aligned} \tag{7.14}$$

Because the 1′-2′-z coordinate system is along the principal material directions, the sign change of only one ILS stress will not change the failure strength because of the inherent symmetry with respect to the 1′ and 2′ axes. Or in other words, there is no shear interaction and thus $F_{45}' = 0$ (Tsai and Wu, 1971). Therefore, the failure criterion in the 1′-2′-z coordinate system shall be

$$F_3'\sigma_z + F_{33}'\sigma_z^2 + F_{44}'\tau_{1'z}^2 + F_{55}'\tau_{2'z}^2 = 1 \tag{7.15}$$

and the strength tensor transformation relationships between the two individual coordinate systems are

$$F_3' = F_3 \tag{7.16.a}$$

$$F_{33}' = F_{33} \tag{7.16.b}$$

$$F_{44}' = F_{44}\cos^2\phi + F_{55}\sin^2\phi - 2F_{45}\sin\phi\cos\phi \tag{7.16.c}$$

$$F_{55}' = F_{44}\sin^2\phi + F_{55}\cos^2\phi + 2F_{45}\sin\phi\cos\phi \tag{7.16.d}$$

$$F_{45}' = (F_{44} - F_{55})\sin 2\phi + 2F_{45}\cos 2\phi = 0 \tag{7.16.e}$$

Then one can determine the shear interactive strength tensor $F_{45}$ in the 1-2-z coordinate system

$$F_{45} = -\frac{\tan 2\phi}{2}(F_{44} - F_{55}) \tag{7.17}$$

Suppose that the uniaxial failure strengths are experimentally characterized along one arbitrary coordinate system, saying with $\phi = \phi_o$; hereafter, Zt and Zc denote the interlaminar tensile and compressive strength components, and $S_{13}$ and $S_{23}$ the two ILS strength components at the θ-interface. The non-interactive strength tensors can be determined by these uniaxial failure strengths (Tsai and Wu, 1971) in the coordinate system with $\phi = \phi_o$.

$$F_3^{\,o} = \frac{Z_c - Z_t}{Z_t Z_c} \tag{7.18.a}$$

$$F_{33}^{\,o} = \frac{1}{Z_t Z_c} \tag{7.18.b}$$

$$F_{44}^{\,o} = \frac{1}{S_{13}^{\,2}} \tag{7.18.c}$$

$$F_{55}^{\,o} = \frac{1}{S_{23}^{\,2}} \tag{7.18.d}$$

Therefore, the quadratic criterion in the coordinate system with $\phi = \phi_o$ can be written as

$$\frac{Z_c - Z_t}{Z_c Z_t}\sigma_z + \frac{1}{Z_c Z_t}\sigma_z^{\,2} + \frac{1}{S_{13}^{\,2}}\tau_{1z}^{\,2} + \frac{1}{S_{23}^{\,2}}\tau_{2z}^{\,2} - \tan 2\phi_o\left(\frac{1}{S_{13}^{\,2}} - \frac{1}{S_{23}^{\,2}}\right)\tau_{1z}\tau_{2z} = 1 \tag{7.19}$$

The first two terms in the above equation make the developed delamination criteria have the capabilities to distinguish the effects of the interlaminar tensile and compressive stress $\sigma_z$ on the delamination failure, depending on the magnitudes of Zt and Zc. The interlaminar compressive stress with the magnitude slightly lower than Zc can resist the delamination failure if Zc > Zt, because the value of the two terms related to $\sigma_z$ are less than zero under such circumstances. However, if the magnitude of the interlaminar compressive stress is close to Zc, it makes contribution to the delamination initiation, because the value of the terms related to $\sigma_z$ is larger

than zero. Similar effects are also found on the delamination initiation imposed by the interlaminar tensile stress if Zc < Zt. In most cases, the interlaminar compressive strength Zc is much higher than the interlaminar tensile strength Zt, therefore the common concepts have been already formed that the interlaminar compressive stress has the potential to constrain the delamination initiation.

For the purposes of convenience, the quadratic criterion should be written in any arbitrary coordinate systems (represented by $\phi$) in terms of the uniaxial failure strengths experimentally characterized. Using the transformation relationships in Equation (7.16), one can easily obtain the fourth-rank strength tensors for the quadratic criterion in Equation (7.13).

$$\begin{aligned} F_{44} &= [\cos^2\phi_o \cos^2\phi + \sin^2\phi_o \sin^2\phi + \tan(2\phi_o)\sin\phi_o \cos\phi_o \cos(2\phi)]\frac{1}{S_{13}^{\ 2}} \\ &+[\sin^2\phi_o \cos^2\phi + \cos^2\phi_o \sin^2\phi - \tan(2\phi_o)\sin\phi_o \cos\phi_o \cos(2\phi)]\frac{1}{S_{23}^{\ 2}} \end{aligned} \tag{7.20.a}$$

$$\begin{aligned} F_{55} &= [\cos^2\phi_o \sin^2\phi + \sin^2\phi_o \cos^2\phi - \tan(2\phi_o)\sin\phi_o \cos\phi_o \cos(2\phi)]\frac{1}{S_{13}^{\ 2}} \\ &+[\sin^2\phi_o \sin^2\phi + \cos^2\phi_o \cos^2\phi + \tan(2\phi_o)\sin\phi_o \cos\phi_o \cos(2\phi)]\frac{1}{S_{23}^{\ 2}} \end{aligned} \tag{7.20.b}$$

$$F_{34} = -\frac{\sin(2\phi)}{2\cos(2\phi_o)}\left(\frac{1}{S_{13}^{\ 2}} - \frac{1}{S_{23}^{\ 2}}\right) \tag{7.20.c}$$

To this point, the quadratic delamination criterion has been developed in any arbitrary coordinate systems and can be written in terms of the uniaxial failure strengths experimentally characterized in one arbitrary coordinate system.

### 7.3.2 Cubic Delamination Criterion

On the basis of Equations (7.11) and (7.12), the cubic criterion (up to the third-order) with respect to the θ-interface in the arbitrary 1-2-z coordinate system can be written as

$$\begin{aligned} &F_3\sigma_z + F_{33}\sigma_z^{\ 2} + F_{44}\tau_{1z}^{\ 2} + F_{55}\tau_{2z}^{\ 2} + 2F_{45}\tau_{1z}\tau_{2z} + \\ &3F_{344}\sigma_z\tau_{1z}^{\ 2} + 3F_{355}\sigma_z\tau_{2z}^{\ 2} + 3F_{345}\sigma_z\tau_{1z}\tau_{2z} = 1 \end{aligned} \tag{7.21}$$

Substituting Equation (7.2) into Equation (7.21), the cubic criterion in terms of the stress components in the 1′-2′-z coordinate system can be generated.

$$\begin{aligned} &F_3\sigma_z + F_{33}\sigma_z{}^2 + (F_{44}\cos^2\phi + F_{55}\sin^2\phi - 2F_{45}\sin\phi\cos\phi)\tau_{1'z}{}^2 + \\ &(F_{44}\sin^2\phi + F_{55}\cos^2\phi + 2F_{45}\sin\phi\cos\phi)\tau_{2'z}{}^2 + \\ &[(F_{44} - F_{55})\sin 2\phi + 2F_{45}\cos 2\phi]\tau_{1'z}\tau_{2'z} + \\ &3(F_{344}\cos^2\phi + F_{355}\sin^2\phi - F_{345}\sin\phi\cos\phi)\sigma_z\tau_{1'z}{}^2 + \\ &3(F_{344}\sin^2\phi + F_{355}\cos^2\phi + F_{345}\sin\phi\cos\phi)\sigma_z\tau_{2'z}{}^2 + \\ &3(F_{344}\sin 2\phi - F_{355}\sin 2\phi + F_{345}\cos 2\phi)\sigma_z\tau_{1'z}\tau_{2'z} = 1 \end{aligned} \tag{7.22}$$

Because the 1′-2′-z coordinate system is along the principal material direction, the interactive tensors are equal to zero; i.e., $F_{45}' = 0$ and $F_{345}' = 0$. Thus, the cubic criterion in the 1′-2′-z coordinate system can be written as

$$F_3'\sigma_z + F_{33}'\sigma_z{}^2 + F_{44}'\tau_{1'z}{}^2 + F_{55}'\tau_{2'z}{}^2 + 3F_{344}'\sigma_z\tau_{1'z}{}^2 + 3F_{355}'\sigma_z\tau_{2'z}{}^2 = 1 \tag{7.23}$$

Comparing Equations (7.22) and (7.23), one can obtain the strength tensor transformation relationships between the two coordinate systems; the second- and fourth-rank tensors are given in Equations (7.16) and (7.17), and the sixth-rank tensors are given as follows:

$$F_{344}' = F_{344}\cos^2\phi + F_{355}\sin^2\phi - F_{345}\sin\phi\cos\phi \tag{7.24.a}$$

$$F_{355}' = F_{344}\sin^2\phi + F_{355}\cos^2\phi + F_{345}\sin\phi\cos\phi \tag{7.24.b}$$

$$F_{345} = -\tan 2\phi(F_{344} - F_{355}) \tag{7.24.c}$$

Now considering the cubic criterion in the coordinate system with $\phi = \phi_o$, the second- and fourth-rank strength tensors $F_3°$, $F_{33}°$, $F_{44}°$ and $F_{55}°$ are those given in Equation (7.18). Finally, the cubic criterion in the coordinate system with $\phi = \phi_o$ can be written in terms of the uniaxial failure strengths.

$$\frac{Z_c - Z_t}{Z_c Z_t}\sigma_z + \frac{1}{Z_c Z_t}\sigma_z^2 + \frac{1}{S_{1z}^2}\tau_{1z}^2 + \frac{1}{S_{2z}^2}\tau_{2z}^2 + \tan 2\phi_o\left(\frac{1}{S_{13}^2} - \frac{1}{S_{23}^2}\right)\tau_{1z}\tau_{2z} + 3F_{344}^{\circ}\sigma_z\tau_{1z}^2 + 3F_{355}^{\circ}\sigma_z\tau_{2z}^2 - 3\tan 2\phi_o(F_{344}^{\circ} - F_{355}^{\circ})\sigma_z\tau_{1z}\tau_{2z} = 1 \quad (7.25)$$

Similarly, the cubic criterion should be written in any arbitrary coordinate systems with the forms of the uniaxial failure strengths experimentally characterized in the coordinate system with $\phi = \phi_o$. The fourth-rank tensor transformation relationships are same as those in Equation (7.20) and the sixth-rank ones can be derived using Equation (7.24):

$$F_{344} = [\cos^2\phi_o\cos^2\phi + \sin^2\phi_o\sin^2\phi + \tan(2\phi_o)\sin\phi_o\cos\phi_o\cos(2\phi)]F_{344}^{\circ} + [\sin^2\phi_o\cos^2\phi + \cos^2\phi_o\sin^2\phi - \tan(2\phi_o)\sin\phi_o\cos\phi_o\cos(2\phi)]F_{355}^{\circ} \quad (7.26.a)$$

$$F_{355} = [\cos^2\phi_o\sin^2\phi + \sin^2\phi_o\cos^2\phi - \tan(2\phi_o)\sin\phi_o\cos\phi_o\cos(2\phi)]F_{344}^{\circ} + [\sin^2\phi_o\sin^2\phi + \cos^2\phi_o\cos^2\phi + \tan(2\phi_o)\sin\phi_o\cos\phi_o\cos(2\phi)]F_{355}^{\circ} \quad (7.26.b)$$

$$F_{345} = -\frac{\sin(2\phi)}{\cos(2\phi_o)}(F_{344}^{\circ} - F_{355}^{\circ}) \quad (7.26.c)$$

Therefore, the two interactive tensors $F_{344}$ and $F_{355}$ must be determined in one arbitrary coordinate system before the cubic criterion can be used to evaluate the delamination failure. Two useful values of $F_{344}^{\circ}$ and $F_{355}^{\circ}$ are hereby recommended, which also can be determined by the uniaxial failure strengths:

$$F_{344}^{\circ} = -\frac{1}{3\sqrt{ZtZc}S_{13}^2} \quad (7.27.a)$$

$$F_{355}^{\circ} = -\frac{1}{3\sqrt{ZtZc}S_{23}^2} \quad (7.27.b)$$

When the experimental data for $F_{344}^{\circ}$ and $F_{355}^{\circ}$ are not available, the corresponding values from above equation can be tentatively selected for the evaluation of delamination failure.

### 7.3.3 Determination of Sixth-Rank Strength Tensors

The second- and fourth-rank strength tensors in quadratic and cubic delamination criteria can be determined by the uniaxial failure strengths in one arbitrary coordinate system. However, the sixth-rank strength tensors $F_{344}$ and $F_{355}$, which physically represent the interactive effects between interlaminar normal and shear stress components in the cubic delamination criterion, are unknown to this point. A feasible method to determine these interactive strength tensors is to perform combined loading tests, such as various combinations of $\sigma_z$ and $\tau_{1z}$ or $\sigma_z$ and $\tau_{2z}$, and best fit the experimental results. However, it is still questionable so far whether the values of the interactive tensors depend on the ratio of the combined stress components. Wu (1972) implied that the interactive tensors are material properties and independent of the stress ratios. This argument is based on the fact that the variation of the interactive tensors experimentally characterized was found to be dependent on the magnitudes of the stress ratios and the magnitudes of the tensors themselves, therefore only the absolute resolutions of these tensors are meaningful. The interactive tensors could be experimentally characterized using the optimal magnitudes of the stress ratios. Nevertheless, the interactive tensors in various failure criteria are generally assumed to be independent of the magnitudes of the stress ratios (Tsai and Wu, 1971, Tennyson *et al.*, 1978, Yeh and Kim, 1996). In the cubic delamination criterion developed herein, this assumption is also adopted.

Difficulties in experimental determination notwithstanding, the range of the sixth-rank strength tensors could be determined by imposing some constraints on the cubic delamination criterion so as to generate physically accepted roots. As an example, let's consider the combination of $\sigma_z$ and $\tau_{1z}$ ($\tau_{2z} = 0$) in the coordinate system with $\phi = \phi_o$; in general, the ratio of $\sigma_z$ and $\tau_{1z}$ could be arbitrary. In order to cover all the magnitudes of the ratio of $\sigma_z$ and $\tau_{1z}$, it is postulated that these two stress components are related by a load parameter $\lambda$,

$$\sigma_z = \lambda k_1 \tag{7.28.a}$$

$$\tau_{1z} = \lambda k_2 \tag{7.28.b}$$

where $0<|k_1|<1$ and $k_2 = \pm\sqrt{1-k_1^2}$. Thus the cubic delamination criterion in Equation (7.25) can be expressed as a third-order failure equation in terms of the load parameter,

$$a\lambda^3 + b\lambda^2 + c\lambda^2 - 1 = 0 \tag{7.29}$$

where

$$a = 3F_{344}^{\circ} k_1 k_2^2 \tag{7.30.a}$$

$$b = \frac{1}{Z_c Z_t} k_1^2 + \frac{1}{S_{13}^2} k_2^2 \tag{7.30.b}$$

$$c = \frac{Z_c - Z_t}{Z_c Z_t} k_1 \tag{7.30.c}$$

and the associated discriminate of Equation (7.29) is

$$D = 27a^2 + a(4c^3 + 18bc) - (4b^3 + b^2c^2) \tag{7.31}$$

Depending on the value of the discriminate, the solutions of Equation (7.29) possess three cases:

(1) two complex root and one real root, if $D > 0$;

(2) three real roots, two of which are identical, if $D = 0$;

(3) three distinct real roots, if $D < 0$;

It is obvious that Case 1 is not physically accepted, since Requirement 4 that corresponding to two colinear loading paths, the failure equation generates two effective distinct roots can not be satisfied. This requirement also can be simply explained that two real roots of $\lambda$, one positive and the other negative, shall be obtained from the failure equation. Since the loading path is designated as soon as the value of $k_1$ is given, the two opposite roots imply that composite materials are of two failure strengths in the opposite loading directions along the colinear loading paths in the stress space. Case 2 presents two distinct real roots, and the interactive strength tensor $F_{344}^{\circ}$ can be directly determined by the condition $D = 0$. However, it is noted that in Case 2 the value of $F_{344}^{\circ}$ is not constant, but a function of $k_1$ in order to satisfy the condition $D = 0$ inside the entire domain of $k_1$ ($0 < |k_1| < 1$). Using the non-constant value of $F_{344}^{\circ}$, one would find that the failure curve displays singularity in the stress space at $k_1 = 0$. This indicates that the cubic criterion predicts the failure strengths around $k_1 = 0$ that are far away from the value of the ILS strength $S_{23}$ with respect to $k_2 = 1$ or $-1$. Therefore, Case 2 presents the failure curve with

singularity in stress spaces, and thus can not be physically accepted on the basis of Requirement 5 aforementioned.

Case 3 presents three distinct real roots, one or two positive and the remaining negative according to the signs of $k_1$ and $k_2$. Wherein two opposite roots are effective and present the closed failure curve in stress spaces that satisfy Requirements 4 and 5 aforementioned. The other one usually presents the open failure curve and the corresponding failure strengths in combined stress states are much higher than the unaxial failure strengths, and thus is not effective (Jiang and Tennyson, 1989). Therefore, the range of $F_{344}°$, which generates effective roots for the failure equation, can be determined from the condition $D < 0$. Suppose $a_1$ and $a_2$ are the two generic roots determined by $D = 0$ and $a_1 < a_2$ at any given value of $k_1$. Since $a_1$ and $a_2$ are functions of the value of $k_1$, the effective range of $F_{344}°$ in the entire domain of $k_1$ shall be: max $[a_1/(3k_1k_2^2)] < F_{344}° <$ min $[a_2/(3k_1k_2^2)]$ according to the assumption that $F_{344}$ and $F_{355}$ are independent of the combined stress states. Likewise, the effective range of $F_{355}°$ can be determined in the same manner by assuming $0<|k_1|<1$ and $k_3=\pm\sqrt{1-k_1^2}$, and shall be: max $[a_1/(3k_1k_3^2)] < F_{355}° <$ min $[a_2/(3k_1k_3^2)]$.

### 7.3.4 Discussions

As shown in Equations (7.13) and (7.20), the quadratic delamination criterion is only in terms of uniaxial failure strengths. Therefore, this criterion can be conveniently employed to evaluate the delamination failure in any arbitrary coordinate systems, if the uniaxial loading tests are already performed in one arbitrary system. However, the quadratic criterion does not have the interactive terms between the interlaminar normal and shear stresses, which would potentially affect its feasibility to generally model the delamination failure towards different material systems.

The cubic delamination criterion in Equations (7.21) and (7.26) covers the quadratic one, if the sixth-rank strength tensors $F_{344}$ and $F_{355}$ are set to be zero. Therefore, the quadratic criterion could be viewed as a special case of the cubic one. Although it is difficult to determine the values of $F_{344}$ and $F_{355}$, the cubic criterion is versatile and can accurately evaluate the delamination failure for different material systems. This intent could be achieved by adjusting

the values of the sixth-rank strength tensors so as to best fit the experimental results. The numerical determination of the failure strengths based on the cubic criterion along $\phi = \phi_o$ is explained as follows. First of all, it is supposed that the values of the sixth-rank strength tensors are known *a priori* and within the range discussed previously. For a given laminated composite, the magnitudes of the three interlaminar stress components are only governed by the load parameter $\lambda$,

$$\sigma_z = \lambda k_1 \tag{7.32.a}$$

$$\tau_{1z} = \lambda k_2 \tag{7.32.b}$$

$$\tau_{2z} = \lambda k_3 \tag{7.32.c}$$

where it is noteworthy that $k_i$ ($i = 1, 2, 3$) are of determined values. Substituting Equation (7.32) into the cubic criterion in Equation (7.25), one can obtain the third-order failure equation same as in Equation (7.29); a, b and c are also of determined values but their expressions are changed.

$$a = 3F_{344}{}^{o} k_1 k_2{}^2 + 3F_{355}{}^{o} k_1 k_3{}^2 + 3\tan 2\phi_o (F_{355}{}^{o} - F_{344}{}^{o}) k_1 k_2 k_3 \tag{7.33.a}$$

$$b = \frac{1}{Z_c Z_t} k_1{}^2 + \frac{1}{S_{13}{}^2} k_2{}^2 + \frac{1}{S_{23}{}^2} k_3{}^2 + \tan 2\phi_o \left(\frac{1}{S_{13}{}^2} - \frac{1}{S_{23}{}^2}\right) \tag{7.33.b}$$

$$c = \frac{Z_c - Z_t}{Z_c Z_t} k_1 \tag{7.33.c}$$

Therefore, the three real distinct roots of the third-order failure equation are determined by

$$\lambda_1 = \sqrt[3]{-\frac{q}{2} + \sqrt{\left(\frac{q}{2}\right)^2 + \left(\frac{p}{3}\right)^3}} + \sqrt[3]{-\frac{q}{2} - \sqrt{\left(\frac{q}{2}\right)^2 + \left(\frac{p}{3}\right)^3}} - \frac{b}{3a} \tag{7.34.a}$$

$$\lambda_2 = \omega \sqrt[3]{-\frac{q}{2} + \sqrt{\left(\frac{q}{2}\right)^2 + \left(\frac{p}{3}\right)^3}} + \omega^2 \sqrt[3]{-\frac{q}{2} - \sqrt{\left(\frac{q}{2}\right)^2 + \left(\frac{p}{3}\right)^3}} - \frac{b}{3a} \tag{7.34.b}$$

$$\lambda_3 = \omega^2 \sqrt[3]{-\frac{q}{2} + \sqrt{\left(\frac{q}{2}\right)^2 + \left(\frac{p}{3}\right)^3}} + \omega \sqrt[3]{-\frac{q}{2} - \sqrt{\left(\frac{q}{2}\right)^2 + \left(\frac{p}{3}\right)^3}} - \frac{b}{3a} \tag{7.34.c}$$

and

$$p = -\frac{b^2}{3a^2} + \frac{b}{a} \tag{7.35.a}$$

$$q = \frac{2b^3}{27a^3} - \frac{bc}{3a^2} - \frac{1}{a} \tag{7.35.b}$$

$$\omega = \frac{-1 + \sqrt{3}i}{2} \tag{7.35.c}$$

wherein only two roots are effective. Depending on the quadrants in stress spaces, it is possible that each one is ineffective in the three roots $\lambda_i$ (i = 1, 2, 3). Thus, in different quadrants, one should select different combinations of $\lambda_i$'s for the effective roots.

The strength tensor transformation and the failure surface with respect to the 30°-interface are demonstrated below on the basis of the quadratic and cubic delamination criteria. The interlaminar strength components are retrieved from the experimental results in Chapter 5. The ILS strengths are experimentally characterized along one of the fiber directions of two plies adjacent to the 30°-interfaces, therefore $\phi_o = \theta/2 = 15°$. Because the interlaminar tensile test was not performed and the interlaminar compressive test was only on the unidirectional and cross-ply specimens, the in-plane transverse tensile strength is used as the approximation to the interlaminar tensile strength Zt and the interlaminar compressive strength of unidirectional laminates as Zc at the 30°-interface. Therefore, the interlaminar tensile and compressive strengths hereby used are not the actual ones that are experimentally characterized at the θ-interfaces and dependent on the FOD angles. These approximations are acceptable, because in Equations (7.19) and (7.25) the terms related to the interlaminar normal stress does not play a dominant role in determining the delamination failure, compared with those related to the ILS stresses. Hence, the magnitudes of the interlaminar strengths hereby employed are: Zt = 41.21 MPa, Zc = 189.83 MPa, $S_{13}$ = 55.48 MPa and $S_{23}$ = 67.53 MPa. It is noteworthy that only the mean values for all the interlaminar strengths are taken into consideration, and thus the mathematical operations are performed in a deterministic sense.

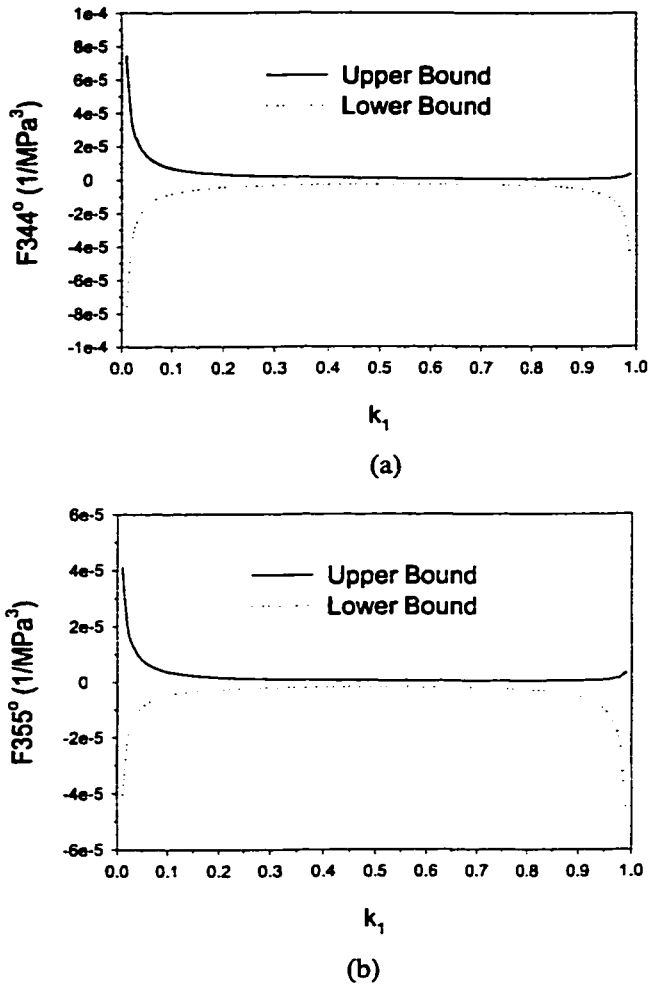


**Figure 7.2.** The upper and lower bounds for the sixth-rank strength tensors along $\phi$ = 15° at the 30°-interface; (a) F344° and (b) F355°.

First of all, the ranges of the sixth-rank strength tensors $F_{344}$ and $F_{355}$ at the 30°-interface are demonstrated using the interlaminar strengths experimentally characterized along one of the fiber orientations of the two adjacent plies. Correspondingly, the 1 axis is fixed along the fiber direction, i.e., $\phi_o$ = 15° in the above formulations, and thus the values of $F_{344}^{\circ}$ and $F_{355}^{\circ}$ are given below are with respect to this coordinate system. The variations of $F_{344}^{\circ}$ and $F_{355}^{\circ}$ at each given value of $k_1$ determined by D = 0 are plotted in Figure 7.2, wherein $0<|k_1|<1$, $k_2=\pm\sqrt{1-k_1^2}$ and $k_3=0$ for $F_{344}^{\circ}$, and $0<|k_1|<1$, $k_2=0$ and $k_3=\pm\sqrt{1-k_1^2}$ for $F_{355}^{\circ}$. The values of $F_{344}^{\circ}$ and $F_{355}^{\circ}$ are found to be almost constant within a wide interval, and vary sharply only when $k_1$ is close to 0 or 1. This implies that the sixth-rank strength tensors $F_{344}^{\circ}$ and $F_{355}^{\circ}$, representing the interaction between the interlaminar normal and shear stresses, do not strongly depend on the

stress ratio within a wide interval. Therefore, the assumption is confirmed to be reasonable that the interactive strength tensors are independent of the ratio of the combined stresses. In the entire domain of $k_1$, the minimum positive value of $F_{344}^{\circ}$ is $5.71\times10^{-7}$ $MPa^{-3}$ and the maximum negative value is $-2.63\times10^{-6}$ $MPa^{-3}$, while the minimum positive value of $F_{355}^{\circ}$ is $3.85\times10^{-7}$ $MPa^{-3}$ and the maximum negative value is $-1.77\times10^{-6}$ $MPa^{-3}$. Following the aforementioned independence assumption, the sixth-rank strength tensors at the 30°-interface in the specified coordinate system (i.e., $\phi = 15°$) shall be within $-2.63\times10^{-6}$ $MPa^{-3} < F_{344}^{\circ} < 5.71\times10^{-7}$ $MPa^{-3}$ and $-1.77\times10^{-6}$ $MPa^{-3} < F_{355}^{\circ} < 3.85\times10^{-7}$ $MPa^{-3}$ in order that the failure equations can generate two effective roots. Hence, the selective ranges for $F_{344}^{\circ}$ and $F_{355}^{\circ}$ are preferably narrow after imposing the constraint conditions on the discriminate of the third-order failure equations. It should be noted that the values of $F_{344}^{\circ}$ and $F_{355}^{\circ}$ recommended by Equation (7.27) are within the previous ranges.

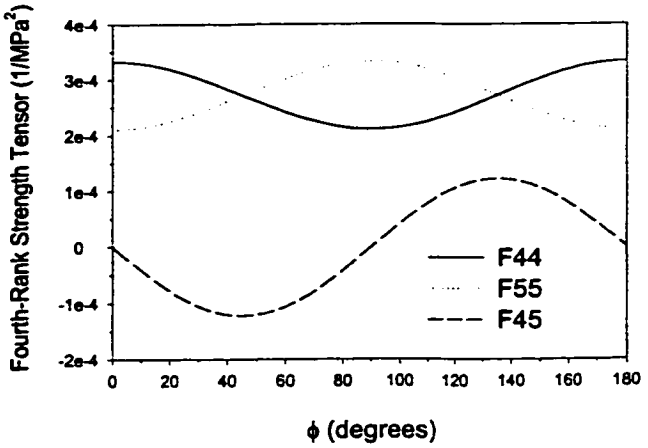


**Figure 7.3.** Variations of fourth-rank strength tensors with $\phi$ at the 30°-interface.

Then, the strength tensor transformation is also demonstrated through the variations of the strength tensors in different coordinate systems, which are represented as the functions of the angle $\phi$. Through Equation (7.20), the fourth-rank strength tensors can be completely determined based on the experimentally characterized interlaminar strengths, and the corresponding variations with respect to $\phi$ are displayed in Figure 7.3. By using $F_{344}^{\circ} = -1.224\times10^{-6}$ $/MPa^3$ and $F_{355}^{\circ} = -8.262\times10^{-7}$ $/MPa^3$ derived from Equation (7.27), the variations of $F_{344}$ and $F_{355}$ with respect to $\phi$ are also calculated through Equation (7.26) and displayed in Figure 7.4. It is observed that both the fourth- and sixth-rank strength tensors vary as a trigonometric function of $\phi$ in each case. There exists a phase angle difference with a value of 90° between $F_{44}$ and $F_{55}$, and

$F_{344}$ and $F_{355}$; i.e., the pair of strength tensors in each case is identical to each other at two values of $\phi$ with the difference equal to 90°. This is because the two ILS stresses are exchanged in the delamination criteria when the coordinate system is rotated at an angle of 90° and are quadratic in the related terms. Furthermore, the values of $F_{45}$ and $F_{345}$, which represent the interaction between the two ILS stresses in non-principal coordinate systems, are of opposite signs with $\phi$ differentiated by 90°. This could be explained by the fact that the ILS stresses are not quadratic in the related terms of the delamination criteria, and the sign of one ILS stress is changed after the aforementioned rotation of 90° [also see Equation (7.2)].

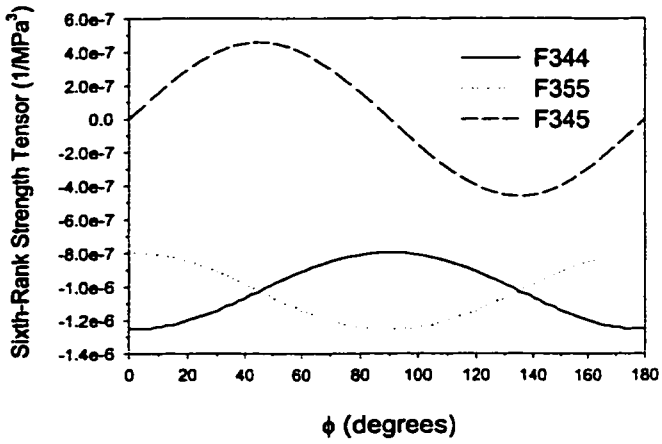


**Figure 7.4.** Variations of sixth-rank strength tensors with $\phi$ at the 30°-interface.

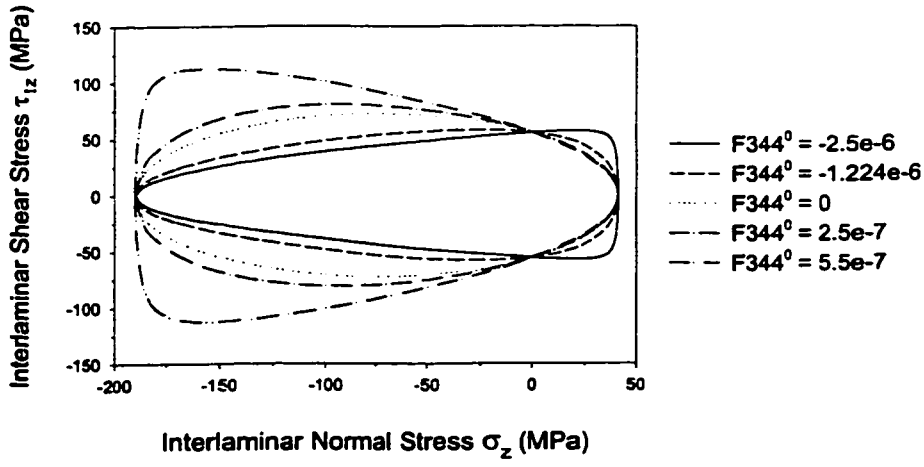


**Figure 7.5.** Failure curves with different values of $F_{344}{}^{\circ}$ from the cubic delamination criterion at the 30°-interface.

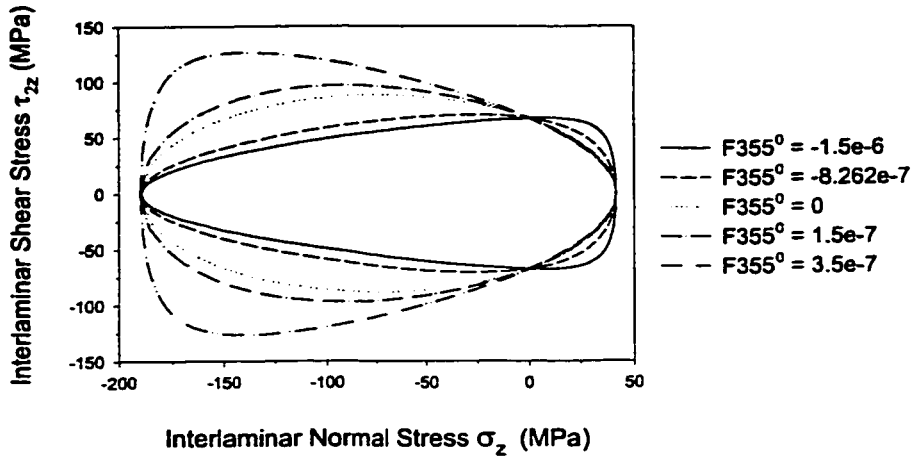


**Figure 7.6.** Failure curves with different values of $F_{355}°$ from the cubic delamination criterion at the 30°-interface.

Finally, the failure curves determined by the quadratic and cubic delamination criteria are demonstrated with different values of $F_{344}°$ and $F_{355}°$ employed, which are illustrated in Figures 7.5 and 7.6. In particular, the failure curves with $F_{344}° = 0$ and $F_{355}° = 0$ represent the quadratic delamination criterion. It is found that the shapes of the failure curves, or in other words the predicted failure strengths, strongly depend on the values of $F_{344}°$ and $F_{355}°$. When the values are close to the associated lower bounds, the delamination criteria predict high failure strengths for $\sigma_z > 0$, but low failure strengths for $\sigma_z < 0$. When the values are close to the higher bounds, low failure strengths are predicted for $\sigma_z > 0$, but high failure strengths for $\sigma_z < 0$. Especially, the failure curves with various values of interactive tensors exhibit significant difference when $\sigma_z$ is in the vicinity of Zt or -Zc. The failure curves with the interactive tensors close to the associated lower bounds make no physical sense and are thus ineffective, because the values of $\tau_{1z}$ and $\tau_{2z}$ along the failure curves are even higher than the pure shear, or ILS strength component $S_{13}$ and $S_{23}$. This is contrary to the common knowledge that both the interlaminar tensile and shear stresses make contributions to generating the delamination failure. The failure curves with the interactive tensors close to the associated higher bounds show the values of $\tau_{1z}$ and $\tau_{2z}$ are higher than the ILS strength components $S_{13}$ and $S_{23}$. This is physically acceptable because the interlaminar compressive stress can resist the delamination initiation when its magnitude is lower than the interlaminar compressive strength. The characteristics of composite materials will determine how much contribution is made by the interlaminar compressive stress to resisting the delamination failure. The cubic delamination criterion is therefore very flexible and can best fit the experimental results by adjusting the sixth-rank strength tensors. Moreover, by adopting the

interactive tensors close to the associated higher bounds, it can be applied to some special types of composite materials in which the interlaminar compressive stress has the strong capability to resist the delamination initiation. The quadratic criterion and the cubic criterion with small values of interactive tensors are applicable to general types of composite materials.

## 7.4 PROBABILISTIC EVALUATION OF DELAMINATION INITIATION

The two innovative delamination criteria are hereby employed to evaluate the random delamination initiation induced by edge effect interlaminar stresses in laminated composites with straight free edges (see Figure 7.7). The numerical results will demonstrate the probability distributions of failure strength $\sigma_u$ of laminated composites governed by delamination initiation. Two types of G40-800/5276-1 laminates are considered with the lay-ups $[15/-15/0]_s$ and $[0/45/-45/0]_s$ respectively. Thus, each laminated composite consists of a number of $\theta$-interfaces and the effects of the $\theta$-dependent ILS strength components on the delamination initiation can be taken into consideration. The randomness involved with the delamination initiation is assumed to result from the large scatter of interlaminar strength components, as shown in Chapters 5 and 6. The other random sources, such as stiffness, fiber orientation and ply thickness and so on, are not taken into account, because the degree of randomness from these random sources is much lower than that from the random interlaminar strength components.

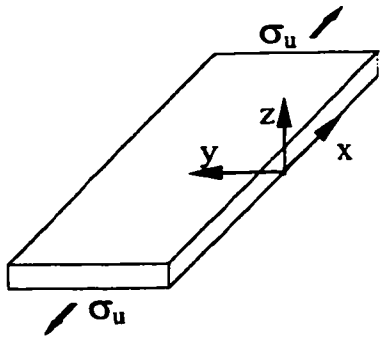


**Figure 7.7.** Schematic description of laminated composites with straight free edges.

Three steps are involved to perform the probabilistic evaluation of delamination initiation: (1) calculating the interlaminar stresses at each interface at free edges; (2) generating random numbers of the interlaminar strength components with given probability density functions; and (3) calculating the sample values of the failure strength in each random number

combination of the interlaminar strength components. In the following, both the calculation of interlaminar stresses and the mathematical operation of delamination criteria are dealt with in the x-y-z coordinate system. Therefore, the strength tensors will be calculated along this coordinate system using Equations (7.20) and (7.26).

### 7.4.1 Interlaminar Stresses at Straight Free Edges

In the regions adjacent to the straight edges of laminated composites, a 3D stress state is generated due to the edge effects, even when the laminates are subjected to in-plane loading. Dependent on the configuration of the laminated composites, the 3D stress state could be large enough to generate the delamination initiation. The quadratic and cubic delamination criteria developed previously can efficiently evaluate the delamination initiation due to the edge effects by taking into consideration the θ-dependent and directionally-dependent ILS strength components.

The interlaminar stresses at each interface in the laminated composites are calculated using the variational solutions developed in Chapter 3, as a special case with straight free edges, therefore no randomness is considered in the interlaminar stress state. It should be noted that the variational solutions degenerated to the straight free edges are identical to that developed by Kassapagolou (1990). Furthermore, because the interlaminar stresses at the free edges are of weak singularity, the so-called "average stress criterion" is employed, which takes the average stress values over the characteristic length away from the free edges to account for the stress singularity. By referring to numerous papers (see Table 2.1), the characteristic length is hereby assumed to be equal to one ply thickness; i.e., $a_o$ = 0.185 mm, although it has been experimentally shown that the characteristic length for the singular stresses seems to be dependent on the stress distribution, geometry size of discontinuities, and so on (Chang *et al.*, 1984). Therefore, each interlaminar stresses in the quadratic and cubic criteria shall be replaced by the corresponding average values, i.e.,

$$\sigma_{,ave} = \frac{1}{a_0}\int_0^{a_0} \sigma dy \tag{7.36}$$

where $\sigma$ symbolically denotes the three interlaminar stresses calculated using the formulations in Chapter 3. The interlminar stresses at each interface in $[15/-15/0]_s$ and $[0/45/-45/90]_s$ laminated composites are displayed in Figures 7.8 and 7.9, and their average values over the characteristic length are tabulated in Tables 7.1 and 7.2. All the interlaminar stresses are normalized with respect to the applied load, and thus the failure load $\sigma_u$ can be easily calculated by substituting the average stress values into the delamination criteria. It can be seen that the ILS stresses in the $[15/-15/0]_s$ laminate are dominant, while the interlaminar normal stresses are dominant in the $[0/45/-45/90]_s$ laminate. Therefore the delamination mechanisms are different between these two types of laminated composites. In the $[15/-15/0]_s$ laminate, the disintegration failure happens immediately following the delamination initiation which will be generated by the ILS stresses (Soni and Kim, 1986). The $[0/45/-45/90]_s$ laminate can further carry loading after the delamination initiation which will be generated by the interlaminar normal stress (Zhou and Sun, 1990)

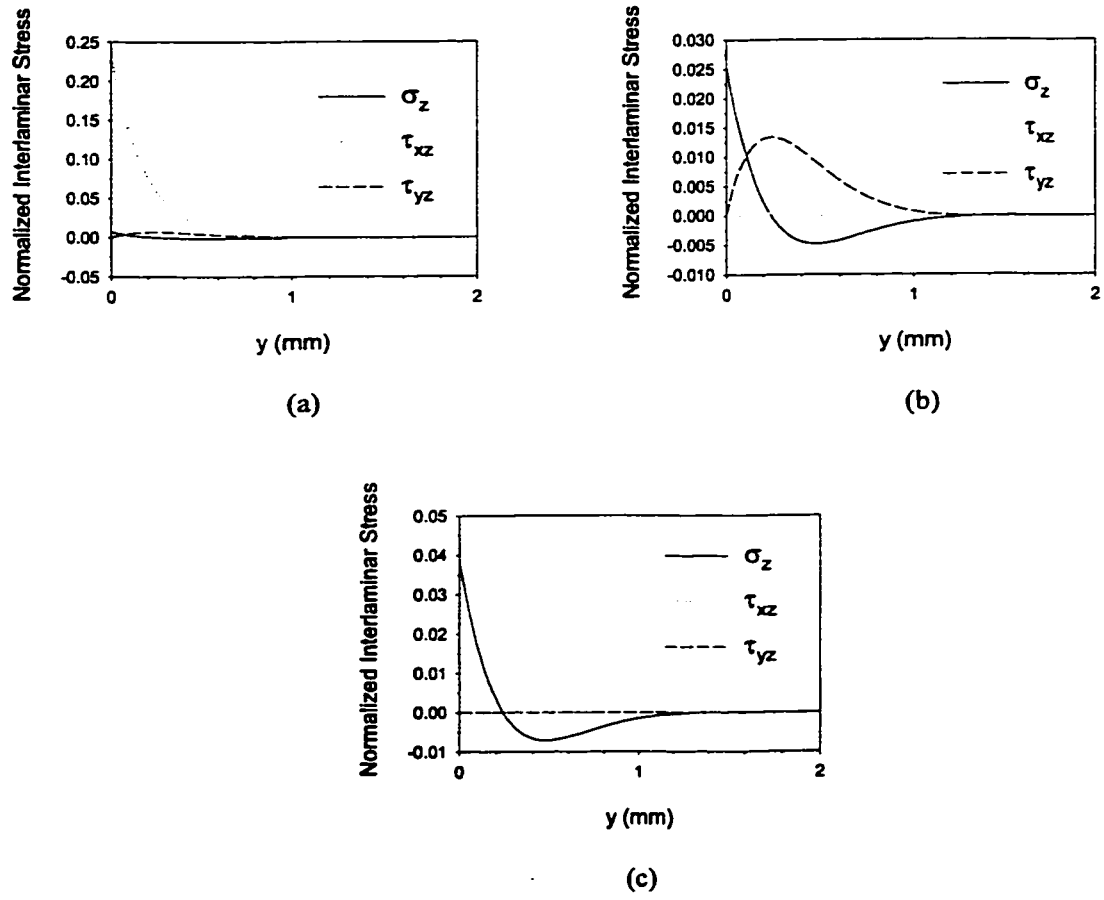


**Figure 7.8.** Interlaminar stress distribution at the free edge in the $[15/-15/0]_s$ laminate; (a) at the 15/-15 interface, (b) at the –15/0 interface and (c) at the midplane.

**Table 7.1.** The average interlaminar stress values at each interface in the $[15/-15/0]_s$ laminate.

| | 15/-15 interface (30°-interface) | -15/0 interface (15°-interface) | 0/0 interface (0°-interface) |
|---|---|---|---|
| $\sigma_{z,ave}$ | 0.0032370 | 0.0129481 | 0.0194221 |
| $\tau_{xz,ave}$ | 0.1449574 | 0.0000000 | 0.0000000 |
| $\tau_{yz,ave}$ | 0.0041622 | 0.0083245 | 0.0000000 |

**Table 7.2.** The average interlaminar stress values at each interface in the $[0/45/-45/90]_s$ laminate.

| | 0/45 interface (45°-interface) | 45/-45 interface (90°-interface) | -45/90 interface (45°-interface) | 0/0 interface (0°-interface) |
|---|---|---|---|---|
| $\sigma_{z,ave}$ | 0.0000599 | 0.0286192 | 0.1140575 | 0.1709965 |
| $\tau_{xz,ave}$ | 0.0000000 | 0.1156283 | 0.0000000 | 0.0000000 |
| $\tau_{yz,ave}$ | 0.0000730 | 0.0347595 | 0.0694459 | 0.0000000 |

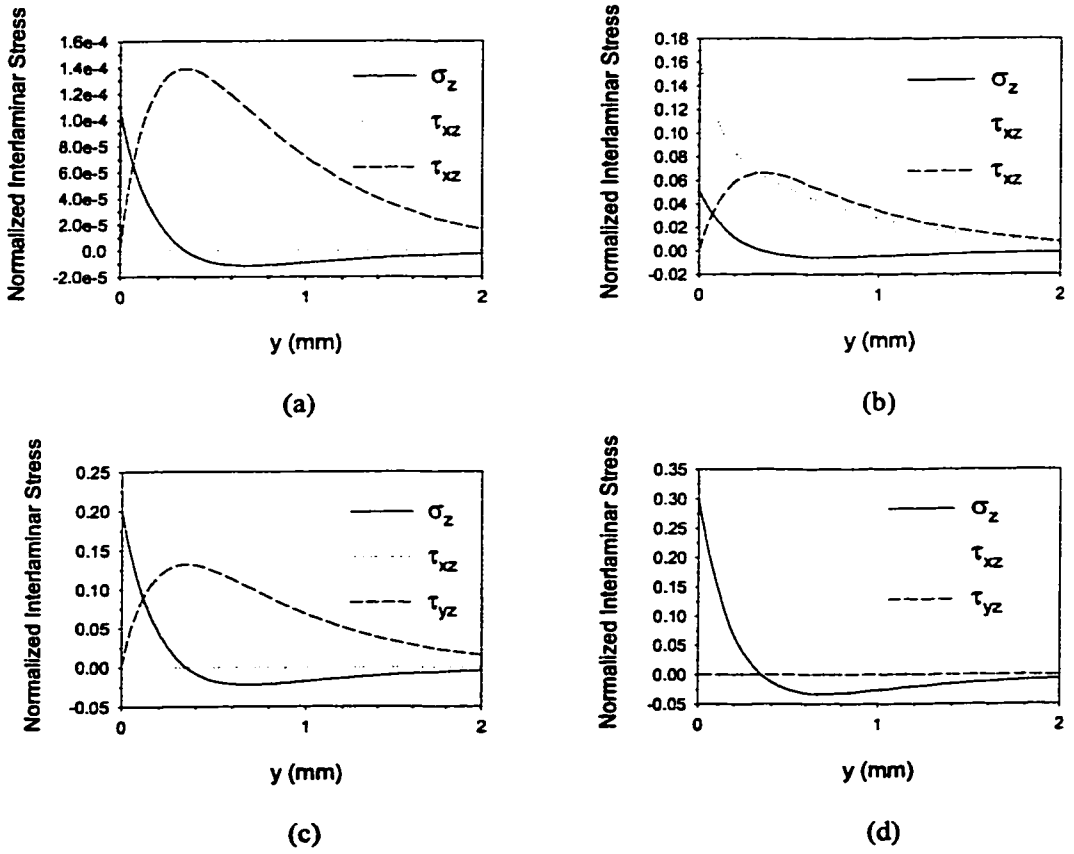


**Figure 7.9.** Interlaminar stress distribution at the free edge in the $[0/45/-45/0]_s$ laminate; (a) at the 0/45 interface, (b) at the 45/-45 interface, (c) at the –45/0 interface and (d) at the midplane.

### 7.4.2 Monte Carlo Simulation

The experimental results in Chapter 5 demonstrate that the interlaminar strength components display larger scatter, therefore it is reasonable that they are treated as random variables which are taken into account in the delamination criteria. Consequently the failure strength governed by the delamination initiation is also a random variable, because it is a function of random interlaminar strength components. However, it is very difficult to analytically determine the probability distributions of the failure strength, especially when the randomness of the interlaminar strength components can not be represented by some standard distributions, e.g., Gaussian or Weibull distribution. As seen in Chapters 5 and 6, the probability density functions of the interlaminar strength components are effectively written in terms of exponential polynomials based on the maximum entropy technique (Siddall, 1983), and thus the random failure strength has to be determined using the numerical methods.

The Monte Carlo Simulation technique is a versatile approach to digitally generate random numbers of independent random variables according to the prescribed probability distributions (Ang and Tang, 1984). However, it must be noted that each laminated composite consists of a number of θ-interfaces, and the θ-dependent ILS strength components are a stochastic process with respect to θ in each case. The random ILS strength components at different θ-interfaces are therefore correlated to one another to some extent. Herein, it is simply assumed that the ILS strength components are uncorrelated and thus the corresponding random numbers at each θ-interface are independently generated. This simplification assumption is made due to two reasons. Firstly, the correlation between the different θ-interfaces is very weak, as demonstrated in Figures 6.6(a) and 6.8(a). Secondly, only the transformation relationships between the second-order correlated and uncorrelated random variables (i.e., their probability distribution functions can be completely determined by the moments up to the second-order) have been developed up to data. To the author's knowledge it is extremely difficult, if not impossible, to transform the fourth-order correlated random ILS strength components into the uncorrelated ones.

The Monte Carlo simulation technique accomplishes the generation of random numbers for the random strength components by transforming the uniformly distributed random numbers between 0 and 1 through their probability distribution functions (Ang and Tang, 1984). Suppose that $u_i$'s ($i = 1, \ldots, n$) are a set of random numbers for the random variable with uniform

probability distribution between 0 and 1. For a random strength component, the cumulative probability distribution at a given value σ is obtained from its probability density function (see Chapter 5);

$$F(\sigma) = \int_{L.B.}^{\sigma} \exp(\lambda_0 + \sum_{i=1}^{4} \lambda_i s^i) ds \tag{7.37}$$

The corresponding set of random numbers for the random strength component is obtained by

$$\sigma_i = F^{-1}(u_i) \tag{7.38}$$

The generation of the uniformly distributed random numbers is a convenient task, and therefore the random numbers of each the strength component can be determined by numerically solving Equation (7.38) without any mathematical difficulties, if the corresponding probability density function is known.

### 7.4.3 Failure Probability Distributions

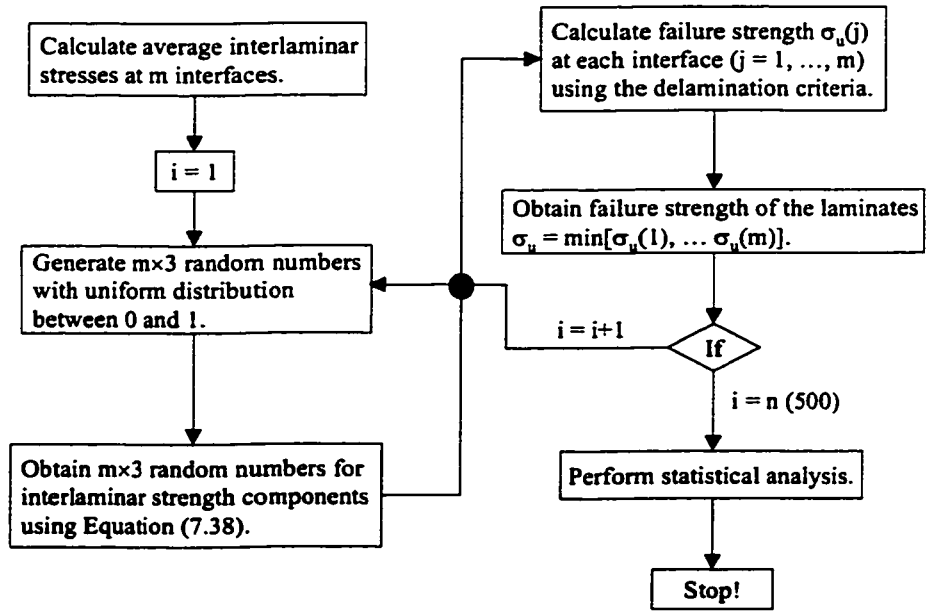


**Figure 7.10.** Flow chart of the procedure for probabilistic evaluation of delamination criteria; m = 5 for the $[15/-15/0]_s$ laminate, and m = 7 for the $[0/45/-45/90]_s$ laminate.

Using the Monte Carlo simulation technique, the random numbers of the interlaminar strength components at each θ-interface can be conveniently generated along one of the fiber orientations of the adjacent plies (i.e., $\phi = \phi_o$), on the basis of the prescribed probability density functions in Chapters 5 and 6. Then, the random numbers of the second-rank and fourth-rank strength tensors in any arbitrary coordinate systems can be obtained from those of the random strength components in conjunction with Equation (7.20). The accurate magnitudes and random characteristics of the sixth-rank strength tensors need to be studied through the combined loading testes. However, the recommendations in Equation (7.27) pertaining to the correlation between the sixth-rank strength tensors and the interlaminar strength components are hereby employed. This implies that the sixth-rank strength tensors are random variables and thus their random numbers can also be obtained from those of the interlaminar strength components using Equation (7.27). The random numbers of the sixth-rank strength tensors in any arbitrary coordinate systems can be determined through Equation (7.26). Finally, the random numbers for each strength tensors are substituted into the quadratic delamination criterion in Equation (7.13) and the cubic delamination criterion in Equation (7.21) to obtain the random numbers of the failure strengths. The entire procedure is demonstrated by the flow chart in Figure 7.10, and five hundreds (i.e., n = 500) repetitions are performed. It should be noted that only the positive roots from the failure equations are hereafter shown, which physically represent the delamination initiation under uniaxial tension. Moreover, there are five θ-interfaces in the $[15/-15/0]_s$ laminate; two 30°-interfaces, two 15°-interface interfaces and one 0°-interface (i.e., midplane), and seven θ-interfaces; four 45°-interfaces, two 90°-interfaces and one 0°-interface (i.e., midplane).

**Table 7.3.** The mean values and coefficients of variation of the failure strengths predicted by the quadratic and cubic delamination criteria.

| | $[15/-15/0]_s$ | | $[0/45/-45/90]_s$ | |
|---|---|---|---|---|
| | Quadratic Cri. | Cubic Cri. | Quadratic Cri. | Cubic Cri. |
| Mean Value (MPa) | 336.82 | 338.97 | 241.22 | 241.60 |
| Coeff. of Variation (%) | 17.88 | 17.99 | 11.01 | 11.13 |

The mean values and coefficients of variation of the failure strengths for $[15/-15/0]_s$ and $[0/45/-45/90]_s$ laminated composites are tabulated in Table 7.3, and the corresponding probability distributions are shown in Figures 7.11 and 7.12. For the $[15/-15/0]_s$ laminate all the 500 sample values are found to be determined by the delamination initiation at the two 15/-15 interfaces. Inside the 500 sample values for the $[0/45/-45/90]_s$ laminate, only 6% are found to be determined

by the delamination initiation at the two -45/90 interfaces, and the other 94% by the delamination initiation at the midplane (i.e., 0/0 interface). It can be observed that the failure strengths predicted by the quadratic and cubic criteria do not present apparent differences in each type of laminated composite, because of the characteristics of interlaminar stresses at each delaminated interface. In the $[15/-15/0]_s$ laminate, the average shear stress $\tau_{xz}$ at the 15/-15 interface is much larger than the normal stress $\sigma_z$ (see Table 7.1), and therefore the magnitudes of the sixth-rank strength tensors do not play an important role in the generation of delamination initiation as shown in Figures 7.5 and 7.6. In the $[0/45/-45/90]_s$ laminate, only the average normal stress $\sigma_z$ exists at the midplanes, and consequently the sixth-rank strength tensors do not affect the predicted failure strengths in such a special case. At the –45/90 interface, the sixth-rank strength tensors will strongly affect the predicted failure strength since the average normal stress $\sigma_z$ is much larger than the average shear stress $\tau_{yz}$. However, only 6% sample values are determined by the delamination at the –45/90 interfaces, and therefore the failure strength of the $[0/45/-45/90]_s$ laminate predicted by the quadratic and cubic delamination criteria do not display apparent difference.

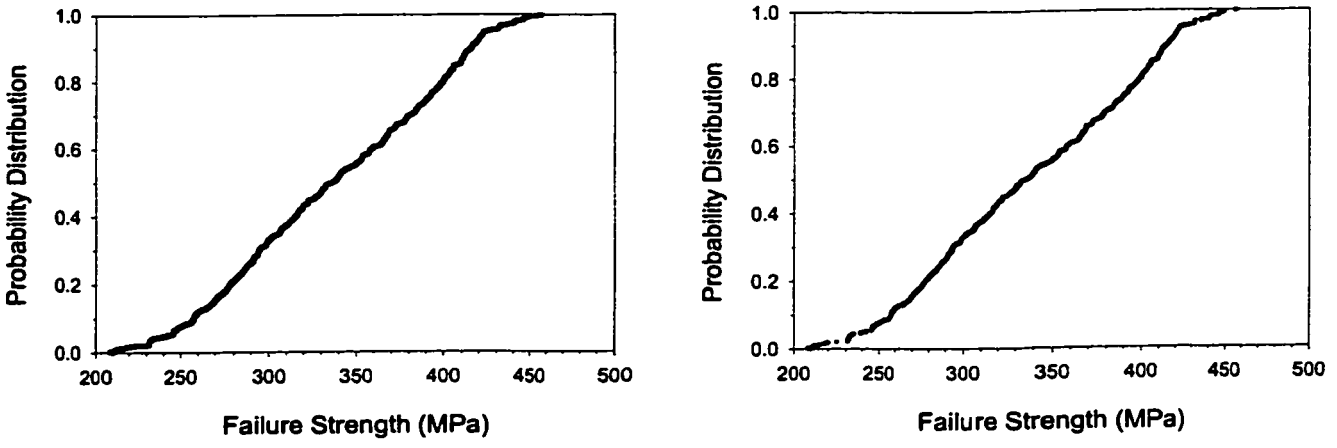


**Figure 7.11.** Probability distribution of the failure strength of the $[15/-15/0]_s$ laminate; (a) predicted by the quadratic delamination criteria, (b) predicted by the cubic delamination criterion.

The delamination initiation does happen at the other interfaces in the $[15/-15/0]_s$ and $[0/45/-45/90]_s$ laminates, because the probability density functions of interlaminar strength components determined by the maximum entropy technique (Siddall, 1983) are specified within the lower and higher bounds (see Chapter 5). This indicates that no sample values of interlaminar

strength components smaller than the lower bounds will be generated using the Monte Carlo simulation technique, even though the number of repetitions is very large. Therefore, the delamination initiation would not be formed at the interfaces with low magnitudes of interlaminar stresses, such as the –15/0 and 0/0 interfaces in the $[15/-15/0]_s$ laminate, and the 0/45 interface in the $[0/45/-45/90]_s$ laminate.

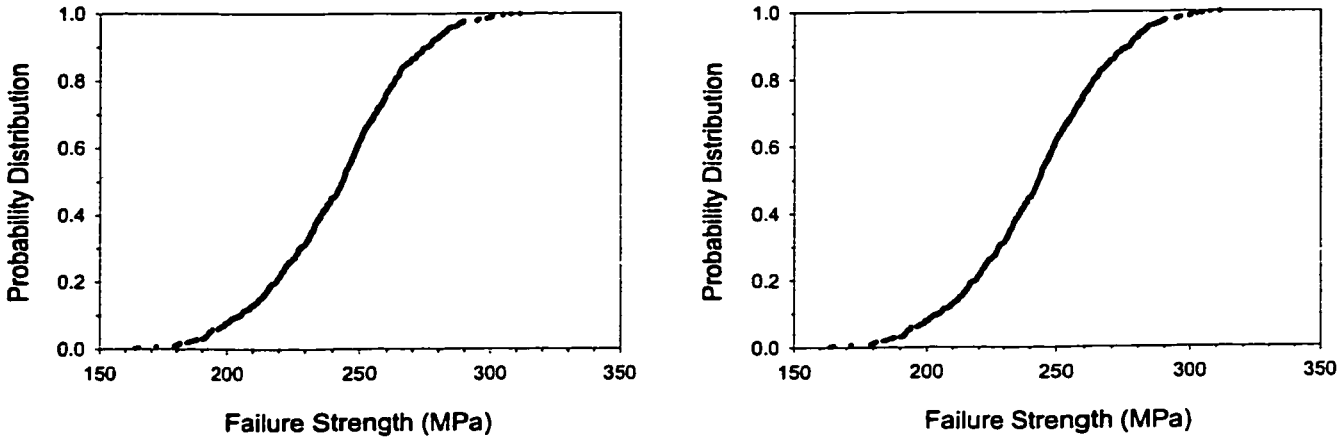


**Figure 7.12.** Probability distribution of the failure strength of the $[0/45/-45/90]_s$ laminate; (a) predicted by the quadratic delamination criteria, (b) predicted by the cubic delamination criterion.

On the basis of the maximum entropy technique (Siddall, 1983), the probability density functions of the failure strengths are also obtained from the 500 sample values in each case and displayed in Figures 7.13 and 7.14. Once again, no apparent differences are observed between the probability density functions predicted by the quadratic and cubic delamination criteria. The failure strengths of the $[15/-15/0]_s$ laminate present large scatter (see Table 7.3), which could be attributed to the high degree of randomness involved with the ILS strength components $S_{13}$ at the 30°-interface, as show in Table 5.7. The probability density function has a hump shape; the sample values are quite uniformly distributed between the lower and higher bounds. The failure strengths of the $[0/45/-45/90]_s$ laminate has smaller scatter than those of the $[15/-15/0]_s$ laminate, because of the low degree of randomness involved with the transverse tensile strength Yt which is approximately employed as the interlaminar tensile strength component. As explained previously, the delamination initiation is mostly formed at the midplanes where only the interlaminar normal stress exists. The failure strengths are thus only determined by the interlaminar tensile strength component Zt. Consequently, the random characteristics of the

failure strengths are almost same as those of the interlaminar tensile strength component, not only in the degree of scatter but the shape of probability density function as well.

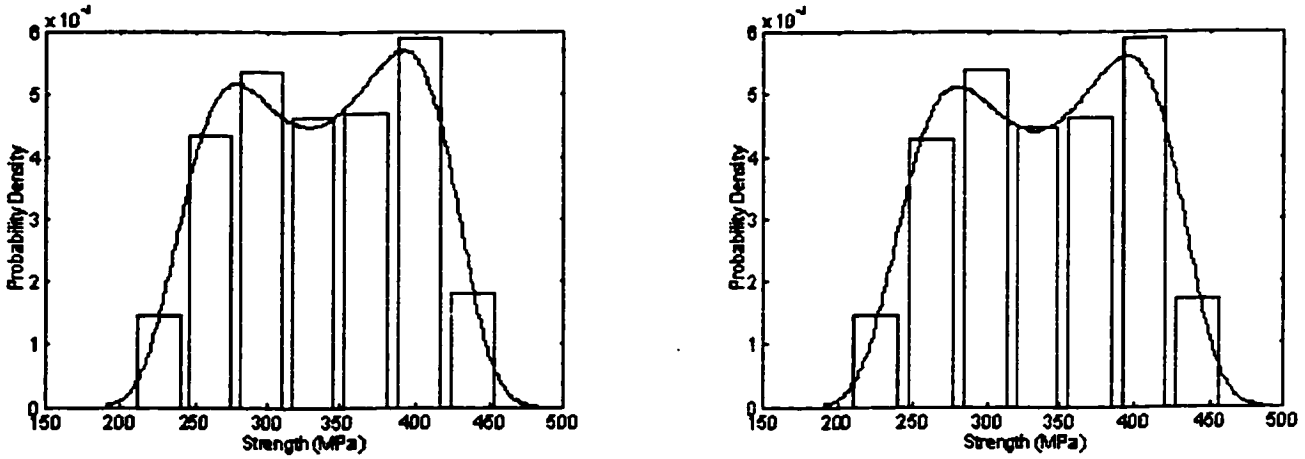


(a) (b)

**Figure 7.13.** Probability density function of the failure strength of the $[15/-15/0]_s$ laminate; (a) predicted by the quadratic delamination criteria, (b) predicted by the cubic delamination criterion.

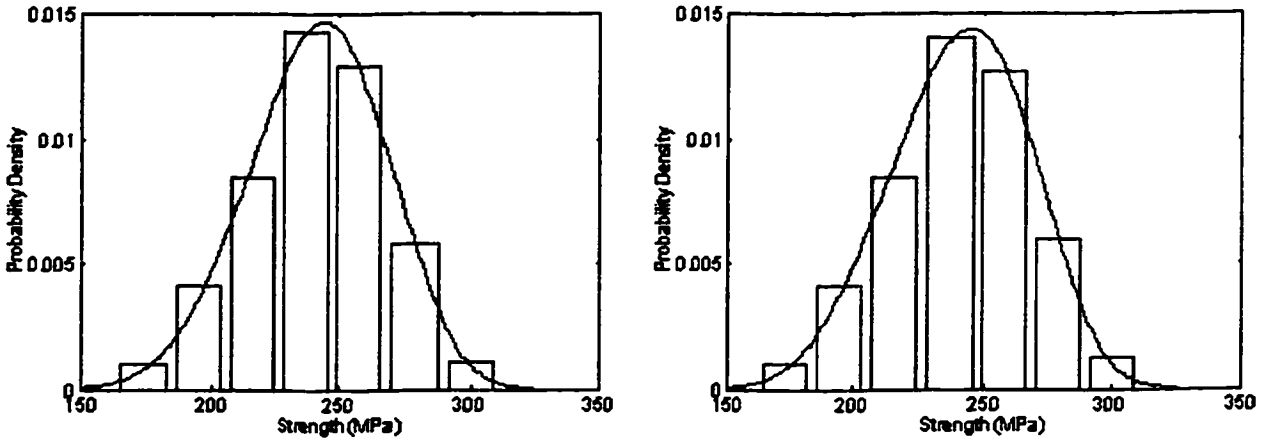


(a) (b)

**Figure 7.14.** Probability density function of the failure strength of the $[0/15/-45/90]_s$ laminate; (a) predicted by the quadratic delamination criteria, (b) predicted by the cubic delamination criterion.

## 7.5 SUMMARY

Two innovative delamination criteria have been developed; the quadratic one in terms of second-order polynomial and the cubic in terms of third-order polynomial. These two criteria pose the capabilities of strength tensor transformation, thereby including the FOD-dependent and directionally-dependent interlaminar strength components. In the cubic delamination criterion,

the magnitudes of the sixth-rank strength tensors representing the interaction between different interlaminar stress components have significant effects on the predicted failure strength, especially when the ratio of the normal stress to shear stress is of larger values. The analytical determination of the value ranges is presented for the sixth-rank strength tensors. Moreover, the expressions of the sixth-rank strength tensors, which are in terms of the interlaminar strength components, are recommended to estimate the tensor values. The predicted failure strengths based on the cubic criterion, which uses the recommended values of the sixth-rank strength tensors are very close to those based on the quadratic criterion in the exemplified cases.

However, the evaluation of the two innovative delamination criteria performed in this chapter is not adequate. Combined loading tests are necessary to experimentally characterize the magnitude and randomness of the sixth-rank strength tensors. One of the effective approaches could be to perform interlaminar shear-compression combined loading tests, e.g., using the testing fixture developed by Benzeggagh *et al.* (1995). Delamination initiation with complex mechanisms, such as that at the edges of traction-free and pin-loaded holes in laminated composites, should be examined by applying these innovative criteria. Also the corresponding experimental work that can generate the delamination initiation under complex interlaminar stress states is necessary to perform the theoretical and experimental comparisons. These further aspects of research are beyond the scope of this thesis.

# CHAPTER 8

# SUMMARY

## 8.1 CONCLUSIONS

The *Stochastic Delamination Model* developed in the present thesis is composed of four major aspects; (1) stress analysis, (2) failure criterion, (3) experimental characterization, and (4) stochastic modeling.

**• Stress Analysis of Edge Effect Stresses in Pin-Loaded Laminated Composites**

A variational solution technique has been developed to yield analytical solutions for the edge effect stresses around pin-loaded holes in laminated composites. From the present solutions, the three-dimensional stress state resulting from the edge effects can conveniently be determined based on the knowledge of in-plane stresses and strains around the pin-loaded holes which can be obtained with the Classical Laminated Plate Theory. In addition, the present solutions for the region inside the no-contact regions can be extended to calculate the free edge effects around traction-free circular holes. Numerical results obtained using the present solutions for cross-ply laminates are in good agreement with those obtained using finite element methods. Following the numerical results, it is concluded that:

(1) The edge effects vanish more quickly near the center of the contact surface, but the maximum interlaminar stress state exists at points not far away from the contact center.

(2) The magnitudes of interlaminar stresses around pin-loaded holes depend on the stacking sequence of laminated composites. Highly concentrated interlaminar stresses exist along the contact surfaces due to the edge effects.

(3) The interlaminar stress component $\tau_{z\theta}$ is much larger than the other two interlaminar stresses $\sigma_z$ and $\tau_{zr}$, and even larger than the in-plane shear stress $\tau_{r\theta}$ along the contact surfaces.

(4) The coefficients of friction strongly affect the three-dimensional contact stress state around the pin-loaded holes.

(5) The discrepancy between the in-plane stress state calculated by the two-dimensional assumptions and that by the three-dimensional stress analysis technique is so large as to influence the predicted strength of the composite pinned joints.

(6) The coefficients of friction can reduce the edge effects around the pin-loaded holes.

**• Experimental Characterization of Effects of FOD Angles on Interlaminar Strengths**

A systematic investigation is conducted to study the effects of fiber orientations on the interlaminar shear (ILS) strengths of CYTEC® G40-800/5276-1 graphite/epoxy laminated composites. The ILS strengths at the θ-interfaces (θ = 0°, 10°, 20°, 30°, 40°, 50°, 60°, 70°, 80° and 90°) are experimentally measured using the modified double notch shear specimens with an elaborately designed lay-up.

The experimental results show that not only the mean values but also the probability distribution forms of ILS strengths depend on the fiber orientations of the neighboring plies around the interfaces. Also, the ILS strengths are found to be directionally-dependent; i.e., different strengths are obtained at a designated interface when the loading directions are changed in the test. Five failure modes are also found by observing the fracture surfaces; i.e., interface crack, in-ply crack, crack jumping, fiber bridging, and fiber breakage. Correlation between fracture surface morphologies and the fiber orientation difference (FOD) angles is observed to some extent. It appears to be quite difficult to obtain the pure delamination failure (i.e., interface crack) inside the whole specimen gage section in the test, which designates the planar cracks propagating along the interfaces between plies in laminated composites. Other failure modes, such as in-ply crack, crack jumping, fiber bridging and fiber breakage, always exist when performing the intended delamination test. However, the local interface cracks can be observed in most cases, although they are subsequently followed by other failure modes. It is found that the failure mode of fiber bridging makes apparent contributions to increasing the ILS strengths. Different fracture

surface morphologies are also displayed with the interfaces when the FOD angle of the surrounding plies is changed.

**• Stochastic Modeling of Variations of Interlaminar Shear Strengths with FOD Angles**

A stochastic simulation model is proposed to implement the analytical investigation on the probabilistic θ-dependent ILS strengths. This simulation algorithm provides a feasible approach to simulate the general non-Gaussian nonstationary stochastic processes within a bounded interval, or in other words, to execute the stochastic interpolation based on experimental sample data that are discretely distributed. It can be seen that this simulation algorithm is efficient to investigate the probabilistic characteristics involved with the θ-dependent ILS strengths obtained from the double notch shear test.

The stochastic simulation algorithm developed would provide a powerful mathematical tool to treat the experimental sample data with considerable scatter, in which certain variation tendencies with respect to physical variables are included. Traditionally, the variation tendencies in the experimental data are judged and then are best fitted by the least square estimate or maximum likelihood estimate techniques. However, when the experimental data have considerable scatter, such as the strengths of composite materials, these deterministic fitting techniques do not work any more because the variation tendency in a deterministic sense would be possibly masked by the scatter. The stochastic simulation techniques, therefore, are essential to uncover the effects of the physical variables on the intended physical phenomena. Moreover, the stochastic simulation techniques can draw more information from the experimental sample data. The probabilistic characteristics, such as the individual probability density functions, in the whole domain of the physical variables can be obtained on the basis of the experimental sample data yielded from a limited number of specimens at discrete physical variables.

**• Failure Criterion for Delamination Initiation**

Two innovative delamination criteria in terms of quadratic and cubic polynomials in each case, are developed based on the Malmeister strength theory and Hashin assumption. The intent of the developed criteria is to include the effects of θ-dependent and directionally-dependent interlaminar strength components into the failure evaluation of laminated composites. This intent is achieved by introducing the capability of strength tensor transformation to the delamination

criteria. The effectiveness of the two developed criteria is verified through evaluating the random delamination failure induced by the straight edge effect interlaminar stresses in two types of laminated composites under uniaxial tension. In the developed criteria, all of the second- and fourth-rank strength tensors in any arbitrary directions at given interfaces are determined by the interlaminar strength components experimentally characterized in one arbitrary direction. In the cubic criterion, however, the sixth-rank strength tensors representing the interaction between the ILS and normal stress components should be experimentally determined using the interlaminar compression-shear or tension-shear combined loading tests. The magnitudes of the sixth-rank strength tensors have significant effects on the predicted failure strength, especially when the ratio of the normal stress to shear stress is of larger values. The analytical determination of the value ranges is presented for the sixth-rank strength tensors. Moreover, the expressions of the sixth-rank strength tensors, which are in terms of the interlaminar strength components, are recommended to estimate their values.

## 8.2 ORIGINALITIES AND CONTRIBUTIONS

The contents of the present thesis have been partially published in a number of journal papers [Zhang *et al.*, 1998(a), 1998(b), 2000(a), 2000(b), 2000(c) and 2000(d)] and conference papers [Zhang *et al.*, 1999(a), 1999(b)]. The original contributions have been addressed in respective chapters, and are summarized as follows.

(1) A *Stochastic Delamiantion Model* is proposed to systematically study the random delamination of graphite/epoxy laminated composites. This model includes many new characteristics and detailed mechanisms behind the delamination failure, which are revealed by the experiments in the present thesis.

(2) Approximate solutions are developed towards the 2D average stresses around pin-loaded holes in composite laminates [Zhang *et al.*, 1998(b)].

(3) Analytical solutions are developed towards 3D contact stresses in pin-loaded laminated composites with and without the effects of friction [Chapter 3, Zhang *et al.*, 1998(a), 1999(a), and 2000(a)]. The solutions can be further employed to compute the 3D edge effect stresses in simple cases; laminated composites with traction-free hole edges or with straight free edges.

(4) A systematic experimental investigation is performed to characterize the material properties of CYTEC® G40-800/5276-1 composite materials; in-plane strengths, interlaminar compressive strengths at two types of θ-interfaces, and interlaminar shear strengths at ten types of θ-interfaces [Chapters 4 and 5, Zhang *et al.*, 1999(b), 2000(b), and 2000(c)]. The modifed double notch shear specimens with elaborate lay-ups are also designed to experimentally measure the ILS strengths.

(5) A series of statistical analysis is performed to deal with the experimental results with large scatter (Chapter 5, Zhang *et al.*, 2000 (b) and 2000(c)].

(6) A stochastic simulation algorithm is proposed to model non-Gaussian nonstationary stochastic processes in order that the probability density functions can be estimated at the FOD angles where the experiments are not executed [Chapter 6, Zhang *et al.*, 2000(d)]. A stochastic interpolation technique is also developed to estimate the higher and lower bounds involved with the stochastic processes of ILS strengths.

(7) Two innovative delamination criteria are developed in order to overcome the shortcomings of the previous empirical delamantion criteria (Chapter 7). The developed criteria pose the capabilities of strength tensor transformation. The distinct characteristics of the ILS strengths, i.e., their dependence on the FOD angles between the surrounding plies of interfaces, and their dependence on the directions even at specified interfaces, are taken into account.

(8) The probability distributions of the delamination failure in various types of laminated composites with straight free edges are studied by using the two innovative criteria and the Monte Carlo simulation technique.

## 8.3 RECOMMENDED FUTURE WORK

The author of the present thesis devoted his five years' efforts to various respects of this research, however, there still remain some issues that should be further studied or improved:

(1) The 3D contact stresses around pin-loaded holes with or without friction should be further calculated using commercial software, such as ANSYS® or NASTRAN®. The rapid development of computational mechanics and computer hardware in recent years makes it

possible to obtain numerical solutions with sufficient accuracy to these complicated physical phenomena.

(2) In the *Stochastic Delamination Model*, the transverse tensile strength is used as an approximation to the interlaminar tensile strengths. Effective testing techniques should be developed to experimentally characterize the effects of FOD angles of surrounding plies on the interlaminar tensile strengths. However, because of the significant difficulties in effectively introducing external loads to the laminated specimens to generate the satisfactory interlaminar tensile stress state, the development of efficient testing techniques is of great challenge.

(3) Experimental characterization and stochastic modeling of the effects of FOD angles on interlaminar compressive strength need to be completely investigated by performing more tests using prism end-loaded specimens with general lay-ups.

(4) The stochastic modeling algorithm hereby developed is not efficient if the numbers of experimental sample data sets are large and they are correlated to some degree. Under this circumference, the so-called sample theorem (Grigoriu, 1993) could be probably used to develop the stochastic modeling algorithm. Furthermore, the stochastic modeling only studies the probabilistic $\theta$-dependent ILS strengths in a phenomenological sense. The physical mechanism as to why the ILS strengths probabilistically depend on the FOD angles, should be investigated on a scale of micro-mechanics. The development of the inherent mathematical modeling will bring up great challenge.

(5) Combined loading tests are essential to experimentally characterize the magnitude and randomness of the sixth-rank strength tensors in the developed cubic delamination criterion. One of the effective approaches could be to perform interlaminar compression-shear combined loading tests, e.g., using the testing fixture developed by Benzeggagh et al. (1995).

(6) The effectiveness of the developed quadratic and cubic delamination criteria should be further evaluated by studying the delamination failure with complex mechanisms, such as at the edges of traction-free and pin-loaded holes in laminated composites. Moreover, experimental work on the delamination failure due to complex interlaminar stress states is also essential to perform the theoretical and experimental comparisons.

## REFERENCES


[1] **Amin, M. and Ang, A. H.-S.**, "Nonstationary Stochastic Models of Earthquake," ASCE Journal of Engineering Mechanics, Vol. 94, 1968, pp. 559-583.

[2] **Ammon, D.**, "Approximation and Generation of Gaussian and Non-Gaussian Stationary Processes," Structural Safety, Vol. 8, 1990, pp. 153-160.

[3] **Ang, A. H. S.** and **Tang, W. K.**, "Probability Concepts in Engineering Planning and Design: Basic Principles," John Wiley and Sons, New York, 1984.

[4] "ASTM Standards and Literature Reference for Composite Materials," First Edition, 1987.

[5] **Avva, V. S.**, **Allen, H. G.** and **Shivakumar, K. N.**, "Through-the-Thickness Tension Strength of 3-D Braided Composites," Journal of Composite Materials, Vol. 30, 1996, pp. 51-68.

[6] **Azzi, V. D.** and **Tsai, S. W.**, "Anisotropic Strengths of Composites," Experimental Mechanics, Vol. 5, 1965, pp. 283-288.

[7] **Bar-Yoseph, P.**, "On the Accuracy of Interlaminar Stress Calculation in Laminated Plates," Computer Methods in Applied Mechanics and Engineering, Vol. 36, 1983, pp. 309-329.

[8] **Bar-Yoseph, P.** and **Avrashi, J.**, "Interlaminar Stress Analysis for Laminated Plates Containing a Curvilinear Hole," Computers and Structures, Vol. 21, 1985, pp. 917-932.

[9] **Benaroya, H.** and **Rehak, M.**, "Finite Element Methods in Probabilistic Structural Analysis: A Selective Review," Applied Mechanics Review, Vol. 41, 1988, pp. 201-213.

[10] **Brewer, J. C.** and **Lagace, P. A.**, "Quadratic Stress Criterion for Initiation of Delamination," Journal of Composite Materials, Vol. 22, 1988, pp. 1141-1155.

[11] **Benzeggagh, M. L.**, **Khellil, K.** and **Chotard, T.**, "Experimental Determination of Tsai Failure Tensorial Terms F for Unidirectional Composite Materials," Composites Science and Technology, Vol. 55, 1995, pp. 145-156.

[12] **Bullock, R. E.**, "Strength Ratios of Composite Materials in Flexure and in Tension," Journal of Composite Materials, Vol. 8, 1974, pp. 200-225.

[13] **Cassenti, B. N.**, "Probabilistic Static Failure of Composite Materials," AIAA Journal, Vol. 22, 1984, pp. 103-110.

[14] **Cederbaum, G. and Elishakoff, I.**, "Reliability of Laminated Plates via the First-Order Second Method," Composite Structures, Vol. 15, 1990, pp. 161-167.

[15] **Chang, C.** and **Yang, H. T. Y.**, "Reliability of Uncertain Flexible Laminated Skewed Plates under Random Compressions," AIAA Journal, Vol. 30, 1992, pp. 464-472.

[16] **Chang, F. K.**, **Scott, R. A.** and **Springer, G. S.**, "The Effect of Laminate Configuration on Characteristic Lengths and Rail Shear Strength," Journal of Composite Materials, Vol. 18, 1984, pp. 290-296.

[17] **Chang, F. K.** and **Springer, G. S.**, "The Strengths of Fiber Reinforced Composite Bends," Journal of Composite Materials, Vol. 20, 1986, pp. 30-45.

[18] **Chang F. K.** and **Chen M. H.**, "The In Situ Ply Shear Strength Distributions in Graphite/Epoxy Laminated Composites," Journal of Composite Materials, Vol. 21, 1987, pp. 708-733.

[19] **Chang, F. K., Tang, J. M.** and **Oeterson, D. G.**, "The Effect of Testing Methods on the Shear Strength Distribution in Laminated Composites," Journal of Reinforced Plastics and Composites, Vol. 6, 1987, pp. 304-318.

[20] **Chang, F. K.** and **Chang, K. Y.**, "A Progressive Damage Model for Laminated Composites Containing Stress Concentration," Journal of Composite Materials, Vol. 21, 1987, pp. 834-855.

[21] **Chang, F. K.** and **Lessard, L. B.**, "Damage Tolerance of Laminated Composites Containing an Open Hole and Subjected to Compressive Loadings: Part I – Analysis," Journal of Composite Materials, Vol. 25, 1991, pp. 2-43.

[22] **Chang, K. Y., Liu, S.** and **Chang, F. K.**, "Damage Tolerance of Laminated Composites Containing an Open Hole and Subjected to Tensile Loadings," Journal of Composite Materials, Vol. 25, 1991, pp. 274-301.

[23] **Chiao, C. C., Moore, R. L.** and **Chiao, T. T.**, "Measurement of Shear Properties of Fibre Composites: Part I – Evaluation of Test Methods," Composites, Vol. 8, 1977, pp. 161-169.

[24] **Chou, I., Kimpara, I., Kageyama, K.** and **Ohsawa, I.**, "Mode I and Mode II Fracture Toughness on Differently Oriented Interlaminae in Graphite/Epoxy Composites," Composite Materials: Fatigue and Fracture, ASTM STP 1230, 1995, pp. 132-151.

[25] **Comptson, P., Jar, P.-Y.** and **Davies, P.**, "Fiber Orientation Effects on Interlaminar Fracture Toughness of Marine Composites," ICCM-11, Gold Coast, Australia, 1997.

[26] **Crossman, F. W.** and **Wang, A. S. D.**, "The Dependence of Transverse Cracking and Delamination on Ply Thickness in Graphite-Epoxy Laminates," Damage in Composite Materials, ASTM STP 775, 1982, pp. 118-139.

[27] **Daniels, H. E.**, "The Statistical Theory of the Strength of Bundles of Threads," Proceedings of the Royal Society, Series A, Vol. 183, No. A995, 1945.

[28] **Davidson, B. D., Altonen, C. S.** and **Polaha, J. J.**, "Effect of Stacking Sequence on Delamination Toughness and Delamination Growth Behaviour in Composite End-Notched Flexure Specimens," Composite Materials: Testing and Design, ASTM STP 1274, 1994, pp. 393-413.

[29] **Deodatis, G.** and **Shinozuka, M.**, "Simulation of Seismic Ground Motion Using Stochastic Waves," ASCE Journal of Engineering Mechanics, Vol. 115, 1989, pp. 2723-2737.

[30] **Deodatis, G.** and **Shinozuka, M.**, "Auto-Regressive Model for Nonstationary Stochastic Processes," ASCE Journal of Engineering Mechanics, Vol. 114, 1988, pp. 1995-2012.

[31] **Deodatis, G., Shinozuka, M.** and **Neal, D.**, "Spatial Strength Variation of Laminated Orthotropic Composites," Journal of Composite Materials, Vol. 23, 1989, pp. 1256-1272.

[32] **de Jong, Th.**, "Stresses Around Pin-Loaded Holes in Elastically Orthotropic or Isotropic Plates," Journal of Composite Materials, Vol. 11, 1977, pp. 313-331.

[33] **de Jong, Th.**, "Stresses Around Pin-Loaded Holes in Composite Materials," Proceedings of the IUTAM Symposium on Mechanics of Composite Materials, Virginia, 1982, pp. 339-353.

[34] **Ditlevsen, D.**, "Narrow Reliability Bounds for Structural System," Journal of Structural Mechanics, Vol. 7, 1979, pp. 453-472.

[35] **Engelstad, S. P.** and **Reddy, J. N.**, "Probabilistic Nonlinear Finite Element Analysis of Composite Structures," AIAA Journal, Vol. 31, 1993, pp. 362-369.

[36] **Ericson, K., Persson, M., Carlsson, L.** and **Gustavsson, A.**, "On the Prediction of the Initiation of Delamination in a [0/90]$_s$ Laminate with a Circular Hole," Journal of Composite Materials, Vol.18, 1984, pp. 495-506.

[37] **Evans, K. E.** and **Zhang, W. C.**, "The Determination of the Normal Interaction Term in the Tsai-Wu Tensor Polynomial Strength Criterion," Composites Science and Technology, Vol. 30, 1987, pp. 251-262.

[38] **Fan, W. X.**, "On Phenomenological Anisotropic Failure Criteria," Composites Science and Technology, Vol. 24, 1987, pp. 269-278.

[39] **Fish, J. C.** and **Lee, S. W.**, "Delamination in Tapered Composite Structures," Journal of Engineering Mechanics, Vol. 34, 1989, pp. 43-54.

[40] **Fish, J. C.** and **O'Brien, T. K.**, "Free-Edge Stress Analysis of Glass-Epoxy Laminates with Matrix Cracks," Composite Materials: Testing and Design, ASTM STP 1120, 1992, pp. 348-364.

[41] **Flaggs, D. L.** and **Kural, M. H.**, "Experimental Determination of the In Situ Transverse Lamina Strength in Graphite/Epoxy Laminates," Journal of Composite Materials, Vol. 16, 1982, pp. 103-116.

[42] **Foye, R. L.** and **Baker, D. J.**, "Design of Orthotropic Laminates," 11th Annual AIAA Conference on Structures, Structural Dynamics, and Materials, Denver, 1970.

[43] **Fukuda, H.** and **Kawabata, K.**, "Strength Estimation of Unidirectional Composites," Transations of the Japan Society of Composite Materials, Vol. 2, 1976, pp. 59-62.

[44] **Goeke, E. C.**, "Compression of "Thick" Composites: Two Test Methods", Composite Materials: Testing and Design, ASTM STP, 1206, 1993, pp. 90-102.

[45] **Gol'denblat, I. I.** and **Kopnov, V. A.**, "Strength of Glass-Reinforced Plastics in the Complex Stress State," Polymer Mechanics, Vol. 1, 1966, pp. 54-59.

[46] **Gramer, H.**, "Mathematical Methods of Statistics," Princeton University Press, Princeton, 1946.

[47] **Grigoriu, M.**, "Simulation of Nonstationary Gaussian Processes by Random Trigonometric Polynomials," ASCE Journal of Engineering Mechanics, Vol. 119, 1993, pp. 328-343.

[48] **Grigoriu, M.**, "Simulation of Stationary Process via a Sampling Theorem," Journal of Sound and Vibration, Vol. 166, 1993, pp. 301-313.

[49] **Gurvich, M. R.** and **Pipes, R. B.**, "Strength Size Effect of Laminated Composites," Composites Science and Technology, Vol. 55, 1995(a), pp. 93-105.

[50] **Gurvich, M. R.** and **Pipes, R. B.**, "Probabilistic Analysis of Multi-Step Failure Process of a Laminated Composite in Bending," Composites Science and Technology, Vol. 55, 1995(b), pp. 413-421.

[51] **Hadcock, R. N.**, "Design Philosophy for Boron/Epoxy Structures," Composite Materials: Testing and Design, ASTM STP 497, 1972, pp. 28-40.

[52] **Hahn, H. T.** and **Tsai, S. W.**, "Non-Linear Behaviour of Unidirectional Composite Lamina," Journal of Composite Materials, Vol. 7, 1973, pp. 102-118.

[53] **Halsey, N., Marlowe, D. E., Mitchell, R. A.** and **Mordfin, L.**, "Non-Metallic Antenna-Support Materials: Pultruded Rods for Antenna Guys Catenaries Communication Structures," AFML TR-76-42, 1976.

[54] **Harlow, D. G.** and **Phoenix, S. L.**, "The Chain of Bundles Probability Model for the Strength of Fibrous Materials I: Analysis and Conjectures," Journal of Composite Materials, Vol. 12, 1978, pp. 195-214.

[55] **Harlow, D. G.** and **Phoenix, S. L.**, "The Chain of Bundles Probability Model for the Strength of Fibrous Materials II: A Numerical Study of Convergence," Journal of Composite Materials, Vol. 12, 1978, pp. 314-334.

[56] **Harlow, D. G.** and **Phoenix, S. L.**, "Probability Distributions for the Strength of Composite Materials I: Two-Level Bounds," International Journal of Fracture, Vol. 17, 1981, pp. 347-371.

[57] **Harris, A. and Orringer, O.**, "Investigation of Angle-Ply Delamination Specimen for Interlaminar Strength Test," Journal of Composite Materials, Vol. 12, 1978, pp. 285-299.

[58] **Hart-Smith, L. J.**, "Some Observations about Test Specimens and Structural Analysis for Fiberous Composites," Composite Materials, Testing and Design, ASTM STP 1069, 1990, pp. 86-120.

[59] **Hashin, Z.**, "Failure Criteria for Unidirectional Fiber Composites," Journal of Applied Mechanics, Vol. 47, 1980, pp. 329-334.

[60] **Hasofer, A. M.** and **Lind, N. C.**, "Exact and Invariant Second-Moment Code Format," ASCE Journal of Engineering Mechanics Division, Vol. 100, 1974, pp. 111-121.

[61] **Hasofer, A. M.**, "Single Trigonometric Models for Narrow-Band Stationary Processes," ASCE Journal of Applied Probability, 19A, 1982, pp. 333-344.

[62] **Hayashi, T.**, "Analytical Study of Interlaminar Shear Stresses in a Laminae Composite Plate," Transaction of Japanese Society for Aeronautics and Space Science, 1967, Vol. 10, pp. 43-48.

[63] **Herakovich, C. T.**, "On the Relationship Between Engineering Properties and Delamination of Composite Materials," Journal of Composite Materials, Vol. 15, 1981, pp. 336-348.

[64] **Herakovich, C. T., Nagarkar, A.** and **O'Brien, D. W.**, "Failure Analysis of Composite Laminate with Free Edges," Modern Development in Composite Materials and Structures, Vinson, J. R. (ed.), ASME, New York, 1981, pp. 53-66.

[65] **Herokovich, C. T.**, "Influence of Layer Thickness on the Strength of Angle-Ply Laminates," Journal of Composite Materials, Vol. 16, 1982, pp. 216-227.

[66] **Hiel, C. C., Sumich, M.** and **Chappell, D. P.**, "A Curved Beam Test Specimen for Determining the Interlaminar Tensile Strength of Laminated Composites," Journal of Composite Materials, Vol. 25, 1991, pp. 854-868.

[67] **Hill, R.**, "A Theory of Yielding and Plastic Flow of Anisotropic Metals," Proceeding of the Royal Society, Series A, Vol. 193, 1948, pp. 281-297.

[68] **Hill, R.**, "The Mathematical Theory of Plasticity," Oxford University Press, London, 1950.

[69] **Hilton, H. H.** and **Yi, S.**, "Stochastic Viscoelastic Delamination Onset Failure Analysis of Composites," Journal of Composite Materials, Vol. 27, 1993, pp. 1097-1115.

[70] **Hisada, T.**, and **Nakagiri, J. B.**, "The Stochastic Finite Element Method in Structural Safety and Reliability," Proceedings of the 5th International Conference on Structural Safety and Reliability, New York, 1985, pp. 385-394.

[71] **Hoa, S. V., Daoust, B. L.**, and **Vu-Khanh, T.**, "Interlaminar Stresses in Tapered Laminates," Polymer Composites, Vol. 9, 1988, pp. 337-344.

[72] **Hoa, S. V.** and **Feng, W.**, "Global/Local Approach Using Hybrid Elements for Composites," Proceedings of 5th International Conference on Computer Aided Design in Composite Material Technology, UK, 1996, pp. 319-328.

[73] **Hoffman, O.**, "The Brittle Strength of Orthotropic Materials," Journal of Composite Materials, Vol. 1, 1967, pp. 200-206.

[74] **Hoshiya, M.**, **Ishii, K.** and **Nagata, S.**, "Recursive Covariance of Structural Response," ASCE Journal of Engineering Mechanics, Vol. 110, 1984, pp. 1743-1755.

[75] **Hsu, P. W.** and **Herakovich, C. T.**, "A Perturbation Solution for Interlaminar Stresses in Bidirectional Laminates," Composite Materials: Testing and Design, ASTM STP 617, 1977, pp. 296-316.

[76] **Hudson, R. C.**, **Davidson, B. D.** and **Polaha, J. J.**, "Effect of Remote Ply Orientation on the Perceived Mode I and Mode II Toughness of θ/θ and θ/-θ Interface," ICCM-10, Vancouver, Canada, 1995, pp. I-133-140.

[77] **Hyer, M. W.** and **Klang, E. C.**, "Contact Stresses in Pin-Loaded Orthotropic Plates," International Journal of Solids and Structures, Vol. 21, 1985, pp. 957-975.

[78] **Ienoe, E. M.** and **Neal, D.**, "Structural Integrity Assessment of Filament-Wound Components," Composite Reliability, ASTM STP 580, 1975, pp. 54-76

[79] **Jackson, A. C.**, "Testing of the L-1011 Advanced Composite Vertical Fin," Proceedings of the Sixth Conference on Fibrous Composites in Structural Design, AMMRC-MS-83-2, Army Materials and Mechanics Research Center, 1983.

[80] **Jackson, W. C.** and **Martin, R. H.**, "An Interlaminar Tensile Strength Specimen," Composite Materials: Testing and Design, ASTM STP, 1206, 1993, pp. 333-354.

[81] **Jackson, W. C.**, "Through-the-Thickness Test Strength of Textile Composites," Composite Materials, Testing and Design, ASTM STP 1274, 1996, pp. 218-238.

[82] **Jenkins, G. M.** and **Watts, D.G.**, *Spectral Analysis and Its Applications*, Holden-Day, Inc., San Francisco, 1968.

[83] **Johnson, W. S.** and **Mangalgiri, P. D.**, "Influence of the Resin on Interlaminar Mixed-Mode Fracture," Toughened Composites, ASTM STP 937, 1987, pp. 295-315.

[84] **Jiang, Z.** and **Tennyson, R. C.**, "Closure of the Cubic Tensor Polynomial Failure Surface," Journal of Composite Materials, Vol. 23, 1989, pp. 208-231.

[85] **Jones, R. M.**, "Mechanics of Composite Materials," Scripta Book Company, Washington, D.C., 1975.

[86] **Joo, J. W.** and **Sun, C. T.**, "A Failure Criterion for Laminates Governed by Free Edge Interlaminar Shear Stress," Journal of Composite Materials, Vol. 26, 1992, pp. 1510-1522.

[87] **Jurf, R. A.** and **Pipes, R. B.**, "Interlaminar Fracture of Composite Materials," Journal of Composite Materials, Vol. 16, 1982, pp. 386-394.

[88] **Kaminski, B. E.**, "Effects of Specimen Geometry on the Strength of Composite Materials," Analysis of the Test Methods for High Modulus Fibers and Composites, ASTM STP 521, 1973, pp. 181-191.

[89] **Kan, H. P.**, **Bhatia, N. M.**, and **Mahler, M. A.**, "Effect of Porosity on Flange-Web Corner Strength," Composite Materials: Fatigue and Fracture, ASTM STP 1110, 1991, pp. 126-138.

[90] **Kassapoglou, C. and Lagace, P.A.**, "An Efficient Method for the Calculation of Interlaminar Stresses in Composite Materials," ASME Journal of Applied Mechanics, Vol. 53, 1986, pp. 744-750.

[91] **Kassapoglou, C. and Lagace, P. A.**, "Closed Form Solutions for the Interlaminar Stress Field in Angle-Ply and Cross-Ply Laminates," Journal of Composite Materials, Vol. 21, 1987, pp. 292-308.

[92] **Kassapoglou, C.**, "Determination of Interlaminar Stresses in Composite Laminates under Combined Loads," Journal of Reinforced Plastics and Composites, Vol. 9, 1990, pp. 33-58.

[93] **Kedward, K. T., Wilson, R. S. and McLean, S. K.**, "Flexure of Simply Curved Composite Shapes," Composites, Vol. 20, 1989, pp. 527-536.

[94] **Kim, R. Y. and Soni, S. R.**, "Experimental and Analytical Studies on the Onset of Delamination in Laminated Composites," Journal of Composite Materials, Vol. 18, 1984, pp. 70-80.

[95] **Kim, R. Y. and Soni, S. R.**, "Failure of Composite Laminates due to Combined Interlaminar Normal and Shear Stresses," Composites 86; Recent Advances in Japan and the United States, Tokyo, Japan, 1986, pp. 341-350.

[96] **Kim, T. and Atluri, S. N.**, "Interlaminar Stresses in Composite Laminates under Out-of-Plane Shear/Bending," AIAA Journal, Vol. 32, 1994, pp. 1700-1708.

[97] **Ko, C. C. and Lin, C. C.**, "Method for Calculating the Interlaminar Stresses in Symmetric Laminates Containing a Circular Hole," AIAA Journal, Vol. 30, 1992, pp. 197-204.

[98] **Ko, W. L.**, "Delamination Stresses in Semicircular Laminated Composite Bars," NASA TM 4026, 1988.

[99] **Ko, W. L. and Jackson, R. H.**, "Multilayer Theory for Delamination Analysis of Composite Curved Bar Subjected to End Forces and End Moments," NASA TM 4139, 1989.

[100] **Ko, W. L. and Jackson, R. H.**, "Open-Mode Delamination Stress Concentrations in Horseshoe and Elliptic Composite Curved Bars Subjected to End Forces," NASA TM 4164, 1990.

[101] **Kutlu, Z. and Chang F. K.**, "Modelling Compressive Failure of Laminated Composites Containing Multiple Through-the-Width Delamination," Journal of Composite Materials, Vol. 26, 1992, pp. 350-387.

[102] **Lagace, P. A. and Weems, D. B.**, "A Through-the-Thickness Strength Specimen for Composites," Test Methods for Design Allowables for Fibrous Composites, ASTM STP 1003, 1989, pp. 197-207.

[103] **Lagace, P. A. and Brewer, J. C.**, "Studies of Delamination Growth and Final Failure Tensile Loading," ICCM-6, 1987, Vol. 5, pp. 262-273.

[104] **Larder, R. A. and Beadle, C. W.**, "The Stochastic Finite Element Simulation of Parallel Fiber Composites," Journal of Composite Materials, Vol. 10, 1976, pp. 21-31.

[105] **Larson, H. J.**, "Introduction to Probability Theory and Statistical Interface", Third Edition, John Wiley and Sons, New York, 1982.

[106] **Law, G. E.**, "A Mixed-Mode Fracture Analysis of ("25/90n)s Graphite/Epoxy Composite Laminates," Effects of Defects in Composite Materials, ASTM STP 836, 1984, pp. 143-160.

[107] **Lee, S. M.**, "Failure Mechanism of Delamination Fracture," Composite Materials: Testing and Design, ASTM STP 972, 1988, pp. 356-365.

[108] **Lekhnitskii, G. S.**, "Anisotropic Plates," Gordon and Beach Science Publisher, New York, 1968.

[109] **Lessard, L. B., Shokrieh, M. M.** and **Schmidt, A. S.**, "Three-Dimensional Stress Analysis of Composite Plates with or without Stress Concentrations," ICCM-9, 1993, pp. 243-250.

[110] **Lessard, L. B., Schmidt, A. S.** and **Shokrieh, M. M.**, "Three-Dimensional Stress Analysis of Free Edge Effects in a Simple Composite Cross-Ply Laminate," International Journal of Solids and Structures, Vol. 33, 1996, pp. 2243-2259.

[111] **Liaw, D. G.** and **Yang, H. T. Y.**, "Reliability of Initially Compressed Uncertain Laminated Plates in Supersonic Flow," AIAA Journal, Vol. 29, 1991, pp. 952-960.

[112] **Lin, C. C., Hsu, C. Y.** and **Ko, C. C.**, "Interlaminar Stresses in General Laminates with Straight Free Edges," AIAA Journal, Vol. 33, 1995, pp. 1471-1476.

[113] **Lin, S. C.**, and **Kam, T. Y.**, "Reliability Analysis of Composite Laminated Subject to Buckling and First-Ply Failure," Proceedings of 5th International Conference on Computer Aided Design in Composite Material Technology, UK, 1996, pp. 329-338.

[114] **Liu, S. C.**, "Evolutionary power spectral density of strong motion earthquake," Bulletin of the Seismological Society of America, Vol. 60, 1970, pp. 891-900.

[115] **Liu, W. K., Belytschko, T., Mani, A.**, "Random Field Finite Element," International Journal of Numerical Methods in Engineering, Vol. 23, 1986(a), pp. 1831-1845.

[116] **Liu. W. K., Belytschko, T., Mani, A.**, "Probabilistic Finite Elements for Nonlinear Structural Dynamics," Computer Methods in Applied Mechanics and Engineering, Vol. 56, 1986(b), pp. 61-81.

[117] **Liu, W. K., Mani, A.**, and **Belytschko, T.**, "Finite Element Methods in Probabilistic Mechanics," Journal of Probabilistic Engineering Mechanics, Vol. 2, 1987, pp. 201-213.

[118] **Lucking, W. M., Hoa, S. V.** and **Sankar, T. S.**, "The Effect of Geometry on Interlaminar Stresses of $[0/90]_s$ Composite Laminates with Circular Holes," Journal of Composite Materials, Vol. 18, 1984, pp. 188-198.

[119] **Malmeister, A.**, "Geometry of Theories of Strength," Polymer Mechanics, Vol. 2, 1967, pp. 324-331.

[120] **Manders, P. W.** and **Kowalski, I. M.**, "The Effect of Small Angular Misalignments and Tabbing Techniques on the Tensile Strength of Carbon-Fiber Composites," Proceedings, 32nd International SAMPE Symposium, 1987, pp. 985-996.

[121] **Mao, T. H.** and **Owen, M. J.**, "Through-the-Thickness Tensile Strength of Fiber-Reinforced Plastics," Composite Materials: Testing and Design, ASTM STP 787, 1982, pp. 5-18.

[122] **Marin, R.**, "Theories of Strength for Combined Stresses and Nonisotropic Materials," Journal of the Aeronautical Sciences, Vol. 24, 1957, pp. 265-268.

[123] **Markham, M. F.** and **Dawson, D.**, "Interlaminar Shear Strength of Fiber-Reinforced Composites," Composites, Vol. 6, 1975, pp. 173-176.

[124] **Marshall, I. H., Arnold, W. S., Wood, J.** and **Mousley, R. F.**, "Observations on Bolted Connections in Composite Structures," Composite Structures, Vol. 13, 1989, pp. 133-151.

[125] **Martin, R. H.** and **Sage, G. N.**, "Prediction of the Fatigue Strength of Bounded Joints Between Multi-Directional Laminates of CFRP," Composite Structures, Vol. 6, 1986, pp. 141-163.

[126] **Martin R. H.**, "Delamination Failure in a Unidirectional Curved Composite Laminate," Composite Materials: Testing and Design, ASTM STP 1120, 1992, pp. 365-383.

[127] **Martin, R. H.** and **Jackson, W. C.**, "Damage Prediction in Cross-Plied Curved Composite Laminates," Composite Materials: Fatigue and Fracture, ASTM STP 1156, 1993, pp. 105-126.

[128] **Martin, R. H., Sriram, P.** and **Hooper, S. J.**, "Using a Mixed-Mode Fatigue Delamination Criterion," Composite Materials: Testing and Design, ASTM STP 1274, 1996, pp. 371-392.

[129] **Mase, G. T., Murthy, P. L. N.** and **Chamis, C. C.**, "Probabilistic Micromechanics and Macromechanics of Polymer Matrix Composites," NASA TM 103669, 1991.

[130] **Matthews, F. L., Wong, C. M.** and **Chryssafitis, S.**, "Stress Distribution Around a Single Bolt in Fiber-Reinforced Plastic," Composites, Vol. 13, 1982, pp. 316-322.

[131] **Matthews, F. L.**, "Bolted Joint", Chapter 18, Think Composites, Tsai, S. W. (ed.), 1988.

[132] **Maxwell, R. E., Toland R. H.** and **Jokson, C. W.**, "Probabilistic Design of Composite Structures," Composite Reliability, ASTM STP 580, 1975, pp. 35-53.

[133] **Miki, M., Murotsu, Y., Tanaka, T., Shao, S.**, "Reliability of Unidirectional Fibrous Composites," AIAA Journal, Vol. 28, 1990, pp. 1980-1986.

[134] **Miki, M., Murotsu, Y., Murayama, N.** and **Tanaka, T.**, "Application of Lamination Parameters to Reliability-Based Stiffness Design of Composites," AIAA Journal, Vol. 31, 1993, pp. 1938-1945.

[135] **Miner, M. A.**, "Cumulative Damage in Fatigue," Journal of Applied Mechanics, Vol. 12, 1945, pp. A159-A164.

[136] **Moses, F.**, "Strength Reliability Developments in Structural Engineering," Structural Safety, Vol. 1, 1982, pp. 3-13.

[137] **Munjal, A. K.**, "Test Methods for Determining Design Allowables for Fiber Reinforced Composites," Test Methods for Design Allowables for Fiber Composites, ASTM STP 1003, 1989, pp. 93-110.

[138] **Murotsu, Y., Miki, M.** and **Shao, S.**, "Reliability Design of Fiber Reinforced Composites," Structural Safety, Vol. 15, 1994, pp. 35-49.

[139] **Naganuma, T., Deodatis, G.** and **Shinozuka, M.**, "An ARMA Model for Two-Dimensional Processes," ASCE Journal of Engineering Mechanics, Vol. 113, 1987, pp. 234-251.

[140] **Nahas, M. N.**, "Survey of Failure and Post-Failure Theories of Laminated Fiber-Reinforced Composites," Journal of Composites Technology & Research, Vol. 8, 1986, pp. 138-153.

[141] **Nakagiri, S., Takabatake, H.** and **Tani, S.**, "Uncertain Eigenvalue Analysis of Composite Laminated Plates by the Stochastic Finite Element Method," Journal of Engineering for Industry, Vol. 109, 1987, pp. 9-12.

[142] **Nakayasu, H., Maekawa, Z.** and **Rackwitz, R.**, "Reliability-Oriented Materials Design of Composite Materials," The 5th International Conference on Structural Safety and Reliability, 1989, pp. 2095-2098.

[143] **Narayanaswami, R.**, and **Adelman, H. M.**, "Evaluation of the Tensor Polynomial and Hoffman Strength Theories for Composite Materials," Journal of Composite Materials, Vol. 11, 1977, pp. 366-377.

[144] **Neal, D., Vangel, M.** and **Todt, F.**, "Statistical Analysis of Mechanical Properties," Engineering Materials Handbook, ASM International, Vol. 1, Composites, 1987, pp. 302-307.

[145] **Newaz, G. M. (ed.)**, "Delamination in Advanced Composites," PA: Technomic Publishing Company, Inc., 1991.

[146] **Nicholls, D. J.** and **Gallagher, J. P.**, "Determination of $G_{IC}$ in Angle Ply Composites Using a Cantilever Beam Test Method," Journal of Reinforced Plastics and Composites, Vol. 2, 1983, pp. 2-17.

[147] **Nishioka, T.** and **Atluri, S. N.**, "Stress Analysis of Holes in Angle-Ply Laminates: An Efficient Assumed Stress "Special-Hole-Element": Approach and a Simple Estimation Method," Computers and Structures, Vol. 15, 1982, pp. 135-147.

[148] **Norris, C. B.**, "Strength of Orthotropic Materials Subjected to Combined Stresses," Report 1816, Forest Product Laboratory, 1962.

[149] **O'Brien, T. K.**, "Characterization of Delamination Onset and Growth in a Composite Laminate," Damage in Composite Materials, ASTM STP 775, 1982, pp. 140-167.

[150] **O'Brien, T. K.**, "Mixed-Mode Strain-Energy-Release Rate Effects on Edge Delamination of Composites," Effect of Defects in Composite Materials, ASTM STP 836, 1984, pp. 104-124.

[151] **O'Brien, T. K.** and **Hooper, S. J.**, "Local Delamination in Laminates with Angle Ply Matrix Cracks: Part I – Tension Test and Stress Analysis," Composite Materials: Fatigue and Fracture, ASTM STP 1156, 1993, pp. 491-506.

[152] **O'Brien, T. K.** and **Salpekar S. A.**, "Scale Effects on the Transverse Tensile Strength of Graphite/Epoxy Composites," Composite Materials: Testing and Design, ASTM STP 1206, 1993, pp. 23-52.

[153] **Pagano, N. J.** and **Halpin, J. C.**, "Influence of End Constraints in the Testing of Anisotropic Bodies," Journal of Composite Materials, Vol. 2, 1968, pp. 18-31.

[154] **Pagano, J. N.** and **Whitney, J. M.**, "Geometry Design of Composite Cylindrical Characterization Specimens," Journal of Composite Materials, Vol. 4, 1970, pp. 360-378.

[155] **Pagano, N. J.**, "Stress Gradients in Laminated Composite Cylinders," Journal of Composite Materials, Vol. 5, 1971, pp. 260-265.

[156] **Pagano, N. J.**, "On the Calculation of Interlaminar Normal Stress in Composite Laminate," Journal of Composite Materials, Vol. 8, 1974, pp. 65-81.

[157] **Pagano, N. J. (ed.)**, "Interlaminar Response of Composite Materials," Elsevier Science Publisher B. V., 1989.

[158] **Papoulis, A.**, "Probability, Random Variables, and Stochastic Processes," Second Edition, McGraw-Hiill, Inc., New York, 1984.

[159] **Paul, P. C., Saff, C. R., Sanger, K. B., Mahler, M. A., Kan, H. P.** and **Kautz, E. F.**, "Analysis and Test Technique for Composite Structures Subjected to Out-of-Plane Loads," Composite Materials: Testing and Design, ASTM STP 1120, 1992, pp. 238-252.

[160] **Peter, P. W. M.**, "The Strength Distribution of 90 Plies in 0/90/0 Graphite Epoxy Laminate," Journal of Composite Materials, Vol. 18, 1984, pp. 545-556.

[161] **Petit, P. H.** and **Waddoups, M. E.**, "A Method of Predicting the Nonlinear Behaviour of Laminated Composites," Journal of Composite Materials, Vol. 3, 1969, pp. 2-19.

[162] **Pindera, M. J., Choksi, C., Hidde, J. S.** and **Herakovich, C. T.**, "A Methodology for Accurate Shear Characterization of Unidirectional Composites," Journal of Composite Materials, Vol. 21, 1987, pp. 1164-1184.

[163] **Pipes, R. B.** and **Pagano, N. J.**, "Interlaminar Stresses in Composite Laminates under Uniform Axial Extension," Journal of Composite Materials, Vol. 14, 1970, pp. 538-548.

[164] **Pipes, R. B.**, "Solution of Certain Problems in the Theory of Elasticity for Laminated Anisotropic Systems," Ph.D. Dissertation, University of Texas, Arlington, 1972.

[165] **Pipes, R. B.** and **Cole, B. W.**, "On the Off-Axis Strength Test for Anisoropic Materials," Journal of Composite Materials, Vol. 7, 1973, pp. 246-256.

[166] **Poursartip, A.**, "The Characterization of Edge Delamination Growth in Laminates under Fatigue Loading," Toughened Composites, ASTM STP 937, 1987, pp. 222-241.

[167] **Priestley, M. B.**, "Power Spectral Analysis of Non-Stationary Random Process," Journal of Sound and Vibration, Vol. 6, 1967, 86-97.

[168] **Puppo, A. H.** and **Evensen, H. A.**, "Interlaminar Shear in Laminated Composites under Generalized Plane Stresses," Journal of Composite Materials, Vol. 5, 1970, pp. 204-211.

[169] **Rackwitz, R.** and **Fiessler, B.**, "Structural Reliability under Combined Random Load Sequence," Computers and Structures, Vol. 9, 1978, pp. 489-494.

[170] **Raju, I. S.** and **Crews, Jr., J. H.**, "Three Dimensional Analysis of $[0/90]_s$ and $[90/0]_s$ Laminates with a Central Hole," NASA TM 83300, 1982.

[171] **Ramkumar, R. L.** and **Whitcomb, J. D.**, "Characterization of Mode I and Mixed-Mode Delamination Growth in T300/5208 Graphite/Epoxy," Delamination and Debonding of Materials, ASTM STP 876, 1985, pp. 315-335.

[172] **Reddy, J. N.**, "Applied Functional Analysis and Variational Methods in Engineering," McGraw-Hill, New York, 1991.

[173] **Reiss, E. L.**, "Extension of an Infinite Plate with a Circular Hole," Journal of the Society for Industrial and Applied Mathematics, Vol. 11, 1963, pp. 840-854.

[174] **Robinson, P.** and **Song, D. Q.**, "A Modified DCB Specimen for Mode I Testing of Multidirectional Laminates," Journal of Composite Materials, Vol. 26, 1992, pp. 1554-1577.

[175] **Rosen, B. W.**, "Tensile Failure of Fibrous Composites," AIAA Journal, Vol. 2, 1964, pp. 1985-1991.

[176] **Ruiz, P.** and **Penzien, J.**, "Stochastic Seismic Response of Structures," ASCE Journal of Engineering Mechanics, Vol. 97, 1971, pp. 441-456.

[177] **Russell, A. J.** and **Street, K. N.**, "Factors Affecting the Interlaminar Fracture Energy of Graphite/Epoxy Laminates," ICCM-4, Tokyo, 1982, pp. 279-286.

[178] **Russell, A. J.** and **Street, K. N.**, "Predicting Interlaminar Fatigue Crack Growth Rate in Compressively Loaded Composites," Composite Materials: Fatigue and Fracture, ASTM STP 1012, 1989, pp. 162-178.

[179] **Rybicki, E. F., Schmueser, D. W.** and **Fox, J.**, "An Energy Release Rate Approach for Stable Crack Growth in the Fiber-Edge Delamination Problem," Journal of Composite Materials, Vol. 11, 1977, pp. 470-487.

[180] **Rybicki, E. F.** and **Schmueser, D. W.**, "Effect of Stacking Sequence and Lay-up Angle on Free Edge Stresses Around a Hole in a Laminated Plate Under Tension," Journal of Composite Materials, Vol. 12, 1978, pp. 300-313.

[181] **Samaras, E. F., Shinozuka, M.** and **Tsurui, A.**, "ARMA Representation of Random Vector Processes," ASCE Journal of Engineering Mechanics, Vol. 111, 1985, pp. 449-461.

[182] **Scop, P. M.** and **Argon, A. S.**, "Statistical Theory of Strength of Laminated Composites," Journal of Composite Materials, Vol. 1, 1967, pp. 92-99.

[183] **Sendeckyj, G. P.**, "A Brief Survey of Empirical Multiaxial Strength Criteria for Composites," Composite Materials: Testing and Design, ASTM STP 497, 1972, pp. 41-51.

[184] **Shao, S., Miki, M.** and **Murotsu, Y.**, "Optimum Fiber Orientation Angle of Multidirectional Laminated Composites Based on Reliability," AIAA Journal, Vol. 31, 1993, pp. 919-920.

[185] **Shiao, M. C., Abumeri, G. H.** and **Chamis, C. C.**, "Probabilistic Assessment of Composite Structures," NASA TM 106368, 1993.

[186] **Shinozuka, M.**, "Simulation of Multivariate and Multidirectional Random Processes," Journal of the Acoustical Society of American, Vol. 49, 1970, pp. 357-367.

[187] **Shinozuka, M.** and **Jan, C.-M.**, "Digital Simulation of Random Processes and Its Application," Journal of Sound and Vibration, Vol. 25, 1972, pp. 111-128.

[188] **Shinozuka, M.**, "Monto Carlo Solution for Structural Dynamics," Computers and Structures, Vol. 2, 1972, pp. 855-874.

[189] **Shinozuka, M.**, "Digital Simulation of Random Processes in Engineering Mechanics with the Aid of FFT Technique," Stochastic Problems in Mechanics, Ariarantnam, S. T. and Leipholz, H. E. (eds.), University of Waterloo Press, Waterloo, Canada, 1974, pp. 277-286.

[190] **Shinozuka, M.**, "Basic Analysis of Structural Safety," Journal of the Structural Division, American Society of Civil Engineers, Vol. 109, 1983, pp. 721-740.

[191] **Shivakumar, K. N.**, Allen, H. G. and Avva, V. S., "Interlaminar Tension Strength of Graphite/Epoxy Composite Laminates," AIAA Journal, Vol. 32, 1994, pp. 1478-1484.

[192] **Shokrieh, M. M., Olivia, P. E., Kotsioprifits, P.** and **Lessard, L. B.**, "Determination of Interlaminar Shear Strength of Graphite/Epoxy Composite Materials in Static and Fatigue Loading," ICCM-10, Vancouver, Canada, 1995, IV-81-88.

[193] **Shokrieh, M. M.** and **Lessard, L. B.**, "Effects of Material Nonlinearity on the Three-Dimensional Stress State of Pin-Loaded Composite Laminates," Journal of Composite Materials, Vol. 30, 1996, pp. 839-861.

[194] **Shyprykevich, P.**, "The Role of Statistical Data Reduction in the Development of Design Allowables for Composites," Test Methods for Design Allowables for Fibrous Composites, ASTM STP 1003, 1989, pp. 111-135.

[195] **Siddall, J. M.**, "Probabilistic Engineering Design: Principles and Applications," Marcel Dekker, Inc., New York. 1983.

[196] **Sneddon, I. N.**, "Fourier Transforms", McGraw-Hill Book Company, Inc., New York, 1951.

[197] **Soni, S. R.** and **Kim, R. Y.**, "Delamination of Composite Laminates Stimulated by Interlaminar Shear," Composite Materials: Testing and Design, ASTM STP 893, 1986, pp. 286-307.

[198] **Soong, T. T.**, "Random Differential Equations in Science and Engineering," Academic Press, Inc., New York, 1973.

[199] **Sperling, U. O.**, "Three-Dimensional Stress Distribution Around Pin Loaded Holes in Composite Laminates," Proceedings of AIAA/ASME/ASCE/AHS 26th Structures, Structural Dynamics and Materials Conference, 1985, pp. 743-750.

[200] **Spilker, R. L.** and **Chou, S. C.**, "Edge Effects in Symmetric Composite Laminates: Importance of Satisfying the Traction-Free-Edge Condition," Journal of Composite Materials, Vol.14, 1980, pp. 2-20.

[201] **Starlinger, A., Duffy, S. F.** and **Gyekenyesi, J. P.**, "Reliability Analysis of Laminated Ceramic Matrix Composites Using Shell Subelement Techniques," AIAA Journal, Vol. 31, 1993, pp. 2181-2183.

[202] **Sun, C. T.** and **Yamada, S. E.**, "Strength Distribution of a Unidirectional Fiber Composites," Journal of Composite Materials, Vol. 12, 1978, pp. 169-176.

[203] **Sun, C. T.**, and **Kelly, S. R.**, "Failure in Composite Angle Structures: Part I – Initial Failure," Journal of Reinforced Plastics and Composites, Vol. 7, 1988, pp. 220-232.

[204] **Sun, C. T.** and **Zhou, S. G.**, "Failure of Quasi-Isotropic Composite Laminates with Free Edges," Journal of Reinforced Plastics and Composites, Vol. 7, 1988, pp. 515-557.

[205] **Tang, S.**, "Interlaminar Stresses Around Circular Cutouts in Composite Plates under Tension," AIAA Journal, Vol. 15, 1977, pp. 1631-1637.

[206] **Tang, S.**, "A Variational Approach to Edge Stresses of Circular Cutout in Composites," Proceedings of AIAA/ASME/ASCE/AHS 20th Structures, Structural Dynamics and Materials Conference, 1979, pp. 326-332.

[207] **Tao, J.** and **Sun, C. T.**, "Influence of Ply Orientation on Delamination in Composite Laminates," Journal of Composite Materials, Vol. 32, 1998, pp. 1933-1947.

[208] **Tarnopol'skii, Yu. M.** and **Kincis, T.**, "Static Test Methods for Composites," Translated from the third, revised and supplemented Soviet edition under the editorship of George Lubin, Van Nostrand Reinhold Company, Inc., 1985.

[209] **Tennyson, R. C., Macdonald, D.** and **Nanyaro, A. P.**, "Evaluation of the Tensor Polynomial Failure Criterion for Composite Materials," Journal of Composite Materials, Vol. 12, 1978, pp. 63-75.

[210] **Tennyson, R. C., Nanyaro, A. P.** and **Wharram, G. E.**, "Application of the Cubic Polynomial Strength Criterion to the Failure Analysis of Composite Materials," Journal of Composite Materials Supplement, Vol. 14, 1980, pp. 28-41.

[211] **Thomas, D. J.** and **Wetherhold, R. C.**, "Reliability Analysis of Continuous Fiber Composite Laminates," Composite Structures, Vol. 17, 1991(a), pp. 277-293.

[212] **Thomas, D. J.** and **Wetherhold, R. C.**, "Reliability Analysis of Composite Laminates with Load Sharing," Journal of Composite Materials, Vol. 23, 1991(a), pp. 1459-1475.

[213] **Timoshenko, S.** and **Goodier, J. N.**, "Theory of Elasticity," McGraw-Hill, New York, 1970.

[214] **Tohgo, K., Hirako, Y.** and **Ishii, H.**, "Mode I Interlaminar Fracture Toughness and Fracture Mechanism of Angle-Ply Carbon/Nylon Laminates," Journal of Composite Materials, Vol. 30, 1996, pp. 650-661.

[215] **Tolf, G.**, "Stresses in a Curved Laminated Beam," Fiber Science and Technology, Vol. 19, 1983, pp. 243-267.

[216] **Tsai, S. W.** and **Azzi, V. D.**, "Strengths of Laminated Composite Materials," AIAA Journal, Vol. 4, 1966, pp. 296-301.

[217] **Tsai, S. W.**, "Strength Theories of Filamentary Structures," Fundamental Aspects of Fiber-Reinforced Plastic Composites, Schwartz, R. T. and Schwartz, H. S. (eds.), Wiley Interscience, New York, 1968.

[218] **Tsai, S. W.** and **Wu, E. M.**, "A General Theory of Strength for Anisotropic Materials," Journal of Composite Materials, Vol. 5, 1971, pp. 58-80.

[219] **Tsai, S. W.**, "A Survey of Macroscopic Failure Criteria for Composite Materials," Journal of Reinforced Plastics and Composites, Vol. 3, 1984, pp. 40-64.

[220] **Vanmarcke, E.**, "Random Fields," MIT Press, Cambridge, 1983.

[221] **Vanmarcke, E.** and **Grigoriu, M.**, "Stochastic Finite Element Analysis of Simple Beams," ASCE Journal of Engineering Mechanics, Vol. 109, 1983, pp. 1203-1214.

[222] **Vanmarcke, E., Shinozuka, M., Nakagiri, S., Schueller, G.** and **Grigoriu, M.**, "Random Fields and Stochastic Finite Element Methods," Structural Safety, Vol. 3, 1986, pp. 143-166.

[223] **Vizzini, A. J.**, "Influence of Realistic Ply-Drop Geometries on Interlaminar Stresses in Tapered Laminates," Composite Materials: Fatigue and Fracture, ASTM STP 1230, 1995, pp. 467-485.

[224] **Von Mises, R.**, "Mechanik der festen Koerper im plastisch deformablen Zustand," Math. Phys., Klasse, 1913, pp. 582-592.

[225] **Von Mises, R.**, "Mechanic der plastischen Formanderung von Kristallen," Z. Angew, Math. Mech., Vol. 8, 1928, pp. 161-185.

[226] **Waddoups, M. E.** and **Eisenman, J. R.** and **Kaminski, B. E.**, "Macroscopic Fracture Mechanics of Advanced Composite Materials," Journal of Composite Materials, Vol. 5, 1971, pp. 446-454.

[227] **Wang, A. S. D.** and **Crossman, W. K.**, "Some New Results on Edge Effects in Symmetric Composite Laminates," Journal of Composite Materials, Vol. 11, 1977, pp. 300-312.

[228] **Wang, A. S. D., Chou, P. C.** and **Lei, S. C.**, "A Stochastic Model for the Growth of Matrix Cracks in Composite Laminates," Journal of Composite Materials, Vol. 18, 1984, pp. 239-254.

[229] **Wang, A. S. D., Slomiana, M.** and **Bucinell, R. B.**, "Delamination Crack Growth in Composite Laminates," Delamination and Debonding of Materials, ASTM STP, 876, 1985, pp. 135-167.

[230] **Wang, S. S.** and **Choi, I.**, "Boundary-Layer Hygroscopic Stress in Angly-Ply Composite Laminates," AIAA Journal, Vol. 20, 1982, pp. 1592-1598.

[231] **Watanabe, N.** and **Okada, T.**, "Stress and Failure Analysis of Cross-Plied Curved Composite Laminates," AIAA Journal, 1995, Vol. 33, pp. 2433-2435.

[232] **Weibull, W.**, "A Statistical Theory of the Strength of Materials," Proceedings of Royal Sweden Institute of Engineering Research, No. 151, Stockholm, Sweden, 1939.

[233] **Weibull, W.**, "A Statistical Distribution Function of Wide Applicability," ASME Journal of Applied Mechanics, Vol. 18, 1951, pp. 293-297.

[234] **Weil, N. A.** and **Daniel, I. M.**, "Analysis of Fracture Probabilities in Nonuniformly Stresses Brittle Materials," Journal of The American Ceramic Society, Vol. 47, 1964, pp. 268-274.

[235] **Wetherhold, R. C.**, "Reliability Calculations for Strength of Fibrous Composite under Multiaxial Loading," Journal of Composite Materials, Vol. 15, 1981, pp. 240-248.

[236] **Whitcomb, J. D., Raju, I. S.** and **Goree, J. G.**, "Reliability of the Finite Element Method for Calculating Free Edge Stresses in Composite Laminates," Computers and Structures, Vol. 15, 1982, pp. 23-37.

[237] **Whitcomb, J. C.**, "Analysis of a Laminate with a Postbuckled Embedded Delamination, Including Contact Effects," Journal of Composite Materials, Vol. 26, 1992, pp. 1523-1535.

[238] **Whitney, J. M.**, "On the Use of Shell Theory for Determining Stresses in Composite Cylinders," Journal of Composite Materials, Vol. 5, 1971, pp. 340-353.

[239] **Whitney, J. M.** and **Nuismer, R. J.**, "Stress Fracture Criteria for Laminated Composites Containing Stress Concentrations," Journal of Composite Materials, Vol. 8, 1974, pp. 253-265.

[240] **Whitney, J. M.**, **Daniel, I. M.** and **Pipes, R. B.**, "Experimental Mechanics of Fiber Reinforced Composite Materials," Prentice-Hall, Inc., New Jersey, 1982.

[241] **Whitney, J. M.** and **Browning, C. E.**, "On Short-Beam Shear Tests for Composite Materials," Experimental Mechanics, 1985, pp. 294-300.

[242] **Whitney, J. M.**, "Reflections on the Development of Tests Methods for Advanced Composites," Composite Materials: Testing and Design, ASTM STP 1120, 1992, pp. 7-16.

[243] **Wisnom, M. R.**, "Relationship Between Strength Variability and Size Effect in Unidirectional Carbon Fiber/Epoxy," Composites, Vol. 22, 1991, pp. 47-52.

[244] **Wu, E. M.**, "Optimal Experimental Measurements of Anisotropic Failure Tensors," Journal of Composite Materials, Vol. 6, 1972, pp. 472-489.

[245] **Wu, E. M.**, "Phenomenological Anisotropic Criterion," Treatise on Composite Materilas, Broutman, Krock and Sendeckyi, Eds., Academic Press, 1973.

[246] **Wu, E. M.** and **Scheublein, J. K.**, "Laminate Strength – A Direct Characterization Procedure," Composite Materials: Testing and Design (Third Conference), ASTM STP546, 1975, pp. 188-206.

[247] **Xaio, J.** and **Li, S. -L.**, "On Mode-II Delamination Fracture Toughness of Multi-Directional Interface in Composite Laminae," ICCM-7, 1989, Guangzhou, China, pp. 669-674.

[248] **Yamada, S. E.** and **Sun, C. T.**, "Analysis of Laminate Strength and Its Distribution," Journal of Composite Materials, Vol. 1978, pp. 275-284.

[249] **Yamazaki, F.** and **Shinozuka, M.**, "Digital Generation of Non-Gaussian Stochastic Fields," ASCE Journal of Engineering Mechanics, Vol. 114, 1988, pp. 1183-1197.

[250] **Yang, L.**, "Reliability of Composite Laminates," Mechanics of Structures and Machines, Vol. 16, 1988-1989, pp. 523-536.

[251] **Yang, L.** and **Ma, Z. K.**, "A Method of Reliability Analysis and Enumeration of Significant Failure Modes for a Composite Structural System," Computers and Structures, Vol. 33, 1989, pp. 337-344.

[252] **Yeh, H.-Y.** and **Kim, C. H.**, "The Yeh-Stratton Criterion for Composite Materials," Journal of Composite Materials, Vol. 28, 1994, pp. 926-939.

[253] **Yushanov, S. P.** and **Joshi, S. P.**, "Stochastic Modelling of Fracture Process in Fiber Reinforced Composites," AIAA Journal, Vol. 33, 1995, pp. 1689-1697.

[254] **Zhang, C.** and **Zhu, T.**, "On Interrelationships of Moduli and Strains in Cross-ply laminated Composites," Composites Science and Technology, Vol. 56, 1996, pp. 131-142.

[255] **Zhang, C.**, **Lessard, L. B.** and **Nemes, J. A.**, "A Closed Form Solution for Stresses at Curved-Free-Edges in Composite Laminates – Variational Approach," Composites Science and Technology, Vol. 57, 1997, pp.1341-1354.

[256] **Zhang, C., Hoa, S. V.** and **Ganesan, R.**, "Edge Effects in Laminated Composites with Pin-Loaded Holes," AIAA Journal, Vol. 36, 1998(a), pp. 1883-1893.

[257] **Zhang, C., Hoa, S. V.** and **Ganesan, R.**, "Approximate Solutions for Stresses Around Pin-Loaded Holes in Composite Laminates," Journal of Reinforced Plastics and Composites, Vol. 17, 1998(b), pp. 800-818.

[258] **Zhang, C.** and **Yeh, H.-Y.**, "A Variational Approach for Straight Edge Effect Stresses in Laminated Composites," Composite Structures, Vol. 43, 1998(a), pp. 243-254.

[259] **Zhang, C.** and **Yeh, H.-Y.**, "An Analytical Model for Thermal Residual Interface-Stresses in Continuous-Fiber-Reinforced Composites," International Journal of Solids and Structures, Vol. 35, 1998(b), pp. 457-477.

[260] **Zhang, C., Ganesan, R.**, and **Hoa, S. V.**, "Analytical Solutions to Three-Dimensional Edge Stresses in Laminated Composites with Circular Holes," CANCAM, Kingston, Canada, 1999(a).

[261] **Zhang, C., Ganesan, R.**, and **Hoa, S. V.**, "Experimental Characterization and Stochastic Modeling of Interlaminar Shear Strengths of Graphite/Epoxy Laminated Composites," ICCM-12, Paris, France, 1999(b).

[262] **Zhang, C., Ganesan, R.** and **Hoa, S. V.**, "Effects of Friction on 3D Contact Stresses in Pin-Loaded Laminated Composites," Journal of Composite Materials, Vol. 34, 2000(a), pp.1382-1415.

[233] **Zhang, C., Hoa, S. V.** and **Ganesan, R.**, "Through-the-Thickness Compressive Strengths of Graphite/Epoxy Laminated Composites: Experimental Characterization and Statistical Analysis," submitted to Composites Science and Technology, 2000(b).

[264] **Zhang, C., Hoa, S. V.** and **Ganesan, R.**, "Interlaminar Shear Strengths of Graphite/Epoxy Laminated Composites. Part I: Experimental Characterization," Submitted to Journal of Composite Materials, 2000(c).

[265] **Zhang, C., Hoa, S. V.** and **Ganesan, R.**, "Interlaminar Shear Strengths of Graphite/Epoxy Laminated Composites. Part II: Stochastic Simulation Using a Random Parametric Approach," Submitted to Journal of Composite Materials, 2000(d).

[266] **Zhang, K. D.** and **Ueng, C. E. S.**, "Stresses Around a Pin-Loaded Hole in Orthotropic Plates," Journal of Composite Materials, Vol. 18, 1984, pp. 432-446

[267] **Zhang, K. D.**, and **Ueng, C. E. S.**, "A Simplified Approach for Interlaminar Stresses Around a Hole in $[0/90]_s$ Laminates," Journal of Composite Materials, Vol. 22, 1988, pp. 192-202.

[268] **Zhu, T. Y.** and **Zong, G. S.**, "On the Application of the Statistical Strength Model of Fiber-Reinforced Composites," Journal of Composite Materials, Vol. 27, 1993, pp. 944-959.

[269] **Zhou, S. G.** and **Sun, C. T.**, "Failure Analysis of Composite Laminates with Free Edges," Journal of Composite Technology and Research, Vol. 12, 1990, pp. 91-97.

[270] **Zweben, C.**, "Tensile Failure Analysis of Fibrous Composites," AIAA Journal, Vol. 6, 1968, pp. 2325-2332.